



# Proceedings of the First Army Research Laboratory Acousto- Optic Tunable Filter Workshop

by Neelam Gupta

ARL-SR-54

March 1997

19970512 149

DTIC QUALITY INSPECTED 3

Approved for public release; distribution unlimited.

The findings in this report are not to be construed as an official Department of the Army position unless so designated by other authorized documents.

Citation of manufacturer's or trade names does not constitute an official endorsement or approval of the use thereof.

Destroy this report when it is no longer needed. Do not return it to the originator.

## CORRECTION

Due to an unexpected mix up, incorrect title, authors' names, and affiliation were printed for the viewgraphs on pages 47-57 in the *Viewgraph Supplement to the Proceedings of the First Army Research Laboratory Acousto-Optic Tunable Filter Workshop*, ARL-SR-54-S, March 1997. Page 47 should read as follows:

**Application of AOTF in Analytical Chemistry, C. D. Tran, Marquette University, Milwaukee, WI.**

We sincerely regret this unfortunate error.

*Neelan Gupta*

Neelam Gupta

Army Research Laboratory

2800 Powder Mill Road

Adelphi, MD 20783-1197

7 April, 1997

# Army Research Laboratory

Adelphi, MD 20783-1197

---

ARL-SR-54

March 1997

---

## Proceedings of the First Army Research Laboratory Acousto- Optic Tunable Filter Workshop

Neelam Gupta, Editor

Sensors and Electron Devices Directorate, ARL

**DTIC QUALITY INSPECTED 3**

---

Approved for public release; distribution unlimited.

---



---

## Abstract

---

Acoustic-optic tunable-filter (AOTF) technology is a recent development that offers potential for rapid, frequency-agile tuning over a large optical wavelength range. An AOTF is an electronically tunable phase grating set up in an anisotropic crystal by the propagation of an ultrasonic wave in the crystal. Such filters have many attractive features, such as small size, lightweight, computer controlled operation, large optical wavelength range of operation, and no moving parts; and their operation can be made ultrasensitive by the use of advanced signal processing algorithms. These filters are being used in many applications such as the design of new spectroscopic instruments, remote detection and monitoring of chemicals, optical communication networks, tuning of laser cavities, etc.

## Foreword

Acousto-optic tunable filter technology (AOTF) has made significant progress in the last 30 years. These electronically tunable filters are finding many applications in various fields, such as chemical and environmental sensing, communications, hyperspectral imaging, pharmaceuticals, medicine, semiconductor processing, space exploration, etc. Due to their compact size and no moving parts, AOTF's offer numerous advantages over traditional grating-based technology. There is a tremendous potential offered by this technology, which remains to be fully utilized. One of the main motivations in organizing this workshop, the first of its kind, was to create a forum of experts and users that would provide the synergy to give a much needed impetus for the rapid development and exploitation of this promising technology.

In the Fall of 1995, I had the great privilege of visiting many Russian institutions involved in the research and development of this technology, and meeting with Russian scientists working in this field. This experience gave me the idea to bring U.S. and Russian scientists together for an intimate exchange of information and ideas for the advancement of AOTF technology. This workshop provided an avenue to implement this idea.

It has been a great deal of work to pull this workshop together, but the outcome has been worth many times the effort. It was a great experience to listen to the experts as well as the newcomers talk about AOTF basic research and applications for two full days.

I would like to thank my sponsors at the Army Materiel Command (AMC) and Army Research Laboratory (ARL) for providing the necessary funds to make this workshop possible. I would also like to thank every attendee for participating in this workshop, especially the Russian scientists for taking this long trip.

Neelam Gupta  
Army Research Laboratory  
Adelphi, MD, USA

# Contents

Foreword .....	i
Agenda .....	1
List of Attendees .....	5

## AOTF Technology

1. An AOTF Technology Overview .....	11
N. Gupta, Army Research Laboratory, USA	
2. Progress of Acoustic-Optic Tunable Filters .....	21
I. C. Chang, Aurora Associates, USA	
3. Collinear AOTF Spectrometers and Their Applications .....	33
V. I. Pustovoit, Central Bureau of Unique Instrumentation of Russian Academy of Sciences, Russia;	
N. Gupta, Army Research Laboratory, USA	
4. Recent Advances in AOTF Design and Fabrication at St. Petersburg at State Academy of Aerospace Instrumentation .....	45
V. V. Kludzin, S. V. Kulakov, and V. V. Molotok, St. Petersburg State Academy of Aerospace Instrumentation, Russia	
5. Application of Acousto-Optic Interaction for Filtration of Arbitrary Polarized Radiation .....	55
V. B. Voloshinov, M. V. Lomonosov Moscow State University, Russia	
6. Improvement of Resolution of Visible Acousto-Optic Tunable Filter in Tellurium Dioxide .....	65
V. Pelekhaty, Brimrose Corp. of America, USA	
7. Growth of AO Crystals with High Anisotropy and Development of Multichannel AO Devices .....	79
Y. B. Pisarevsky, Institute of Crystallography of Russian Academy of Sciences, Russia	
8. Progress in AOTF Technology for WDM Systems .....	87
D. A. Smith and A. A. Patil, Case Western Reserve University, USA	
9. Integrated Acousto-Optic Tunable Filters for Blue-Green Spectral Region .....	101
C. S. Tsai and A. M. Matteo, University of California, Irvine, USA	

## Applications for Chemical Sensing

10. Application of Acousto-Optic Tunable Filters in Analytical Chemistry .....	111
C. D. Tran, Marquette University, USA	
11. Application of AOTF Technology for Chem/Bio Detection .....	137
N. Gupta and N. F. Fell, Jr., Army Research Laboratory, USA	

## Contents (cont'd)

### Applications for Chemical Sensing (cont'd)

- 12. Solving Process Problems with AOTF-Based NIR Spectroscopy ..... 149  
S. Medlin, C. Westgate, W. Danley, and U. Eschenaur, Brimrose  
Corp. of America, USA
- 13. Application of AOTFs to High Fidelity Spectroscopic Imaging ..... 165  
E. N. Lewis, L. H. Kidder, I. W. Levin, and S. R. Goldstein, National  
Institutes of Health, USA

### Applications for Imaging

- 14. Factors Affecting AOTF Image Quality ..... 179  
L. J. Denes, B. Kaminsky, M. Gottlieb, and P. Metes, Carnegie Mellon  
Research Institute, USA
- 15. An AOTF Camera for Multispectral Imaging ..... 189  
S. Aimizu, R. T. Obermyer, C. J. Thong, M. J. Uschak, and  
S. G. Sankar, Advanced Materials Corporation, USA; L. J. Denes,  
D. A. Purta, and M. Gottlieb, Carnegie Mellon Research Institute, USA
- 16. Simultaneous Multispectral Imaging with a 12 Parallel Channel Tunable  
Camera ..... 199  
J. A. Carter III and D. R. Pape, Photonics Systems Inc., USA;  
M. L. Shah, MVM Electronics Inc., USA
- 17. Polarimetric Hyperspectral Imaging Systems and Applications ..... 205  
L.-J. Cheng, C. Mahoney, G. Reyes, and C. LaBaw, Jet Propulsion  
Laboratory, USA; G. P. Li, University of California, Irvine, USA
- 18. Multiplexing Methods in AOTF multispectral Imaging (**Paper Not Available**)  
P. Treado and J. Turner, University of Pittsburgh, USA
- 19. Multispectral Imaging using Acousto-Optic Tunable Filter (AOTF) ..... 215  
T. Vo-Dinh, D. Hueber, and F. Moreau, Oak Ridge National Laboratory, USA
- Photographs from the Workshop ..... 223
- Distribution ..... 229
- Report Documentation Page ..... 231

# **First ARL Workshop on Acousto-Optic Tunable Filter Technology**

Center for Adult Education, University of Maryland, College Park, MD

**Tuesday, September 24, 1996**  
**AOTF Technology**

## **Morning Session, Chair Andree Filipov, USARL-SEDD**

- 8:30 - 8:55 Check-in/Registration/Continental Breakfast
- 8:55 - 9:00 Administrative Announcements
- 9:00 - 9:20 Welcome & ARL Overview, John Pellegrino, Director, Sensors and Electron Devices Directorate, US Army Research Laboratory
- 9:20 - 9:40 AOTF Overview, Neelam Gupta, USARL
- 9:40 - 10:10 Progress in AOTF Technology, I. C. Chang, Aurora Associates, Santa Clara, CA
- 10:10 - 10:40 Break
- 10:40 - 11:10 Collinear AOTF Spectrometers: Problems, Results, Methods of Spectral Measurements, V. I. Pustovoyt, Central Bureau of Unique Instrumentation, Moscow, Russia, and N. Gupta, USARL
- 11:10 - 11:40 Recent Advances in AOTF Design and Fabrication at SPSAAI, V. V. Kludzin, S. V. Kulakov, and V. V. Molotok, St. Petersburg State Academy of Aerospace Instrumentation, St. Petersburg, Russia
- 11:40 - 1:00 Lunch

## **Afternoon Session, Chair Neelam Gupta, USARL-SEDD**

- 1:00 - 1:30 Application of AO Interaction for Filtration of Arbitrary Polarized Radiation, V. Voloshinov, Physics Department, Moscow State University, Moscow, Russia
- 1:30 - 2:00 Improvement of Resolution of Visible AOTF in TeO<sub>2</sub>, V. Pelekhaty, Brimrose Corp. Of America, Baltimore, MD
- 2:00 - 2:30 Growth of Acousto-optic Crystals with High Anisotropy and Development of Multichannel Acousto-optical Processors, Y. B. Pisarevsky
- 2:30 - 3:00 Break

- 3:00 - 3:30 Progress in AOTF Technology for WDM Systems, D. Smith, Case Western Reserve University, Cleveland, OH
- 3:30 - 4:00 Integrated AOTF for Blue-Green Spectral Region, C. S. Tsai and A. M. Matteo, University of California, Irvine, CA
- 4:00 - 5:00 AOTF Demonstrations
- 6:30 Banquet, University Of Maryland, College Park

**Wednesday, September 25, 1996**  
**AOTF Applications**

**Morning Session, Chair Andrzej Miziolek, USARL-WMRD**

- 8:30 - 9:00 Registration/Continental Breakfast
- 9:00 - 9:30 Application of AOTF in Analytical Chemistry, C. D. Tran, Marquette University, Milwaukee, WI
- 9:30 - 10:00 Application of AOTF Technology for Chem/Bio Detection, N. Gupta and N. F. Fell Jr., US Army Research Laboratory, Adelphi, MD
- 10:00 - 10:30 Break
- 10:30 - 11:00 An AOTF-Based Near-Infrared Spectrometer for Process Control, S. Medlin, U. Eschenaur, and W. Danley, Brimrose Corp. Of America, Baltimore MD
- 11:00 - 11:30 Application of AOTF to Near IR Spectroscopy and High Fidelity Spectroscopic Imaging, E. N. Lewis, National Institutes of Health, Bethesda, MD
- 11:30 - 1:00 Lunch

**Afternoon Session, Chair James Gillespie, USARL-ISTD**

- 1:00 - 1:30 Factors Affecting AOTF Image Quality, L. J. Denes, B. Kaminsky, M. Gottlieb, and P. Metes, Carnegie Mellon Research Institute, Pittsburgh, PA
- 1:30 - 2:00 An AOTF Camera for Multispectral Imaging, S. Simizu, R. T. Obermyer, C. J. Thong, M. Uschak, S. G. Sankar, Advanced Materials Corp., Pittsburgh, PA, D. J. Denes, D. A. Purta, and M. Gottlieb, Carnegie Mellon Research Institute, Pittsburgh, PA
- 2:00 - 2:30 Simultaneous Multispectral Imaging with a 12 Parallel Channel Tunable Camera, J. A. Carter III, D. R. Pape, Photonics Systems, Inc., Melbourne, FL, and M. L. Shah, MVM Electronics, Inc., Melbourne, FL

- 2:30 - 3:00      Break
- 3:00 - 3:30      Polarimetric Hyperspectral Imaging Systems, L.-J. Cheng, G. Reyes, and  
C. La Baw, Jet Propulsion Laboratory, CA, and G. P. Li, University of  
California, Irvine, CA
- 3:30 - 4:00      Multiplexing Methods in AOTF Multispectral Imaging, P. Treado, and J.  
Turner, University of Pittsburgh, Pittsburgh, PA
- 4:00 - 4:30      Remote Spectral Imaging System Based on an AOTF, T. Vo-Dinh, Oak  
Ridge National Laboratory, Oak Ridge, TN
- 4:30              Workshop Closing

**List of Attendees—First ARL Workshop on AOTF Technology, September 24–25, 1996**

Dr. Ish Aggarwal  
Naval Research Laboratory  
Code 5603  
Washington D.C. 20375  
Phone: (202) 767-9316  
Fax: (202) 767-9311  
E-mail: ish.aggarwal@nrl.navy.mil

Mr. James A. Carter III  
Photonic Systems Inc.  
1800 Penn Street, Suite 6  
Melbourne, FL 32901  
Phone: (407) 984-8181  
Fax: (407) 952-7748  
E-mail: jcarter@photon-sys.com

Dr. I. C. Chang  
Aurora Associates  
3350 Scott Blvd., B-20  
Santa Clara, CA 95054  
Phone: (408) 748-2960  
Fax: (408) 748-2962  
E-mail: AurorAssoc@aol.com

Dr. Carl L. Chen  
Brookhaven National Laboratory  
Bldg 197C, DAT/SSN  
Upton, NY 11973  
Phone: (516) 344-3152  
Fax: (516) 344-7533  
E-mail: chen1@bnl.gov

Dr. Li-Jen Cheng  
Jet Propulsion Laboratory  
M/S 300-329  
4800 Oak Grove Drive  
Pasadena, CA 91109  
Phone: (818) 354-9510  
Fax: (818) 393-4820  
E-mail: li-jen.cheng@jpl.nasa.gov

Dr. Dominique Daganais  
SFA@Naval Research Laboratory  
Optical Science Division  
Code 5603  
Washington D.C. 20375  
Phone: (202) 767-9347  
Fax: (202) 767-9257  
E-mail: daganais@nrlfa1.nrl.navy.mil

Mr. William J. Danley  
Brimrose Corporation of America  
5020 Campbell Blvd.  
Baltimore, MD 21236  
Phone: (410) 931-7200  
Fax: (410) 931-7206  
E-mail: wdanley@brimrose.com

Mr. Clyde DeLuca  
Army Research Laboratory  
2800 Powder Mill Road  
Adelphi, MD 20783  
Phone: (301) 394-4163  
Fax: (301) 394-1170  
E-mail: dell@arl.mil

Dr. Louis J. Denes  
Carnegie Mellon Research Inst.  
700 Technology Drive, P.O. Box 2950  
Pittsburg, PA 15230-2950  
Phone: (412) 268-3469  
Fax: (412) 268-7759  
E-mail: ld2s@andrew.cmu.edu

Dr. Nick Fell  
Army Research Laboratory  
2800 Powder Mill Road  
Adelphi, MD 20783  
Phone: (301) 394-2145  
Fax: (301) 394-1170  
E-mail: nfell@vax1.arl.mil

Mr. Andree Filipov  
Army Research Laboratory  
2800 Powder Mill Road  
ADELPHI, MD 20783  
Phone: (301) 394-2521  
Fax: (301) 394-4214  
E-mail: filipov@arl.mil

Dr. James B. Gillespie  
Army Research Laboratory  
2800 Powder Mill Road  
Adelphi, MD 20783  
Phone: (301) 394-1880  
Fax: (301) 394-1170  
Email: jdillesp@arl.mil



**List of Attendees—First ARL Workshop on AOTF Technology, September 24–25, 1996**

John Goodell  
1201 Southview Rd  
Baltimore, MD 21218  
Phone: (410) 243-1613  
Fax: (410) 243-1613  
Email: pwhd47a@prodigy.com

Dr. Neelam Gupta  
AMSRL-SE-EO  
Army Research Laboratory  
2800 Powder Mill Road  
Adelphi, MD 20783  
Phone: (301) 394-2451  
Fax: (301) 394-1170  
E-mail: Ngupta@arl.mil

Dr. Milton Gottlieb  
Carnegie Mellon Research Institute  
700 Technology Drive, P.O. Box 2950  
Pittsburg, PA 15230-2950  
Phone: (412) 268-7845  
Fax: (412) 268-7759  
E-mail: mg6b@andrew.cmu.edu

Mr. Jeffrey S. Himmel  
Army Research Laboratory  
AMSRL-PS-ED  
Fort Monmouth, NJ 07703-5601  
Phone: (908) 427-2375  
Fax: (908) 427-4805  
E-mail: jhimmel@arl.mil

Mr. Dan Heglund  
Brookhaven National Laboratory  
Box 5000 Bldg 701  
Upton, NY 11973  
Phone: (516) 344-4069  
Fax: (516) 344-1427  
E-mail: heglund@bnl.gov

Mr. Boris Kaminsky  
Carnegie Mellon Research Institute  
700 Technology Drive, P. O. Box 2950  
Pittsburg, PA 15230-2950  
Phone: (412) 268-6439  
Fax: (412) 268-7759  
Email: borisk@andrew.cmu.edu

Dr. James O. Jensen  
ERDEC  
Attn: SCBRD-RTE-E3549  
APGEA, Edgewood, MD  
Phone: (410) 671-5665  
Fax: (410) 671-3160  
Email: jojensen@cbdcom.apgea.army.mil

Dr. Edwin D. Lancaster  
AMSRL-WT-PC  
Army Research Laboratory  
APG MD 21005-5066  
Phone: (410) 278-6155  
Fax: (410) 278-6150  
Email: elancast@arl.mil

Prof. Victor V. Kludzin  
St. Petersburg State Academy of  
Aerospace Instrumentation  
67, B. Morskaya Str.  
St. Petersburg 100000, RUSSIA  
Phone: +7 (812) 1084204  
Fax: +7 (812) 1084204  
Email: molotok@softjoys.ru

Mr. Dan McCarthy  
Army Research Laboratory  
2800 Powder Mill Road  
Adelphi, MD 20783  
Phone: (301) 394-2463  
Fax: (301) 394-1170  
Email: dan@sig1.arl.mil

Dr. E. Neil Lewis  
National Institute of health  
Bldg 5, Room B1-38  
Bethesda, MD 20892  
Phone: (301) 496-6847  
Fax: (301) 496-0825  
Email: neil@spy.nidk.nih.gov

Mr. Lawrence J. Mizerka  
Night Vision Directorate  
10221 Burbeck Road, Suite 430  
Fort Belvoir, VA 22060-5806  
Phone: (703) 704-3666  
Fax: (703) 704-1752  
Email: lmizerka@nvl.army.mil

**List of Attendees – First ARL Workshop on AOTF Technology, September 24–25, 1996**

Dr. Kevin L. McNesby  
AMSRL-WT-PC  
Army Research Laboratory  
APG MD 21005-5066  
Phone: (410) 278-6163  
Fax: (410) 278-6150  
Email: mcnesby@arl.mil

Dr. Victor V. Molotok  
St. Petersburg State Academy of  
Aerospace Instrumentation  
67, B. Morskaya Str  
St. Petersburg 100000, Russia  
Phone: 7-812-108-42-04  
Fax: 7-812-108-42-04  
Email: molotok@softjoys.ru

Dr. Andrzej W. Miziolek  
Army Research Laboratory  
AMSRL-WM-PC  
Aberdeen, MD 21005-5066.  
Phone: (410) 278-6157  
Fax: (410) 278-6150  
Email: miziolek@arl.mil

Dr. Vladimir Pelekhaty  
Brimrose Corp. of America  
5020 Campbell Blvd  
Baltimore, MD 21236  
Phone: (410) 931-7200  
Fax: (410) 931-7206  
Email: vlad@brimrose.com

Mr. Dennis R. Pape  
Photonic Systems Incorporated  
1800 Penn Street, Suite 6.  
Melbourne, FL 32901  
Phone: (407) 984-8181  
Fax: (407) 952-7748  
Email: dpape@snap.org

Dr. Piotr Becla  
Massachusetts Inst. of Technology  
Room 13-4111  
Cambridge, MA 02139  
Phone: (617) 253-6940

Dr. John Pellegrino  
Army Research Laboratory  
2800 Powder Mill Road  
Adelphi, MD 20783  
Phone: (301) 394-4617  
Fax: (301) 394-2092  
Email: john\_pellegrino@arl.mil

Prof. Vladislav I. Pustovoit  
Central Design Bureau for  
Unique Instrumentation  
117342 Moscow, Russia  
Phone: 7-095-333-61-02  
Fax: 7-095-334-75-00  
Email: slava@pvi.compnet.ru

Dr. Yuri Pisarevsky  
Institute of Crystallography  
Moscow, Russia  
Phone: 7-095-330-68-83  
Fax: 7-095-330-19-56  
Email: pisarev@robust.msk.ru

Dr. S. G. Sankar  
Advanced Materials Corporation  
700 Technology Drive, Suite 3311  
Pittsburgh, PA 15230-2950  
Phone: (412) 268-5649  
Fax: (412) 268-3300  
Email: amc@advanced-material.com

Capt. Alan C. Samuels  
ERDEC  
APGEA, Edgewood, MD  
Phone: (410) 671-5665  
Fax: (410) 671-3160  
Email:

Prof. David A. Smith  
Dept. of Electrical Engineering  
Case Western Reserve University  
Cleveland, OH 44106  
Phone: (216) 368-4073  
Fax: (216) 368-2668  
Email: das23@go.cwru.edu

**List of Attendees – First ARL Workshop on AOTF Technology, September 24–25, 1996**

Satoru Simizu  
Advanced Materials Corporation  
700 Technology Drive, Suite 3311  
Pittsburgh, PA 15230-2950  
Phone: (412) 268-5650  
Fax: (412) 268-3300  
Email: simizu@andrew.cmu.edu

Prof. Chieu Tran  
Dept. of Chemistry  
Marquette University, P. O. Box 1881  
Milwaukee, WI 53201  
Phone: (414) 288-5428  
Fax: (414) 288-7066  
Email: 6607tranc@vms.csd.mu.edu

Mr. Chee J. Thong  
Advanced Materials Corporation  
700 Technology Drive, Suite 3311  
Pittsburgh, PA 15230-2950  
Phone: (412) 268-5121  
Fax: (412) 268-3300  
Email: cjthong@cmu.edu

Prof. Chen S. Tsai  
Dept. of Elect. & Computer Eng  
Engineering Gateway BldG.,  
University of California,  
Irvine, CA 92697  
Phone: (714) 824-5144  
Fax: (714) 824-3732  
Email: cstsai@uci.edu

Dr. Sudhir Trivedi  
Brimrose Corporation of America.  
5020 Campbell Blvd.  
Baltimore, MD 21236  
Phone: (410) 668-5800  
Fax: (410) 668-4835  
Email: strivedi@brimrose.com

Mr. Michael Uschak  
Advanced Materials Corporation  
Pittsburgh, PA 15230-2950  
700 Technology Drive, Suite 3311,  
Phone: (412) 268-5121  
Fax: (412) 268-3300  
Email: mu2a@anorsw.cmu.edu

Mr. John Turner  
University of Pittsburgh  
Chevron Science Center, Room 314  
Pittsburgh, PA 15260  
Phone: (412) 521-2407  
Fax: (412) 521-2407  
Email: jftst2+@pitt.edu

Prof. Vitaly Voloshinov  
Moscow State University  
Dept. of Physics  
119899 Moscow, Russia  
Phone: 7-095-939-44-04  
Fax: 7-095-292-65-11  
Email: volosh@osc162.phys.msu.su

Dr. Tuan Vo-Dinh  
Oak Ridge National Laboratory  
P. O. Box 2008, MS-6101  
Oak Ridge, TN 37831-6101  
Phone: (423) 574-6249  
Fax: (423) 576-7651  
Email: tvo@ornl.gov

Mr. Eddie Young  
Neos Technologies, Inc  
4300C Fortune Place,  
Melbourne, FL 32904  
Phone: (407) 676-9020  
Fax: (407) 722-4499  
Email: ehy@palmnet.net

## **AOTF Technology**

## **An AOTF Technology Overview**

**Neelam Gupta**

*Sensors and Electron Devices Directorate*

*Army Research Laboratory*

*2800 Powder Mill Road*

*Adelphi, MD 20783-1197*

*Phone: (301) 394-2451*

*email:NGupta@arl.mil*

### **Abstract**

Acousto-optic tunable-filter (AOTF) technology is a recent development that offers potential for rapid, frequency-agile tuning over a large optical wavelength range. An AOTF is an electronically tunable phase grating set up in an anisotropic crystal by the propagation of an ultrasonic wave in the crystal. Such filters have many attractive features, such as small size, lightweight, computer controlled operation, large optical wavelength range of operation, and no moving parts; and their operation can be made ultrasensitive by the use of advanced signal processing algorithms. These filters are being used in many applications such as the design of new spectroscopic instruments, remote detection and monitoring of chemicals, optical communication networks, tuning of laser cavities, etc.

### **1. Introduction**

An acousto-optic tunable-filter (AOTF) is an electronically tunable phase grating set up in an anisotropic crystal by the propagation of an ultrasonic wave in the crystal. Such filters contain no moving parts and offer high-speed wavelength tuning. Such tuning can be done sequentially or randomly, depending upon the programmed instructions for the applied radio frequency (rf). AOTFs are finally beginning to replace conventional grating technology based optical instruments in a wide range of filtering, sensing, and imaging applications that can benefit from the size, speed, ruggedness, reproducibility, and accuracy of AOTFs. In this paper, I present the historical development of AOTF technology.

### **2. Developments of AOTF Technology**

Acousto-optics (AO) deals with the interaction of sound and light. Such an interaction in crystals was theoretically predicted by Brillouin in 1922 [1] and was experimentally verified by Debye and Sears in 1932 in the U.S. [2]. In such an interaction a moving transmission grating is set up in the crystal by the alternating planes of compression and rarefaction created by a propagating sound wave, and the incident light is diffracted similarly to the diffraction of x-rays in crystals. The grating constant is equal to the wavelength of the sound wave in the crystal and can be easily changed by changing the frequency of the acoustic wave. Fundamental operation of an AO device can be described as follows. A high-frequency electrical signal is converted into an ultrasonic wave by a piezoelectric oscillator (transducer) bonded to an AO medium; the sound wave travels through

the medium and diffracts light in a certain direction. Much progress has been made in AO system design and applications due to the development of lasers as coherent light sources, high-frequency acoustic transducers, and materials with excellent acoustic and optical properties with large photo-elastic constants. These days, AO modulators and beam deflectors are widely used in commercial laser applications, such as laser printers and scanners.

Even though so much progress was achieved in AO, the effect responsible for an AOTF was not discovered until much later because, until 1967, the discussion of AO interaction was confined to only isotropic crystals. The AO interaction in anisotropic crystals was first discovered in 1967 by Dixon [3]. Two years later, Harris and Wallace [4] used this effect to propose the design of a collinear AOTF in lithium niobate ( $\text{LiNbO}_3$ ), and in the later part of 1969, the first collinear AOTF in  $\text{LiNbO}_3$  was demonstrated [5]. In such a collinear AOTF, the incident light, the acoustic wave, and the diffracted beam all travel in the same direction. A number of different crystals (e.g., quartz,  $\text{LiNbO}_3$ , etc.) with different crystal orientations allow collinear diffraction of light into the orthogonal polarization by propagation of either longitudinal or shear acoustic waves. Chang [6] generalized the concept of the AOTF design by designing a noncollinear AOTF in  $\text{TeO}_2$ , a birefringent crystal, which cannot be used for collinear interaction due to its crystal symmetry; in such a cell, the incident light, the diffracted light, and the acoustic wave do not travel in the same direction.

The progress in AOTF technology and its applications has been made by many teams of scientists and engineers working in university, industry, and government laboratories. A list of organizations in various countries that are presently working on this technology and its applications is shown below. To provide a historical perspective to the progress in this field, the chronological development of AOTF technology in the United States and other Western countries is given in table 1. Similar information for the work done in the Former Soviet Union (FSU) is listed in table 2.

#### Organizations involved in AOTF technology and its applications

##### **USA**

Advanced Materials Corporation, PA  
Army Research Laboratory (ARL), MD  
Army's Chemical and Biological Defense Command (CBDCOM), MD  
Army's Communication and Electronics Command (CECOM), VA  
ATT Labs, NJ  
Aurora Associates, CA  
Brimrose Corporation of America, MD  
Carnegie Mellon Research Institute, PA  
Case Western University, OH  
Jet Propulsion Laboratory (JPL), CA  
National Aeronautics and Space Administration (NASA), MD  
National Institute of Health (NIH), MD  
NEOS, FL  
New Focus, CA

Marquette University, WI  
Oak Ridge National Laboratory (ORNL), TN  
Pennsylvania State University, PA  
Photonics Systems, FL University of California, Irvine, CA  
Unique Telecom Products, CT  
University of Pittsburgh, PA  
etc.

#### **Russia**

Central Bureau of Unique Instrumentation, Moscow  
Moscow State University, Moscow  
Institute of Crystallography, Moscow  
St. Petersburg State Academy of Aerospace Instrumentation, St. Petersburg  
etc.

#### **Japan**

Panasonic  
NEC  
National Aerospace Laboratory  
etc.

#### **Europe:**

U.K.  
Germany  
Italy  
etc.

**Table 1. AOTF Milestones in the West**

Year	Contributors	Development
1921	Billouin [1]	Theoretical prediction of AO interaction
1932	Debye et al. [2]	Experimental demonstration of AO interaction
1955	Rosenthal [7]	Theoretical discussion of color control by ultrasound grating
1967	Dixon [3]	Acoustic diffraction of light in anisotropic media
1969	Harris et al. [4]	Collinear AOTF proposed
1969	Harris et al. [5]	Collinear AOTF demonstrated
1972	Nieh et al. [8]	Analysis of collinear AOTF
1974	Kusters et al. [9]	Optimization for AOTF design
1974	Chang [6]	Noncollinear AOTF in TeO <sub>2</sub>
1975	Isomat [10]	First commercial offering of AOTF
1976	Watson et al. [11]	First imaging AOTF spectrometer
1977	Ohmachi et al. [12]	Integrated optics collinear AO interaction

**Table 2. AOTF Milestones in the Former Soviet Union**

Year	Contributors	Development
1922	Mandelstamm [13]	Prediction and investigation of scattering of light by phonons
1933	Rytov [14]	Theoretical and experimental investigation of Bragg diffraction
1957	Baransky [15]	Selection of spectral components in a Hg lamp
1969	Ermilin [16]	Observation of collinear diffraction in LiNbO <sub>3</sub>
1975	Vizen et al. [17]	Fabrication of quartz collinear AOTF
1975	Voloshinov et al. [18]	Noncollinear AOTF in LiNbO <sub>3</sub>
1976	Magdich et al. [19]	TeO <sub>2</sub> noncollinear AOTF
1983	Magdich et al. [20]	Industrial fabrication of AOTF instruments in visible, UV, and near-IR
1987	Pustovoit et al. [21]	First spaceborne AOTF spectropolarimeter
1996	Pustovoit et al. [22]	AOTF used for underwater gas detection

### 3. AOTF Concepts

As explained earlier, there are two types of AOTF cells: collinear and noncollinear. This section is a brief overview of the underlying concepts of these two types. Figure 1 shows the propagation of light and sound in a collinear AOTF cell [23]. The wave vectors for the incident and diffracted light are  $\mathbf{k}_{\text{in}}$  and  $\mathbf{k}_{\text{diff}}$ , respectively, and for sound wave it is  $\mathbf{q}_{\text{sound}}$ . The incident light is linearly polarized by a polarizer in front of the crystal medium of interaction. As this polarized light passes through the crystal perpendicular to the optic axis, it is diffracted in the same direction by a sound wave traveling collinear to the incident optical beam. Since the polarization of the diffracted beam is perpendicular to the incident light beam, it can be separated from the incident beam with the use of an analyzer. Due to the conservation of energy, the frequency of the diffracted light is Doppler shifted. Because the frequency of the incident light is around  $10^{14}$  Hz and the frequency of the ultrasonic beam is around  $10^8$  Hz, the Doppler frequency shift is insignificant and can be ignored. Based on the conservation of momentum, a tuning relationship between the center wavelength of the filter and the applied rf frequency can be established:

$$\mathbf{k}_{\text{diff}} = \mathbf{k}_{\text{in}} + \mathbf{q}, \quad (1)$$

$$\lambda = (n_o - n_e)v_s/\Omega, \quad (2)$$

where  $\lambda$  is the center wavelength of the filter,  $n_o$  and  $n_e$  are the refractive indices of the crystal corresponding to the propagation of light along the ordinary and extraordinary axes, respectively, and  $v_s$  and  $\Omega$  are the speed and frequency of the acoustic wave, respectively. The bandwidth,  $\Delta\lambda$ , of the AOTF is equal to  $\lambda^2/\Delta nL$ , where  $L$  is the length of the AO interaction (same as the length of the crystal), and  $\Delta n$  is the difference of the two refractive indices.



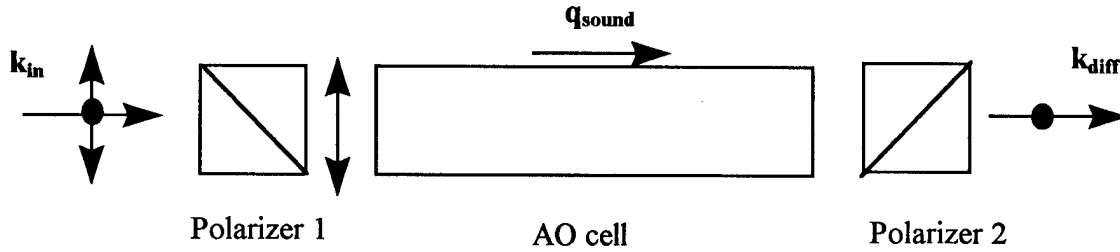


**Figure 1. A collinear AOTF cell.**

As an example we can calculate the rf frequency range and the corresponding filter bandwidth for a quartz collinear AOTF operating in the spectral wavelength region 400–800 nm. Taking  $\Delta n = 0.009$ ,  $v_s = 5.75 \times 10^5$  cm/sec, and  $L = 15$  cm, the rf frequency range is 130 to 65 MHz, and  $\Delta \lambda$  is 0.12 nm at 400 nm. Neglecting the spectral dependence of the refractive index values, the wave-number resolution  $\Delta k$  has a value of  $7.4 \text{ cm}^{-1}$  in the entire spectral region of interest.

Figure 2 shows the schematic layout of a noncollinear AOTF cell. Here the diffracted beam is spatially separated from the undiffracted beam. This may look like a regular Bragg cell, but due to the anisotropic nature of the AO interaction involved, the polarization of the diffracted beam is orthogonal to that of the incident beam, and each of these beams travels with a different speed in the crystal. Since detailed discussions of noncollinear AOTFs are available in many excellent review articles [24–27], no further details will be given here.

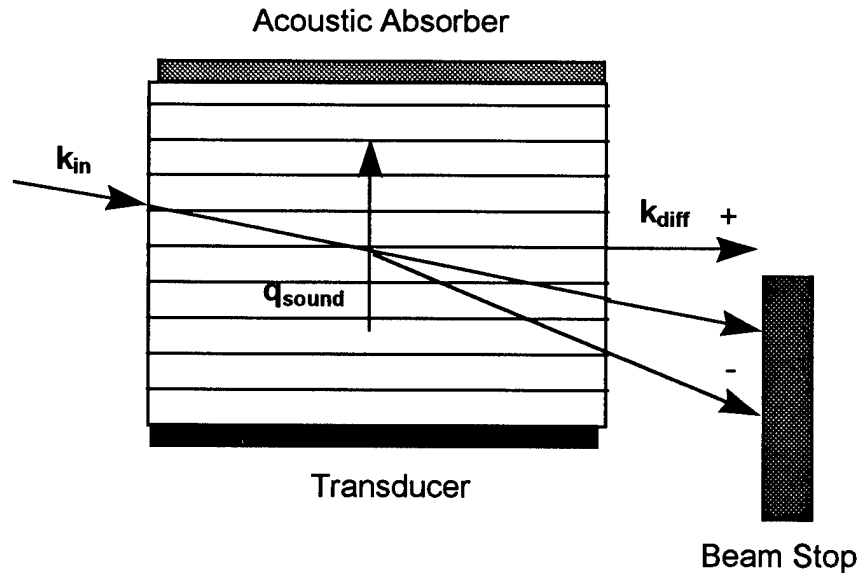


**Figure 2. A noncollinear AOTF cell.**

The tuning relationship for a noncollinear AOTF is approximated by Eq. (3).

$$\lambda = (\sin^4 \theta_i + \sin^2 2\theta_i)^{1/2} (n_o - n_e) v_s / \Omega, \quad (3)$$

where  $\theta_i$  is the angle of incidence.  $\theta_i = 90^\circ$  corresponds to the collinear case and Eq. (3) reduces to Eq. (2).

#### 4. AOTF Design

An AOTF cell is designed by bonding a transducer on an anisotropic crystal that has been cut with a specific orientation and polished. The acoustic waves are generated in this crystal by the application of an rf signal to the transducer. The tuning range for a single transducer is about one octave in acoustic frequency. An AOTF cell can be designed with multiple transducers to cover a wider frequency range of operation.

The key elements in an AOTF cell design are material selection, choice of crystal geometry, transducer design and bonding, design of AOTF cell architecture, electronics for the operation and control of AOTF, computer interface, signal processing algorithms, and software.

Performance of AOTFs is primarily limited by the availability of superior materials. To qualify as a candidate for use as an interaction medium for an AOTF, a material must be optically birefringent and transparent in the operating wavelength range of interest. Also, it must have a low acoustic attenuation in the acoustic frequency range of operation, and it must have a large AO figure of merit. Table 3 lists a number of important crystal materials used to design AOTF cells and their spectral ranges of coverage. A number of tellurium dioxide ( $\text{TeO}_2$ ) AOTFs are now commercially available.

**Table 3. AOTF Materials**

Material	Spectral band ( $\mu\text{m}$ )	Type of cell
$\text{LiNbO}_3$	0.4–4.5	Collinear
Crystal quartz ( $\text{SiO}_2$ )	0.25–0.8	Both
$\text{MgF}_2$	0.2–0.7	Noncollinear
$\text{CaMoO}_4$	0.4–4.5	Collinear
$\text{TeO}_2$	0.35–4.5	Noncollinear
$\text{Tl}_3\text{AsSe}_3$	1.1–17	Both
$\text{Hg}_2\text{Cl}_2$	0.35–20	Noncollinear

#### 5. AOTF Applications

AOTFs are very powerful tools for all kinds of spectroscopic applications, including absorption, emission, fluorescence, Raman, and laser-induced breakdown spectroscopy (LIBS) [28–31]. They are lightweight, compact, and very useful for field-portable applications. They have no moving parts, are all solid-state construction, require low power, and are insensitive to vibrations. They have high spectral resolution, large field of view and high throughput. They offer high-speed tuning and scanning of wavelengths and have reliable and reproducible operation under computer control. The wavelength tuning can be random or sequential, and an AOTF can be operated at multiple frequencies. AOTFs can be used for generating an arbitrary spectral signature and can be

used for polarization-sensitive applications. Such filters can be used as a replacement for filter wheels and gratings. Laser wavelength tuning applications use AOTF both inside and outside the laser cavity. AOTF spectrometers have been designed with both high sensitivity and high resolution. AOTF instruments are used for detection of chemical and biological agents and for medical applications, as well as for environmental sensing applications. They are also very useful in multispectral and hyperspectral imaging applications [32,33]. Such instruments are increasingly being used for process and quality control in various manufacturing applications in pharmaceutical and chemical industries [34]. AOTFs have been used with telescopes for astronomical observations [11]. Such instruments are very useful on board satellites and for exploration of space. An AOTF spectrometer will be used on the space station for water quality monitoring, and the use of AOTFs is planned for a Mars rover to observe and analyze of the surface of Mars and for a future comet lander [35]. These days, AOTFs are becoming valuable system components in wavelength division multiplexing (WDM) communication networks because of their broad continuous electronic wavelength tuning capability and narrow filter bandwidth. Multiwavelength filtering capability adds another dimension of flexibility to network design that cannot be achieved by any other filter [36]. These considerations have contributed greatly to the research and development taking place in the integrated-optic  $\text{LiNbO}_3$  AOTFs.

## 7. Conclusions

AOTF technology has evolved a great deal since its inception 30 years ago. Advantages in size, time of measurement, cost, programmability, and sensitivity offered by AOTF devices make them suitable candidates for chemical sensing, frequency tuning, and imaging applications requiring portability, robustness, and compact size, both in laboratory and field testing setups. This very promising technology can become more widely used if the fabrication is made more automated and the cost per unit is lowered. More research is needed to develop new materials and to improve the quality of existing materials to expand the wavelength range of operation to shorter UV and longer IR regions.

## Acknowledgments

The author would like to thank M. Gotlieb, V. Voloshinov, and V. I. Pustovoit for their input in preparing tables 1 and 2.

## References

1. L. Brillouin, "Diffusion de la Lumiere et des Rayons X par un Corps Transparent Homogene: Influence de l'Agitation Thermique," *Ann. Phys. (Paris)* **17**, 88–122, 1921.
2. P. Debye and F. W. Sears, "On the Scattering of Light by Supersonic Waves," *Proc. Nat. Acad. Sci. (USA)* **18(6)**, 409–414, 1932.
3. R. W. Dixon, "Acoustic Diffraction of Light in Anisotropic Media," *IEEE J. Quantum Electron.* **QE-3**, 85–93, 1967.
4. S. E. Harris and R. W. Wallace, "Acousto-Optic Tunable Filter," *J. Opt. Soc. Am.* **59**, 744–747, 1969.

5. S. E. Harris, S. T. K. Nieh, and D. K. Winslow, "Electronically Tunable Acousto-Optic Filter," *Appl. Phys. Lett.* **15**, 325–326, 1969.
6. I. C. Chang, "Noncollinear Acousto-Optic Filter with Large Angular Aperture," *Appl. Phys. Lett.* **25**, 370–372, 1974.
7. A. H. Rosenthal, "Color Control by Ultrasonic Wave Gratings," *Opt. Soc. Am.* **45**, 751–756, 1955.
8. S. T. K. Nieh and S. E. Harris, "Aperture-Bandwidth Characteristics of the Acousto-Optic Filter," *J. Opt. Soc. Am.* **62**, 672–676, 1972.
9. J. A. Kusters, D. A. Wilson, and D. L. Hammond, "Optimum Crystal Orientation for Acoustically Tuned Optic Filter," *J. Opt. Soc. Am.* **64**, 434–440, 1974.
10. Isomat Data sheet, "Acousto-Optic Tunable Filter TOF 100," May 1975.
11. R. B. Watson, S. A. Rappaport, and E. E. Frederick, "Imaging Spectrometer Study of Jupiter and Saturn," *Icarus* **27**, 417–423, 1976.
12. Y. Ohmachi and J. Noda, "LiNbO<sub>3</sub> TE-TM Mode Converter Collinear Acousto-Optic Interaction," *IEEE J. Quantum Electron.* **QE-13**, 43–46, 1977.
13. L. Mandelstam, *Journal of Russian Phys. Chem. Soc.* **58**, 381, 1926. (In Russian)
14. S. Rytov, *Russian Journ. Tech. Phys.* **3**, 1045, 1933. (In Russian)
15. K. Baransky, "Excitation of Hypersonic Oscillations in Quartz," *Soviet Crystallography* **2**, 299–302, 1957. (In Russian)
16. K. Ermilin and N. Reshetnikov, *Proc. All-Union Conf. on Acoustoelectronics and Quantum Acoustics*, Kharkov, USSR, 138, 1971. (In Russian) [Performed work in 1969 as a student at the Moscow State University.]
17. F. Vizen, Y. Kalinnikov, and R. Mikaelyan, "Tunable AO Filter on base of Single Crystal of Quartz," *Proc. of Coordination Workshop on Acousto-optics*, Tomsk, USSR **1**, 36, 1975. (In Russian)
18. V. Voloshinov and V. Khaptanov, "Tunable AO Filter on Base of Lithium Niobate Single Crystal," M.S. Thesis by V. Khaptanov, Moscow State University, Dept. of Physics, 1975. (In Russian)
19. L. Magdich, V. Molchanov, and I. Ponomareva, "Application of anisotropic diffraction of radiation in AO instruments," *Laser Technology and Optoelectronics*, Ser. 11, v 3, 100–104, 1979. (In Russian) [Work performed in 1976.]
20. Private communication with Voloshinov (who communicated with Magdich) 1997.
21. Private communication with Pustovoit, 1996.
22. Private communication with Pustovoit, 1996.
23. V. I. Pustovoit and V. E. Pozhar, "Collinear Diffraction of Light by Sound Waves in Crystals: Devices, Applications, New Ideas," *Photonics and Optoelectronics* **2**, 53–69, 1994.
24. I. C. Chang, "Acousto-Optic Tunable Filter," in *Acousto-Optic Signal Processing Theory and Implementation*, N. J. Berg and J. N. Lee, eds., Marcel Dekker, New York, 139–159, 1983.
25. M. S. Gottlieb, "Acousto-Optic Tunable Filter," in *Design and Fabrication of Acousto-Optic Devices*, A. P. Goutzoulis and D. R. Pepe, eds., Marcel Dekker, New York, 197–283, 1994.
26. X. Wang, "Acousto-Optic Tunable Filters Spectrally Modulate Light," *Laser Focus World* **28**, 173–180, May 1992.
27. C. D. Tran, "Acousto-Optic Devices," *Anal. Chem.* **64**, 971A–981A, 1992.
28. N. Gupta and N. F. Fell, Jr., "A Compact Collinear AOTF Raman Spectrometer," submitted for publication in special issue of *Talanta* on applications of AOTF, 1997.

29. E. N. Lewis, P. J. Treado, and I. W. Levin, "A Miniaturized, No-Moving-Parts Raman Spectrometer," *Appl. Spectrosc.* **47**, 539–543, 1993.
30. D. H. Hueber, C. L. Stevenson, and T. Vo-Dinh, "Fast Scanning Synchronous Luminescence Spectrometer Based on Acousto-Optic Tunable Filters," *Appl. Spectrosc.* **49**, 1624–1631, 1995.
31. A. Z. Miziolek, C. Williamson, K. L. McNesby, N. F. Fell, S. E. Medlin, B. E. Forch, R. G. Daniels, N. Gupta, E. R. Cespedes, B. H. Miles and J. Cortes, "Alternative Approaches to Sampling and Data Collection for Laser-Induced Breakdown Spectroscopy," paper presented at OSA Topical Meeting on Laser Applications to Chemical and Environmental Analysis, Orlando, FL, March 1996.
32. L. J. Cheng, I. C. Mahoney, G. F. Reyes, and H. R. Suiter, "Target Detection using an AOTF Hyperspectral Imager," *Proc. SPIE* **2237**, 257–259, 1994.
33. T. Yoshizawa, "Development of an Imaging Spectral-polarimeter," *Proc. SPIE* **2873**, 50–53, 1996.
34. X. Wang, J. Soos, Q. Li, and J. Crystal, "An Acousto-Optic Tunable Filter (AOTF) NIR Spectrometer for On-line Process Control," *Process Control and Quality* **5**, 9–16, 1993.
35. Private communication with X. Wang, Brimrose Corp. of America, Baltimore, MD, 1996.
36. K. W. Cheung, D. A. Smith, J. E. Baran, and J. J. Johnson, "Wavelength-selective Circuit and Packet Switching using Acousto-Optic Tunable Filters," *Proc. IEEE Global Telecommunications Conf.* **3**, 1541–1547, 1990.

# Progress of Acousto-Optic Tunable Filters

I. C. Chang, Aurora Associates, Santa Clara, California 95054

## Abstract

This paper presents recent progress of AOTFs at Aurora Associates. The discussion will focus on the new types of AOTFs for the following applications: (a) wavelength routing switch for fiber optic communications and (b) imaging spectrometer for the infrared (2 to 5  $\mu\text{m}$ ). The critical issues for each of these applications will be addressed. Experimental results of these AOTFs will be reported.

## 1.0 Introduction

The acousto-optic tunable filter (AOTF) is an electronically tunable optical filter based on acousto-optic (AO) diffraction in a birefringent crystal [1]. It combines the functions of spectral filtering, modulation, polarization converting, and optical imaging in a single, compact device. A list of the salient features of the AOTF include: wide tuning range with rapid random access tuning rate, large angular aperture while maintaining high spectral resolution, and it is capable of operating in the amplitude modulation, wavelength modulation and multi-wavelength mode. In addition, the small size, light weight and rugged construction make the AOTF compatible to the harsh environmental requirements of field use.

Despite these unique attractive features, there has been no significant growth of the commercial market since the invention of the AOTF more than twenty years ago. The primary reason appears to be due to the lack of market development of AOTF product for various applications. Such an effort is necessary in order to gain user's acceptance over the more matured conventional technologies such as grating-based spectrometers, or stacks of interference filters (color wheels). This situation has been changed in recent years, as the result of significant technical progress in the deploying of the AOTF to diverse fields of applications that include: astronomy [2], biology [3], and fiber optic communication [4].

Another more basic reason that hinders the growth of the AOTF market is the performance limitations of the device. For instance, up to now, the  $\text{TeO}_2$  AOTF has shown to be the only practical AOTF with a sizable growth potential. Since  $\text{TeO}_2$  transmits between 0.4 and 5 micrometers, most of the AOTF deployment has been primarily limited to the visible and near infrared (NIR) spectral regions. To fully exploit the potential of AOTF technology, device performance such as this limited spectral range must be overcome.

This paper discusses the device performance limitations of the AOTF and presents recent progress of AOTF performance. The discussion focuses primarily on two types of applications; (a) extending the operating wavelength of imaging AOTFs to mid-wave infrared (MWIR) and (b) a polarization-independent AOTF switch for wavelength division multiplexing (WDM) optic communication.

## 2.0 AOTF Performance Limitation

In order to address the issue of AOTF performance limitations, it is appropriate to briefly review the early development of AOTF technology. The first AOTF was based on collinear AO interaction in a birefringent crystal [5]. Birefringence is necessary in order to satisfy the phase matching condition in a collinear interaction geometry. One important advantage of the collinear AOTF is that a long interaction length can be used to realize a narrow passband and increased diffraction efficiency. However, the collinear AOTF has a number of disadvantages that include low AO figure of merit, the required use of polarizers, and complex fabrication process. As a result, the potential of a practical collinear AOTF appears to be limited. The only exception is the integrated optics type based on the collinear interaction of surface acoustic wave (SAW) and guided optical waves.

A more popular type of AOTF uses a noncollinear interaction geometry as shown in Figure 1 where the optical and the acoustic waves are noncollinear. The first noncollinear AOTF [6], [7] had a small angular aperture since the phase matching condition is critically dependent on the angle of the incident light.

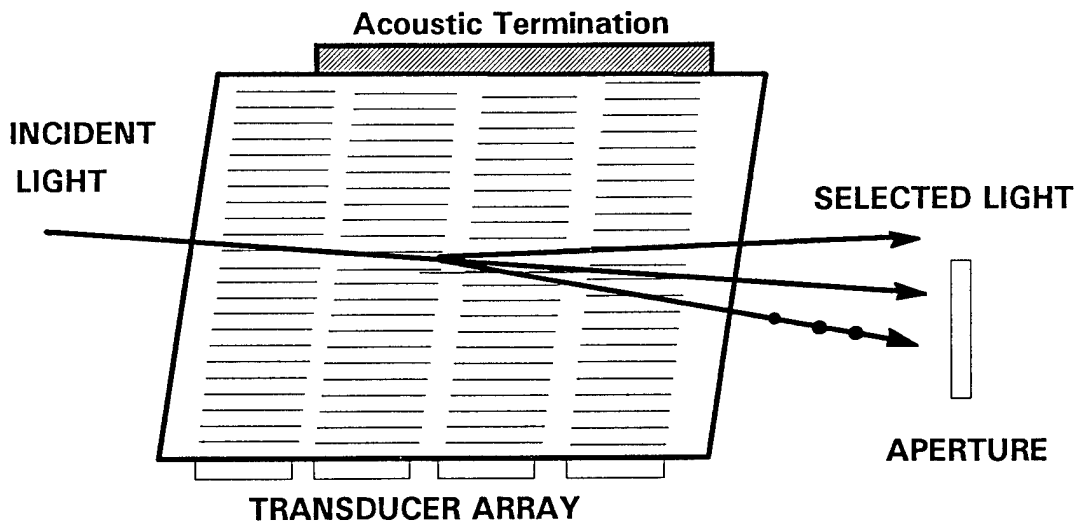


Figure 1. Schematic of a noncollinear AOTF.

For most practical applications, the noncollinear AOTF used today is the type that satisfy the noncritical phase matching (NPM) condition [8]. The NPM type of AOTF provides a large angular aperture while maintaining narrow bandwidth. This unique feature is obtained by choosing the wavevectors for the incident and diffracted optical wavevector loci to be parallel [8].

Compared to the collinear type, the noncollinear AOTF offers the advantages that are crucial to practical implementation: (a) the choice of broader classes of AOTF materials such as  $\text{TeO}_2$ , (b) greater design freedom for meeting the specified requirement of spectral resolution, efficiency and angular aperture, (c) the ease of implementing acoustic apodization for suppression of sidelobes, (d) spatial separation of the incident and deflected beams, i.e., operation without the use of polarizers, and (e) greatly simplified manufacturing process.

The noncollinear AOTF has one basic limitation; the walkoff of acoustic beam from the optical wavefront limits the maximum interaction length. This yields poor spectral resolution and lower diffraction efficiency compared to a collinear AOTF with the same AO material and modes. The success of the noncollinear AOTF has been largely due to the large AO figure of merit of  $\text{TeO}_2$ .

The earlier effort on the AOTF has been focused on developing the new AOTF materials and design concepts for overcoming these two major performance limitations of the noncollinear  $\text{TeO}_2$  AOTF. In the following, we shall focus our discussion of performance improvement for the two specific applications: MWIR spectral imaging and wavelength routing switch for fiber optic communication.

### 3.0 Low Power Mid-Wave Infrared AOTF

The use of tunable spectral filter in an IR focal plane for remote sensing is an application area of great importance. The most critical issue has been the limited transparency range and high drive power of the  $\text{TeO}_2$  AOTF. Since the drive power is proportional to the square of the wavelength, an AOTF operated at  $5\mu\text{m}$  requires 100 times the drive power of an AOTF operated at  $0.5\mu\text{m}$ .

For mid-wave infrared (MWIR), the most critical issue for the  $\text{TeO}_2$  AOTF is the high drive power requirement. For a  $\text{TeO}_2$  AOTF with a nominal aperture  $1\text{cm}^2$ , the RF drive power required at  $3.5\mu\text{m}$  is as high as 15 watts.

The drive power can be significantly reduced by using the acoustic resonance technique [9]. The concept of the acoustically resonant AOTF is illustrated in Figure 2.

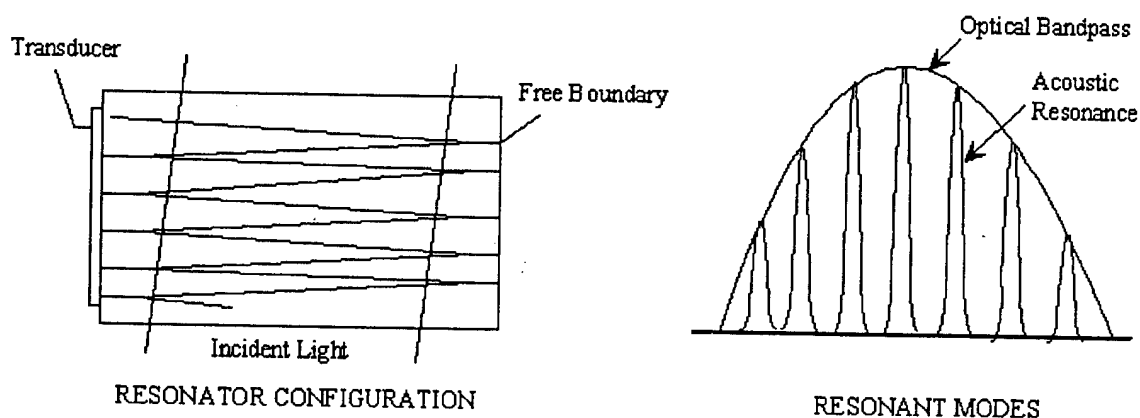


Figure 2. Acoustically resonant AOTF configuration.



Recently, we completed a Phase I SBIR Program. The objective of the program was to develop a dual polarization AOTF for the mid-wave infrared (MWIR) region.

Due to the extremely large acoustic walkoff in  $\text{TeO}_2$  ( $\sim 55^\circ$ ), the usable active area in a  $\text{TeO}_2$  AOTF is small, typically one tenth to one fifth of the overall crystal. The chosen approach is to use optical prisms that may be optically contacted to the  $\text{TeO}_2$  surface. The simplest type of optical prism uses an isotropic material (e.g., glass) with a refractive index about equal to that of  $\text{TeO}_2$ . The optical prism material must be transparent in the optical wavelength range of interest. Another method is to cut a prism from the  $\text{TeO}_2$  filter block and arrange the  $\text{TeO}_2$  prisms to cover the usable optical aperture.

In order to verify the feasibility of acoustically resonant AOTFs, several feasibility models of acoustically resonant  $\text{TeO}_2$  AOTF are chosen for fabrication, test and evaluation.

Optical measurement was also made with a HeNe laser at  $3.39 \mu\text{m}$ . The net diffracted efficiency at resonance was about 220%/Watt. The resonance gain is estimated to be greater than 20. The higher resonance gain is due to the smaller acoustic attenuation at the low acoustic frequency at 30 MHz. This result of optical measurement is in good agreement with the RF measurement of the acoustic resonator finesse, which was found to be equal to 22.

Figure 3 shows the bandpass of the resonant AOTF as the acoustic frequency is swept across the laser line at  $3.39 \mu\text{m}$ . Maximum efficiency obtained was about 80 percent. The FWHM of the resonant AOTF was 15nm.

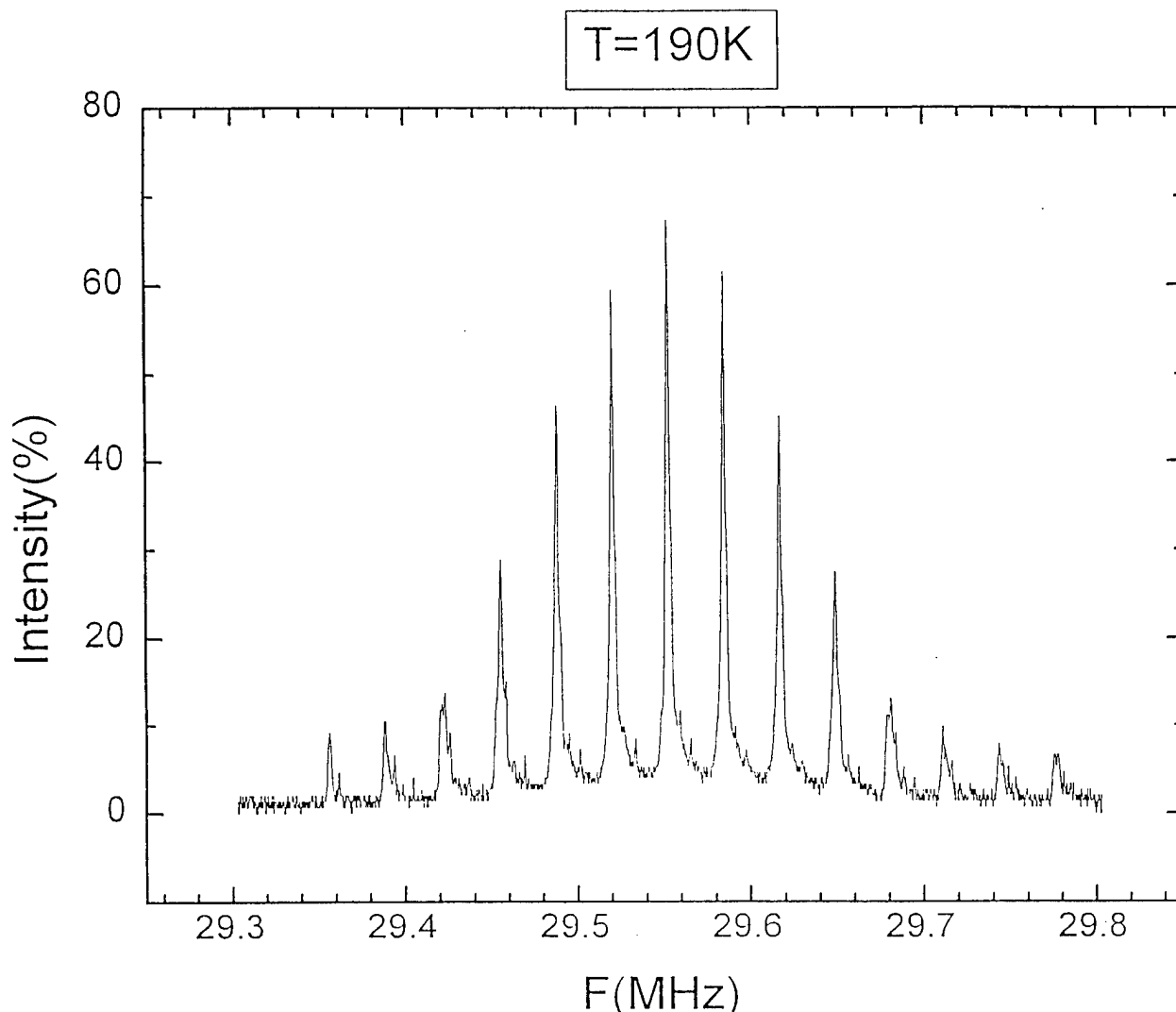


Figure 3. Bandpass of an acoustically resonant TeO<sub>2</sub> AOTF measured at 3.39  $\mu\text{m}$  ( $T = 190^\circ\text{K}$ ).

## 4.0 Collinear Beam AOTF

The use of the AOTF as a wavelength routing switch in WDM optical network is another application area of great importance. For the WDM network the AOTF offers the unique capability of simultaneously and independently selecting a large number of wavelengths. For this reason, the AOTF-based WRS (AOWRS) was chosen as the core device in the ARPA-funded optical network consortium (ONTC) demonstration testbed. Until recently, all the AOWRS were the integrated optics type that uses collinear interaction of surface acoustic wave (SAW) and guided optical waves. The confinement of SAW significantly reduces the drive power. This low drive power requirement is important for selecting a large number of wavelengths. The development of the integrated AOWRS was discussed in detail in a recent review paper [5]. The AOWRS implemented in present integrated optic structure suffers from several performance limitations: high optical insertion loss, polarization dependent loss, and most importantly, high sidelobes that sets the wavelength spacing for an acceptable crosstalk.

An AOWRS based on bulk wave  $\text{TeO}_2$  AOTF is desirable since it offers the important advantages of design flexibility, wide tuning range, operation without the use of polarizers and ease of transducer apodization for sidelobe suppression. However, as mentioned in the previous section, due to the limited interaction length the  $\text{TeO}_2$  AOTF has the major deficiencies of low spectral resolution and high drive power.

In our early work on AOTFs we have demonstrated increased resolution by using acoustic mode conversions. Internal mode conversion (IMC) [10] or external mode conversion (EMC) [11] techniques allow the increase of the AOTF FWHM to a few  $\text{cm}^{-1}$ . Figure 4 shows the bandpass of a visible  $\text{TeO}_2$  AOTF swept through a HeCd laser line. The measured FWHM of the AOTF was  $4\text{cm}^{-1}$  or  $0.8\text{\AA}$  at  $442\text{nm}$  [12]. The peak diffracted light efficiency was about 96%. This bandwidth is wider than the desired value needed for the intended applications. Significant increase of the AOTF resolution by extending the interaction length appears impractical.

Recently, we have introduced a new type of noncollinear AOTF. It is called collinear beam (CB) AOTF since the acoustic beam (i.e., group velocity direction) is collinear with the incident optical beam [13], [14]. The most significant feature of the CB AOTF is that it realizes an extended interaction length and thus the advantages of narrow passband and low drive power.

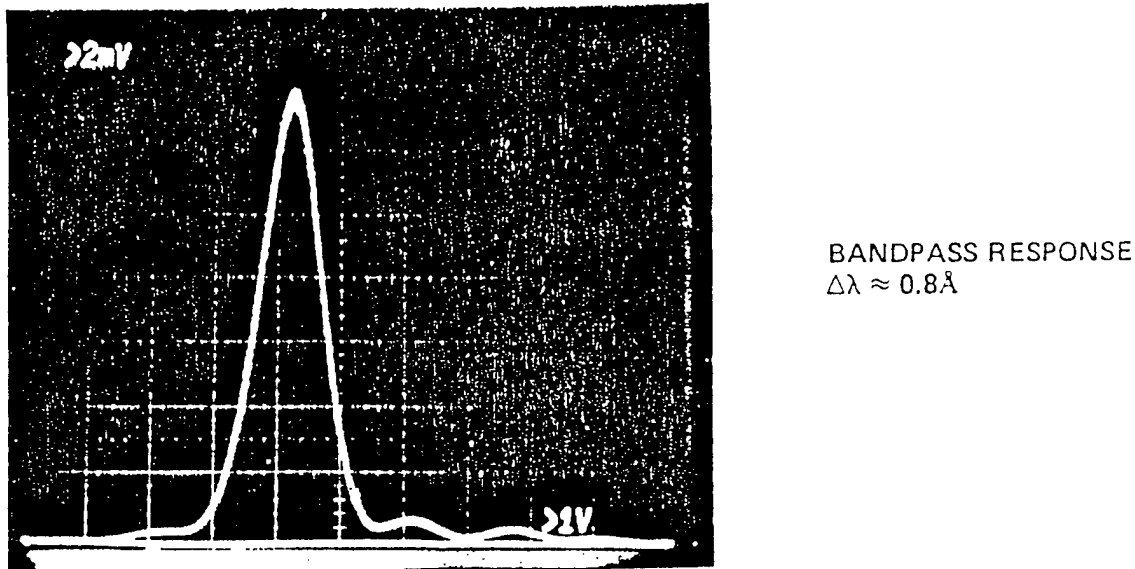
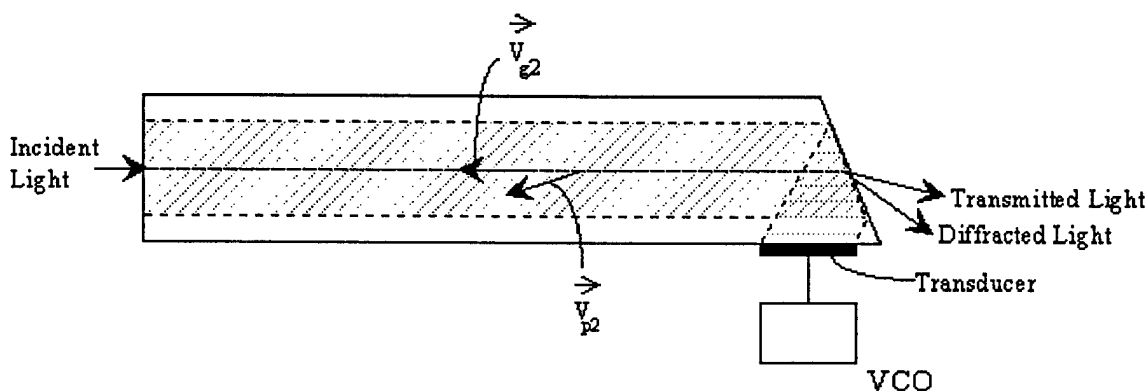


Figure 4. Bandpass of a visible  $\text{TeO}_2$  AOTF swept through a HeCd laser line.

Figure 5 shows the schematic of a collinear beam AOTF. To minimize wavelength dispersion an ordinary polarization is chosen for the incident optical beam. The acoustic wave launched from the transducer is reflected from the prism surface that is chosen so that the acoustic group velocity is collinear with the incident ordinary ray. When the momentum matching condition is satisfied, an extra-ordinarily polarized diffracted optical beam at the passband wavelength will be generated in the crystal. The diffracted narrowband optical beams coupled out of the prism surface may be selected using polarizers or spatial separations.



**Figure 5. Collinear Beam AOTF using Internal Acoustic Reflection (IAR).**

Figure 6 shows the bandpass response of a fiber-pigtailed CB AOTF obtained by monitoring the diffracted light intensity as the acoustic frequency was swept through a laser diode at  $1.55\mu\text{m}$ . The transmission of the diffracted light reaches a peak amplitude when the acoustic frequency is about 38.24 MHz. The measured  $\sim 3\text{dB}$  point was found to be at 38.1 and 38.36 MHz. The acoustic frequency bandwidth of 25 KHz corresponds to an optical filter FWHM of 1nm at 1.523 nm.

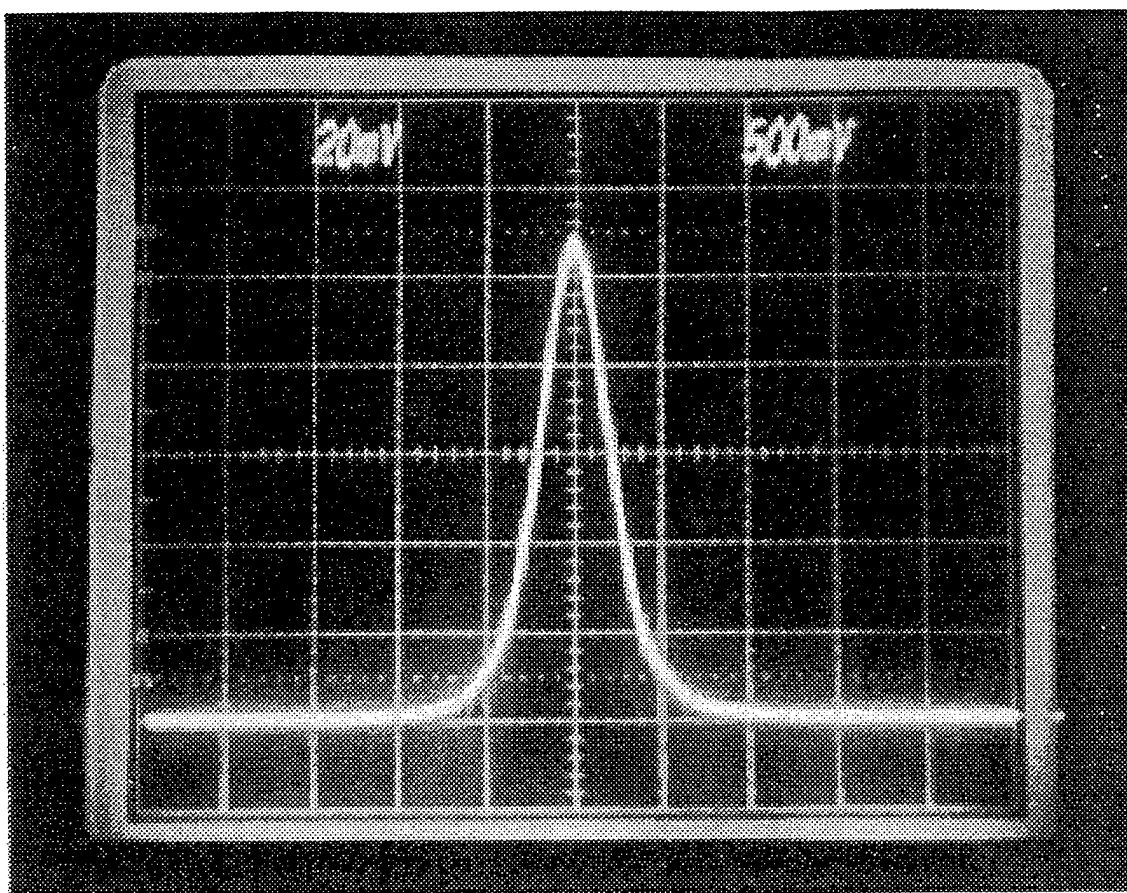
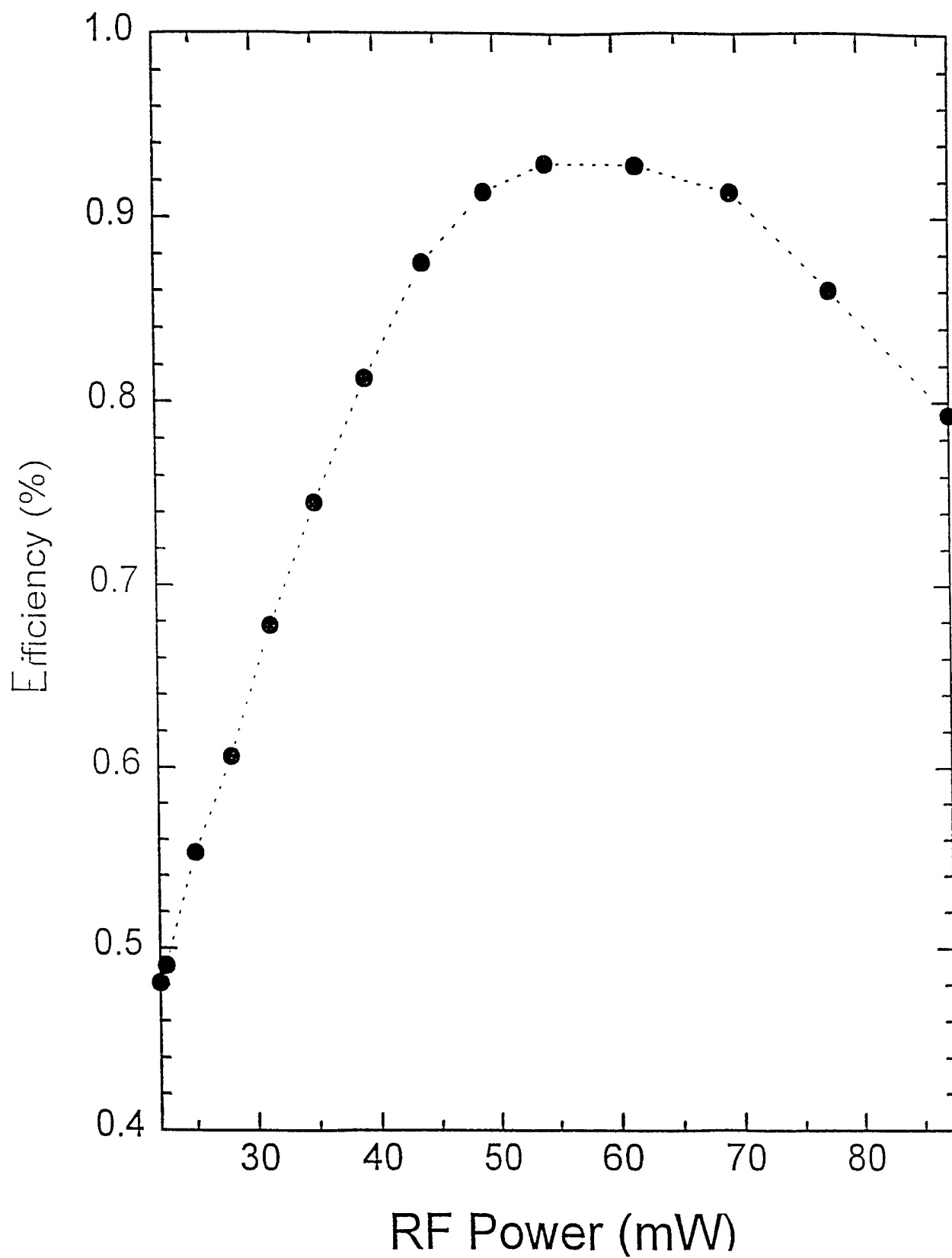


Figure 6. Bandpass of CBAOTF as RF is Swept Through a Laser Line at  $1.523\ \mu\text{m}$ .

The filter efficiency was also measured as a function of drive power. The diffracted light reaches 70 percent when the input RF power is 50 mW.

Like the conventional AOTF, the peak diffraction efficiency of the CBAOTF also saturates to a peak value of 95% when the drive power is increased to about 55 mW. Further increase of drive power results in a decrease of the diffraction efficiency. Figure 7 shows the measured diffraction efficiency of the CB AOTF as a function of drive power.



**Figure 7.** Measured diffraction efficiency of CBAOTF vs. drive power.

The sidelobes with low bandpass are the most significant characteristics of the CBAOTF. For wavelength division multiplexing (WDM) applications, to avoid cross-talk between nearest wavelength channels, this will greatly increase the effective channel separation and, consequently, the usable number of channels within the bandwidth of the erbium doped fiber amplifier. For a closer examination of the sidelobe, the bandpass response of the CBAOTF was plotted in dB scale. Figure 8 shows the bandpass response is asymmetric. The levels of the sidelobes 3nm away from the center wavelength at the low and high frequency sides are 27 and 21.3dB, respectively.

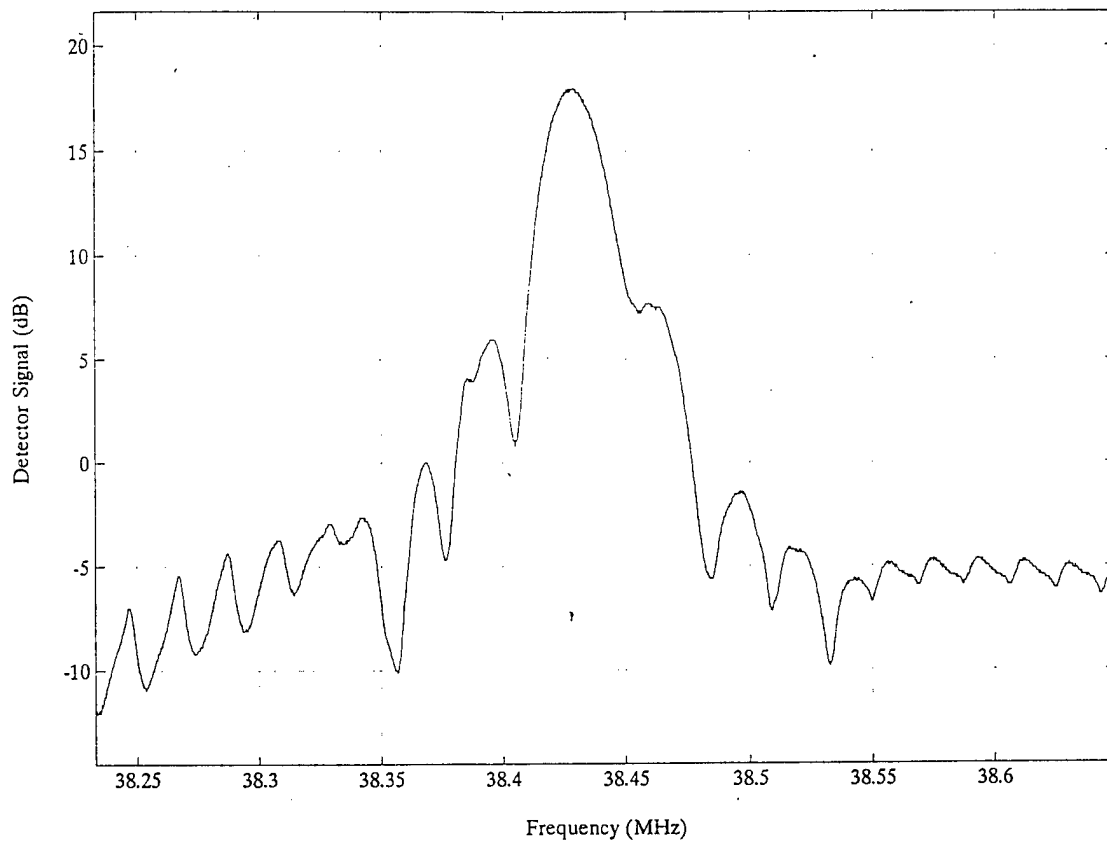


**Figure 8. Bandpass of a CBAOTF (in dB) measured at 1.55 $\mu$ m.**

Another critical requirement for the AOWRS is that its operation must be independent of the polarization of the incident light beam. Figure 9 shows the photo of a three-terminal polarization independent (PI) CBAOTF using a polarization diversity configuration. Based on this encouraging result, the CBAOTF appears quite promising as the AOWRS for WDM applications.

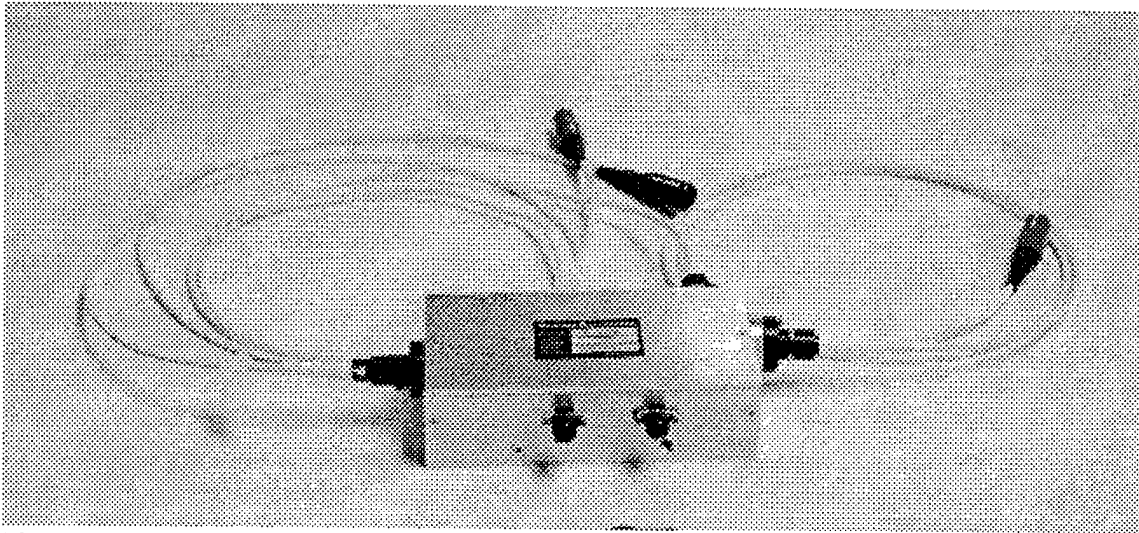


**Figure 9. Three-terminal polarization-independent CB AOTF using polarization diversity configuration.**



## REFERENCES

1. I.C. Chang, *Acousto-Optic Tunable Filters*, Opt. Eng. **20**, (Nov. 1981), 824-289.
2. D.A. Glenar, B. Seif, and J. Bergstrahl, *Acousto Imaging Spectropolarimeter for Remote Sensing*, Applied Optics **33**, (1994), 7412 - 7424. and D.A. Glenar, J.J. Hillman, M. LeLouran and J. Drummond, Bulletin of the American Astron. Society **26**, (1994) papers 01.32 and 13.13.
3. P.J. Treado, I.W. Levin and E.N. Lewis, *Near Infrared Acousto-Optic Filtered Spectroscopic Microscopy: A Solid-State Approach to Chemical Imaging*, Appl. Spectroscopy **46**, (1992), 553 - 559.
4. D.A. Smith et al, *Evolution of the Acousto-Optic Wavelength Routing Switch*, J. Lightwave Tech. **14**, (1996), 1005.
5. S.E. Harris and R.W. Wallace, *Acousto-Optic Tunable Filter*, J Opt. Soc. Am. **59** (June 1969), 744 - 747.
6. I. C. Chang, *Noncollinear Acousto-Optic Tunable Filters*, IEEE/OSA Conf. on Laser Engineering and Applications (1973), paper no. 7.4.
7. T. Yano and A. Watanabe, *Acousto-Optic TeO<sub>2</sub> Tunable Filter Using Far-off Axis Anisotropic Bragg Diffraction*, Appl. Optics **15** (1976), 2250-2258.
8. I.C. Chang, *Noncollinear Acousto-Optic Filter with Large Angular Aperture*, Appl. Phys. Lett. **25** (1974), 370 - 372.
9. I.C. Chang, P. Katzka, J. Jacob and S. Estrin, *Programmable Acousto-Optic Filter*, IEEE Ultrason. Symp. Proc., (Sept. 1979).
10. I.C. Chang, U.S. Patent 4,720,177.
11. I.C. Chang, U.S. Patent 4,685,772.
12. I.C. Chang, *Acousto-Optical Signal Processing Devices and Applications*, International Ultrasonics Conference Proceedings, London, England (July 1985).
13. I.C. Chang, *Collinear Beam Acousto-Optic Tunable Filters*, Electron. Lett. **28** (1992), 1255.
14. I.C. Chang, U.S. Patent 5,329,397, *Collinear Beam AOTF*.

# Collinear Acousto-Optic Spectrometers and Their Applications

V. I. Pustovoit

*Central Bureau of Unique Instrumentation of the Russian Academy of  
Sciences, Moscow, Russia 117342*

&

Neelam Gupta

*U.S. Army Research Laboratory, Adelphi, MD 20783, USA*

## Abstract

Acousto-optic spectrometer (AOS) technology offers potential for the design of highly accurate analytical instruments operating at high speed without any moving mechanical parts. This technology also has the advantages of high sensitivity due to the large optical throughput and the ability to enhance the signal-to-noise ratio (SNR) multifold by the use of advanced signal processing algorithms. AOS instruments are extremely flexible and can be operated real-time with complete computer control. They allow both random and sequential wavelength access operation, as well as simultaneous operation at multiple wavelengths. This paper reviews the work done in Russia and the Former Soviet Union (FSU) in the last 20 years in the development and application of this technology.

## 1. Introduction

In many fields of science, such as ecology, medicine, industrial processing, education, forecasting of natural disasters, etc., there is a great need for objective, quantitative, and reliable real-time spectral information which can be obtained from portable, ruggedized optical instruments. Such information cannot be obtained by available conventional instruments because of their sensitivity to vibrations and mechanical movements. However, we can design new optical instruments based on the collinear diffraction of light by ultrasonic waves propagating in an anisotropic crystal; these instruments could carry out such measurements with high accuracy in the ultraviolet (UV), visible, and infrared (IR) spectral regions. Electronically tunable diffraction gratings based on acousto-optic (AO) interaction in birefringent crystals can be used in the design of robust spectrometers for remote detection of optical spectra produced by the absorption, emission, and scattering of light by different gases in the atmosphere, from sea water of varying composition, and from vegetation on land.

In this paper, we present a review of the work done in the development and application of portable collinear acousto-optic spectrometers (AOS's) designed for remote sensing and other applications in Russia and the Former Soviet Union (FSU) in the last 20 years. So far, such AOS's have been developed in the spectral region from 250 to 4000 nm. This paper presents specific examples of AOS applications and their test results, as well as a general discussion of collinear AOS technology. The advantages and applications of AOS technology are discussed in

section 2, the theory of operation and examples of applications of collinear AOS devices are described in section 3, and the conclusion and summary are included in section 4.

## **2. Advantages and Applications of AOS**

Traditional optical spectrometers are based on diffraction gratings and prisms. Operation of these dispersive elements requires mechanical movement, and the elements are sensitive to vibration. These are clear disadvantages in field-portable instruments and in instruments for use in settings with the potential for vibrations and impact. On the other hand, the electronically tunable diffraction gratings used in AOS technology are immune to vibrations and are reliable with reproducible operation. AOS thus offers many advantages over traditional optical spectrometers. Because of their immunity to vibrations and other inherent features, AOS instruments can be used in many demanding applications where portable spectrometers are required.

### **2.1 Advantages of AOS**

AOS's have several advantages in comparison to traditional optical spectrometers.

- (i) They have high spectral resolution ( $< 0.07$  nm in UV).
- (ii) The diffracted light in an AOS has higher intensity because the diffraction is from a bulk phase grating in the crystal produced by the ultrasonic wave.
- (iii) AOS could have high SNR because it allows the implementation of new measurement techniques based on amplitude modulation, synchronous detection schemes, and the use of high-accuracy signal processing algorithms.
- (iv) The AOS allows highly accurate measurement of optical intensity (spectral brightness), because we can have exact analytical knowledge of the instrument's transfer function based on detailed mathematical analysis.
- (v) The absence of mechanical moving parts in AOS's and its insensitivity to vibrations and impacts leads to robust operation.
- (vi) AOS technology can be used in extremely demanding applications, such as on aircraft (including helicopters) and spacecraft because of its light weight and compact size.
- (vii) AOS technology provides the possibility of an adaptive measurement mode through changes in operating characteristics. Such a mode could be used for the detection of compounds that could not be detected previously.
- (viii) AOS technology allows the possibility for multiple measurements and storage of randomly selected spectral bands, which can be used for analysis and identification of weak signals.
- (ix) The cost for mass production is low. The cost of an AOS is several times cheaper than that of traditional grating-based instruments.
- (x) One of the most important advantages of collinear AOS's is their ability to transmit color images of an object without any spatial distortions. This can be extremely useful in designing new imaging systems for detection and identification of a variety of objects in many different situations. Grating-based spectrometer systems do not offer such capability, since once the grating is written, it is permanent and cannot be changed.

(xi) AOS technology allows high-speed performance: the instrument response time is in tens of microseconds.

## **2.2 Applications of AOS's**

AOS's can be used for a variety of applications:

(a) Ecology: remote inspection of land and ocean surfaces from instruments based in space, aircraft, and ships; measurement of harmful gas concentrations in the atmosphere; real-time measurement of vegetation covers on land; monitoring of sea-water pollution; etc. (In the FSU, such monitoring was carried out for the Baltic Sea, the Sea of Okhotsk, Kara Sea, Barents Sea, the Sea of Japan, etc.)

(b) Prevention and monitoring of natural disasters and accidents: earthquake; forest fire; volcanic eruption; explosions in mines, etc. (In the FSU this was planned for Kamchatka, Sakhalin, Kurils, Lake Baikal, the Black Sea, etc.)

(c) Medical applications: early diagnosis of cancer; diagnosis of blood diseases; color selection of materials in false teeth production; etc.

(d) Monitoring (for ecological safety) of production facilities and industrial processes: constant monitoring of harmful gases discharged into the atmosphere and impurities in waste waters; safety control of plasmochemical processes in microelectronics (detection of organic chemicals); automatic detection of concentration and composition of necessary components in industrial manufacturing; etc.

(e) Remote monitoring of unauthorized warfare production facilities and drug interdiction: remote detection of chemical and biological agents prohibited by international treaties and conventions; biological weapons production facilities; military nuclear facilities; illegal drug processing plants; etc.

(f) Forecasting of natural disasters: investigation of volcanic activity; detection of earthquake precursors for different tectonic regions of land and seafloors.

## **3. Collinear AOS Designs and Examples of AOTF Applications**

The basic optical architecture of a collinear AOS consists of one or more acousto-optic tunable filter (AOTF) cells, a pair of cross-polarizers, a photodetection system, and input/output optics. Figure 1 shows the schematic layout of a collinear AOS. A refractive index phase grating is set up in the birefringent crystal by the propagating acoustic wave. When the unpolarized wideband light is incident upon the input port of the AOS, only linearly polarized light passes through the first polarizer and propagates collinearly with the acoustic wave through the phase grating. The anisotropic AO interaction causes the production of diffracted light with orthogonal polarization, which is passed through the analyzer and later detected by the photomultiplier tube (PMT) detector. The incident and diffracted light beams and the acoustic beam propagation

vectors satisfy the phase matching conditions that arise from the conservation of momentum:  $\mathbf{k}_{\text{diff}} = \mathbf{k}_{\text{in}} + \mathbf{q}$ , where  $k_{\text{diff}} = 2\pi m_o/\lambda$  is the wavevector corresponding to the diffracted light,  $k_{\text{in}} = 2\pi m_e/\lambda$  is the wavevector corresponding to the incident light, and  $q = f/v$  is the acoustic wavevector.  $\lambda$  is the optical wavelength,  $n_o$  and  $n_e$  are the ordinary and extraordinary indices of refraction,  $f$  is the frequency and  $v$  is the speed of sound waves in the crystal. This equation can be simplified to obtain the tuning condition for the optical filter: the central wavelength of the filter,  $\lambda = (n_o - n_e)v/f$ . This can be used to obtain the optical resolution or linewidth of the filter,  $\Delta\lambda = \lambda^2/L\Delta n$ . The spectral resolution depends upon the wavelength of light, the AO interaction length in the crystal (here the length of the crystal), and the difference in the two refractive indices,  $\Delta n$ .

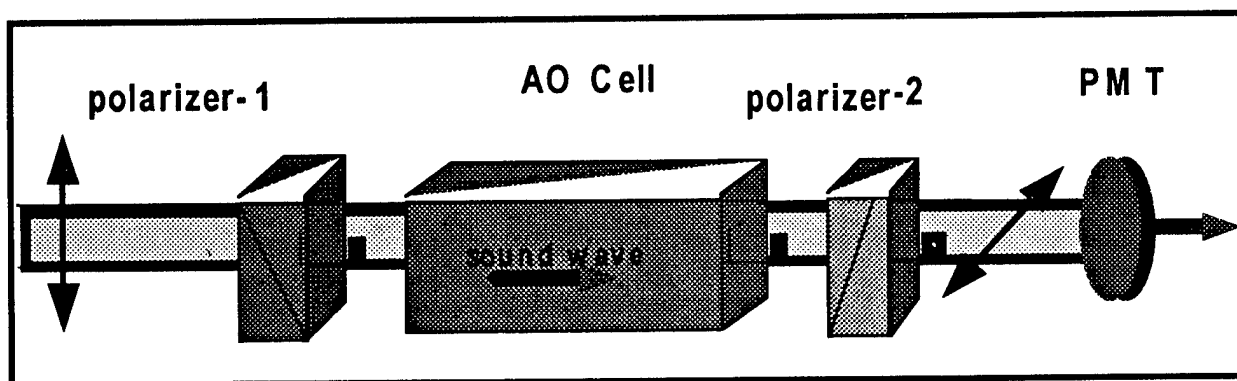
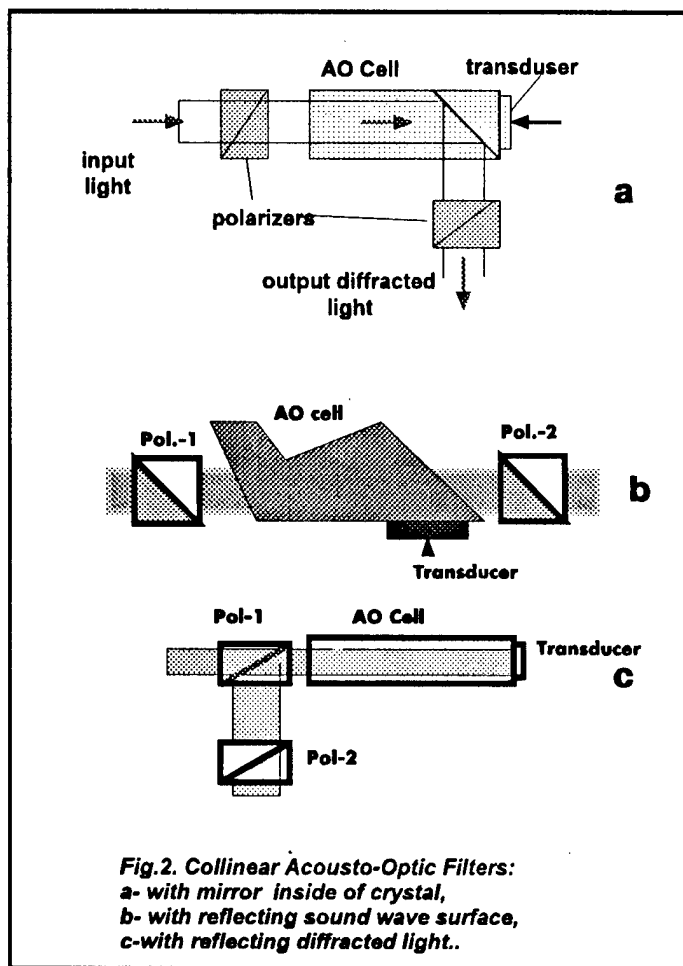


Figure 1. Schematic of a collinear, polarizing AO spectrometer. White light passes through polarizer 1, is polarized (in the diagram plane), then incident on the AO cell in which the sound wave propagates. As a result of an AO interaction, a diffracted light wave with orthogonal polarization is produced, passes through polarizer 2, and is detected by a PMT [1-7].

Optical layouts of some of the AOS devices developed over the last 20 years are shown in figure 2. The most important factors for all these devices are the choice of the crystal material and the geometry of AO interaction in each of these AOTF cells.

AOTF cells have also been used as frequency-selective elements in lasers. An electronically tunable dye laser with multifrequency operation was designed that uses a quartz ( $\text{SiO}_2$ ) or calcium molybdate ( $\text{CaMoO}_4$ ) AO cell, as shown in figure 3. A commercial rhodamine laser was modified by placing an AOTF cell inside the resonator cavity and replacing the partially transmitting output mirror with a 100-percent reflective one. In the simplest scheme, the AOTF within the resonator cavity forms and tunes the spectral profile of the output laser line [8]. If more than one (maximum of four) acoustic wave is generated in the AO cell, then lasing occurs at all corresponding optical wavelengths.

Another more complex design contained a Fabry-Perot (FP) etalon as well as an AOTF [9]. Lasing produced from such a resonant cavity has much narrower linewidth than the simplest scheme discussed earlier: 0.004 vs 0.05 nm, the FP passband being 0.04 nm. The laser can be tuned stepwise over etalon peaks. One can adjust the wavelength of the laser line by tuning the FP etalon slightly (at an angle  $<1^\circ$ ), which does not affect the output light intensity.



The basic electrical and optical layouts for an AOS are shown in figure 4. The high-frequency signal is generated by a special programmable frequency synthesizer. A schematic of the optical layout and a photograph of a satellite-borne polarimetric AOS are shown in figures 4 and 5, and some examples of remote measurements by this instrument are shown in figure 6.

Some problems must be overcome in designing an AOS. The first requirement is to design and fabricate effective transducers, over a broad rf band, that can excite a strong sound wave in the crystal. These days, transducers are made of thin plates of lithium niobate,  $\text{LiNbO}_3$ , which are first welded on the crystal, and then reduced to the necessary thickness by polishing. The most serious problem in the AOS design is the choice of a suitable geometry for the interaction between light and sound waves, such that the sound waves reflected from the edges

of the crystal are quickly absorbed and do not interact with the light wave. If such interactions are not avoided, the accuracy of spectral measurements will be greatly reduced. It is also necessary to make sure that the SNR with respect to the background is quite high. This is usually achieved by using an amplitude modulation of the sound waves and then synchronously detecting the photocurrent.

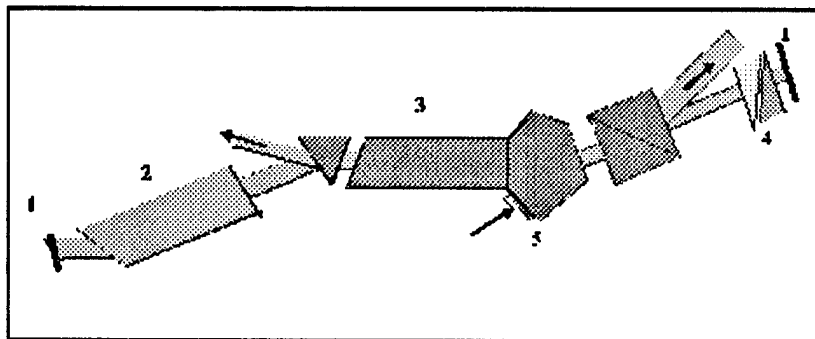


Figure 3. Tunable laser with AOTF within the cavity. (1: mirrors, 2: active medium, 3: AO filter, 4: Fabry-Perot etalon, and 5: transducer.)

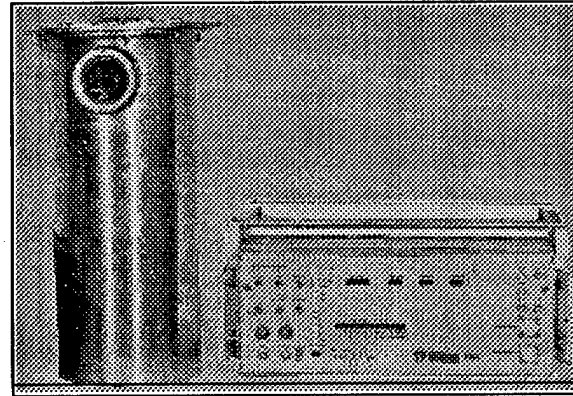
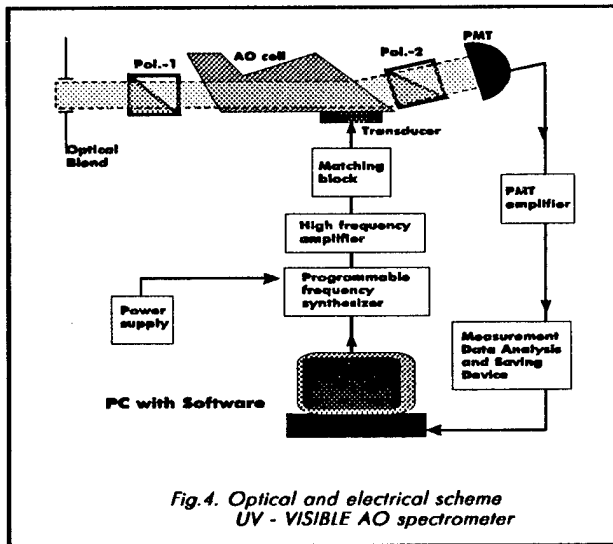


Figure 5. Spaceborne polarizing AOS in the visible range. It was on spacecraft "Ocean" in 1987-90.

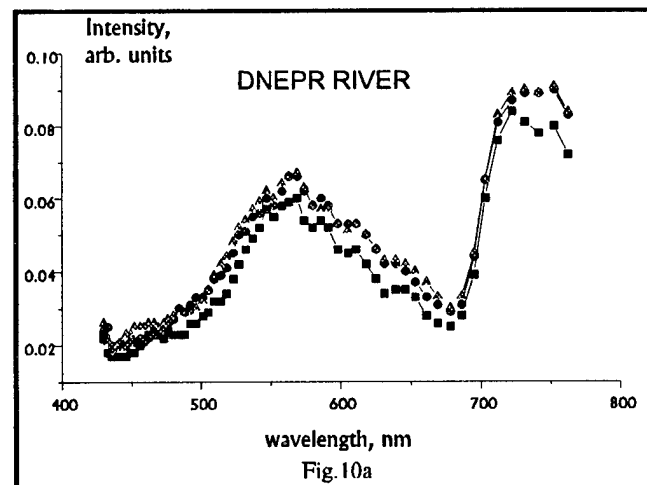
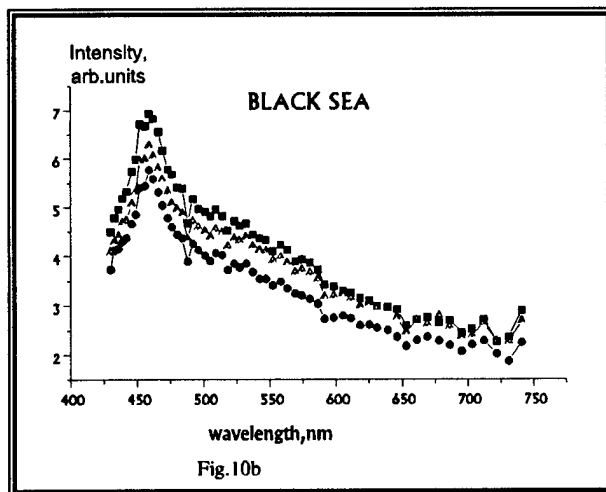


Figure 6. Spectra of reflected sunlight from water surface: (a) Black Sea and (b) Dnepr River.

The main optical characteristic of AO devices is described by the product of the spatial aperture  $S$  and the field of view (FOV),  $\Delta\Omega$ . This product  $\Delta\Omega \cdot S$  (which is the etendue with unity transmission) for four basic types of spectral devices is given below:

for gratings,  $\Delta\Omega \cdot S = S \cdot p/R$ ;

for interferometers,  $\Delta\Omega \cdot S = 2\pi$ ;

for collinear AOTFs,  $\Delta\Omega \cdot S = \pi n_o n_e/R$

Noncollinear AOTF with largest FOV  $\Delta\Omega \cdot S = (\pi/2)N^{1/6}/R$ ;

where  $S$  is the input aperture grating;  $p$  is a number which depends upon both the grating design and angular aperture and has a value close to 0.5;  $R = \lambda/\Delta\lambda$  is the spectral resolving power of the instrument;  $n_o$  and  $n_e$  are the two refractive indices for the AOTF crystal; and  $N$  is the total number of grating periods in the crystal. For a collinear quartz AOTF,  $n_o n_e \sim 2.4$ ; for the largest FOV noncollinear AOTF (using  $\text{TeO}_2$ ),  $\Delta\Omega \cdot S \cdot R \sim 30$ . Thus for an AOTF this product is one order of magnitude higher than for a grating. The AOTF thus has a higher SNR, and the precision of measurements is correspondingly higher. The transmission of an AOTF depends on the design of the AO cell and input power. It can be 100 percent for linearly polarized light.

Collinear AO cells are most useful in spectrometry. Two families of spectrometers were designed in the Laboratory of Acousto-Optics and Optoelectronics (VNIFIRI) in Mendeleevo (near Moscow), Russia, using collinear quartz AOTF cells: the first is a general-purpose spectrometer family, called "Quartz," and the second is a spectropolarimeter family used for remote sensing from satellite and airborne platforms, called "Trasser." The Quartz spectrometer type [10] consists of two units: one optical unit consisting of the AOTF cell and PMT and one electronic unit for the generation and control of the rf signal and for processing of the photocurrent signal. A microprocessor is used to select a mode of operation and to process and display information. The "Quartz-4" device has the following characteristics: a tuning range of 430–800 nm; a bandpass of 0.09–0.58 nm; a data rate of 62.5 readings per second; and a photometric range of  $(0.01\text{--}2.5) \times 10^7 \text{ W/sr m}^2$ . High-speed, automatic operation facilitates rapid data processing and collection. In comparison with the AOS [11] based on the noncollinear paratelluride cell, the Quartz family exhibits higher resolution but requires higher input acoustic power. However, this higher power is not very critical considering the total power budget.

Figure 7 shows the photograph of one of the Quartz AOS. A number of Quartz devices are being used in scientific research for process control and for measurements in medicine and biology [10,12–161]. In a colorimetry measurement application, high resolution ensures precise hue identification [10]. In a medical application, an AOS was used to investigate reflection spectra of unstained biological tissues. The measurements show that the difference between the spectra of pathological and normal tissues can be used in malignant tumor diagnostics. In microelectronics the Quartz spectrometer is used in monitoring the plasma-chemical etching of integrated circuit (IC) chips [14;151]. Evaluation of plasma emission spectra chronograms can be used to determine the most useful spectral lines and to calibrate the plasma-chemical processes.

One example of a Trasser type of AOS is shown in figure 8. Such an AOS has roughly the same characteristics as the Quartz-4, except for the photometric range:  $(0.05\text{--}50) \times 10^7 \text{ W/sr-m}^2$ . There are two versions: one for spaceborne applications and another for air and marine measurements. Their main features are high spectral resolution and polarization sensitivity; the latter is achieved by the use of two crossed AO cells with the orientation of input light polarization aligned orthogonal to each other. Each apparatus is equipped with an internal light source to calibrate the sensitivity. Space, air, and marine testing of these instruments has demonstrated their reliability and their ability to measure phytoplankton concentrations.



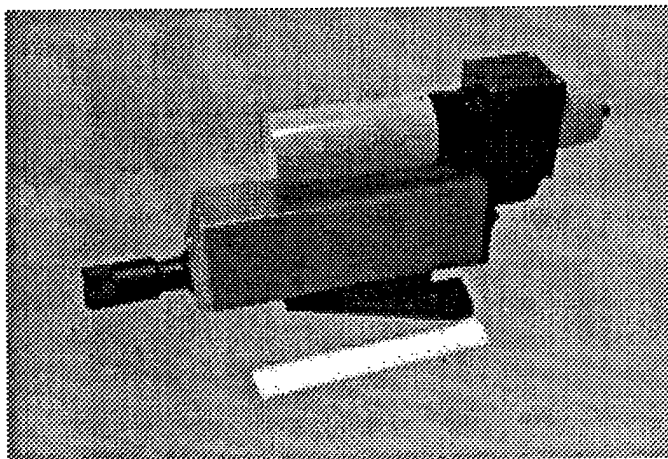


Figure 7. One of the Quartz AOS.

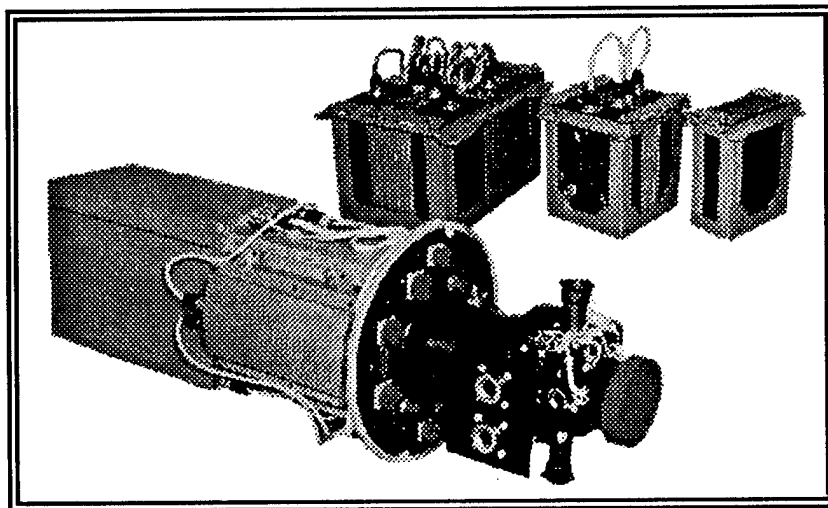


Figure 8. Spaceborne collinear AOS called "Trasser-Okean" flown aboard satellite "Ocean."

In the last two years, two new collinear AOS devices were designed for operation in the UV and visible bands. For both of these instruments, bulky old-fashioned Soviet electronic components have been replaced by state-of-the-art IC's, and the second electronic controller has now been eliminated by the incorporation of the rf generator and synthesizer, wide-band rf amplifier, PMT power supply, and signal processing modules into a personal computer tower. The technical specifications for the UV range instruments are included in Table 1. Three different kinds of visible-to-near-IR AOS were developed for applications in different settings: instruments designed to be used in the laboratory and two-channel instruments for spectropolarimetric measurements on airborne platforms and for space applications. Table 2 contains specifications for these three kinds of AOS's. The airborne and space instruments have built-in calibration lamps for each channel and can also be calibrated by incident solar radiation.

Table 1: Specifications for UV Acousto-Optic Spectrometer

Parameter	Value
Spectral range (nm)	255–430
Spectral resolution (nm)	0.07 or better
Time of measurement/spectral point (ms)	20
Maximum number of spectral points	8000
Minimum frequency step (kHz)	10
Input/output optical window diameter (mm)	6
Angular FOV (°)	2
Diffraction efficiency at 300 nm (%)	20

Table 2: Specifications for Visible Acousto-Optic Spectrometer

Parameter	Value for new laboratory model	Value for each channel of airborne model	Value for each channel of spaceborne model
Spectral range (nm)	400–800	440–780	420–780
Spectral resolution (nm)	0.1–0.5	0.3–0.5, on command	0.02
		0.02	
Wavelength accuracy (nm)	0.3	0.3	0.3
Sensitivity (W)	$10^{-12}$	$10^{-12}$	$10^{-12}$
Maximum number of spectral points	4096	128 (4096)	4096
FOV (°)	2	2	2
Diameter of input window (mm)	6	6	6

UV AOS were designed for remote sensing of gases [17–27], with xenon lamps used as the light source. For analyzing a large number of impurities, the data acquisition rate is the most critical factor. The acquisition time for an AOS is very short. The acquisition time for a Fabry-Perot interferometer (FPI) is much slower since, for high resolution, a whole interferogram needs to be measured regardless of the spectral band of interest. In a classical grating-based spectrometer, it is possible to choose an arbitrary spectral interval, but choosing several separate spectral intervals is not easy. This task involves time losses associated with scanning between intervals. For atmospheric measurements, the classical grating and Fourier transform (FT) spectrometers are not suitable because of the vibrations caused by the air turbulence. Even though such spectrometers are currently used for environment monitoring with high data-acquisition rates, they have a predetermined spectral range of operation and no spectral tuning is allowed. In contrast, an AOTF can be used with rapid wavelength tuning and allows the choice of an arbitrary wavelength operation with a very high speed (tens of microseconds per spectral point). For an AOS, it typically takes around 0.1 s to detect more than 1000 samples, which is the characteristic time of atmospheric turbulence. A grating-based spectrometer, DOAS, designed by the Swedish company Opsis, takes the same number of samples in the same time, but it is not as flexible as the AOS: it cannot perform random wavelength access because it contains moving mechanical parts. In summary, the greatest advantages of an AOTF-based instrument over traditional spectral instruments are the capability for programmable random wavelength selection for either a single or a multiple wavelength operation, and the ability to scan a full spectral range sequentially with

very high speed. Also, higher spectral resolution from an AOS device can be obtained by using more than one AO cell sequentially with phase matching [28,29].

Optimal choice of spectral points depends upon the impurity contents for a particular measurement situation. AOTF-based high-speed adaptive gas analyzers can be designed by the judicious selection of the spectral channels corresponding to a specific measurement condition. The results [24–26] of measuring concentrations of various gases in the laboratory chambers (with different optical lengths) and in the atmosphere are listed in Table 3.

Table 3: Measurements of Air Pollution

Impurity	Chemical formula	Minimum concentration (mg/m <sup>3</sup> for 200- m pathlength)	Maximum concentration (mg/m <sup>3</sup> for 30-m pathlength)	Environmentally safe dose for populated areas (mg/m <sup>3</sup> )
Sulfur dioxide	SO <sub>2</sub>	0.02	50	0.05
Nitric dioxide	NO <sub>2</sub>	0.02	40	0.04
Formaldehyde	HCOH	0.01	100	0.03
Benzene	C <sub>6</sub> H <sub>6</sub>	0.03	10	0.1
Toluene	C <sub>6</sub> H <sub>5</sub> CH <sub>3</sub>	0.04	15	0.6
p-xylene	C <sub>6</sub> H <sub>4</sub> (CH <sub>3</sub> ) <sub>2</sub>	0.03	12	0.2
m-xylene	C <sub>6</sub> H <sub>4</sub> (CH <sub>3</sub> ) <sub>2</sub>	0.06	30	0.2
o-xylene	C <sub>6</sub> H <sub>4</sub> (CH <sub>3</sub> ) <sub>2</sub>	0.3	50	0.2
Naphthalene	C <sub>10</sub> H <sub>8</sub>	0.003	0.5	
Phenol	C <sub>6</sub> H <sub>5</sub> OH	0.003	1	0.02

Another possible feature of the AOTF technology that is of great interest is the ability to transmit spectral images with polarization information [30–32]. This can be used to visualize gas distribution from a localized leak due to a faulty pipe or a reservoir.

#### 4. Conclusion and Summary

We have described the progress made in the development and application of collinear AOS technology in Russia and FSU in the past 20 years. Many of these instruments were used in the remote sensing and collection of oceanic and atmospheric data. Many of these data are still unprocessed because of the political changes in this part of the world. At present, the development of this technology is continuing in collaboration with U.S. scientists; in the past two years new, more sensitive, better performing instruments operating in UV, visible, and near-IR have been developed that use state-of-the-art electronic components. More work is ongoing in the development of instruments in the mid- and long-IR spectral ranges.

#### Acknowledgment

The authors would like to thank V. E. Pozhar and V. V. Timoshenko for their invaluable help in the preparation of this paper.

## References

- [1] S. E. Harris and R. W. Wallace, "Acousto-optic tunable filter," *J. Opt. Soc. Am.* **59**, pp.744–747 (1969).
- [2] R. W. Dixon, "Acoustic Diffraction of light in anisotropic media," *IEEE J. Quantum Electron.* **QE-3**, pp.85–93 (1967).
- [3] I. C. Chang, "Tunable Acousto-Optic Filters: an Overview," *Proc. SPIE*, **90**, pp.12–22 (1976).
- [4] V. I. Pustovoi and V. E. Pozhar, "Коллинеарная диффракция: возможности и перспективы", (Collinear Diffraction: Capabilities and Trends) в кн. "Акустооптические устройства радиэлектронных систем", Изд. "Наука", Ленинград, (Russian), pp. 36–47 (1988).
- [5] I. C. Chang. "AO devices and applications," Chap.12 in *Handbook of Optics*, ed. M. Bass, McGraw-Hill, 1995.
- [6] В. М. Епихин, Ф. Л. Визен, Н. В. Никитин, Ю. К. Калинин. "Неколлинеарный акустооптический фильтр с оптимальными угловыми характеристиками". Журн. Технич. Физики, т. 52, в. 12, 2405–2410 (1982).
- [7] Е. Г. Ананьев, В. Э. Пожар, В. И. Пустовойт. "Акустооптические методы измерения спектров оптического излучения". *Оптика и спектроскопия*, т.62, в.1, с.159–165 (1987).
- [8] А. Yu. Abramov, M. M. Mazur, and V. I. Pustovoi, "Перестраиваемый лазер на основе акусто-оптического фильтра" *Pisma ZhTF*, v. 9, p. 264 (1983). ["Tunable Dye Laser with Acousto-Optic Filter", *Sov. Phys. Techn. Physics Let.*, 32(12), 1472–1473 (1988)].
- [9] М. М. Mazur, Kh. М. Makhmudov, and V. I. Pustovoi, "Перестраиваемый лазер с акусто-оптическим фильтром из  $\text{CaMoO}_4$ ", *Kvantovaya elektronika*, v.15, 711–713 (1988). ["Tunable Dye Laser with an Acousto-Optic  $\text{CaMoO}_4$  Filter", *Sov. J. Quantum Electronics*, 18(4), 453–455 (1988),]
- [10] V. N. Zhogun, H. V. Gazarov, and N. S. Kostin, *Metrological Research Automatization in Radioengineering and Physicotechnical Measurements*. Trudy VNIIFTRI, p. 12 (1985).
- [11] *Kvantovaya Elektronika* (Quantum Electronics), Акустооптический спектрометр "КВАРЦ-4" (Russian), "Acousto-optic spectrometer "QUARTZ-4", v.16, p.173 (1989).
- [12] S. V. Bezdenzhnyh., H. V. Gazarov, V. N. Zhogun, V. I. Pustovoi et al., "Automatic Apparatus Based on Acoustooptic Filter for Recognition of Surface Color Shade," *Pribory i Tekhnika Experimenta. (Scientific Instruments and Experimental Technique)*, pp. 165–168 (1987).
- [13] V. L. Shabarov, V. N. Zhogun, O. V. Ivanov, V. I. Pustovoi et al., *Zhurnal Prikladnoi Spektroskopii* (Applied Spectroscopy Journal), v.47, pp. 825–828 (1987).
- [14] F. L. Visen, V. N. Vorobiev, V. I. Pustovoi, V. N. Zhogun, V. A. Tyablikov, S. I. Zemtovsky, *Mikroelektronika* (Microelectronics), "Контроль методом акусто-оптической спектрометрии равномерности и селективности плазмохимического травления кремниевых структур," (in Russian) т. 20, в. 1, pp. 49–54 (1991).
- [15] V. I. Pustovoi., V. N. Zhogun, and A. V. Tyablikov, "Разработка на основе акусто-оптического спектрометра метода эталонирования качества процессов размерного травления" (Russian), *Электронная техника, сери 3, Микроэлектроника*, в. 2(136), pp. 59–67 (1990).
- [16] S. V. Besdenzhnyh., E. I. Bushuev, H. V. Gasarov., V. I. Pustovoi et al., "Опыт

- применения акусто-оптического спектрометра для измерения коэффициента яркости моря" (Russian). *Methods and Apparatus of Precision Spectrometry: Trudy VNIIFTRI* p.114–122 (1987).
- [17] M. Blanco, J. Coello, H. Ituriaga et al. "Principal components regression for mixture resolution in control analysis by UV-visible spectrophotometry," *Appl. Spectros.* **48**, pp.37–43 (1994).
- [18] U. Platt, D. Perner, and H. W. Patz. "Simultaneous measurement of atmospheric  $\text{CH}_2\text{O}$ ,  $\text{O}_3$ , and  $\text{NO}_2$  by differential optical absorption," *J. Geophys. Res.* **84**, pp. 6329–6334 (1979).
- [19] U. Platt and D. Perner, "Direct measurements of atmospheric  $\text{CH}_2\text{O}$ ,  $\text{HNO}_2$ ,  $\text{O}_3$ ,  $\text{NO}_2$  and  $\text{SO}_2$  by differential optical absorption in the near UV," *J. Geophys. Res.* **85**, pp.7453–7458 (1980).
- [20] H. Edner, A. Sunesson, S. Svanberg, et al., "Differential optical absorption spectroscopy system used for atmospheric mercury monitoring," *Appl. Opt.* **25**, pp. 403–409 (1986).
- [21] H. Edner, P. Ragnarson, S. Spannare, and S. Svanberg, "Differential optical absorption spectroscopy (DOAS) system for urban atmospheric pollution monitoring," *Appl. Opt.* **32**, pp. 327–333 (1993).
- [22] R. L. Nelson, "Role of TAS AOTF in commercial stack analyzer," *Proc. SPIE*, **753**, pp. 103 (1987).
- [23] Ch. V. Gazarov, V. E. Pozhar, and V. N. Zhogun, "Acousto-optical spectrometer for air pollution monitoring," *Proc. SPIE*, **2107** (1992).
- [24] М. М. Мазур, В. Э. Пожар, В. Н. Шорин. *Законодательная и прикладная метрология*, N. 3, pp. 34–37. Оптические газоанализаторы на основе акустооптических фильтров 1995.
- [25] М. М. Мазур, В. Э. Пожар, and V. N. Shorin, "Spectral optical gas analysers on the basis of acousto-optical tunable filters for air impurity monitoring," *Abstracts of 2nd International symposium on Chromatography and Spectroscopy in Environment monitoring (ISCSE '96)*, June 18–21, 1996, St. Petersburg., [М. М. Мазур, В. Э. Пожар, В. Н. Шорин. *Тезисы 2-го Межд. Симпозиума по Хроматографии и спектроскопии в анализе окружающей среды*, 1996, июнь 18–21, С.-Петербург., Спектрально-оптические газоанализаторы на основе акустооптических фильтров для контроля содержания примесей.]
- [26] Ying Liu, B. R. Upadhyaya, and M. Naghedolfeizi, "Chemometric data analysis using artificial neural networks," *Appl. Spectrosc.* **47**, pp. 12–23 (1993).
- [27] R. Haus, K. Schafer, W. Bautzer et al., "Mobile Fourier-transform infrared spectroscopy monitoring of air pollution," *Appl. Opt.* **33**, pp. 5682–5689 (1994).
- [28] V. E. Pozhar and V. I. Pustovoi, "Collinear diffraction in several AO cells placed consequently," *Sov. Quant. Electronics* **12**, pp. 2180–2182 (1985).
- [29] V. I. Pustovoi and V. E. Pozhar, "Collinear diffraction of light by sound waves in crystals: devices, applications, new ideas," *Photonics and Optoelectronic* **2**, pp. 53–69 (1994).
- [30] F. L. Vizen and V. I. Pustovoi, "Development and investigation of spectral acousto-optical imaging system," Scientific Report 07.03.15.05, VNIIFTRI (Insitute of physical technical and radioengineering measurements, Mendeleevo, Moscow region), 1986 (in Russian).
- [31] V. N. Zhogun and V. I. Pustovoi, "Development and investigation of spectral acousto-optical imaging instrument for visible and near-IR ranges," Scientific Report 07.03.11.14 VNIIFTRI, 1989 (in Russian).
- [32] V. E. Pozhar and V. I. Pustovoi, "Possibilities of new vision system creating on basis of acousto-optical imaging spectrometers," *Radiotechnica I Electronica*, (in Russian, Radiotechnics and Electronics), v. 41, N.10, 1996 (to be published).

# Recent Advances in AOTF Design and Fabrication at St.Petersburg State Academy of Aerospace Instrumentation

V.V.Kludzin, S.V.Kulakov, V.V.Molotok

St. Petersburg State Academy of Aerospace Instrumentation,

Laboratory of Acousto - Optic Systems,

67 B.Morskaia St., St.Petersburg, 190000, Russia,

Phone/FAX: +7 (812) 108-4204, E-mail:molotok@softjoys.ru

Acousto-optic tunable filters (AOTF) are intended to yield spectral parts out of their input optical fields, and they utilize some features and advantages of acousto-optic interaction in anisotropic materials. As it is in conventional systems for optical spectroscopy, the AOTF key element is a diffraction grating, although the dynamic (moving) acoustic grating with electronically tunable parameters is used, which is different from static gratings used in conventional spectroscopy. Moreover, the 3D nature of acousto-optic interaction in anisotropic media presents several advantages over the conventional systems (increased angular aperture, extended dynamic range, etc.). Those advantages give the acousto-optic filtering methods a very promising feature, and, in some applications, these methods become almost indispensable.

We can point out the fundamental advantages of the acousto-optic tunable filters:

1. Controllable tuning by an electronic signal.
2. Fast switching speed.
3. Extended angular aperture.
4. Compatibility with electronic analog and digital modules.
5. Simple design and small sizes.

Many existing variants in AOTF design allow us to find feasible solutions for most consistent requirements given by different application demands.

## 1. Variants of acousto-optic tunable filters

Similar to conventional spectrometer systems, an AOTF can be manufactured basing on a well-known Bragg interaction [1-5]. Such AOTF is shown in Fig.1. The typical feature of such AOTF is an optical scheme transforming an arbitrary input light distribution into a collimated light beam. The quality of this collimation must be highest in the plane of acousto-optic interaction. AOTF resolution considerably depends on the size  $d$  of the output diaphragm:

$$d \leq \frac{k\lambda F}{D}.$$

where  $k \leq 1$ ,  $\lambda$  is the optical wavelength,  $D$  and  $F$  are the size of the acousto-optic cell and focal length, respectively.

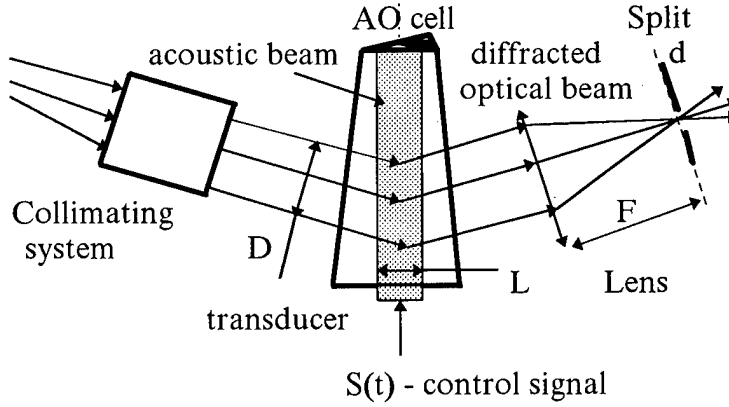


**Fig.1. The isotropic acousto-optic tunable filter**

In general case, spectral filtering in AOTF is performed by utilizing two independent mechanisms: by spatial filtering with the diaphragm  $d$  in the focal plane of the output lens and by spectral-angular selectivity inherent in a bulk periodic structure generated by an acoustic wave. The latter factor becomes dominating when the diffraction parameter  $Q$  [2, 5] increases, or when quasi-collinear and collinear interaction regimes are used. The first mechanism gives the resolution power  $R_s$  determined by the number of grooves in the diffraction grating:

$$R_s = \frac{fD}{v}.$$

The second one yields the resolution  $R_o$  determined by the diffraction spread of acoustic wave

$$R_o = \frac{fL}{v} \tan \Theta_o,$$

where  $f$ ,  $v$  are the frequency and velocity of the acoustic wave,  $0.5\Theta_o$  is the Bragg angle, and  $L$  is the interaction length.

If we select the parameters of our system in a such way that  $R_s = R_o$ , we could achieve the maximum possible spectral resolution of

$$\frac{\delta\lambda}{\lambda} = \frac{0.66}{R},$$

which is 30% better than the resolution obtained by using only one filtering mechanism. In this case, the shape of the spectral response is

$$g(\lambda) \sim \left\{ \text{sinc} \left[ \pi R \left( \frac{\lambda}{\lambda_0} - 1 \right) \right] \right\}^4$$

The most important thing here is a considerable drop in the side lobes level, which makes the shape of the spectral response look like "a button" increasing the dynamic range of the whole system.

But the anisotropic regimes of the acousto-optic interaction seem to be more interesting for the most applications [5-10]. The main parameters of different acousto-optic interaction regimes used in AOTF manufacturing are presented in Table 1.

A brief comparative analysis of different interaction regimes could be useful to understand their capabilities. The main disadvantage of systems with the isotropic interaction is a strong dependence of their resolution on the collimating quality of the light beam coming onto their acousto-optic cell. This factor drastically restricts the angular aperture in the interaction plane and makes it difficult to process optical fields with arbitrary spatial coherence.

Still, the systems with the isotropic interaction have some clear advantages:

1. They are insensitive to the polarization of the input optical field.
2. More materials can be used in their manufacturing under different technical requirements.
3. They have high angular aperture in the plane perpendicular to the plane of acousto-optic interaction.
4. The isotropic materials are comparatively less expensive, and their workpieces can be larger.

The quasi-collinear regime of the anisotropic interaction, which parameters and wave vector geometry are presented in row 2 in Tab.1 has the same disadvantage that the isotropic variant, and its resolution is determined by the diffraction spread of the acoustic column.

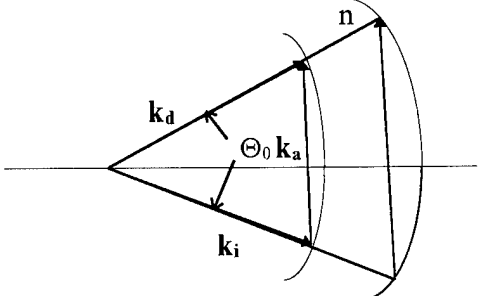
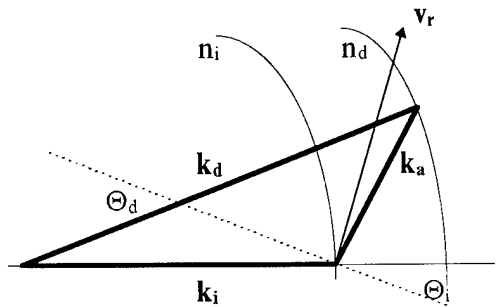
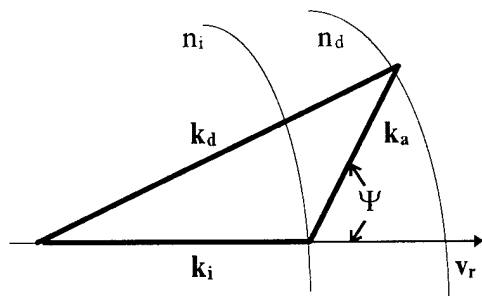
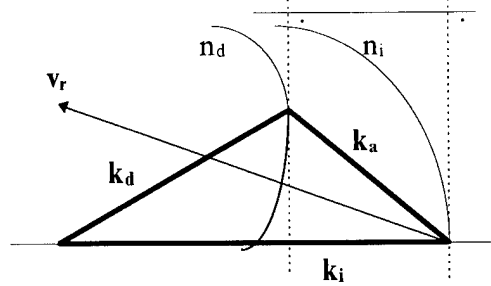
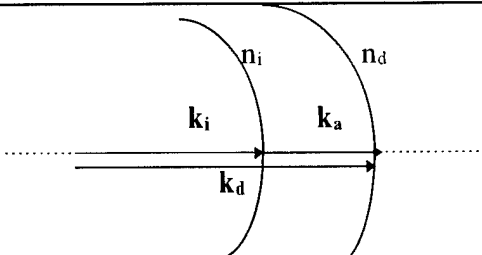
The sub-collinear regime of the anisotropic interaction (row 3) requires that acoustic anisotropy be used and it orients the vector of the incident optical wave along the direction of acoustic power propagation. This eliminates the influence of acoustic diffraction spread and increases the resolution. This regime does not increase the angular aperture considerably in comparison with the first regimes.

Row 4 shows the main parameters of the tangential anisotropic interaction first proposed by Dr. I.C. Chang [9]. This regime can give large angular aperture with acceptable resolution. The main condition of this geometry is the requirement that the tangents to the ends of the incident and diffracted optical vectors must be parallel. The same condition can be expressed mathematically as

$$\tan \Theta_i \tan(\Theta_a - \Theta_i) = 2,$$



Table 1. The geometry of different regimes of acousto-optic interaction

1		$\lambda f = n v \sin \Theta_0$ $k_a = \frac{2\pi f}{v}, \quad k_i = k_d = \frac{2\pi n}{\lambda}$ $\delta \lambda \approx \frac{\lambda^2}{D \sin \Theta_0}$ <p><i>isotropic</i></p>
2		$\lambda f = \Delta n_0 v \sin \Theta_i$ $k_i = \frac{2\pi n_i}{\lambda}, \quad k_d = \frac{2\pi n_d}{\lambda}$ $\delta \lambda \approx \frac{\lambda^2 \cos \Theta_i}{\Delta n_0(\lambda) L \sin^2 \Theta_i}$ <p><i>quasicollinear</i></p>
3		$\lambda f \cong v \frac{\Delta n(\lambda, \Theta_i)}{\cos \Psi}$ <p><i>subcollinear</i></p>
4		$\lambda f = \Delta n v \sqrt{(\sin^4 \Theta_i + \sin^2 2\Theta_i)}$ $\delta \lambda \approx \frac{\lambda^2 \cos(\Theta_a - \Theta_i)}{\Delta n_0(\lambda) L \sin^2 \Theta_i}$ $\operatorname{tg} \Theta_i \operatorname{tg}(\Theta_a - \Theta_i) = 2$ <p><i>Tangential</i></p>
5		$\lambda f = \Delta n(\lambda) v$ $\delta \lambda = \frac{\lambda^2}{\Delta n(\lambda) L}$ <p><i>collinear</i></p>

where  $\Theta_i$ ,  $\Theta_a$  are the incident angle of the optical wave and acoustic vector, respectively, measured from the crystal's optical axis. The disadvantage of this interaction regime is the facts that the crystal's volume is used not very rationally, and that the optical input and output can be rather inconvenient.

Crystals with low symmetries allow us to combine the sub-collinear and tangential interaction regimes, thus to combine their advantages [10].

The degenerated case of the anisotropic interaction is the collinear regime (row 5) when not only the incident and diffracted optical vectors, but the acoustic phase and ray vectors are oriented toward one direction. The advantages of such regime are large aperture (the same in both planes), simple design and rational use of the crystal. The disadvantages are polarization sensitivity during processing and strong requirements to the quality of the polarizing elements operating in a wide spectral range.

It should be pointed out that the high resolution and wide angular aperture are contradicting requirements, as generally  $\Delta\Psi R = \text{const}$  for all interaction regimes.

Nevertheless, when for the isotropic regime the angle  $\Delta\Psi$  is flat (2D) and defined in the diffraction plane, this angle is 3D (stereo angle) for the collinear and tangential regimes.

One of possible designs of the collinear AOTF is shown in Fig.2. In this layout, the light diffraction by the shear acoustic wave in  $\text{CaWO}_4$  crystal is used. The phenomenon of the transformation of the longitudinal wave into the shear one at the beveled face is used to enter the shear wave into the medium of interaction. The same face (as it is an optical prism) is used to spatially separate diffracted and passing by waves which have different polarization. Thus, it is possible to make the requirements to the quality of the polarizing elements less strict. The disadvantage of this scheme is the requirement to take into account the prism dispersion when the system operates in a wide spectral range.

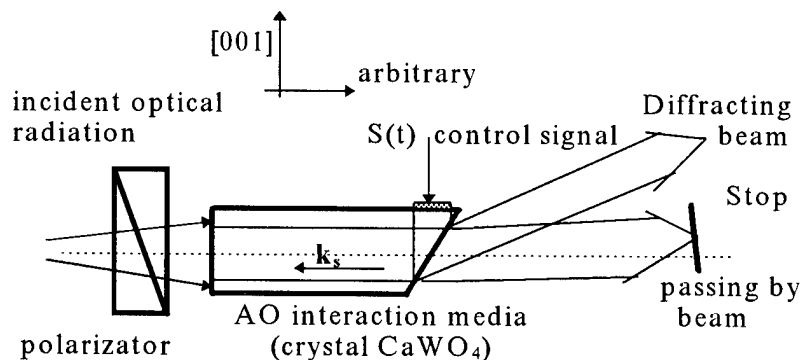


Fig.2. Collinear AOTF

## 2. The main parameters of AOTF

The main parameters of AOTF are: spectral resolution, tuning range and time, optical transmission coefficient, angular aperture, dynamic range, etc. It seems unfeasible to maximize the main parameters simultaneously, due to contradicting trends during the process of maximizing separate parameters. The AOTF resolution is determined by the maximum possible sizes of the medium of interaction and is fundamentally limited by the acoustic attenuation for all interaction regimes.

The AOTF optical transmission coefficient is determined by the photoelastic properties of the material and depends on the acoustic power of the control signal. As a rule, this coefficient increases with the AOTF resolution. Due to the phase nature of acousto-optic interaction, the transmission coefficient quadratically decreases when the AOTF is tuned into the long wavelength part of its spectral range, that is why the problem of acceptable AOTF transmission coefficient becomes essential for the IR range. The AOTF dynamic range determines the ability of the system to process optical fields with different power levels and depends (as it does in antennas) on the sidelobe level in its spectral response.

Some possible ways to increase some non-contradicting AOTF parameters are illustrated by the experimental results shown in Fig.3.

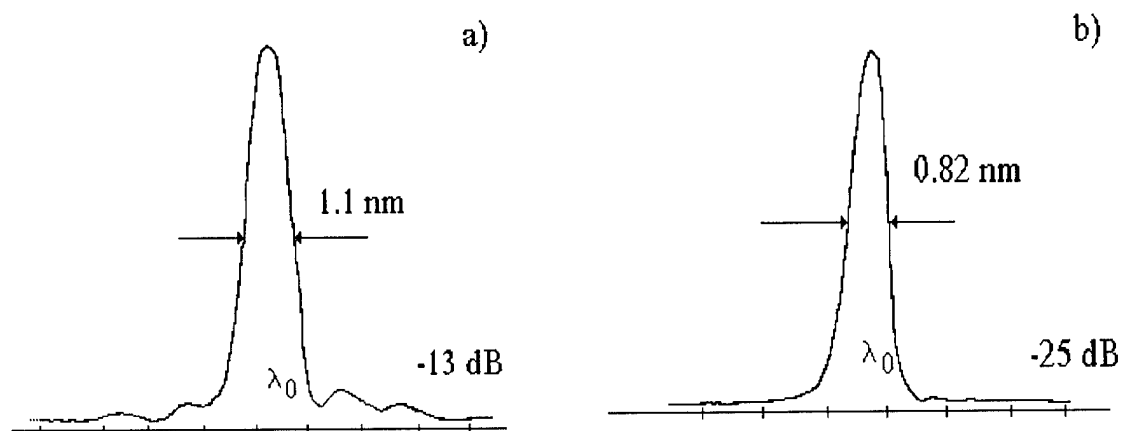


Fig.3. The spectral responses of AOTF ( $\lambda_0=0.63 \mu\text{m}$ )

Using the quasi-collinear interaction in the  $\text{TeO}_2$  crystal, a spectral response for  $\lambda=0.63 \mu\text{m}$  was obtained (Fig.3a). Fig.3b shows the same response for the autocollimating scheme where the diffracted beam is reentered into the medium of interaction and diffracts for the second time. Together with the predicted small improvement in the resolution, considerable decreased side lobes ( $<-25 \text{ dB}$ ) can be seen.

At the present time, only limited number of materials can be used to manufacture anisotropic AOTF. The main parameters of such materials are presented in Table 2.

Generally, all regimes of acousto-optic interaction (including the isotropic one) are possible in the crystals of the trigonal class, although the output of these regimes will be different. Theoretically, the highest AOTF resolution can be achieved in the  $\text{LiNbO}_3$  crystals, as it has the lowest acoustic attenuation among all those crystals. Practically, the resolution in this crystal is limited by the technologically acceptable workpiece size and local inhomogeneity of birefringence. For spectral filtering in the IR region, the crystals with high acousto-optic figure of merit are to be used to reduce the control signal power. For this purpose, the  $\text{Tl}_3\text{AsSe}_3$  crystal developed and tested by Dr. M.Gottlieb [5] can be used instead of the well-known  $\text{TeO}_2$  crystal.

**Table 2. Physical parameters of acousto-optic materials**

Material	Transparency range, $\mu\text{m}$	Refraction index ( $\lambda=0.63 \mu\text{m}$ )	Acoustic velocity $v \cdot 10^5 \text{ cm/sec}$	Figure of merit, $M_2 \cdot 10^{-18} \text{ c}^3/\text{g}$	Range of control frequencies, MHz ( $\lambda=0.63 \mu\text{m}$ )	Possible interaction regimes
$\text{TeO}_2$	0.36 - 5	$n_0=2.26$ $n_e=2.41$	0.617	600 - 1000	50 - 100	w/o collinear
$\text{LiNbO}_3$	0.4 - 4.5	$n_0=2.28$ $n_e=2.2$	3.9 6.57	3 - 8	400 - 600	all regimes
$\text{CaWO}_4$ ( $\text{CaMoO}_4$ )	0.4 - 4.5	$\Delta n =  n_0 - n_e  = 0.016$	2.3	$\sim 10$	60	collinear
$\text{SiO}_2$	0.15 - 4	$n_0=1.542$ $n_e=1.551$	5.75	$\sim 2$	80	all regimes
$\text{Tl}_3\text{AsSe}_3$	1.25 - 17	$n_0=3.38$ $n_e=3.19$ ( $\lambda=1.5 \mu\text{m}$ )	1.0	$\sim 700$	100 ( $\lambda=1.5 \mu\text{m}$ )	all regimes

### 3. AOTF used for modulating spectrum width of a wideband optical signal

In a wide sense, the term "tunable" means some additional features in an AOTF implemented by the shape of its control signal. As an example, in some tasks, the AOTF spectral response should be normalized in a given spectral range, to reduce the full tuning time in the range. In the tasks of "fast" filtering of optical fields in the range  $\Delta\lambda$ , an irregular width of the spectral response at the borders of the range can be often seen, when a conventional chirp control signal is used. This is the result of the general dependence of the resolution  $\delta\lambda$  on the wavelength in the form of  $\delta\lambda \sim \lambda^2$ .

If our task permits such operation, this spectral response can be normalized by making it wider at the short-wave region of the range  $\delta\lambda(\lambda) = \text{const} = \delta\lambda(\lambda_{\text{max}})$  by selecting an appropriate frequency variation law in the control signal and optimizing its parameters. In this case, the number of resolving points  $N$  and the full scanning time  $T$  decrease. Calculations show that, for the bulk acousto-optic interaction, the parabolic frequency law in the control signal can reduce scanning time in  $\sqrt{N}$  times, where  $N$  is the number of sampling points in the "slow" scanning regime.

To illustrate those techniques, we discuss an AOTF used in a system modulating the spectrum width of a spread-spectrum optical signal. In this case, the optical signal with wide spectrum (i.g., a LED signal) comes onto the AOTF input, which control signal is modulated with a rectangular pulse with a given duration and clock rate. The clock rate is taken from the condition  $T \leq D/v$ , where  $D$  is the AOTF optical aperture, and the pulse duration can vary in  $0 < \tau < T$ . In this case, the width of the spectral response  $\delta\lambda$  varies depending on the duration of the control signal traveling in the optical aperture, i.e., on  $\tau$  ( $\delta\lambda = k\tau$ ). At the same time, the AOTF transmission coefficient varies proportionally to  $1/\tau^2$ , but this can be compensated by synchronous changing the amplitude (power) of the control signal.

The experimental results for a collinear AOTF made of the  $\text{CaWO}_4$  crystal are presented in Fig.4 and 5. Fig.4a shows the AOTF spectral response when its aperture is fully filled with the control signal ( $\tau = T$ ), Fig.4b when  $\tau \approx 0.5T$ , the acoustic power in the pulse being the same. Fig.5a and 5b show the discrete spectral responses when the several pulses are simultaneously in the aperture. The number of the pulses can be found basing on the number of the partial responses in the overall response. It is seen that the time structure of the optical distribution is stationary, although the control signal is modulated. It is obvious that other response shapes are possible when the control signal has appropriate waveform and parameters.

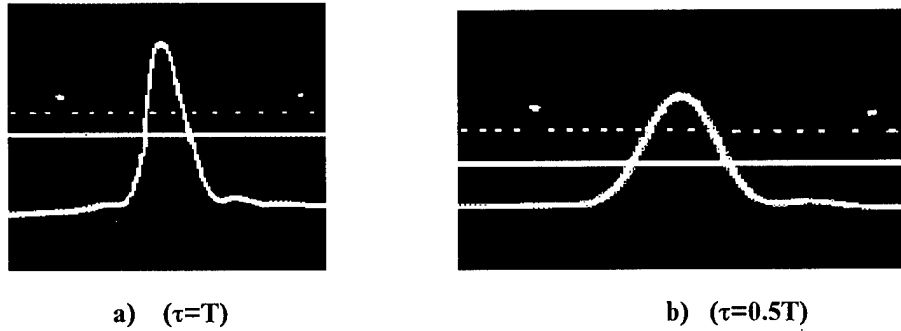


Fig.4. Spectral responses of  $\text{CaWO}_4$  collinear AOTF

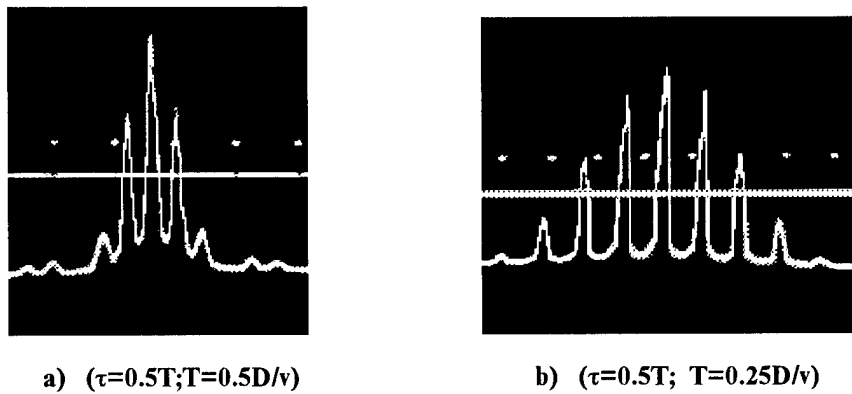


Fig.5

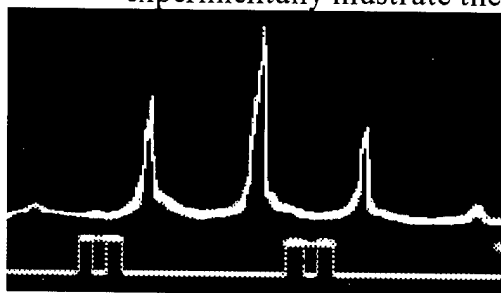
## 4. AOTF used in conventional spectrometry

Table 4 presents the main parameters of acousto-optic spectrometers with different interaction regimes.

**Table 4. Spectrometer parameters**

AOTF materials	Analysis range, $\mu\text{m}$	Control frequency range, MHz	Resolution, nm ( $\lambda=0.63 \mu\text{m}$ )	Transmission coefficient	Analysis time, ms	Interaction regimes
Water	0.4-0.7	28-50	2.5	0.5 $P \approx 0.1 \text{ W}$	$\geq 2$	Isotropic
PbMoO <sub>4</sub>	0.6-1.1	90-160	1.5	0.5 $P \approx 0.5 \text{ W}$	1	Isotropic
LiNbO <sub>3</sub>	0.5-1.0	7-14	6	0.65 $P \approx 0.2 \text{ W}$	1	Sub-collinear
TeO <sub>2</sub>	0.65-1.5	25-55	1.2	0.8 $P \approx 0.05 \text{ W}$	$> 3.5$	Quasi-collinear
CaWO <sub>4</sub>	0.56-1.04	35-65	1.1	0.5 $P \approx 0.5 \text{ W}$	5	Collinear $\Delta\Psi \approx 4.5^\circ$

All the devices in this table (except the last one) have small angular apertures and thus require their input optical beams be strongly collimated. Fig.6-8 experimentally illustrate the capabilities of these acousto-optic spectrometers.



**Fig.6**

Fig.6 presents the response for System 3 to the light from a He-Ne laser ( $\lambda=0.63 \mu\text{m}$ ). Acoustic interference in the LiNbO<sub>3</sub> crystal is responsible for the discrete shape of the response, and its envelope the well-known theoretical dependence for its waveform.

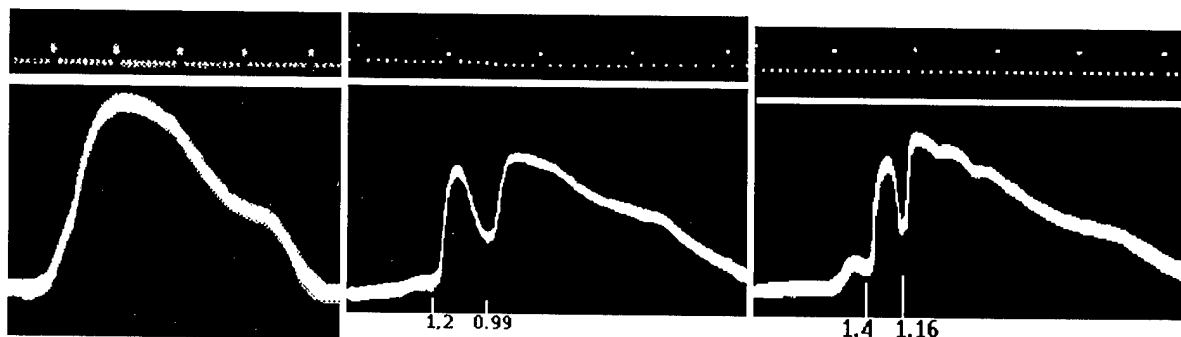


**Fig.7**

Fig.7a shows the spectral response of System 4 to the light from an electric bulb, and fig.7b and 7c show the absorption spectra of water and acetone, respectively

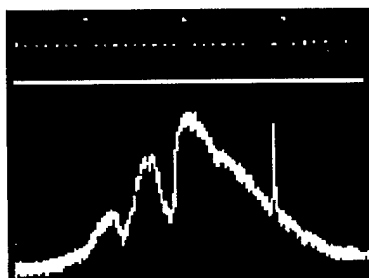


Fig.8

Fig.8 shows the spectral response of System 5 (a collinear AOTF) which is the absorption spectrum of neodymium glass. Here, a reference signal from a He-Ne laser is presented. The noticeable weighting in the spectral response is due to the spectral characteristic of a photoreceiver, and the noise is due to bad polarization selection.

## Conclusion

Acousto-optic tunable filters, regardless of their specific layouts, have several obvious advantages resulting from their electronic control and a large variety of available materials. Some typical features of some anisotropic interaction regimes make it possible to manufacture AOTF with extended angular apertures. Nevertheless, this requirement is not so strict in some applications, and the medium of interaction can be selected from larger number of available materials and diffraction regimes. In some cases, the advantages of isotropic media are worth remembering.

Considerable increase in tuning speed in a given spectral range can be achieved by "normalizing" the spectral response. Changes in the shape and parameters of the control signal completely determine the waveform shape of the AOTF spectral response.

It is obvious that the potential capabilities of acousto-optics are not reached in this application, and their utilization is a matter of future.

## References

1. O.Gusev, V.Kludzin. Acoustooptic measurements, Leningrad, 1987 (in Russian: О.Гусев, В.Клудзин. Акустооптические измерения, Ленинград, изд-во ЛГУ, Ленинград, 1987)
2. V.Balakshy, V.Parygin, L.Chirkov. Physical principles of acoustooptic, Radio and Svyaz, 1978 (in Russian: В.Балакший, В.Перыгин, Л.Чирков. Физические основы акустооптики, Радио и связь, М., 1978)
3. R.Sprague. A review of acoustooptic signal processors. Proc.SPIE, v.185, 1979, p.130-155
4. J.Jacob, I.C.Chang. Development of an AOTF spectrometers. Proc.SPIE, v.202, 1979, p.40-46
5. Design and Fabrication of Acoustoptic Devices. Ed.by A.Goutzoulis, D.Pape. Marcel Dekker Inc., New York, 1994
6. Dixon R.W. Acoustic diffraction of light in anisotropic media. IEEE Journ., QE-3, #2, 1967, p.85-93
7. Nien S.T.K., Harris S.E. Aperture-bandwidth characteristics of the filter. JOSA, 1972, v.62, #5, p.62-676
8. Yano T., Watanabe A. New noncollinear acoustooptic tunable filter using birefringence in TeO<sub>2</sub>. Appl. Phys. Letters, 1978, v.24, #6, p.256-258
9. Chang I.C. Noncollinear acoustooptic filter with large angular aperture. Appl. Phys. Letters, 1974, v.25, p.370-373
10. Sivanayagam A., Findlay D. High resolution noncollinear acoustooptic filters with variable passband characteristics: design. Appl.Optics, 1984, v.233, #24, p.4601-4608.

# Application of Acousto-Optic Interaction for Filtration of Arbitrary Polarized Radiation

Vitaly B. Voloshinov

Physics Department, M.V. Lomonosov Moscow State University  
119899 Moscow, Russia

## 1. Introduction

Acousto-optic methods of control of coherent and non-coherent optical beams find wide applications in modern science and technology [1-4]. As known, the principle of acousto-optic devices operation is based on the phenomenon of light diffraction by acoustic waves in a solid medium [1,2]. The diffraction may be used for control of practically all parameters of radiation. In particular, intensity and spectral composition of a non-monochromatic optical beam may be regulated by means of tunable acousto-optic filters, i.e. instruments applying the diffraction [5,6].

In the majority of acousto-optic methods of modulation, scanning and spectral filtration, it is assumed that incident light is linearly polarized. Moreover, the direction of optical polarization is fixed and may not be changed during operation of an instrument. In opposite case, control of unpolarized beams as well as of optical rays with circular or elliptical polarization becomes not efficient. In order to obtain linear polarization of radiation with the desirable direction of the electrical vector, it is usually necessary to use polarizers or phase plates in combination with acousto-optic cells. However, in practice, application of a polarizer or a phase plate at a filter input is not tolerable because of optical energy losses. Informative signals and fruitful information are inevitably lost in this case. It is evident that for isotropically polarized light up to 50% of the input optical energy is cut off by polarizers and may not be used during further processing of light.

The following practical cases in optics, spectroscopy, information processing and optical communication may be mentioned in this context. For example, the problem of unpolarized light filtration is urgent during processing of low-power optical radiation in astronomy, in remote sensing and spectral-polarization analysis of images, in waveguide communications and in other branches of science and technology [7-12].

## 2. Acousto-Optic Interaction Geometry in $\text{TeO}_2$

Experimental investigation of the filtration of arbitrary polarized beams was performed using birefringent crystals of tellurium dioxide. Hence, the analysis to be presented in this paper will be also made on base of  $\text{TeO}_2$  crystals. However, basic statements and proposals are valid for many other crystalline materials. Therefore, it is possible to generalize the conclusions of the paper to other birefringent crystals.



## 2.1 Wavevector Diagrams

Principles of acousto-optic filters operation are usually treated using wavevector diagrams [1-4]. The diagrams are illustrating the case of acousto-optic interaction in  $(1\bar{1}0)$  plane of  $\text{TeO}_2$ .

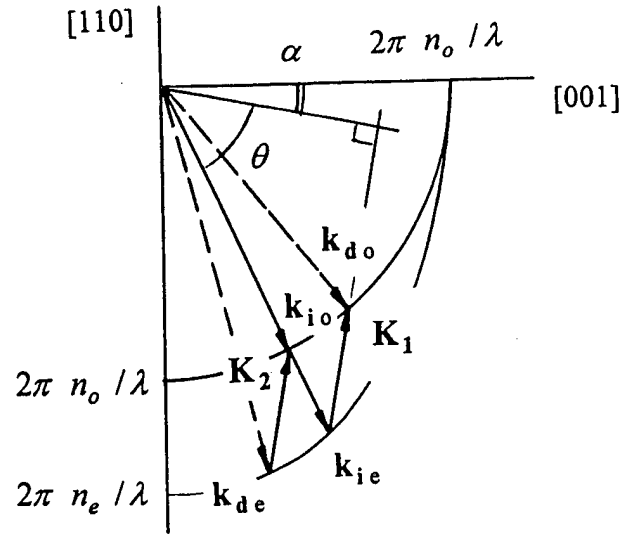


Figure 1. Wavevector diagrams of interaction in tellurium dioxide

As seen in Fig.1, slow shear acoustic waves are propagating in the interaction plane at  $\alpha$  angle relative to  $[110]$  axis. The presented picture corresponds to the regime of interaction with low sensitivity to polarization of light if light and sound propagation directions are properly chosen [8-10]. Momentum conservation laws for extraordinary (e) and ordinary (o) polarized components of optical beams incident at  $\theta$  angle on ultrasound may be written in the following form [11-12]

$$k_{ie} + K_1 = k_{do} ; \quad k_{io} - K_2 = k_{de} , \quad (1)$$

where optic  $k$  and acoustic  $K$  wavevector lengths are equal to

$$k_{io} = 2\pi n_{io} / \lambda = k_{do}$$

$$k_{de} = 2\pi n_{de} / \lambda$$

$$k_{ie} = 2\pi n_{ie} / \lambda$$

$$K_1 = 2\pi f_1 / V$$

$$K_2 = 2\pi f_2 / V .$$

In the above equations,  $\lambda$  - wavelength of light;  $n_{io}$  and  $n_{ie}$  - indexes of refraction for ordinary and extraordinary components of incident light;  $k_{io}$  and  $k_{ie}$  -

corresponding optical wavenumbers of incident waves;  $V$  and  $f$  - phase velocity and frequencies of ultrasound. Index of refraction for extraordinary diffracted beam  $n_{de}$  as well as the diffracted wavevector length  $k_{de}$  may be also found from the diagram. The characteristic feature of the interaction consists in the fact that the two acoustic wavevector lengths are equal to each other, so that  $f_1 = f_2$  [11,12]. Consequently, incident arbitrary polarized beam is divided in the medium into two portions, i.e. into ordinary and extraordinary polarized components. These orthogonally polarized beams interact with ultrasound independently in accordance with the conservation laws Eq.(1).

## 2.2 Acousto-Optic Filtration Scheme

As a result of the interaction, a couple of diffracted optical beams appear at the crystal output. These beams are forming +1 and -1 diffraction orders and are propagating in space symmetrically relative to the transmitted beam, as illustrated in Fig.2. It is seen in the vector diagram that light in +1 diffraction order originates from the extraordinary polarized component of incident radiation. The beams of +1 diffraction order are up-shifted in optical frequency because of Doppler effect [1,2]. On the contrary, down-shifted extraordinary polarized beams in -1 diffraction order originate from the ordinary polarized incident component. Zero diffraction orders correspond to the transmitted light which consists of two parallel optical rays slightly shifted in space because of birefringence of the medium.

The major disadvantage of the examined interaction geometry appears from the spatial separation of the two filtrated beams. In practice, it is usually necessary to collect and to utilize both filtrated rays. Analysis of the problem and experimental investigation of the filter demonstrated that these beams propagate at the filter output at angles up to  $16^\circ - 18^\circ$  if  $\alpha = 18^\circ - 18.9^\circ$  [11,12]. Integration of the two rays in order to form a single filtrated beam requires application of various optical elements, e.g. lenses. Unfortunately, it leads to additional expenditures.

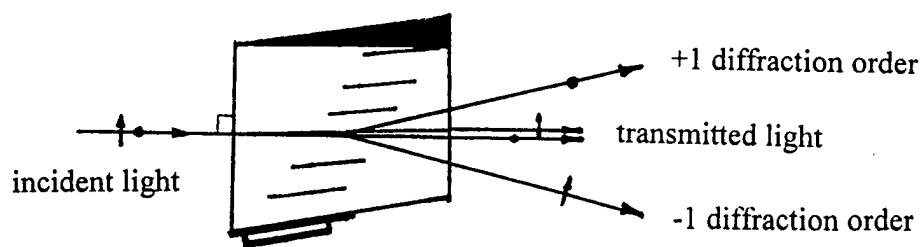


Fig.2. Propagation of optical beams at the filter output

## 2.3 Interaction with Adjacent Diffracted Beams

Wavevector diagrams in Fig.3 illustrate the regime of diffraction in tellurium dioxide that may be considered as a modification of the interaction scheme described in the above sections of the paper.

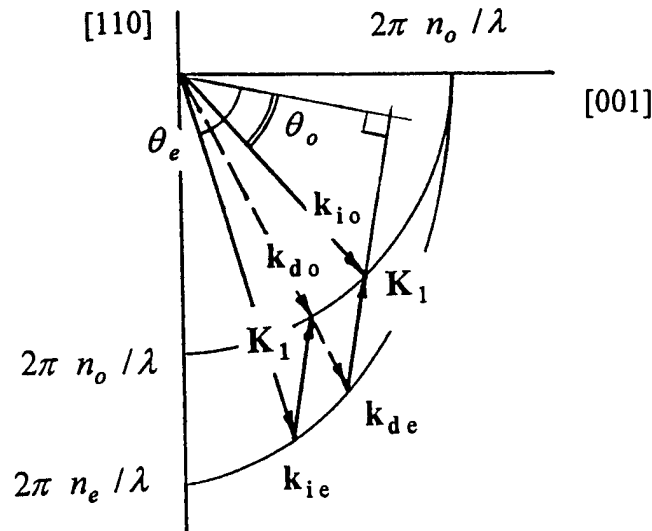


Figure 3. Wavevector diagram for adjacent diffracted beams

The principal difference between the two presented cases consists in unequal incidence angles. It may be seen in Fig.3 that  $\theta_o$  for ordinary and  $\theta_e$  for extraordinary polarized components of input radiation are different from each other, as shown in Fig.4. According to the pictures, optical beams in Fig.2 and Fig.4 are propagating along different directions in the crystal. Hence, vector diagrams in Fig.3 are different from the diagrams in Fig.1. Nevertheless, both diagrams are described by similar vector relations, i.e. by Eq.(1). It is seen in Fig.4 that a polarization beam splitter is used at the cell input to divide unpolarized incident light into ordinary and extraordinary components.

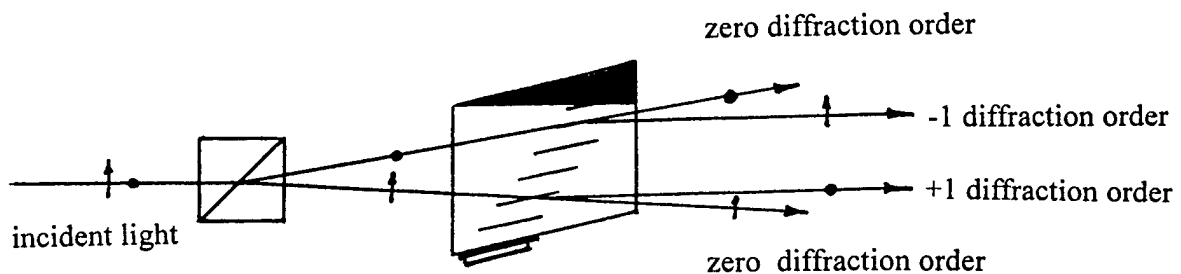


Figure 4. Block-scheme of the filter with adjacent diffracted beams

Adjacent filtrated light beams of  $\pm 1$  diffraction orders appear in the acoustic column of the cell. The filtrated beams propagate collinearly in space because their wavevectors are coinciding, as indicated in Fig.3. Consequently, the filtrated radiation consists of two optical beams propagating at the output of the device in one and the same direction. This feature of the interaction may be considered as advantageous compared to the previously examined geometry.

## 2.4 Acousto-Optic Filtration with Combined Diffracted Beams

In order to form a single diffracted beam, it is proposed to use a lens in combination with the polarization splitter, as presented in Fig.5. The peculiarity of the scheme consists in the common, for the two orthogonally polarized incident optical components, area of the beams intersection. The filtrated light is generated just in the area of intersection, hence, the diffracted rays of  $\pm 1$  orders overlap in space and form a single optical beam at the filter output.

A number of cells applying the investigated acousto-optic interaction regimes in  $\text{TeO}_2$  were fabricated and tested. Acousto-optic filters on base of the cells were intended for operation in visible light as well in infrared region of spectrum. Spectral bandwidths of the devices were equal to  $\Delta\lambda = 4-8 \text{ \AA}$  in visible light, about  $\Delta\lambda = 25 \text{ \AA}$  at  $\lambda = 1.5 \mu\text{m}$  and  $\Delta\lambda = 120 \text{ \AA}$  at  $\lambda = 3.4 \mu\text{m}$ . All the described devices demonstrated the capability to process arbitrary polarized light.

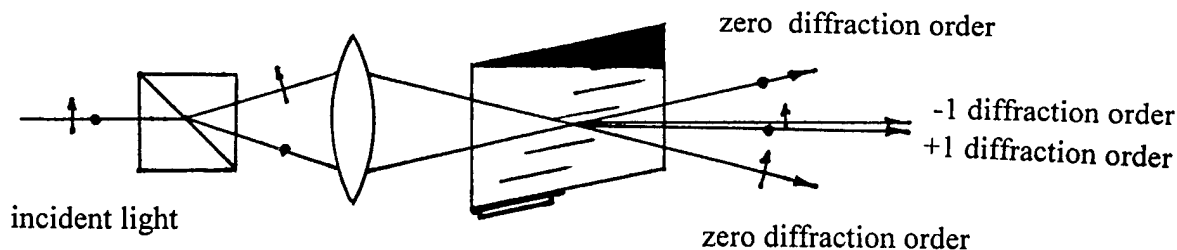


Figure 5. Block-scheme of the filter with combined diffracted beams

### 3. Filtration without Amplitude Modulation of Radiation

Experimental investigation of the filters demonstrated that filtrated radiation possessed portions of optical energy with up- and down-shifted frequencies. Total difference in optical frequencies was equal to doubled frequency of ultrasound  $2f$ . In many cases, it leads to undesirable intensity modulation of the filtrated radiation. For example, if the filtrated light is directed into a waveguide and propagates along a fibre then undesirable modulation of optical intensity may be observed. Beat frequencies of the modulation are dependent on optical wavelengths values. For near infrared region they are equal to a few hundreds of megahertz.

#### 3.1 Wavevector Diagrams of Interaction

The revealed disadvantages of the examined regimes of diffraction and proposed schematic solutions are not typical of the double-channel device applying far-off-axis geometry of interaction in tellurium dioxide. Two acoustic waves are launched in the crystal in order to provide the possibility of unpolarized radiation filtration. The acoustic waves are propagating symmetrically to  $[110]$  axis of the crystal, as demonstrated by vector diagrams in Fig.6.

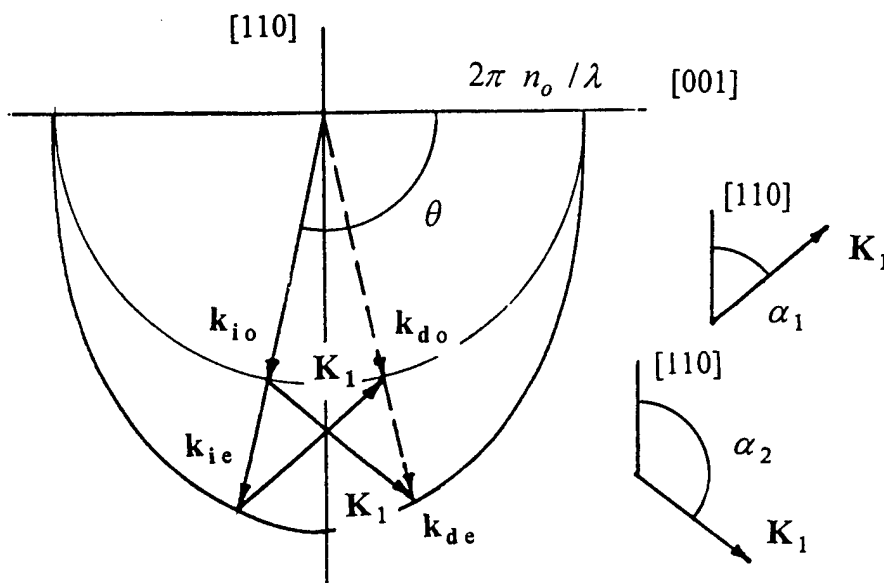


Figure 6. Vector diagrams of far-off-axis interaction

Arbitrary polarized radiation is incident on the crystal at  $\theta$  angle, as shown in picture. Ordinary polarized portion of light are described by  $k_{i0}$  optical wavevector while

$k_{ie}$  corresponds to extraordinary polarized incident radiation. Directions of ultrasound propagation are chosen in such a manner that only up-shifted diffraction takes place in the crystal. According to the vector diagram, it may be written

$$k_{ie} + K_1 = k_{do} ; \quad k_{io} + K_1 = k_{de} \quad (2)$$

Equation 2 confirms the prediction of equal Doppler shifts of diffracted beams. Due to symmetry of the picture relative to  $[110]$  axis, both diffracted optical wavevectors coincide in space. It means that there exists a possibility to obtain ordinary and extraordinary polarized portions of filtrated light propagating along one and the same direction in the crystal.

### 3.2 Acousto-Optic Cell of the Filter

Configuration of the filter cell is shown in Fig.7. Two piezotransducers are generating slow shear acoustic waves in  $\text{TeO}_2$  at tilt angles  $\alpha_1 = 20^\circ$  and  $\alpha_2 = 160^\circ$  relative to  $[110]$  axis. Arbitrary polarized light is normally incident on the input facet of the cell and propagates in the crystal at  $\theta = 110^\circ$  relative to  $[001]$  axis of the material. For optical wavelengths of incident radiation at  $\lambda = 0.63 \mu\text{m}$ , acoustic frequency of Bragg synchronism is equal to  $f = 215 \text{ MHz}$ . Orthogonally polarized diffracted beams, similar to input light, have normal incidence on the output facet of the cell. In this way a single filtrated optical beam at the filter output is provided.

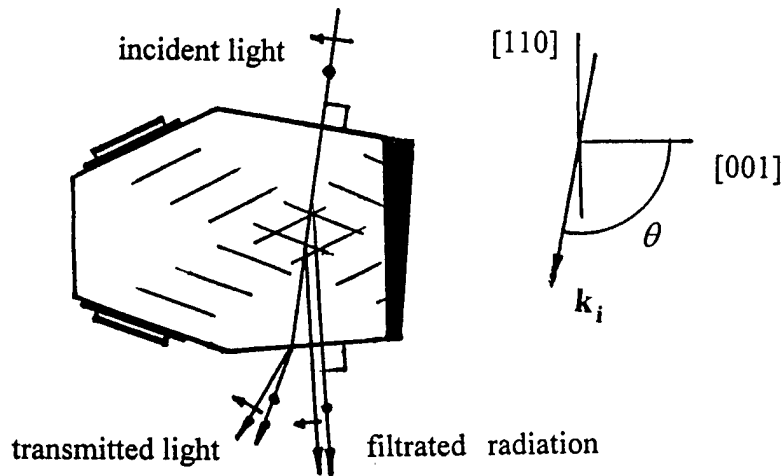


Figure 7. Acousto-optic cell configuration

The designed filter is characterized by narrow spectral bandwidths. For example, in visible light  $\Delta \lambda = 1.0 - 1.8 \text{ \AA}$  while spectral bandwidths in near infrared region are less than

$\Delta \lambda \leq 12 \text{ \AA}$  The obtained resolution value may be considered as high in comparison with the devices in Fig.2 and Fig.4. On the other hand, the developed filter, relative to traditional devices, has a lower bandwidth of tuning over optical wavelengths. As proved by the analysis, dispersion of refraction indexes is responsible for the narrowing of the tuning interval.

## 4. Conclusions

The performed theoretical and experimental investigation confirmed the statement that diffraction of light by ultrasonic waves in a birefringent crystal may be used for spectral filtration of arbitrary polarized radiation. Special choice of light and ultrasound propagation directions in a crystal results in the principle possibility to obtain narrow spectral bandwidths of filtrated wavelengths. Various optical block-schemes and schematic solutions of tunable filters for operation with unpolarized light were analysed theoretically and tested in experiments. Advantages of the examined interaction regimes, from the point of view of practical applications in acousto-optic filters, were demonstrated. Peculiarities and disadvantages of the proposed optical schemes of filtration were revealed.

As a result of the performed research, a number of acousto-optic cells on base of tellurium dioxide single crystals were designed and fabricated. The cells were successfully used in tunable filters operating with arbitrary polarized radiation in visible light as well as in infrared region of spectrum.

## References

1. V.Balakshy, V.Parygin and L.Chirkov, *Physical Principles of Acousto-Optics*, Radio and Communication, Moscow, (1985).
2. A. Korpel, *Acousto-Optics*, Marcel Decker, N.Y., (1988).
3. P.Das and C.DeCusatis, *Acousto-Optic Signal Processing*, Artech House, N.Y., (1991).
4. J.Xu and R.Stroud, *Acousto-Optic Devices*, Wiley, N.Y., (1992).
5. S.Harris and R.Wallace, *Acousto-Optic Tunable Filter*, JOSA, **59** (1969), 744-747.
6. I.C.Chang, *Tunable Acousto-Optic Filters: An Overview*, Proc. SPIE, **90** (1976), 12-22.
7. D.Suhre, M.Gottlieb, L.Taylor and N.Melamed, *Spatial Resolution of Imaging Noncollinear Acousto-Optic Tunable Filter*, Opt. Eng. **31** (1992), 2118-2121.
8. Z.Azamatov, I.Belikov, V.Voloshinov, et.al., *Light Beams Scanning in Paratellurite Crystals*, Moscow Univ. Physics Bulletin **39** (1984), 70-76.

9. V.Epikhin, F.Visen and V.Poustovoit, *Acousto-Optical Filtration of Radiation with Arbitrary Polarization*, Sov. Tech. Phys. **57** (1987), 1910-1917.
10. V.Voloshinov and O.Mironov, *Wide-Angular Acousto-Optic Tunable Filter for Middle Infrared Region of Spectrum*, Sov. Optics and Spectroscopy **68** (1990), 452-457.
11. V.Voloshinov and V.Molchanov, *Acousto-Optical Modulation of Radiation with Arbitrary Polarization Direction*, J. Opt. Laser. Tech. **27** (1995), 307-313.
12. V.Voloshinov, V.Molchanov and J.Mosquera, *Spectral and Polarization Analysis of Optical Images by Means of Acousto-Optics*, J. Opt. Laser. Tech. **28** (1996), 119-127.



## Improvement of Resolution of Visible Acousto-Optic Tunable Filter in Tellurium Dioxide

Vladimir Pelekhaty, Brimrose Corp., Baltimore, Maryland

Tellurium dioxide ( $\text{TeO}_2$ ) became a very popular crystalline material as an interaction medium for acousto-optic tunable filters (AOTFs) in both visible and infrared spectral regions. This is due to its significant optical birefringence and high acousto-optic figure of merit for slow shear wave propagating closely to  $[110]$  direction. All this results in the high efficiency and compactness of tellurium dioxide based AOTFs. Unfortunately, their resolution is not as high as their efficiency, especially in the visible range. Essential improvement in resolution can turn  $\text{TeO}_2$ -based AOTFs into very attractive spectrally selective components for a variety of optical sensors and instruments in such areas as atomic emission and absorption, laser induced breakdown, and Raman spectroscopy.

Conventional non-collinear AOTF composed of  $\text{TeO}_2$  (Fig. 1) has intrinsic drawbacks associated with this crystal. Firstly, the slow shear wave has enormously big energy walk-off angle ( $55^\circ$ - $57^\circ$ ), which shortens the acousto-optic interaction length  $L$  down to half of the length of the transducer. Interaction length is known to be a crucial parameter of acousto-optic interaction: the spectral resolution of the AOTF is inversely proportional to  $L$ , and acousto-optic efficiency is proportional to  $L^2$ .

The spectral resolution of non-collinear AOTF (Fig. 2) is depending on device configuration and improves significantly as the optical beam propagates at higher polar angles. At those higher polar angles occurs a very beneficial polarization insensitive mode of operation, indicated on Fig. 2 by the equality of off-axis acoustic angles for both ordinary and extraordinary optical input beams.

As it is shown on Fig. 3, optical throughput of the AOTF is optimized at higher polar angles as well. Even the second order approximation gives deceptive infinite polar acceptance angle when it is not valid any more, but third-order correction still shows three times larger polar acceptance angle than azimuthal one.

Design and operation of non-collinear AOTF at higher polar optical angles is complicated by the fact that the required frequency of acoustic wave can reach values up to 400 MHz (Fig.3). At this point the extremely high attenuation (up to 290 dB/cmGHz<sup>2</sup>) of the slow shear acoustic wave propagating closely to the  $[110]$  direction starts to play its negative role. Reconstructed from experimental data theoretical dependence of the attenuation from the direction of propagation of shear acoustic wave (Fig. 5) allowed us to calculate the attenuation suffered by it in conventional non-collinear AOTF. As it is shown on Fig. 6, attenuation grows up to 15 dB/cm at optical angles of interest, resulting in absorption of the energy of acoustic wave before

it even can reach the region of acousto-optical interaction. Thus, walk-off and attenuation deadlock the efforts to improve the resolution of conventional non-collinear AOTF by forcing to acute ( $\approx 20^\circ$ ) polar optical propagation angles, which results in poor resolution of several nanometers in visible range; not to mention the unusual and not practical shape of the device at higher optical angles and the large amount of wasted material in its manufacture.

The basic idea of our newly designed AOTF (see Fig. 7) is to launch a much less attenuated (about  $9 \text{ dB/cmGHz}^2$ ) shear wave close to z-axis. It supposed to deliver almost all the acoustic energy to the area of acousto-optic interaction and to be reflected into a proper slow shear wave from the free crystal-air interface, which could be chosen to be parallel to the optical beam. Although the slow shear wave starts to decay quickly after reflection, it is able to cross the optical beam before being totally absorbed in the crystal, which in turn eliminates any need in acoustic absorber.

Diagram on Fig. 8 shows that wavevectors of incident and reflected shear acoustic waves have to have their tips to be on the same perpendicular to the reflective surface depicted by the bold line. Rigorous calculations by the formulae analogous to those governing the total internal reflection of the extraordinary optical wave in uniaxial crystal for every pair of polar optical propagation and off-axis acoustic propagation angles provide the value of polar angle of propagation for an incident acoustic wave, as it is shown on Fig. 9.

The new design benefits from the fact that the length of acousto-optic interaction is now about 1.5 times longer than the length of the transducer, doubling the interaction length compared to the case of conventional AOTF with the same transducer length. It also makes easily realizable both polarization insensitive and wide angular aperture modes of operation.

Based on this new design, an AOTF with an optical aperture of  $0.5 \text{ cm}^2$  and field of view angle of  $\pm 1.5^\circ$  was built and tested. It demonstrated spectral resolution of about  $1 \text{ \AA}$  at violet and about  $3 \text{ \AA}$  at red with the possibility of further optimization and improvement still existing. Fig. 10 and Fig. 11 show the spectra of miniature mercury and neon lamps illustrating its high resolution and throughput. Resolution of the prototype hand-held spectrophotometer with F-number of 2.5 built based on this AOTF (Fig. 12) is slightly spoiled by the full aperture operation.

In conclusion it is worth to mention that all the described procedures are straight forward applicable to the newly developed highly efficient acousto-optical mercurous halide crystals which belong to the same crystal group as tellurium dioxide and have all its advantages and drawbacks even exaggerated.

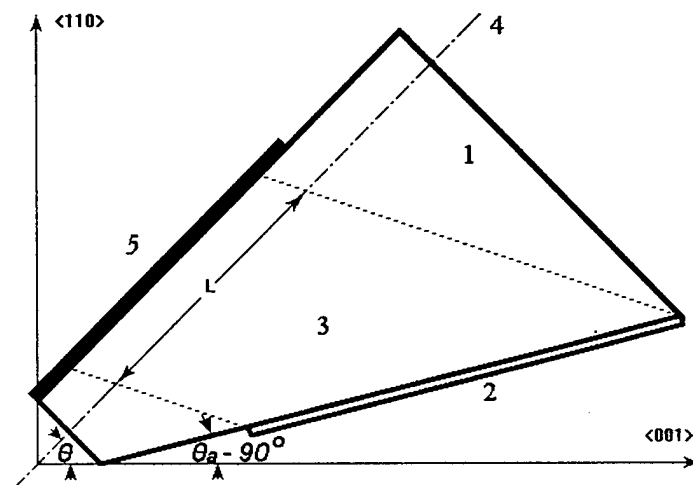


Fig. 1.

Conventional noncollinear AOTF: 1 - tellurium dioxide crystal; 2 - piezoelectric transducer; 3 - acoustic shear wave; 4 - optical beam axis (dashed-dotted); 5 - acoustic absorber;  $L$  - acousto-optic interaction length;  $\Theta$  - polar optical propagation angle;  $\Theta_a$  - acoustical polar propagation angle.

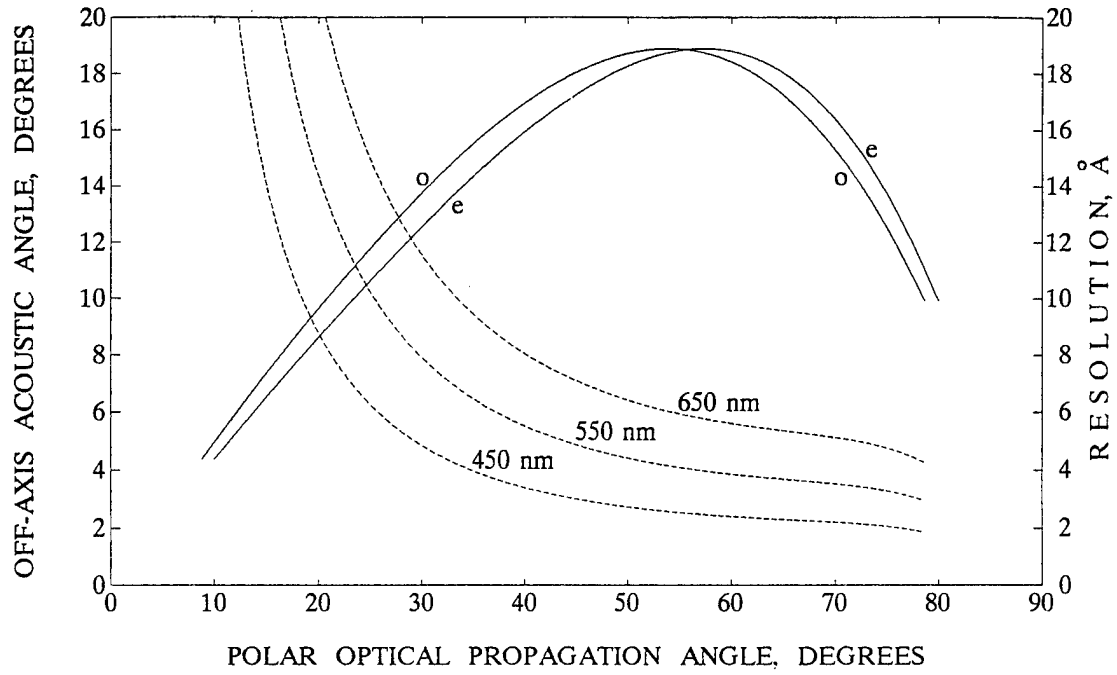


Fig. 2.

Resolution of noncollinear AOTF with 1 cm long transducer for blue (450 nm), green (550 nm), and red (650 nm) wavelengths (dashed curves) and off-axis acoustic propagation angles  $\Theta_a$ -90° (solid) depending on polar propagation angle of ordinary (o) and extraordinary (e) optical input beam. Their intersection point at  $\text{atan}(\sqrt{n_e^2/n_o^2 + 1}) = 55.6^\circ$  and  $\text{atan}(1/2\sqrt{n_e^2/n_o^2 + 1}) = 18.9^\circ$  indicates the polarization insensitive mode of operation.

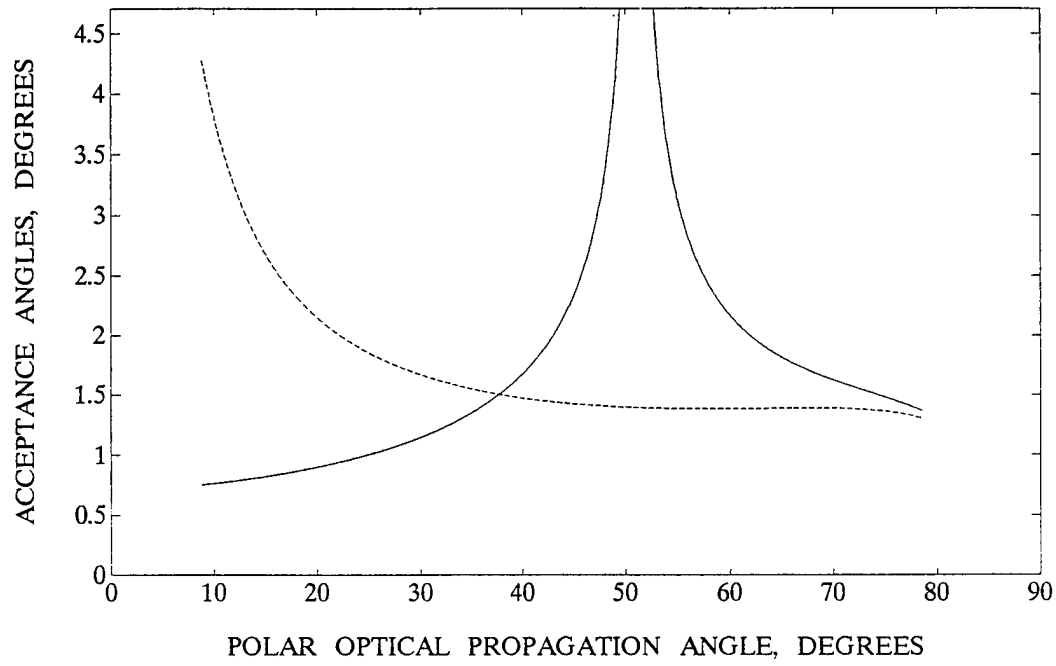


Fig. 3.

Azimuthal  $\Delta\phi = \pm(0.9\lambda/\Delta nL(2\cos^2\Theta + \sin^2\Theta))^{1/2}$  (dashed curve ) and polar (solid curve)  $\Delta\Theta = \pm(0.9\lambda/\Delta nL(2\cos^2\Theta - \sin^2\Theta))^{1/2}$  acceptance (half) angles inside of tellurium dioxide noncollinear AOTF with 1 cm long transducer versus polar optical propagation angle  $\Theta$ . The upper limit of the ordinate axis is imposed by third-order approximation of polar acceptance angle  $(\lambda/\Delta nL)^{1/3} = 4.7^\circ$  (at  $\lambda = 550$  nm).

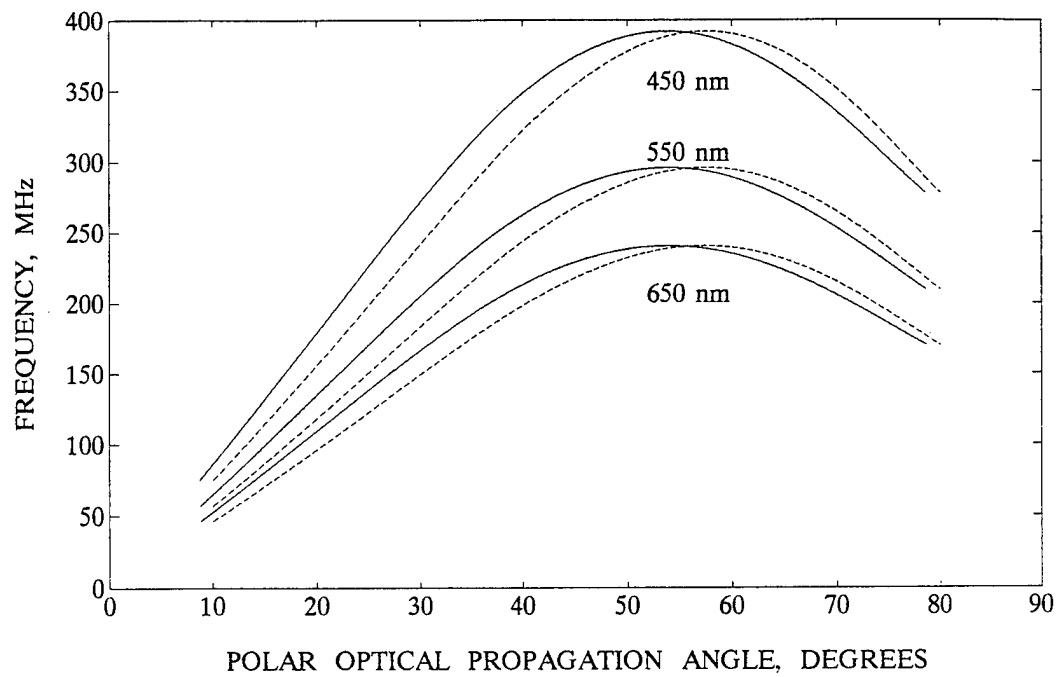


Fig. 4.

Dependencies of the frequency of acoustic wave for filtering blue (450 nm), green (550 nm), and red (650 nm) wavelengths upon polar propagation angle of ordinary (solid curves) and extraordinary (dashed curves) input optical beam.

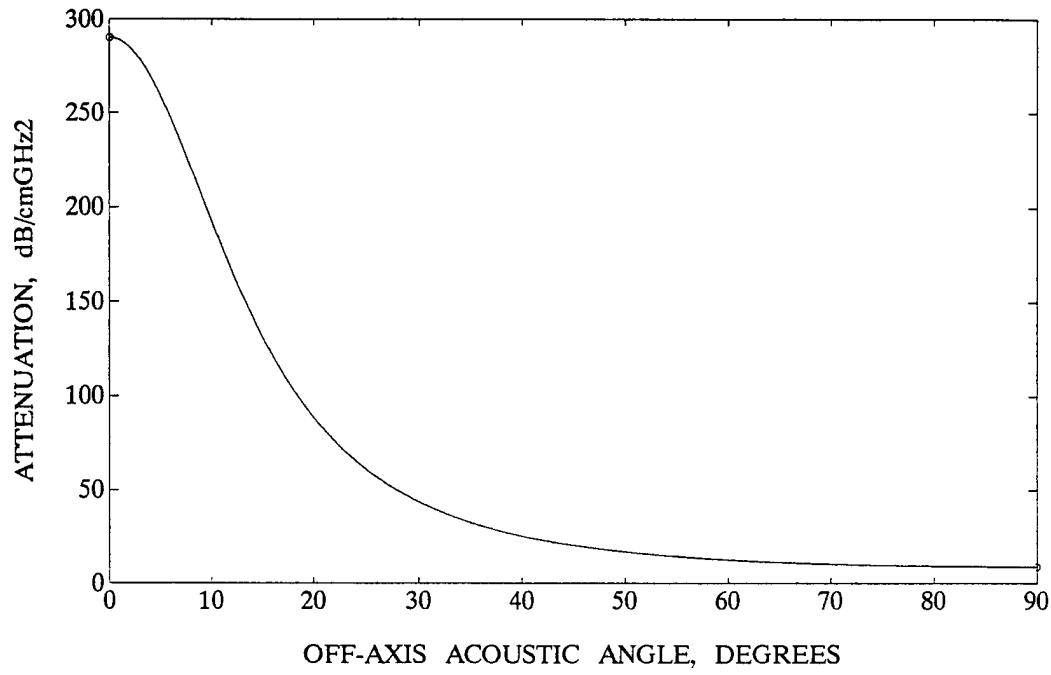


Fig. 5.

Attenuation of slow shear acoustic wave propagating in [001]-[110] or  $z$ - $t$  plane at different angles off  $t$  axis. Circles -- experimental data for  $\Gamma_t = 290$  and  $\Gamma_z = 9$  dB/cmGHz<sup>2</sup>. Solid curve -- interpolation by the formula:

$$\Gamma(\Theta_a) = \frac{\Gamma_t V_t^3 \sin^2 \Theta_a + \Gamma_z V_z^3 \cos^2 \Theta_a}{(V_t^2 \sin^2 \Theta_a + V_z^2 \cos^2 \Theta_a)^{1.5}}, \text{ where } V_t = 616 \text{ m/s and } V_z = 2104 \text{ m/s.}$$

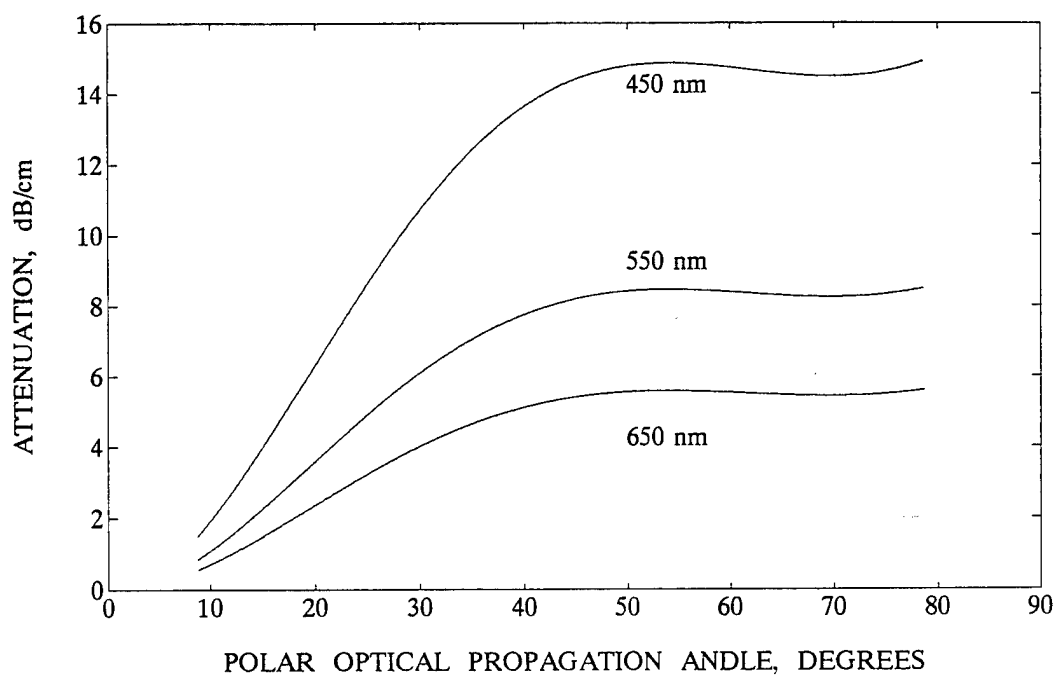


Fig. 6.

Attenuation of slow shear acoustic wave in tellurium dioxide noncollinear AOTF tuned to filter blue (450 nm), green (550 nm), and red (650 nm) wavelengths depending on polar optical propagation angle.



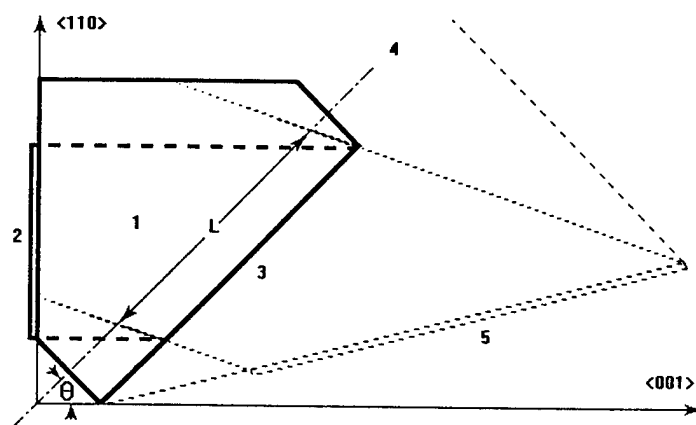


Fig. 7.

A schematic of the new AOTF: 1 - Tellurium dioxide crystal; 2 - piezoelectric transducer; 3 - reflective surface; 4 - optical beam axis (dashed-dotted); 5 - hypothetical conventional type AOTF to provide the same acousto-optical interaction length  $L$ .

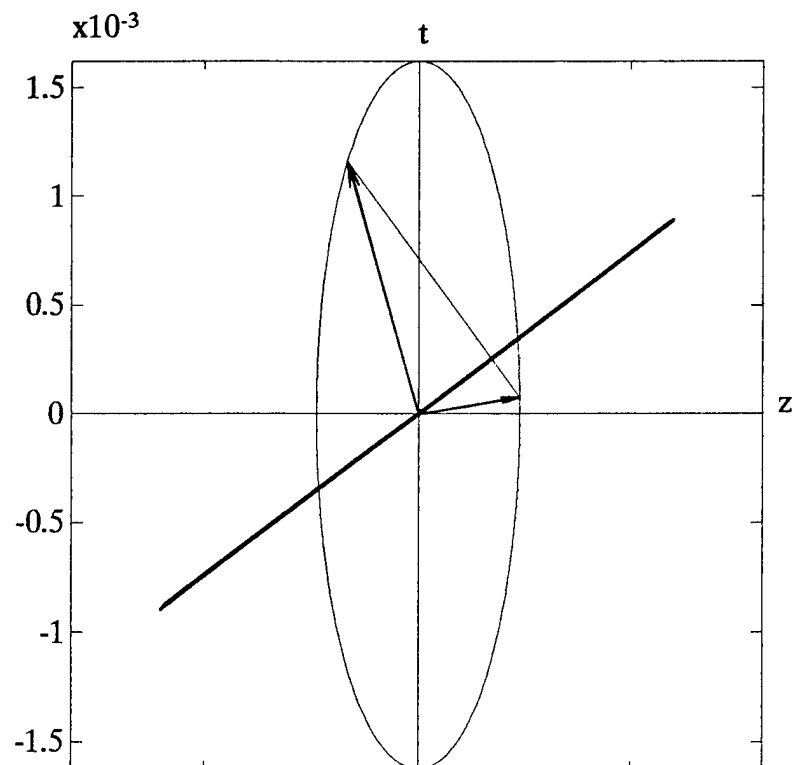


Fig. 8.

Diagram of acoustic wavevectors of incident shear acoustic wave (shorter vector) and reflected (longer one) from bold free interface, which are superimposed on the slowness ellipse in  $z$ - $t$  plane of tellurium dioxide.

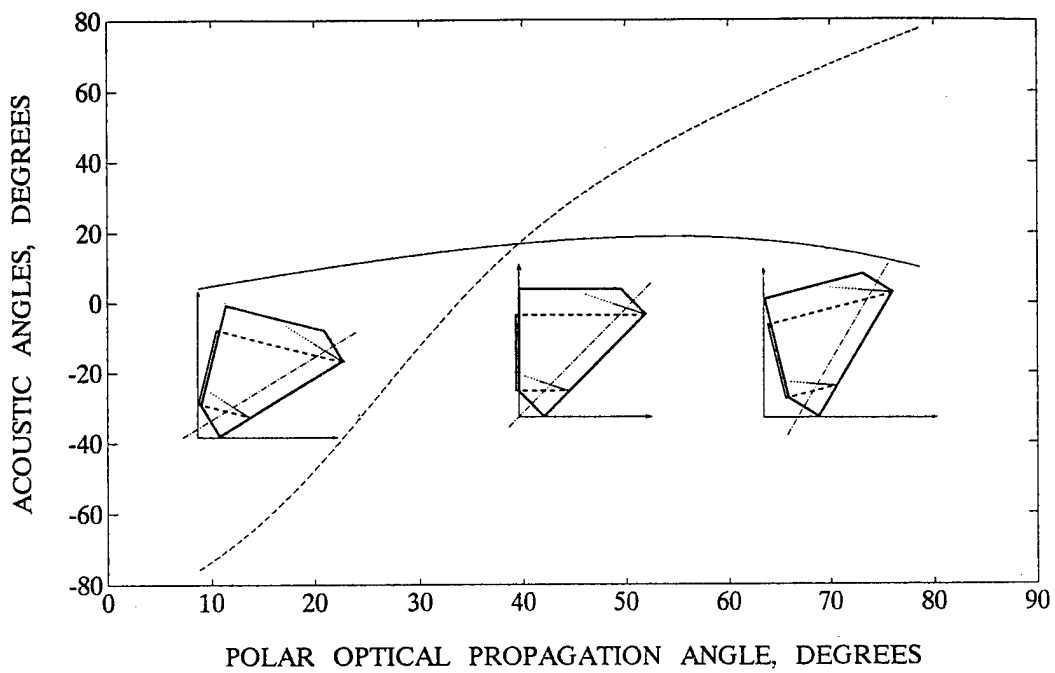


Fig. 9.

Calculated values of polar angle of incidence (dashed curve) of shear acoustic wave to be reflected into a slow shear wave propagating at proper off-axis angle (solid curve) from the free interface parallel to the direction of optical propagation. Inserts illustrate different types of device configuration.

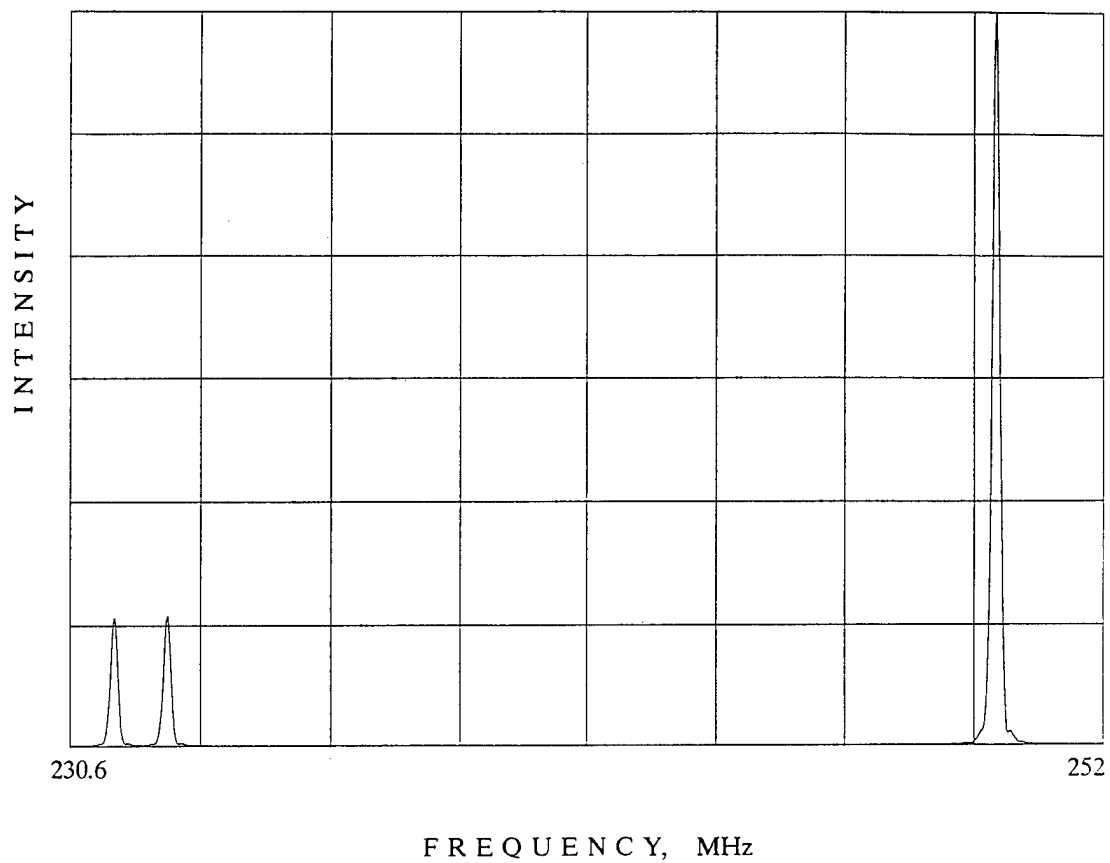


Fig.10.

Spectrum of the miniature mercury lamp featuring strong green line at 546.07 nm and two close yellow lines at 576.96 nm and 579.07 nm filtered by the new AOTF.

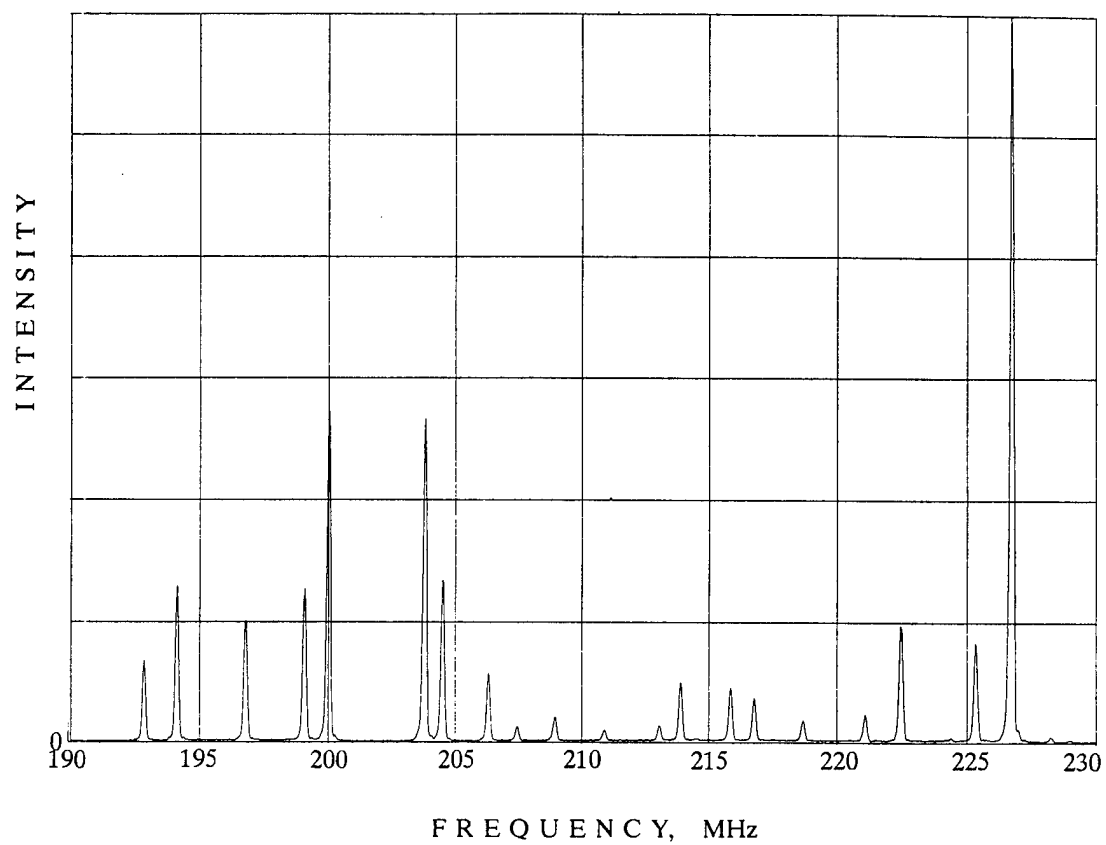


Fig.11.

Spectrum of the miniature neon spectral lamp in yellow-red part of a visible spectral region filtered by the new AOTF.

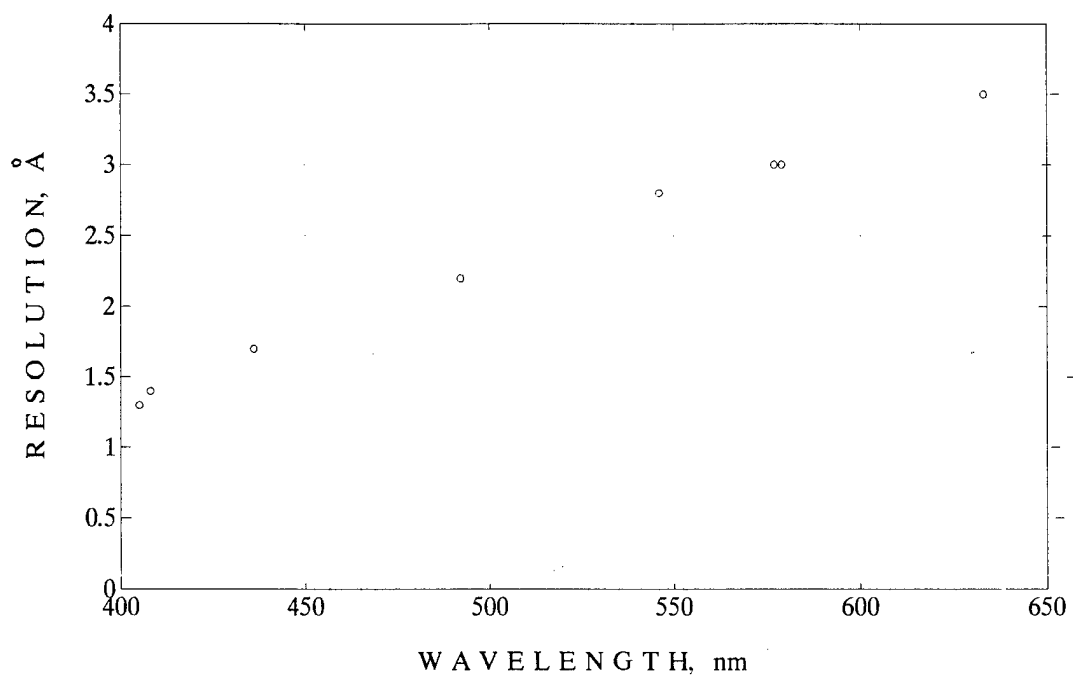


Fig.12.

Resolution of the prototype hand-held spectrophotometer built based on new AOTF measured throughout the visible spectrum.

# Growth of AO Crystals with High Anisotropy and Developments of Multichannel AO Devices

Yu. V. Pisarevsky

Institute of Crystallography Russian Academy of Science, Moscow

## 1. Selection of acoustooptical materials

It is well-known that any transparent material could be used as acoustooptic media. Criteria of selection could be divided on two groups. First one is include material constants connected with main devices parameters. In second group we could include properties of materials connected with technology of devices production and conditions of devices work.

First group parameters are usually represented by acoustooptical figure of merit (AOFM)  $M_2$ <sup>1</sup>

$$M_2 = n^6 p^2 / \rho V^3, \quad (1)$$

where  $n$  is the index refraction,  $p$  the photoelastic component,  $\rho$  the density, and  $V$  the acoustic velocity. It should be noted that  $n$  related to 2nd rank tensor dielectric permittivity,

$p$  related to 4th rank photoelastic tensor and  $V$  related to 4th rank elastic tensor.

Frequently also are used modified expressions for figure of merit. According to Gordon<sup>2</sup> if acoustooptic bandwidth of devices is important  $M_1$  figure of merit is work

$$M_1 = n^7 p^2 / \rho V \quad (2)$$

Chang<sup>3</sup> introduced figure of merit for AOTF as the product of resolving power and the total filter throughput

$$M_f = n^8 p^2 / \rho V^3 \quad (3)$$

For max of all  $M$  we need  $n$  and  $p$  as much as possible and  $\rho$  and  $V$  as low as possible.

One more parameter is extremely important to acoustooptical devices. This is the intrinsic acoustical loss of material  $\alpha$  which related to 4th rank tensor.

First and very useful method for acoustooptical material selection was proposed by Pinnow<sup>4</sup>. He proposed to calculate average scalar values of  $n, p$  and  $V$  on the base of knowledge of tabulation data of simple inorganic substances. In this case we can

calculate index refraction in a simple way to its density and chemical composition with Gladstone and Dale relation

$$n-1/\rho = \sum_i q_i R_i \quad (4)$$

where  $R_i$  are specific refractive index of the components whose weight percentage are  $q_i$ . As for to sound velocities Pinnow established the empirical relation

$$\log (V/\rho) = -b M + d \quad (5)$$

where  $M$  is mean atomic weight and  $b$  and  $d$  are experimentally determined constants. As for to photoelastic constants Pinnow proposed the magnitudes of the maximum photoelastic components :

$$p_{max} = \begin{array}{ll} 0.21 & (\text{water-insoluble oxides}) \\ 0.35 & (\text{water-soluble oxides}) \\ 0.2 & (\text{alkali halides}) \end{array} \quad (6)$$

Pinnow's approach sometimes allow to obtain good results immediatly . In other case it good as first approximation.

Restrictions of above method connected first of all with anisotropy .Usualy anisotropy of index refraction is less than 5-10%. So in most cases we could calculate index refraction with accuracy of better than 5 - 10 %. Sometimes index refractions anisotropy reach 50% and more ( for example  $n_o = 1.96$  and  $n_e = 2.61$  for  $\text{Hg}_2\text{Cl}_2$  ) but such value still is not so important for estimation.

Much more strong could be anisotropy of sound velocities. On the Fig 1 represented sections of phase velocities for mercurium halides<sup>4</sup>. Ones can see that longitudinal sound velocities changed with propagation direction almost two times and shear velocities more than three times. Above tham practically impossible to predict from (5) extremely low values of slow shear mode along (110) direction.

Other restrictions of Pinnow method connected with organic compounds. Because of weak intermolecular forces organic compounds have low sound velocities simultaneously with low density. This is the reason why in spite of relatively small index refractions we have found compounds with high AOFM such as phthalates and orthosulfobensoates<sup>5</sup>.

Photoelastic constants related to 4th rank tensor also frequently have strong anisotropy. Photoelastic constants of tellurium dioxide changes more than 10 times. Special feature of photoelastic constans is the their various signs. So for complex compounds photoelastic constants could be less than ones of components. On Fig 2 are represented our data of photoelastic constants of cubic zirconia as a function of  $\text{Y}_2\text{O}_3$  concentration<sup>6</sup>. Values of  $p_{12}$  and  $p_{44}$  decrease with increasing of  $\text{Y}_2\text{O}_3$  concentration.



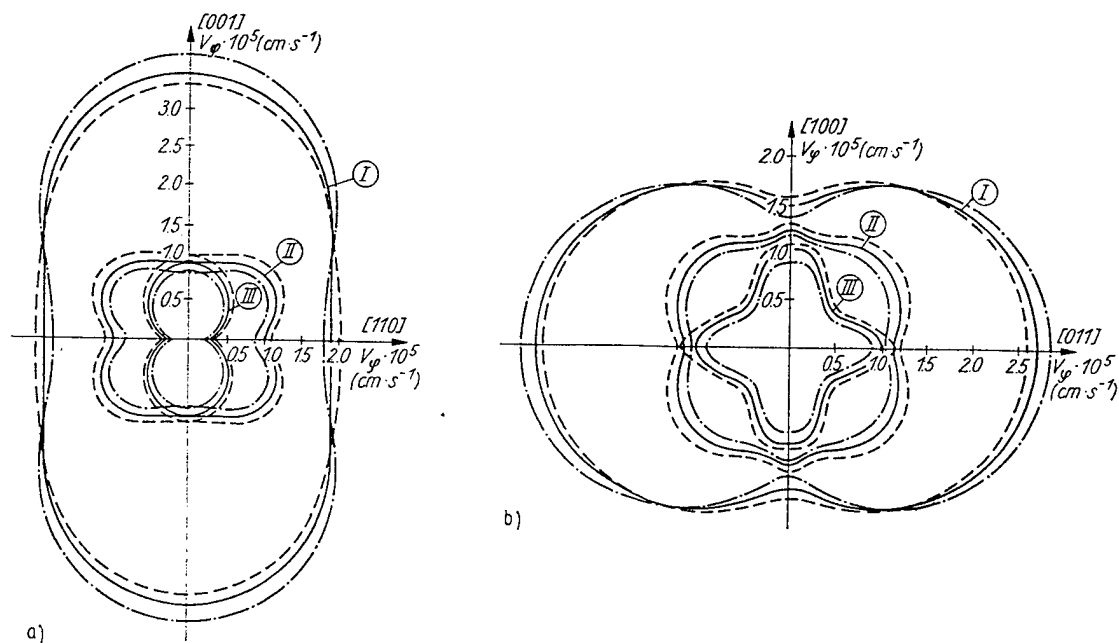


Fig.1. Sections of phase velocity  $V_f$  for  $\text{Hg}_2\text{Cl}_2$  (—), for  $\text{Hg}_2\text{Br}_2$  (---) and  $\text{Hg}_2\text{I}_2$  (----).  
a) (110) sections; b) (011) sections : I - L-waves, II, III - S-waves

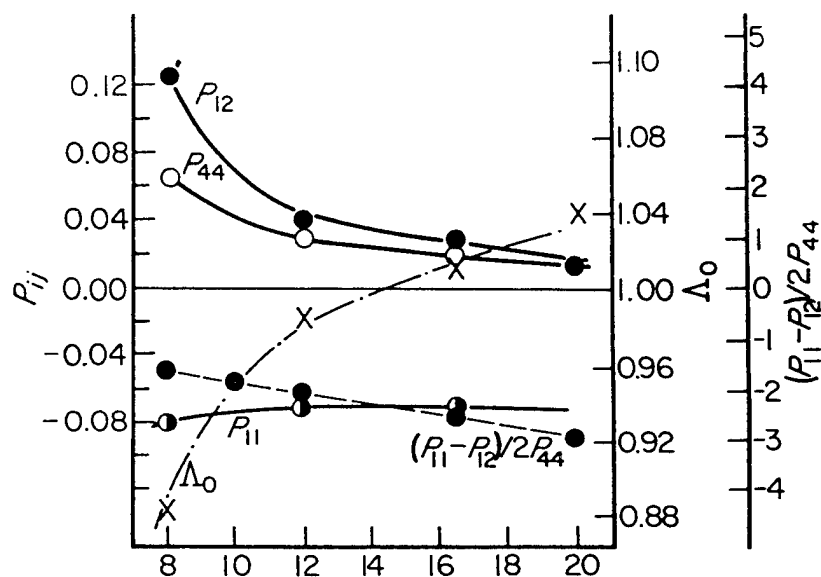


Fig.2. Photoelastic constants, photoelastic anisotropy parameter and  $\Lambda_0$  parameter of  $\text{ZrO}_2 - \text{Y}_2\text{O}_3$  crystals as a function of  $\text{Y}_2\text{O}_3$  concentration

Relation (6) sometimes work only for isotropic acoustooptic interactions with longitudinal sound waves.

For AOTF we use only anisotropic acoustooptic interaction with rotation of plane polarisation both longitudinal and shear waves. So selection materials for AOTF is most difficult things compare with other AO devices.

One way is selection among crystals with high anisotropy as proposed by Uchida  $\text{TeO}_2$  and proposed by us mercurium halides.

## 2. Growth of $\text{TeO}_2$ and $\text{Hg}_2\text{Hal}_2$

We developed multi-purpose system for single crystal growth from the melt which can be employed for laboratory use as well as in factory production. Crystallisation can carried out either in vacuum or in any gas atmosphere, under normal and surplus pressure.

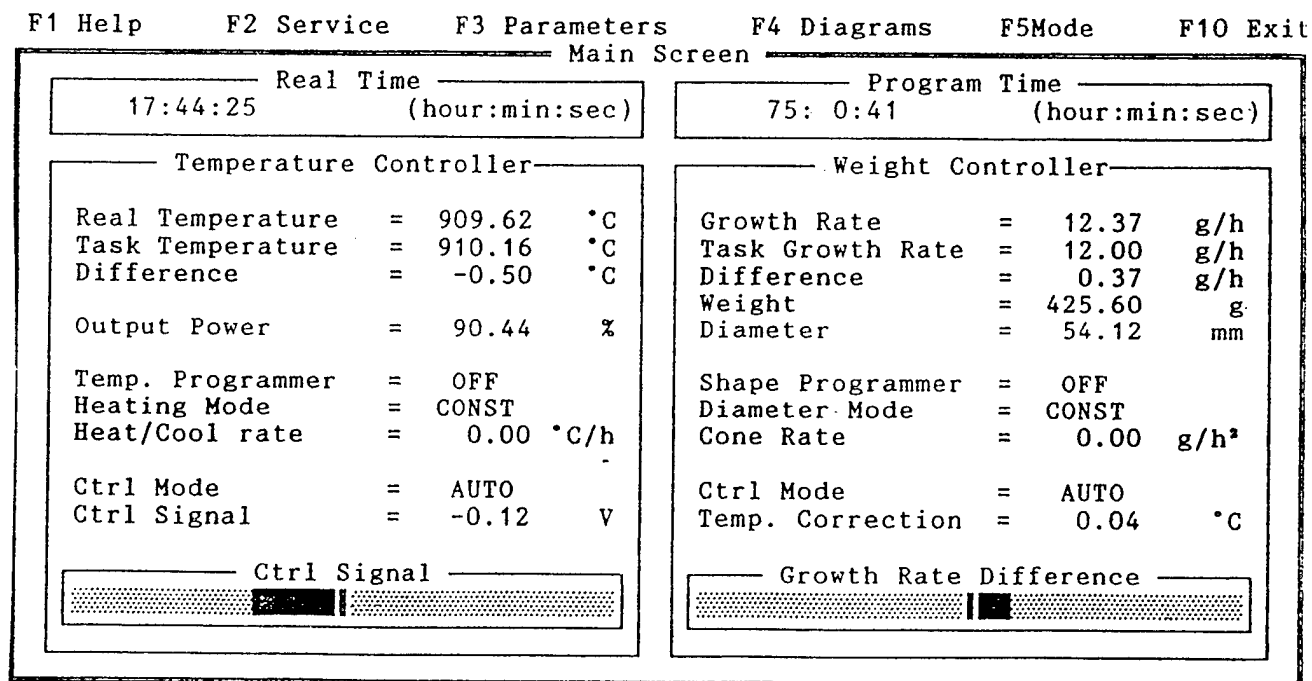
As the whole crystallisation process is controlled by computer, this installation is very easy to operate.

The system can serve :

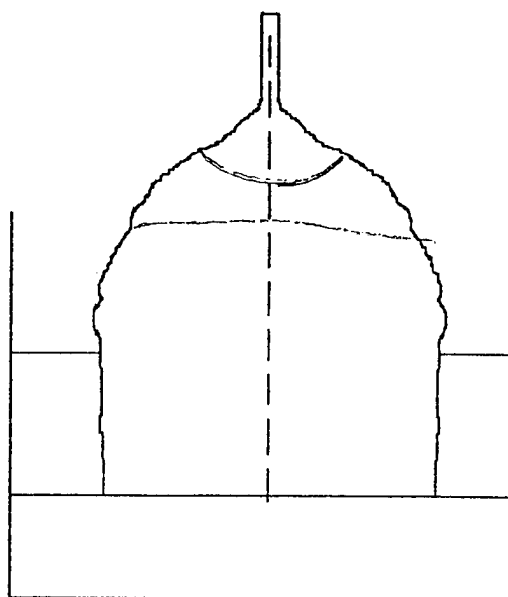
-as a research tool for new crystal growing. The machine is build up from independent moveable hardware modules, so system can be extended easily. The system is released for the Chzochralski growth method but other classic methods (Bridgemen, Stockbarger, Kiropulos) are also available.

-for the commercial production .

We are growing  $\text{TeO}_2$  by Chzochralski method 45 -70 mm diameter and 30 - 50 mm length. Usualy we use 110 pulling direction but sometimes (upon request) also 100 direction. On fig 3 are represented PC display parameters under control.



## Estimated Crystal Shape



Current Weight	[ gram ]	426.2
Current Diameter	[ mm ]	48.5
Crystal Height	[ mm ]	59.0
Delta Melt Level	[ mm ]	21.3
Process Time	[ h:min]	85 : 12

On fig 4 one can see shape of growing crystal and starting and current levels of melt.

We grow  $\text{Hg}_2\text{Hal}_2$  (Hal- Cl,Br,I) with diameter 20-25 mm and length 20- 30 mm from the gaz phase in fused quartz ampules.

Both purity of starting material and crystall growth technology are important for quality of  $\text{TeO}_2$  and  $\text{Hg}_2\text{Hal}_2$  crystals.

For quality control we tested various optical, x-ray and  $\gamma$ - ray methods. We suppose that most important defects for AO applications are twins and inclusions. We usually are producing twin control help with special conometer. Sometimes we use Twiman interferometer and some other methods for precise control. We are checking inclusions help with laser scattering.

### 3. Development of multichannel AO devices

During last years we participated in various applied projects and designed various AO devices . Among them :

- two coordinate deflector( 1.06 mkm, 0.51 mkm, 0.63 mkm);
- 100 mks processor;
- noncolinear AOTF;
- 12th channel processors
- 12th channel AOTF

Multichannel AOTF are usefull for simultaneously envirovment control of various components. Singlechannel properties of AOTF are described in many papers<sup>3</sup>. The key difference of multichannel device is possible dencity of channels.

On Fig 5 represented the foto of 12th channel  $\text{TeO}_2$  cell. In spite of small sound velocities of  $\text{TeO}_2$  and  $\text{Hg}_2\text{Hal}_2$  we could not keep channel close to each other because of elastic anisotropy.

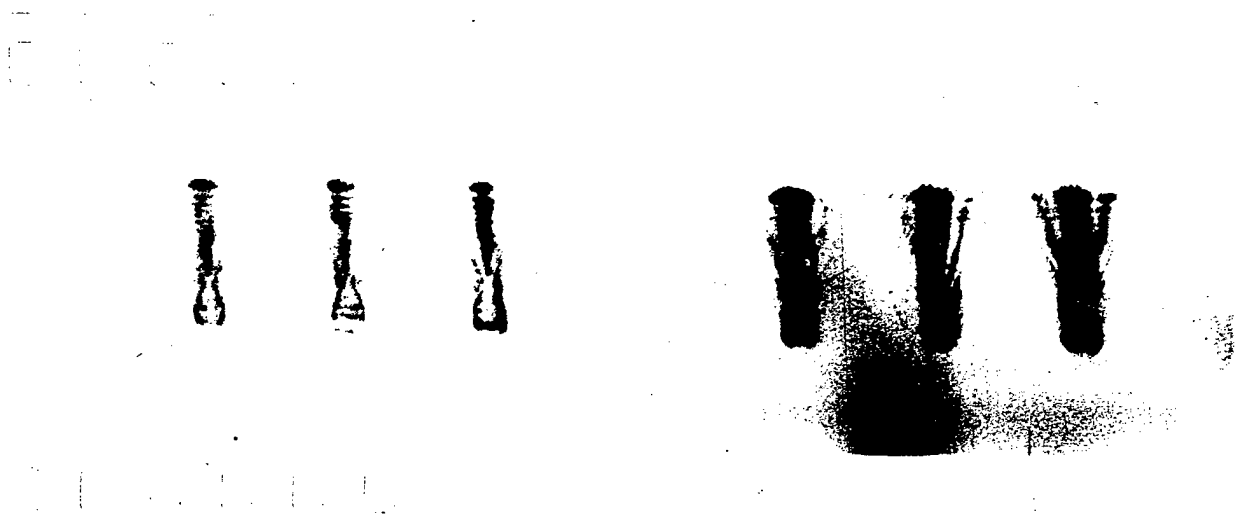


$\text{TeO}_2$  element  
 $\text{LiNbO}_3$  plate

Fig.5. Foto of 12-channel  $\text{TeO}_2$  AO cell

We calculated propagation of finite aperture sound beam near 110 derection. Elastic anisotropy parameter fall from 40 till 18 for cut rotated from 110 direction on  $7^\circ$  at (110) plane.

On fig 6 experimental result of acoustic energy distribution are shown.



From fig 6 ones can see near field inhomogenities of ultrasonic beam .

### References

1. D.A.Pinnow. Guide line for the Selection of Acoustooptic Materials. IEEE J.Quant. El.vol.QE-6,N4 1970 pp223-237.
- 2.E.I.Gordon. Figure of merit for acousto-optic deflection and modulators devices. IEEE J Quant. El. vol QE-2,1966, pp104-105.
- 3.I.E.Chang. Tunable Acousto-optic Filters: An Overview. Opt. Eng.vol.16,1977, pp455-460.
4. C.Barta,I.M.Silvestrova, N.A.Moiseeva, Yu.V.Pisarevsky. Propagation of acoustic waves in Crystals of Univalent Mercury Halides. Kristall und Technik vol15.1980, pp843-848
- 5.Silvestrova I.M.,Vinogradov A.V.,Turskaya T.P.Belikova G.S., Pisarevsky Yu.V.,Elastic, Piezoelectric,Acoustooptic Properties of Cesium Orthosulfobensoate Single Crystals. Sov. Phys. Cryst. vol35,1990,pp906-911.
- 6.I.I.Chisty, I.L.Fabelinskii, V.F.Kitaeva, V.V.Osiko, Yu.V.Pisarevsky. Experimental Study of the Propertiwis of  $ZrO_2 - Y_2O_3$  and  $HfO_2 - Y_2O_3$  Solid Solutions. J.Raman Spectr. vol .6 1977 pp

# Progress in AOTF technology for WDM systems

David A. Smith and Anand A. Patil

Department of Electrical Engineering and Applied Physics

Case Western Reserve University

Cleveland, OH 44106-7221 USA

Phone (216)-368-4073 Fax (216)-368-2668 E-Mail: das23@po.cwru.edu

**Abstract** - Technology of the integrated acousto-optic filter has advanced remarkably over the last several years, leading to polarization diversity WDM switches, filters and switches with controllable passband shape and AOTFs with internal gain. Along with these technological developments, AOTFs have advanced in many important applications areas including WDM optical communication systems, gain equalization of optical amplifier chains, intracavity tuning of lasers and optical spectrometry. The evolution of the AOTF will be reviewed and several applications will be presented.

## 1. Introduction

### 1.1. Overview

In modern advanced multi-wavelength optical networks, many densely-packed independent wavelength channels are usually packed into the low-loss spectral region of silica fiber, often in the EDFA gain band. Each wavelength channel is manipulated as a separate carrier, which contains independent TDM data, by transparent wavelength-selective optical filters or wavelength-channel routers. Acousto-optic tunable filters (AOTFs) were found to be excellent candidates for serving as WDM switches/routers. Efforts of the ARPA-funded Optical Network Technology Consortium (ONTC) led to the successful demonstration of a WDM network which uses AOTF wavelength-routing to achieve a dynamically-interconnected system of nodes [1]. In this paper, we present a brief review of the evolution of AOTF technology and some important applications including WDM add-drop multiplexing, WDM crossconnects, EDFA gain equalization and fast tunable lasers.

### 1.2. AOTF Concepts

An integrated AOTF [2] uses a surface acoustic wave (SAW) to generate a birefringence grating seen by an incoming polarized beam of light. In a collinear AOTF, this birefringence acts to cause a polarization transformation between TE and TM states. If the interaction strength, integrated over the length of the interaction, is just strong enough, a perfect polarization flip (100% TE-TM conversion) is achieved. The required phase-matching conditions ensures a narrow spectral passband. The resonant polarization conversion bandwidth is about  $\Delta l/l = L_b/L$ , where  $L$  is the device interaction length,  $L_b = 1/Dn$  is the polarization beat length, and  $Dn$  is the waveguide effective index birefringence.

Fig. 1 schematically shows the action of an AOTF on either a white light or a discrete WDM-type input spectrum. The switching speed equals to the acoustic transit time, i.e.  $t = L/V_s$ , where  $V_s$  is the SAW velocity. Typical values of interest for LiNbO<sub>3</sub>-based AOTFs (for 1.55  $\mu\text{m}$  WDM systems) are  $V_s = 3.7 \text{ km/s}$ ,  $Dn = 0.08$ ,  $L_b = 20 \text{ mm}$ ,  $f_s = 175 \text{ MHz}$  (SAW frequency),  $L = 2 \text{ cm}$ ,  $t = 6 \text{ ms}$  and  $\Delta l = 1.5 \text{ mm}$ .

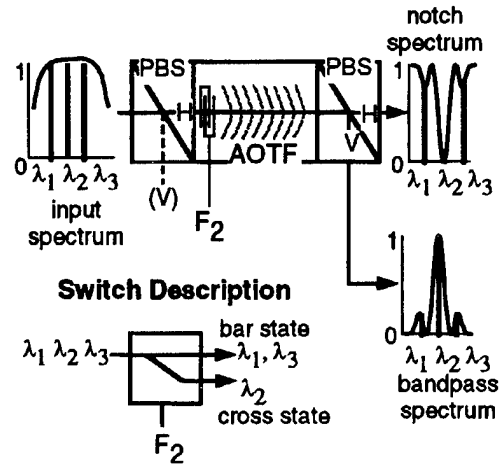


Figure 1. An acousto-optic tunable filter (AOTF) operating on either a continuous or discrete input optical spectrum. Wavelength channel 2 has been diverted by the activation of the corresponding resonant photoelastic grating followed by polarization splitting.

The structure of a typical polarization-diversity AOTF and key fabrication procedures are shown in Fig. 2. The collinear AOTFs have been developed on x-cut y-propagating LiNbO<sub>3</sub> for its combined advantages of a mature fabrication technology and good acousto-optic and piezoelectric figures of merit. Details of acoustic and optical waveguides, IDT design and integral polarization splitters can be found in previous publications [2][3].

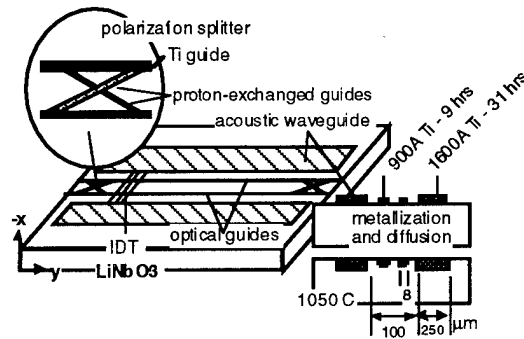


Figure 2. Design and fabrication parameters for a fully-integrated AOTF showing input and output polarization splitters flanking the two active waveguides of this polarization-diversity structure.

## 2. Passband Engineering

### 2.1. SAW Coupler Apodization

A uniform acousto-optic interaction strength results in a sinc-squared optical transmission function which has high sidelobes which result in severe intensity crosstalk in WDM systems. However, by tailoring the interaction profile, the corresponding passband shape can be altered. For example, a half sinusoidal interaction-strength apodization results in a -10-dB sidelobe reduction. This gradual onset and cutoff of the





As a first approximation to the Song flattened filter design, Jackel et al. used two cycles of a uniform saw coupler (100 micron saw guide cores with 20 micron gap) and simply attenuated the second cycle using a partial acoustic absorber (Fig. 6), resulting in appreciable flattening, as evidenced by a squaring the notch shape in the filter bar state [7].

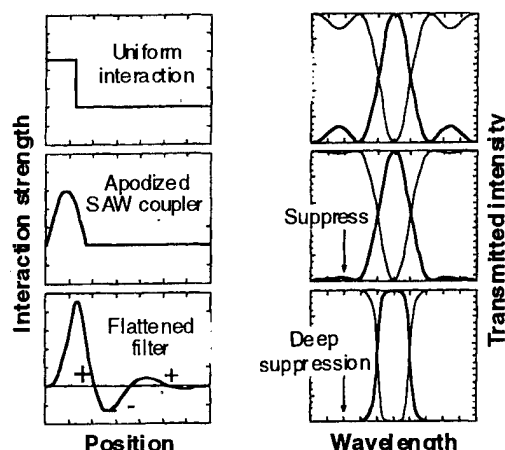


Figure 5. The progression of passband-engineered devices from the uniform interaction strength (top rows) to the apodized filter (center rows) and to the passband-flattened interaction (bottom rows) from the point view of AO interaction amplitude profile (left column) and predicted passbands (right column).

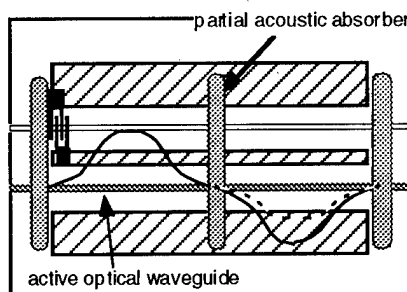


Figure 6. Double-length SAW coupler with slight leakage across a partial absorber in order to approximate the decaying oscillating amplitude profile required for passband flattening. The dotted line shows SAW amplitude without the partial absorber.

Passband shapes have improved over the years as depicted in Fig. 7, showing the progression from very high sidelobes due to gross birefringence non-uniformity (Fig. 7-I) have been resolved, resulting in "textbook"-shaped sidelobes (Fig. 7-II), and as apodization has reduced sidelobe levels (Fig. 7-III) and flattening has been attempted (Fig. 7-IV).

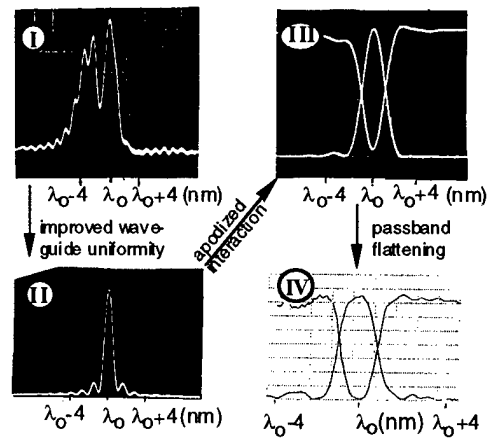


Figure 7. Evolution of AOTF passbands from the uniform SAW coupling with non-uniform birefringence (I) to with uniform SAW profiles (II) to apodized passband for low sidelobe performance (III) to preliminary passband flattened designs (IV).

More sophisticated structures have been developed to attain the predicted degree of flattening that a tapered-onset, decaying amplitude multi-cycle AO profile is predicted to achieve. Fig. 8 shows a tapered-gap zero-gap SAW coupler designed to obtain significant flattening [4].

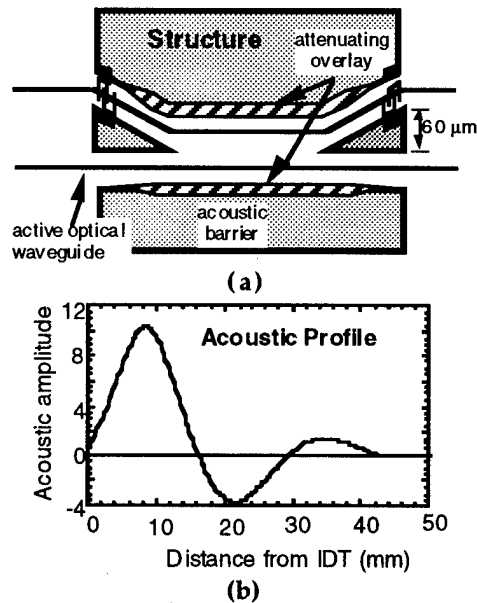


Figure 8. (a) Dual linear tapered zero-gap coupler with an attenuating overlay designed for passband flattening; (b) Calculated SAW amplitude profiles for right- and left-going SAW beams.

Evaluating complicated SAW profiles requires noninvasive real-time measurement of the photoelastic coupling. Fig. 9 shows a short-RF-pulse probe apparatus for evaluating the SAW interaction strength along the device developed by Aronson et al. [7] and applied to passband flattening filters by Rashid et al. [8].

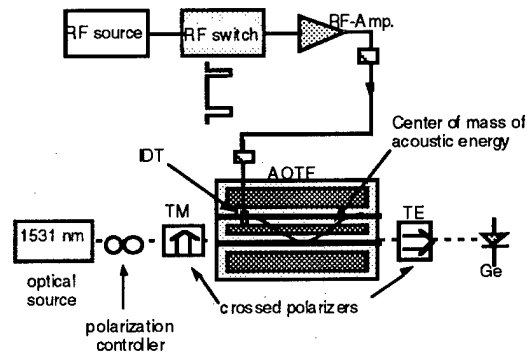


Figure 9. Schematic set-up of RF-pulse probing the SAW profile along an AOTF. Burst pulses as short as 100 ns (duty cycle < 2%) are used.

The filter under study incorporated a linear-tapered onset, and three full cycles of SAW amplitude in a length of only 39 mm by using a zero gap SAW coupler. Anticipating birefringence non-uniformity, nichrome heater coils (shown in Fig. 10) were placed above each SAW amplitude peak and arranged to adjust the current through each coil independently to perform local temperature tuning of  $D_n$ . The filter passband was evaluated at various levels of partial absorber attenuation and while varying the birefringence to obtain best flatness. In experiments to date, dramatic improvement of passband flatness has been achieved in moving from one to two cycles, but it appears that uncompensated birefringence variations have made three-cycle devices actually worse than two-cycle ones. The effective device length for two cycles was only 27.5 mm. Figure 11 compares the one and best two cycle passband shapes. Table 1 compares the passband widths at various crosstalk levels for the one- and two-cycle devices. We compared the results obtained with our temperature-compensated two-cycle, tapered-onset, zero-gap SAW-coupler-apodized filter with the best reported previous results [7] in the last row of Table 1. Jackel et al.'s results have been normalized so that the 3-dB widths agree (Their actual 3-dB filter width was 1.78 nm). The best flatness was achieved, surprisingly, for a birefringence non-uniformity worse than that measured for the "uncompensated" profile. This is not yet understood.

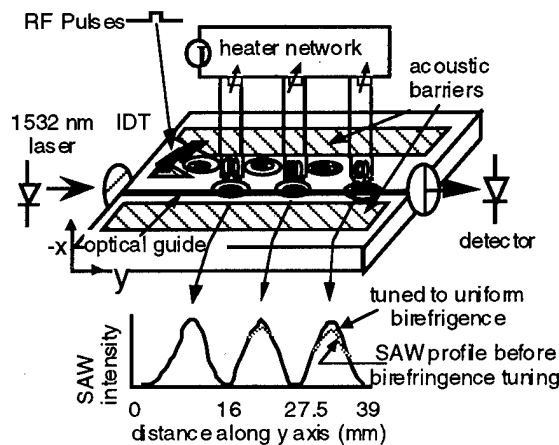


Figure 10. Three wire-heaters are arranged on top of a linear tapered AOTF to fine tune the birefringence distribution along the device in order to achieve desired passbands.

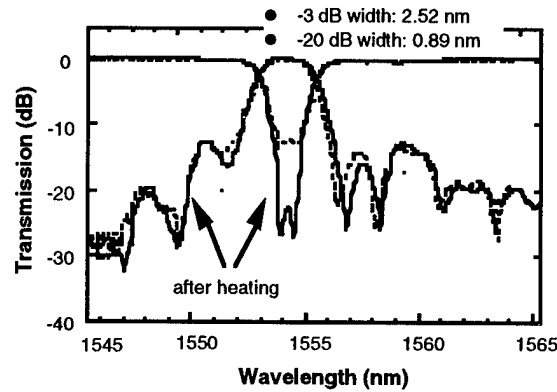


Figure 11. Comparison of passbands of a linear tapered AOTF obtained both before and after applying temperature tuning.

Table 1. Comparison of bar-state widths (in unit of nm) of one-cycle and two-cycle devices.

# cycles	-3 dB width	-10 dB width	-15 dB width	-20 dB width
one	2.52	0.89	0.22	N/A
two	2.52	1.56	1.11	0.89
two [7]	2.52	1.26	0.95	0.42

### 3. Technical Issues

#### 3.1. Imposed Frequency Shifts

It should be pointed out that the polarization conversion is accompanied by an imposed optical frequency shift equal in magnitude to the acoustic frequency, but with a sign determined by the associated phonon absorption/emission processes. For example, since  $n_z < n_x$  in  $\text{LiNbO}_3$  (i.e.,  $n_{\text{TE}} < n_{\text{TM}}$  in x-cut y-propagating samples), a light beam co-propagating with the SAW beam must gain momentum in TE-to-TM conversion,

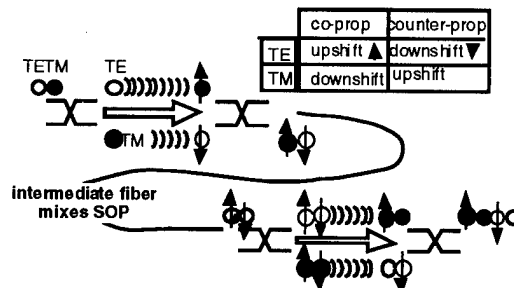


Figure 12. Polarization flipping causes different optical frequency shifting for TE light from TM light. A series of two AOTFs can impose coherent interference due to that frequency shift. Inset table summarizes the directions of optical frequency shift and the associated SAW propagation.

therefore absorb a phonon to have its frequency upshifted. Similarly, during TM-to-TE conversion, the frequency is decreased by  $f_s$ . The signs of frequency shifts are just opposite for the case of SAW and light counterpropagating. Frequency shifts can be suppressed in two-stage filters or made common mode by using opposing SAW waves for orthogonal polarizations. The absolute shift is small in wavelength terms, even over long AOTF cascades.

### 3.2. Passband Interactions

Although the AO switch has been said to offer simultaneous and independent multi-channel switching, the true situation is far from that ideal. Two or more SAWs present a complex grating to the incoming light since the combined SAW wave is a traveling beat pattern as depicted in Fig. 13.

The optical passband due to a SAW beat pattern is calculated by evaluating the progressive polarization transformation step by step through the device. The transmission function shape can be found at each instant in time and then analyzed as a function of time for the moving grating. The time-varying grating, observed by the time-average of an optical spectrum analyzer makes passband notches in the bar state degrade (Fig. 14a). Intermodulation of the optical signals is observed at the acoustic difference frequency and multiples thereof, causing BER degradation [10][11]. By a technique of running nearest-neighbor SAW channels in opposite directions along the same two-cycle passband-flattened device, it is possible to reduce intermod dramatically as shown in Fig 14b [12].

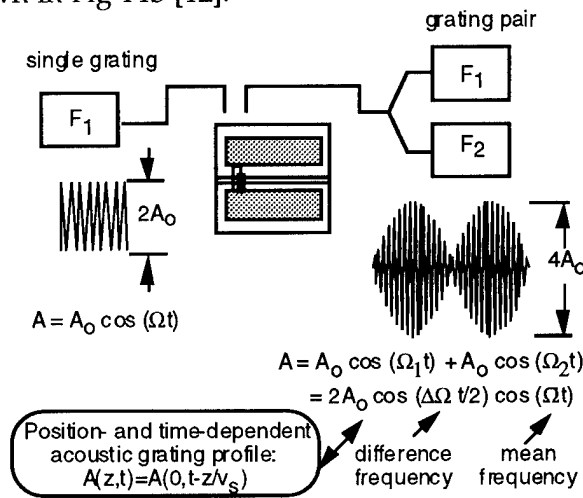


Figure 13. Schematic illustration of the AOTF interchannel modulation associated with simultaneous operation of two channels.

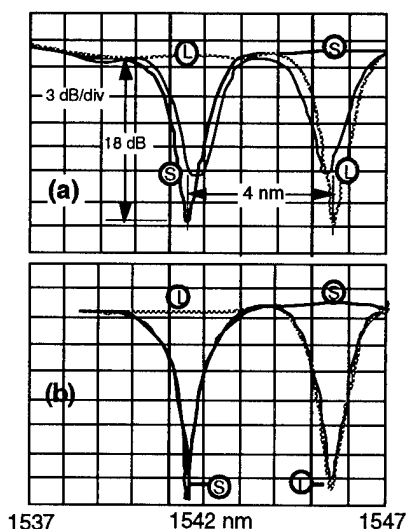


Figure 14. Experimental observation of AOTF interchannel passband attraction and notch degradation for single apodized AOTF, and improved performance of a wavelength-dilated passband flattened AOTF.

### 3.3. Coherent Crosstalk

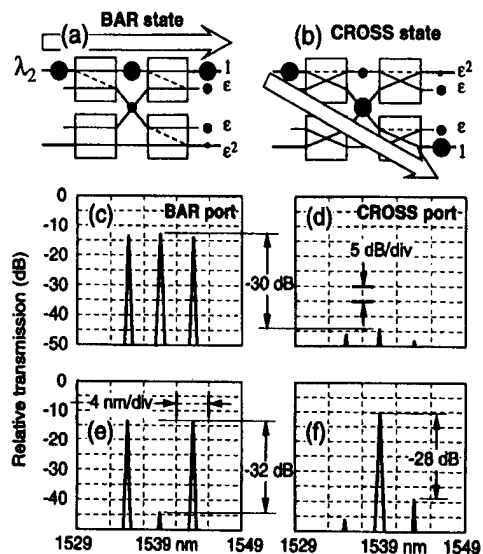


Figure 15. Switch dilation used to reduce interchannel crosstalk.

Leakage of wavelength channel power and its passage through multiple paths and subsequent recombination results in coherent crosstalk, for which the electric field amplitudes add within the receiver bandwidth, producing extreme crosstalk sensitivity. Goldstein [13] has shown that  $< -30$  dB intensity crosstalk is required in even modest-sized networks in order for crosstalk to be low enough for error-free communication. In order to attain the desired low crosstalk levels, switch space dilation has been required [14], in which the single  $2 \times 2$  switch has been replaced by a 4-element AO switch array. Such arrays reduce interchannel and interport crosstalk to second-order as demonstrated in Fig. 15. For close channel spacing, an additional level of wavelength dilation has been required [15].

## 4. Applications

### 4.1. WDM Routing

The AOTF has been used in WDM systems for wavelength add/drop multiplexing as well as for larger WDM crossconnect elements based on the 2x2 WDM base element as shown in Fig. 16.

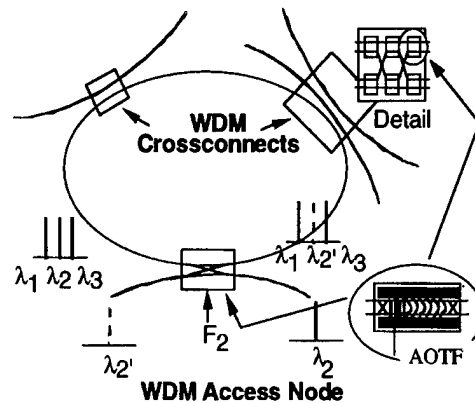
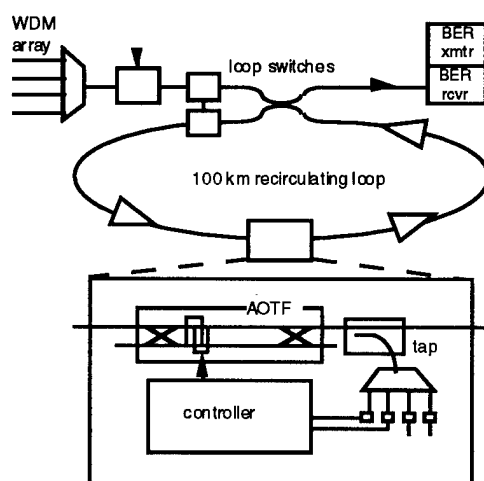


Figure 16. Example of a WDM network consisting of wavelength Add/Drop multiplexers.

### 4.2. EDFA Gain Equalization

One key difficulty in implementing a wide-area WDM system is that the EDFA gain is not uniform with wavelength, especially when incorporating cascades of amplifiers for which a newly-generated gain peak appears at  $\sim 1560$  nm. Because of its ability to function as a multiple-passband filter with independent control of each wavelength passband, the AOTF with active feedback can be used to dynamically equalize the EDFA gain [16]. Figure 17 shows the experimental setup in which a recirculating fiber loop was used to replicate a linear long-distance link containing a cascade of EDFA's. An AOTF is situated, in effect, after every 3 EDFAs and is in a feedback loop which monitors the output powers at each WDM channel and adjusts the AOTF notch depth at each wavelength so as to force the output powers equal.

Our loop consists of 3 EDFA's, each having a small-signal gain of  $\sim 25$  dB, 95 km of dispersion-shifted fiber, an acousto-optic tunable filter with active feedback and an acousto-optic modulator gating switch. Three signal wavelengths were externally modulated at 2.5 Gbit/s and were located at 1552.0, 1555.8, and 1560.2 nm, covering a wavelength range of 8.2 nm. The output of the loop includes an EDFA preamp, a 0.3-nm angle-tuned optical filter, a p-i-n receiver, an electronic  $\sim 1.5$ -GHz low-pass-filter, and a clock-recovery circuit. The AOTF passbands respond three orders-of-magnitude faster than the EDFA gain, thereby providing transparent gain equalization. After 1,000-km transmission in a recirculating-loop experiment, the maximum power differential was reduced from 20 dB to 1 dB for three 2.5-Gbit/s WDM channels covering an  $\sim 8$ -nm wavelength range [17]. Furthermore, the SNR differential among the three channels was  $\sim 3$  dB.



**Figure 17.** Recirculating EDFA loop experiment to simulate very long amplifier chains in which a multichannel AOTF-based gain equalizer (inset) is placed to maintain equalized S/N over great distances. The AOTF can be operated in either bar- or cross-state.

Figure 18a shows the optical spectrum of the 3 WDM channels before the loop, while Figure 18b shows the optical spectrum after propagating 1,000 km without an intra-loop AOTF equalizer. Without equalization, the power differential among the three channels is  $\sim 20$  dB, with both the power and the SNR of the 1552-nm channel significantly below the longer-wavelength channels. Figure 18c shows the optical spectrum after the signals have propagated 1,000 km with active AOTF equalization. The power differential among the three WDM channels was reduced to only 1 dB, and all 3 channels achieved a high SNR. Figure 18d shows the equalized output optical spectrum of signal propagation through 1,000 km for the case in which the input power of the 1552-nm channel was decreased by 3 dB. Figure 18e shows the equalized output optical spectrum when the power of Channel 2 was increased by 3. In Figure 18f, Channel 2 turned completely "OFF". There is no significant difference between any of the above equalized spectra, clearly showing active equalization using the AOTF when channel powers are dynamically changing. The limitation of this notch filter method is the accumulation of the amplified spontaneous emission (ASE) between channels. Recent experiments have shown cross-state AOTF gain equalization over 2500 km with ASE suppression [18].

### 4.3. Tunable Lasers

AOTF-based lasers have been demonstrated by a number of authors, including ring lasers [19],[20] and fully-self-contained Er-doped  $\text{LiNbO}_3$  devices pumped externally [21]. Fig. 19 depicts two designs. Usually these devices use two stages to eliminate the AO-induced frequency shift.



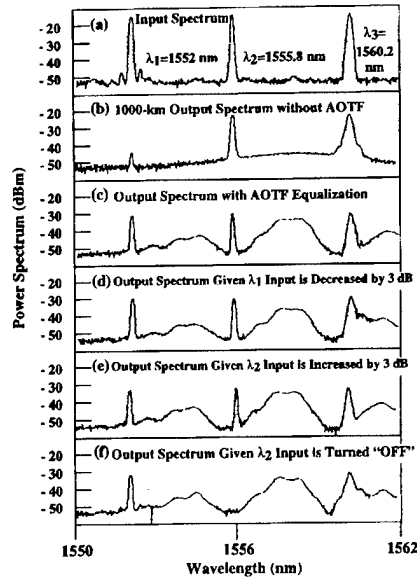


Figure 18. Optical spectrum of: (a) the input to the loop, (b) the output at 1,000 km without AOTF, (c) the output at 1,000 km with AOTF active equalization, (d) the output at 1,000 km when the power of 1552 nm is reduced 3 dB, (e) the output at 1,000 km when the power of 1555.8 nm is increased 3 dB, (f) the output at 1,000 km when the power of 1555.8 nm is turned "OFF".

## 5. Conclusion

The AOTF continues to advance in its degree of integration. Continued improvements in passband engineering promise to provide near-rectangular passbands in the near future and unexpected new applications arise frequently in this dynamic field of AOTF research and development.

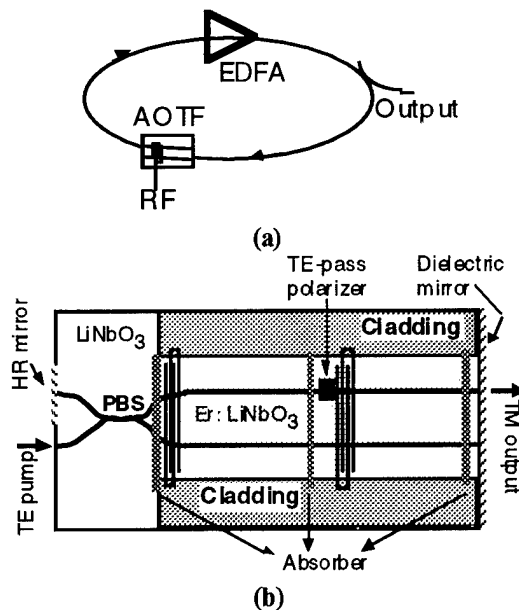


Figure 19. Schematic of ring lasers using an AOTF as the wavelength tuning element, (a) EDFA loop, (b) integrated Er:Ti:LiNbO<sub>3</sub> structure (after [21]).

## References

1. Brackett et al., *A scaleable multi-wavelength Multihop Optical Network*, J. of Lightwave Technol. (1993), vol. 11(5/6), 736-753.
2. Smith et al., *Evolution of the acousto-optic wavelength-routing switch*, J. Lightwave Technol. (1996), vol. 14, 1005-1019.
3. Herrmann, et al., *Integrated Acousto-Optical mode converters with weighted coupling using Surface Acoustic Waves directional couplers*, Electron. Lett. (1992), vol. 28, 979.
4. Chakravarthy et al., *Passband Engineering of Acousto-optic Tunable Filters*, poster, 7th European Conference on Integrated Optics, April 3-6 1995, Delft, The Netherlands.
5. Schmid et al., *Full wafer scale fabrication of A-O 2x2 wavelength-selective space switches on LiNbO<sub>3</sub>*, Proc. ECIO'95, PDP-ThP1,(1995), 21-24.
6. Song, *Proposal for acousto-optic tunable filters with near-ideal bandpass characteristics*, Appl. Opt. (1994), vol. 33(31), 7458-7460.
7. Jackel et al., *A Passband-Flattened Acousto-Optic Filter*, IEEE Photonics Technol. Lett. (1995), vol. 7(3), 318-320.
8. Aronson, *Acoustic pulse measurements of Acousto-Optic Tunable Filter properties*, Proc. Integrated Photonics Res. Conf., paper PD-6 (Dana Point, CA, Feb. 23-25, 1995).
9. Rashid et al., *The use of RF-pulse SAW profilometry for passband engineering of Acousto-Optic Tunable Filters*, to be published in Opt. Lett..
10. Smith et al., *Passband Collisions and multi-channel crosstalk in acousto-optic filters and switches*, Proc. European Conference on Integrated Optics '95, Delft, the Netherlands.
11. Tian and H. Herrmann, *Interchannel interference in multiwavelength operation of integrated acousto-optic tunable filters and switches*, J. Lightwave Technol. (1995), vol. 13(6), 1146-1154.
12. Jackel et al., *Multichannel operation of AOTF switches: reducing channel-to-channel interaction*, Photon. Technol. Lett. (1995), vol. 7, 370-372.
13. Goldstein et al., *Performance implications of component crosstalk in transparent lightwave networks*, Photon. Technol. Lett. (1994), vol. 6, 657-670.
14. Smith et al., *Reduction of crosstalk in an acousto-optic switch by means of dilation*, Opt. Lett. (1994), vol. 19, 99-101.
15. Jackel et al., *Demonstration of simultaneous and independent switching of eight wavelength channels with 2 nm spacing using a wavelength-dilated acousto-optic switch*, LEOS'95 PDP (1995).
16. Su et al., *Gain equalization in multiwavelength lightwave systems using acousto-optic tunable filters*, IEEE Photon. Technol. Lett. (1992), vol. 4(3), 269-271.
17. Huang et al., *Experimental demonstration of dynamic equalization of three 2.5-Gbit/s WDM channels over 1000 km using acousto-optic tunable filters*, OFC'96, paper WM6 (1996), San Jose, CA.
18. Huang et al., *Experimental demonstration of active equalization and ASE suppression of three 2.5-Gbit/s WDM-network channels over 2500 km using AOTF as transmission filters*, Submitted to CLEO'96.
19. Smith, et al., *Acoustically-tuned erbium-doped fiber ring laser*, Optics Letters (1991), vol. 16, 387-389.
20. Frankel et al., *Rapid continuous tuning of a single-polarization fiber ring laser*, IEEE Photon. Technol. Lett. (1994), vol. 6, 591-593.
21. I. Baumann et al., *Acoustically-tunable Ti:Er:LiNbO<sub>3</sub> waveguide laser*, Proc. ECOC'94 (1994), vol. 4, 99-102.

# INTEGRATED ACOUSTO-OPTIC TUNABLE FILTERS FOR BLUE-GREEN SPECTRAL REGION \* †

Chen S. Tsai and Anna M. Matteo

Department of Electrical and Computer Engineering and  
Institute for Surface and Interface Science  
University of California, Irvine  
Irvine, California 92697

## ABSTRACT

A detailed analysis and numerical simulation of guided-wave collinear acousto-optic interactions in several cuts of  $\text{LiNbO}_3$  waveguide substrates relevant to high-performance tunable optical filtering has been carried out. For example, it was shown that the acoustic drive power requirements for 100%  $\text{TM}_0 \rightarrow \text{TE}_0$  mode conversion in Z-cut configuration is significantly lower than the corresponding values for the  $\text{TE}_0 \rightarrow \text{TM}_0$  mode conversion in the X-cut configuration at the optical wavelengths of 0.50, 0.80, 1.15, and 1.55  $\mu\text{m}$ . At the center optical wavelength of 0.50  $\mu\text{m}$ , an acoustic drive power requirement as low as 0.17 mW/mm for 100%  $\text{TM}_0 \rightarrow \text{TE}_0$  mode conversion and an optical bandwidth as narrow as 0.78 nm can be achieved in the Z-cut waveguide (X-propagating SAW) at the guiding layer thickness of 0.6  $\mu\text{m}$ , and interaction length of 30 mm.

## 1. Introduction

The desirable features of  $\text{LiNbO}_3$  substrate-based integrated acoustooptic (AO) tunable filters (IAOTF) [1-6] such as broad optical wavelength tunability, narrow filter bandwidth, and low drive power requirements, have been recently exploited for their applications as useful components in fiber optic wavelength-division multiplexed (WDM) systems [4]. The IAOTFs make use of AO interaction between light waves confined in a single-mode optical waveguide and the surface acoustic wave (SAW) in the  $\text{LiNbO}_3$  substrates. The AO interaction involves a narrow-band optical wavelength  $\text{TE} \leftrightarrow \text{TM}$  mode conversion when a SAW at an appropriate phase-matching frequency, determined by the intrinsic wavelength-dependent birefringence of  $\text{LiNbO}_3$ , is propagated. Large optical wavelength tuning range is obtained by adjusting the phase-matching condition for different optical wavelengths by simply tuning the SAW frequency. To the best of our knowledge, all prior works have involved optical wavelength of 0.6328  $\mu\text{m}$  or

---

\* This work was supported by the UC MICRO Program and TIR Technology, Inc.

† Presented at First Army Research Laboratory Workshop on Acoustooptic Tunable Filters Technology, Sept. 24-25, 1996.

longer. For example, optical filter bandwidths of 1.2 nm and 0.32 nm have been achieved, respectively, at the optical wavelengths of 1.532  $\mu\text{m}$  [7] and 0.800  $\mu\text{m}$  [8]. Low drive power requirement is realized by confining both the SAW and the light waves into corresponding acoustic and optical channel waveguides, and by using X-cut Y-propagating LiNbO<sub>3</sub> substrate which provides efficient electric to acoustic conversion. Recently, significant reduction in sidelobe levels of the filters was accomplished using the techniques of weighted-coupling [6,9], facilitated for example by focused SAW [10] and uniform-gap SAW directional coupling [11,12]. Weighted-coupling using tapered-gap SAW directional coupling [13] was also proposed to achieve a sidelobe level as low as -41db.

Practical laser sources that cover the blue-green spectral region are gradually being realized. A variety of commercial and military applications using such laser sources are anticipated. The objective of this paper is to report on high-resolution, large-tuning range, and fast-tuning speed ( $\mu\text{s}$ ) IAOTF in the blue-green spectral region (0.45 to 0.55  $\mu\text{m}$ ).

## 2. Analysis and Numerical Simulation of Guided-Wave Collinear AO Interaction

### 2.1 Analysis

The results of a detailed theoretical study on guided-wave collinear AO interactions in Ti-indiffused (TI) LiNbO<sub>3</sub> planar waveguide are now presented. The mode conversion from the incident TE<sub>0</sub> (or TM<sub>0</sub>) guided-mode light into the TM<sub>0</sub> (or TE<sub>0</sub>) guided-mode light induced by a co-propagating SAW as shown in Fig. 1 is analyzed using the coupled-mode theory. The optical waveguide supports both the TE<sub>0</sub>- and TM<sub>0</sub>- guided modes. An interdigital SAW transducer is fabricated on the top of the optical waveguide to generate the SAW. Both the incident guided-mode light, in either the TE<sub>0</sub> or TM<sub>0</sub> polarization, and the SAW propagate in the positive X<sub>1</sub> direction. The interaction between the incident guided-mode light and the SAW results in a mode-converted light from the incident light polarization into the orthogonal component when one of the following phase matching conditions is satisfied:

$$\bar{\beta}_{TE} - \bar{\beta}_{TM} + \bar{K}_a = 0, \text{ (for the TE}_0 \rightarrow \text{TM}_0 \text{ mode conversion),} \quad (1a)$$

$$\text{and } \bar{\beta}_{TM} - \bar{\beta}_{TE} + \bar{K}_a = 0, \text{ (for the TM}_0 \rightarrow \text{TE}_0 \text{ mode conversion),} \quad (1b)$$

In Eqs. (1a)-(1b),  $\bar{\beta}_{TE}$  and  $\bar{\beta}_{TM}$  denote the propagation constants of the TE<sub>0</sub> and TM<sub>0</sub> guided-mode light, respectively, and  $\bar{K}_a$  the propagation constant of the SAW.

### 2.1.1 Mode Conversion Efficiency

The  $TE_o \rightarrow TM_o$  (or  $TM_o \rightarrow TE_o$ ) mode-conversion efficiency is derived as follows:

$$\eta = \sin^2 \left\{ \left( \sqrt{|K|^2 P_a + \Delta^2} \right) L \right\} / \{1 + \Delta^2 / (P_a |K|^2)\} \quad (2)$$

where  $L$  and  $P_a$  denote the interaction length and the acoustic drive power density, respectively, and the parameter

$$2\Delta = |\bar{\beta}_{TM} - \bar{\beta}_{TE}| - \bar{K}_a \quad (3a)$$

denotes the deviation from perfect phase matching condition. Finally,  $K$  denotes the overlap integral between the optical guided-modes and the acoustic field, and is given by:

$$K = \frac{\omega \epsilon_o}{4} \int \bar{E}_{TE}^* \Delta \epsilon \bar{E}_{TM} dx_3, \text{ (for } TE_o \rightarrow TM_o \text{ mode conversion),} \quad (3b)$$

$$\text{and } K = \frac{\omega \epsilon_o}{4} \int \bar{E}_{TM}^* \Delta \epsilon \bar{E}_{TE} dx_3, \text{ (for } TM_o \rightarrow TE_o \text{ mode conversion).} \quad (3c)$$

In Eqs. (3b)-(3c)  $\Delta \epsilon$  denotes the strain-induced permittivity tensor changes, as given in [15], calculated for unit acoustic drive power density. Finally,  $\bar{E}_{TE}$  and  $\bar{E}_{TM}$  denote the electric field vectors of the  $TE_o$  and  $TM_o$  guided-modes, respectively, calculated under power normalization.

### 2.1.2 Acoustic Center Frequency

From Eqs. (1), the relation between the acoustic frequency  $f_a$  and the selected (filtered) optical wavelength  $\lambda$  is derived as follows:

$$f_a = V_a \Delta n_{eff} / \lambda \quad (4a)$$

where  $V_a$  is the velocity of the SAW at the acoustic frequency  $f_a$  in the Ti:LiNbO<sub>3</sub>/LiNbO<sub>3</sub> substrate, and

$$\Delta n_{eff} = |\bar{\beta}_{TM} - \bar{\beta}_{TE}| / k_o = |n_{eff}^{TM} - n_{eff}^{TE}| \quad (4b)$$

in which  $n_{eff}^{TE}$  and  $n_{eff}^{TM}$  are the effective refractive index of the  $TE_o$  and  $TM_o$  guide-mode light, respectively, and  $k_o$  is the propagation constant of the incident light in free-space.

### 2.1.3 Acoustic Drive Power Density Requirement

Using Eq. (2), under the condition of perfect phase matching ( $D=0$ ), the acoustic drive power density required for 100% mode conversion,  $P_{100}$ , is derived as follows:

$$P_{100} = \left\{ \pi / 2|K|L \right\}^2 \quad (5)$$

### 2.1.4 Optical Bandwidth (FWHM)

The optical bandwidth associated with the collinear AO interaction in the LiNbO<sub>3</sub> substrate is typically very narrow ( $< 10$  nm). Consequently, the value for  $\Delta n_{eff}$ , as given in Eq. (4b), can be considered constant with the optical wavelength within the range defined by the optical bandwidth. Under this assumption, the deviation from the perfect phase matching condition corresponding to the generic optical wavelength  $\lambda_2$ , can be written as follows:

$$2\Delta = \Delta n_{eff} \frac{2\pi}{\lambda_2} - K_a = \Delta n_{eff} \frac{2\pi}{\lambda_2} - \Delta n_{eff} \frac{2\pi}{\lambda} \approx \Delta n_{eff} \frac{2\pi}{\lambda^2} \Delta\lambda \quad (6)$$

where  $\lambda$  denotes the center optical wavelength.  
Using Eq. (6), Eq. (2) can be rewritten as:

$$\eta = \left\{ \sin^2 \left\{ x|K|\sqrt{P_a}L \right\} \right\} / \chi^2 \quad (7)$$

where

$$\chi = \sqrt{1 + (\pi\Delta n_{eff} \Delta\lambda / \lambda |K|\sqrt{P_a})^2} \quad (8)$$

When the acoustic drive power density given in Eq. (5) is set equal to  $P_{100}$  and the mode conversion efficiency in Eq. (7) set to 0.5, the following expression for  $2\Delta\lambda$  (full-width at half-maximum, FWHM) is obtained:

$$\text{FWHM} = 2\Delta\lambda = 0.4\lambda^2 / L\Delta n_{eff} \quad (9)$$

## 3. Numerical Results

The formulation presented in the previous subsection has been applied to evaluate the collinear AO interactions in the X- and Z-cut Ti:LiNbO<sub>3</sub> /LiNbO<sub>3</sub> waveguides, where the AO grating is induced by a SAW propagating in the Y- and X- direction, respectively. The numerical calculations have been carried out for four practical optical wavelengths, namely,  $\lambda = 0.50, 0.80, 1.15$ , and  $1.55 \mu\text{m}$ . The corresponding ordinary and extraordinary refractive indices of the LiNbO<sub>3</sub> substrate

corresponding ordinary and extraordinary refractive indices of the  $\text{LiNbO}_3$  substrate have been taken from [13]. The increases in the ordinary ( $\Delta n_o$ ) and extraordinary ( $\Delta n_e$ ) refractive indices due to the Ti-indiffusion process are assumed to be equal to 0.02 and 0.04, respectively. For each optical wavelength different guiding layer thicknesses ( $d$ ) have been considered, namely,  $d = 0.6, 1.0$ , and  $1.5 \mu\text{m}$  at  $\lambda = 0.5 \mu\text{m}$ ;  $d = 1.0, 1.5$ , and  $2.0 \mu\text{m}$  at  $\lambda = 0.8 \mu\text{m}$ ;  $d = 1.2, 1.5$  and  $2.0 \mu\text{m}$  at  $\lambda = 1.15$ , and  $d = 1.5, 2.0$ , and  $2.5 \mu\text{m}$  at  $\lambda = 1.55 \mu\text{m}$ . In the following only sample results with special attention to the center optical wavelength of  $0.5 \mu\text{m}$  are presented:

### 3.1 Mode Conversion Efficiency

It has been shown that for an acoustic wave co-propagating with the guided-wave light, the phase matching conditions corresponding to the  $\text{TE}_o \rightarrow \text{TM}_o$  (see Eq. 1(a)) and to  $\text{TM}_o \rightarrow \text{TE}_o$  (see Eq. 1(b)) mode conversions can be achieved only in the X-cut and Z-cut  $\text{Ti LiNbO}_3$  waveguide, respectively. For example, Fig 2 shows the  $\text{TM}_o \rightarrow \text{TE}_o$  mode conversion efficiency versus the acoustic drive power density, at the interaction length of 30 mm, in the Z-cut configuration for different guiding layer thicknesses at the optical wavelength of  $0.50 \mu\text{m}$ .

A comparison of the mode conversion efficiency at different optical wavelengths has been carried out for the acoustic drive power density range of 0-100 mW/mm at the guiding layer thickness of  $1.5 \mu\text{m}$  and interaction length of 30 mm. The comparison is presented in terms the mode conversion efficiency in the X-cut and Z-cut configurations, respectively, for optical wavelengths of 0.80, 1.15, and  $1.55 \mu\text{m}$  in the X-cut configuration and 0.50, 0.80, 1.15 and  $1.55 \mu\text{m}$  in the Z-cut configuration. Accordingly, the following conclusions are obtained:

- In both the X- and Z- cut configurations, the acoustic drive power density required to obtain a given mode conversion efficiency is seen to be significantly reduced as the optical wavelength decreases. At the optical wavelength of  $0.50 \mu\text{m}$ , an acoustic drive power density as low as 0.17 mW/mm is required to achieve 100%  $\text{TM}_o \rightarrow \text{TE}_o$  mode conversion efficiency in the Z- cut configuration at the guiding layer thickness of  $0.6 \mu\text{m}$  and interaction length of 30 mm.
- A significantly lower acoustic drive power density is required in the Z- cut configurations, to achieve 100%  $\text{TM}_o \rightarrow \text{TE}_o$  mode conversion efficiency, than in the corresponding requirements in the X- cut configurations.
- A good agreement between the calculated results and the experimental results reported in the literature [9] has been found.
- At the optical wavelength of  $1.55 \mu\text{m}$ , a 100% mode conversion efficiency cannot be achieved within the acoustic drive power density in the range 0-100 mW/mm. The actual power requirement, as calculated from Eq. (5), is equal to 240 mW/mm. This value is in agreement with the high values of RF drive power reported in the literature, and relevant to X-cut AO filters using unconfined SAWs at the optical wavelength of  $1.55 \mu\text{m}$ .

### 3.2 Optical Bandwidth (FWHM)

Figs. 3 shows the optical bandwidth versus the  $TM_0 \rightarrow TE_0$  mode conversion efficiency at perfect phase matching, in the Z-cut configuration, at the interaction length of 30 mm, for different guiding layer thicknesses at the optical wavelengths of 0.50  $\mu\text{m}$ . A comparison of the optical bandwidth at different optical wavelengths and given guiding layer thickness of 1.5  $\mu\text{m}$ , and interaction length of 30 mm for the X- and Z-cut configurations has been carried out. It is seen that FWHMs as narrow as 0.78 and 0.79 nm can be achieved in the Z- cut and X- cut configurations, respectively, at the optical wavelength of 0.50  $\mu\text{m}$ , guiding layer thickness of 0.6  $\mu\text{m}$ , and interaction length of 30 mm.

### 4. Conclusion

The detailed computer calculations have concluded that at the center wavelength of blue-green region (e.g. 0.5  $\mu\text{m}$ ), an acoustic drive power requirement as low as 0.17 mW/mm for 100%  $TM_0 \rightarrow TE_0$  mode conversion efficiency and an optical bandwidth as narrow as 0.78 nm can be achieved in the Z-cut waveguide (X-propagating SAW) at the guiding layer thickness of 0.6  $\mu\text{m}$ , and interaction length of 30 mm.

### 5. References

- [1] Y. Ohmach and J. Noda, *IEEE Quantum Electron.*, **OE-13**, 43-46, 1977.
- [2] B. Kim and C.S. Tsai, *IEEE J. Quantum Electron.*, **OE-15**, 642-647, 1979.
- [3] J. Frangen, H. Herrman, R. Ricken, H. Seibert, W. Sohler, and E. Strake, *Electron. Lett.*, Vol. **25**, 1583-1584, 1989.
- [4] D.A. Smith, J.E. Baran, J.J. Johnson, and K.W. Cheung, *IEEE J. Sel. Areas Comm.*, Vol. **8**, 1151-1159, 1990.
- [5] D.A. Smith and J.J. Johnson, *IEEE Photon. Technol. Lett.*, Vol. **3**, 923-925, 1991.
- [6] A. Kar-Roy and C.S. Tsai, *IEEE J. Quantum Electron.*, Vol **30**, pp. 1574-1586, 1994.
- [7] B.L. Heffner et al., *Electron. Lett.*, Vol. **24**, 1562-1563, 1988.
- [8] I. Hinkov, H. Hinkov, *Electron. Lett.*, Vol. **27**, 1211-1213, 1991.
- [9] Y. Yamamoto, C.S. Tsai, and K. Esteghamat, *Proc. Ultrasonics Symposium* (IEEE, New York, 1990), pp. 605-608 (IEEE Catalogue No. 90CH2938-9); Also, Y. Yamamoto, C.S. Tsai, K. Esteghamat, and H. Nishimoto, *IEEE Trans. On Ultrasonics/Ferroelectrics/Frequency Control*, Vol. **40**, 813-818, 1993.
- [10] A. Kar-Roy and C.S. Tsai, *IEEE Photon. Technol. Lett.*, Vol. **4**, 1132-1135, 1992.
- [11] D.A. Smith and J.J. Johnson, *Appl. Phys. Lett.*, Vol. **61**, 1025-1027, 1992.
- [12] H. Hermann and S. Schmid, *Electron Lett.*, Vol. **28**, 979-980, 1992.
- [13] A. Kar-Roy and C.S. Tsai, *J. Lightwave Tech.*, Vol. **12**, 977-982, 1994.
- [14] A.M. Matteo, Nhan Do, C.S. Tsai, "Collinear Guided-Wave Acoustooptic Interactions in  $\text{LiNbO}_3$ ," (to be published).
- [15] C.J. G. Kirby, "Refractive Index of Lithium Niobate, wavelength dependence: Tables," in *Properties of Lithium Niobate*, EMIS Datareview No. 5, 139-142, 1989.



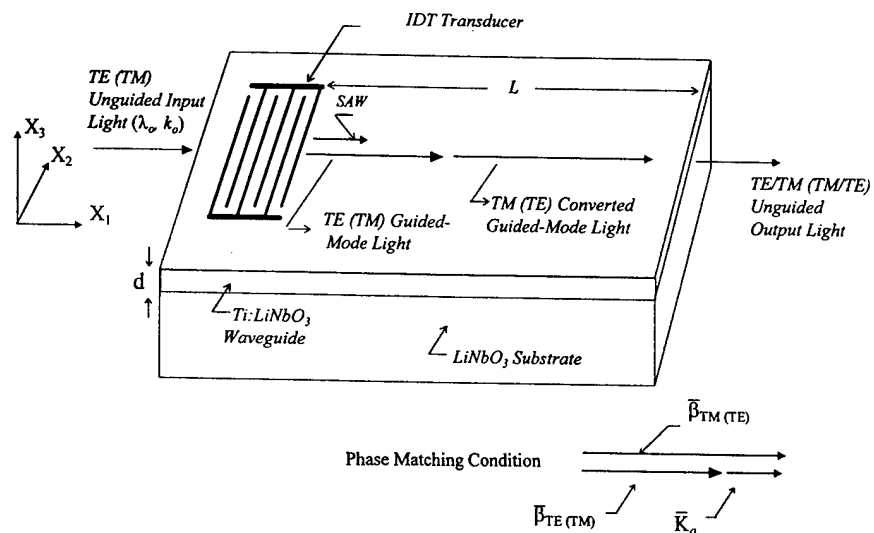


Fig. 1 Geometry for Guided-Wave Collinear Acoustooptic Interactions in Ti: LiNbO<sub>3</sub> Waveguides.

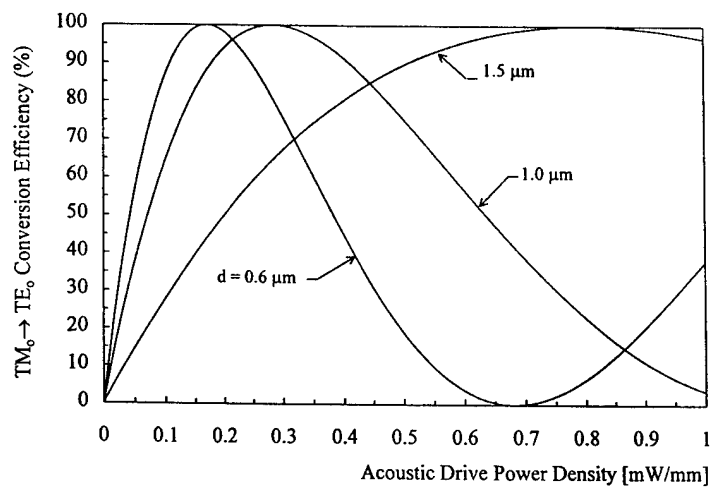


Fig. 2. TM<sub>0</sub> → TE<sub>0</sub> Mode Conversion Efficiency Versus the Acoustic Drive Power Density in the Z-cut Configuration at the Optical Wavelength of 0.5 μm

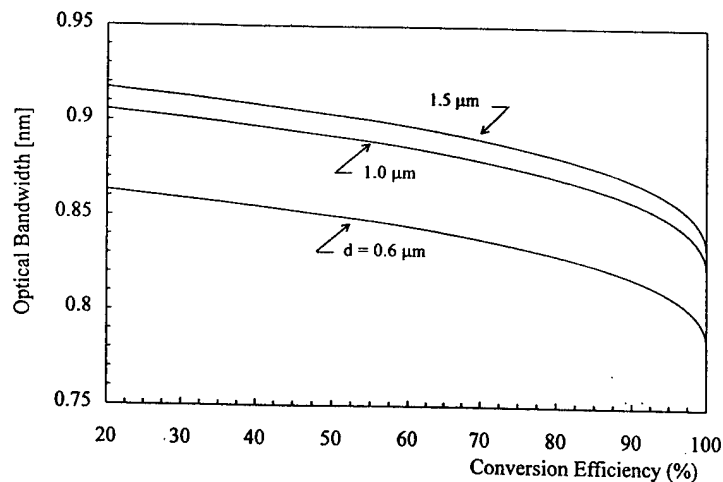


Fig. 3. Optical Bandwidth Versus the TM<sub>0</sub> → TE<sub>0</sub> Mode Conversion Efficiency in the Z-cut Configuration at the Optical Wavelength of 0.50 μm

## **Applications for Chemical Sensing**

# **APPLICATIONS OF ACOUSTO-OPTIC TUNABLE FILTERS IN ANALYTICAL CHEMISTRY**

Chieu D. Tran

Department of Chemistry, Marquette University

P. O. Box 1881, Milwaukee, Wisconsin 53201-1881

- 
1. Introduction
  2. Applications in Spectroscopy
    - 2.1 AOTF based Fluorimeter
    - 2.2 AOTF based Thermal Lens Spectrophotometers
    - 2.3 Near Infrared Spectrophotometer based on the AOTF and an Erbium doped fiber amplifier
  3. Applications in Chemical Separations
    - 3.1 Chromatography
    - 3.2 Flow Injection Analysis
- 

## **ABSTRACT**

Advantages of acousto-optic tunable filters have been exploited to develop novel analytical instruments which are not feasible otherwise. The instrumentation development and unique features of such AOTF based instruments including the multidimensional fluorimeter, the multiwavelength thermal lens spectrometer, the near-infrared spectrometer based on erbium doped fiber amplifier (EDFA), and detectors for high performance liquid chromatography (HPLC) and flow injection analysis (FIA), will be described.

## 1. INTRODUCTION

Acousto-optic tunable filter (AOTF) is an all-solid state, electronic dispersive device which is based on the diffraction of light in a crystal [1-9]. Generally, the filter is fabricated from an anisotropic  $\text{TeO}_2$  crystal onto it an array of  $\text{LiNbO}_3$  piezoelectric transducers are bonded. A radio frequency (RF) signal is applied to the transducers which, in turn, generates an acoustic wave propagating through the  $\text{TeO}_2$  crystal. These propagating acoustic waves produce a periodic moving grating which will diffract portions of an incident light beam. A light beam propagating as an e-ray is converted into an o-ray and in addition, is spatially separated from the original e-ray by interaction with, and diffraction from, an acoustic wave propagating in the same medium [1-9]. Conservation of momentum must be satisfied in order for this conversion to be cumulative [1-9]. As a consequence, for a fixed acoustic frequency and sufficiently long interaction length, only a very narrow band of optical frequencies can approximately satisfy the phase matching condition and be diffracted. The wavelength of the diffracted light can therefore, be tuned over large spectral regions by simply changing the frequency of the applied RF signal. The scanning speed of the AOTF is, therefore, defined by the speed of the acoustic wave in the crystal, which is on the order of microseconds. As a consequence, compared to conventional gratings, the AOTFs offer such advantages as being all-solid -state (contains no moving parts) having rapid scanning ability ( $\mu\text{s}$ ), wide spectral tuning range and high throughput, allowing high-speed random or sequential wavelength access, and giving high resolution (a few angstroms). The AOTF has offered unique means to develop novel instruments which are not possible otherwise. The instrumentation development and unique features of such AOTF based instruments including the multidimensional fluorimeter, the multiwavelength thermal lens spectrometer, the near-infrared spectrometer based on erbium doped fiber amplifier (EDFA), and detectors for high performance liquid chromatography (HPLC) and flow injection analysis (FIA), will be reported in this paper.

## 2. APPLICATIONS IN SPECTROSCOPY

### 2.1 AOTF-based Fluorimeter

Fluorescence technique has been demonstrated to be a sensitive method for trace characterization. Since realtime samples are generally mixtures of many different compounds, their analyses usually require measurements of the fluorescence spectra at different excitation wavelengths (because absorption spectra of compounds in the mixture are different). Fluorimeter based on multichannel detection (e.g., videofluorimeter) has been developed to alleviate this time consuming process [10,11]. While the instrument has proven to be a very powerful method for the determination of multicomponent trace chemical species, its applications are still limited because of such factors as high cost, low sensitivity, slow in the data acquisition (the fastest is on the order of milliseconds) and complicated data analysis [10,11]. These limitations can be eliminated if the AOTF is used to develop a new generation multidimension spectrofluorimeter.

As explained above, an incident white light is diffracted by the AOTF into a specific wavelength when a specific RF is applied to it. It is important to realize that the diffracted light needs not be a monochromatic light. Multiwavelength light can be diffracted from the AOTF when more than one RF signals are simultaneously applied into the filter [1-9]. As a consequence, the AOTF can be used as a polychromator. Compared to conventional polychromators, advantages of this electronic AOTF polychromator include its ability to individually amplitude-modulate each wavelength of the diffracted multiwavelength light at different frequency. This is accomplished by individually and sinusoidally modulating each applied RF signal at a different frequency. This feature together with the fast scanning ability make the AOTF to be uniquely suited for the development of a novel, all solid-state, nonmoving parts multidimensional spectrofluorometer.

The schematic diagram of the AOTF based multidimensional fluorimeter is shown in Fig 1 [2,3]. Two AOTF's were used in this instrument: one for excitation and the other for emission. The first AOTF was used to specifically diffract white incident light into a specific wavelength(s) for excitation. Depending on the needs, the second AOTF (i.e., the emission AOTF) can be used as either a very fast dispersive device or a polychromator. In the first configuration (i.e., the rapid scanning fluorimeter), the sample was excited by a single excitation wavelength; the emitted light was analyzed by the emission AOTF which was scanned very fast. A speed of  $4.8 \text{ \AA}/\mu\text{s}$  was found to be the fastest speed which the AOTF can be scanned with a reasonable S/N and resolution. With this speed, a spectrum of 150 nm can be measured in 312  $\mu\text{s}$ . Faster scanning is possible, but because of the limitation due to the speed of the acoustic wave, may undesiredly lead to the degradation in the S/N and spectral resolution [2,3]. In the second configuration (i.e., multidimensional fluorimeter), both AOTFs were used as a polychromator. Several different rf signals were simultaneously applied into the first AOTF to provide multiple excitation wavelengths. The emission was simultaneously analyzed at several wavelengths by the emission AOTF. With this configuration, the fluorimeter can be used for the analysis of multicomponent samples, and the maximum number of components it can analyze is, in principle,  $a \times b$  where  $a$  and  $b$  are the number of excitation and emission wavelengths, respectively [3]. In fact, multicomponent samples e.g., mixtures of rhodamine B, fluorescein, eosin and 4-(dicyanomethylene)-2-methyl-6-[p-(dimethylamino)styryl]-4-H-pyran (DMP) can be simultaneously analyzed at a limit of detection of  $10^{-10} \text{ M}$  [2,3].

## 2.2 AOTF-based Thermal Lens Spectrophotometer

The fluorescence technique is very sensitive and can be used for the determination of trace chemical species at very low concentration. However, the technique is not applicable to all compounds because only few molecules are fluorescent. It is, therefore, important that novel technique which has the same sensitivity as the fluorescence technique but is applicable to non-fluorescent compounds be developed. Thermal lens technique is one of such possibilities.

The thermal lens technique is based on the measurement of the temperature rise that is produced in an illuminated sample by nonradiative relaxation of the energy absorbed from a laser [12-17]. Because the absorbed energy is directly measured in this case, the sensitivity of the technique is similar to that of the fluorescence technique, and is relatively higher than the conventional absorption measurements. In fact it has been calculated and experimentally verified that the sensitivity of the thermal lens technique is 237 times higher than that by conventional absorption techniques when a laser of only 50 mW power was used for excitation [12-17]. Absorptivities as low as  $10^{-7}$  have been measured using this ultrasensitive technique [12-17]. Potentially, the technique should serve as an excellent method for trace chemical analysis because it has high sensitivity, in situ and non-destructive ability, and requires a minimum amount of sample. Unfortunately, its applications to the area of general trace chemical analysis are not so widespread in comparison to other spectrochemical methods. A variety of reasons might account for its limited use, but the most likely one is probably due to the low selectivity. The majority of reported thermal lens spectrometers employ only a single excitation wavelength [12-17], and as a consequence can only be used for the analysis of one component samples. A multiwavelength thermal lens spectrometer is needed to analyze, in realtime, multicomponent samples without any pretreatment. AOTF offers a unique means for the development of the first, all solid state, no-moving part fast scanning multiwavelength thermal lens instrument.

The schematic diagram of the AOTF based multiwavelength thermal lens spectrometer is shown in Fig 2 [4,18]. This instrument is based on the use of the AOTF as a polychromator. An argon ion laser operated in the multiline mode was used as the light source. This multiwavelength laser beam was converted into the excitation beam with appropriate number of wavelengths by means of a  $\text{TeO}_2$  AOTF. In this case, four different wavelengths were used. They were obtained by simultaneously applying four different rf signals to the AOTF. These rf signals were provided by four different oscillators (osc1, osc2, osc3 and osc4). To differentiate each wavelength from the others, the applied rf's were sinusoidally amplitude modulated at four different frequencies by four modulators (mod1, mod2, mod3 and mod4). The four AM modulated rf signals were then combined by means of a combiner, and amplified by a rf power amplifier (amp). The amplified, AM modulated signal was then applied onto the AOTF to enable it to diffract the incident multiline laser beam into beam which has the four different wavelengths. The probe beam, provided by a He-Ne laser, was aligned to overlap with the pump beam at the sample cell by means of a dichroic filter (DF). The heat generated by the sample absorption of the pump beams changes the intensity of the probe beam. The intensity fluctuation of the probe beam was measured by a photodiode (PD2) placed behind a 632.8 nm interference filter (F) and a slit (S). A lens was used to focus the probe beam, and the distance between this lens and the sample was adjusted to give maximum thermal lens signals. The signal intensity, measured as the relative change in the probe beam center intensity, was recorded by a microcomputer through an AD interface board [4,18].

Compared with other multiwavelength thermal lens instruments, this all solid state

thermal lens spectrophotometer has advantages that include its ability to simultaneously analyze multicomponent samples in microsecond time scale, without the need for any prior sample preparation. In fact, with this apparatus and with the use of only 12 mW multiwavelength excitation beam, multicomponent samples including mixtures of lanthanide ions ( $\text{Er}^{3+}$ ,  $\text{Nd}^{3+}$ ,  $\text{Pr}^{3+}$  and  $\text{Sm}^{3+}$ ) can be simultaneously determined with a LOD of  $10^{-6} \text{ cm}^{-1}$  [18].

### 2.3 Near Infrared Spectrophotometer based on the AOTF and an Erbium Doped Fiber Amplifier

The use of the near infrared spectrometry in chemical analysis has increased significantly in the last few years [15-17,19-25]. The popularity stems from the advantages of the technique, namely its wide applicability, noninvasive and on-line characteristics. Near infrared region covers the overtone and combination transitions of the C-H, O-H and N-H groups, and since all organic compounds possess at least one or more of these groups, the technique is applicable to all compounds [19-25]. There is no need for pretreatment of the sample, and since NIR radiation can penetrate a variety of samples, the technique is noninvasive and has proven to be potentially useful for noninvasive, on-line measurements. In fact, NIR technique has been used in industries for on-line measurements for quality control and assurance. However, its applications are not as widely as expected. This may be due to a variety of reasons but the most likely ones are probably due to the limitations on the speed, stability and light throughput of the currently available instruments. To be effectively used as a detector for on-line measurements, the NIR instrument needs to have high and stable light throughput, to suffer no drift in the baseline, and can be rapidly scanned. These impose severe limitations on conventional NIR spectrophotometers because such instruments generally have relatively low and unstable light throughput, suffer some degree of baseline drift, and can only be scanned very slowly. AOTF, with its ability to rapidly scan as well as to control and maintain the intensity of light at a constant level, offers a means to alleviate some of these limitations.

It has been shown recently that stimulated emission can be achieved in a fiber when the fiber is doped with rare earth ions such as  $\text{Er}^{3+}$ , and optically pumped by an ion laser or YAG laser [26,27]. Now, for the first time, a lasing medium can be confined in a material as flexible and as small (less than  $10 \mu\text{m}$ ) as a single mode fiber [19,20]. Because of such features, the length of the doped fiber can be adjusted to as long as few miles to enable the fiber to have optical output in the range of kilowatts. Furthermore, the doped fiber can be pumped by a high power diode laser fusion-spliced directly into the doped fiber. It is thus, evidently clear that this all-fiber, compact EDFA can provide near infrared light with highest intensity and widest spectral bandwidth compared to other (cw) near-IR light sources currently available. A novel, compact, all solid state, fast scanning near infrared spectrophotometer which has no moving part, high and very stable light throughput can, therefore, be developed by use of this EDFA as a light source and AOTF as a dispersive element to scan and control the intensity of the diffracted light. Schematic diagram of such a spectrophotometer is shown in Figure 3 (with the insert

showing the construction of the EDFA). As illustrated, the near infrared light from the output of the EDFA was dispersed to monochromatic light and spectrally scanned by means of a non-collinear AOTF which was fabricated from  $\text{TeO}_2$ . A driver constructed from a voltage control oscillator (VCO) provided the RF signal to the AOTF. The RF signal from this driver was amplitude-modulated at 50 kHz by a home-built modulator and amplified by a RF power amplifier prior to being applied to the AOTF. The light diffracted from the AOTF was split into two beams (i.e., sample and reference beams) by means of a beamsplitter (BS). Intensity of the light in the sample and reference beams was detected by thermo-electrically cooled InGaAs detectors. Each detector is equipped with a thermoelectric cooler, and a temperature controller was used to cool it down and to keep its temperature constant. The output signals from the (reference and sample) detectors which were amplitude modulated at 50 kHz were connected to lock-in amplifiers (Stanford Research Systems Model SR 810) for demodulating and amplifying. The signal from the reference beam can be used either as a reference signal for a double beam spectrophotometer or as a reference signal for the fed-back loop to stabilize the intensity of the light in the sample beam in a manners similar to those used previously. The signals from the lock-in amplifiers were then connected to a microcomputer through a 16 bit A/D interface board. A software written in C++ language was used to control the frequency and the power, and to scan the applied RF signal. The same software also facilitated the data acquisition, analysis (e.g., to calculated the absorption spectra), and to save the data in ASCII format for the subsequent data-processing using other software packages.

As expected, the sensitivity of this EDFA-AOTF based spectrophotometer is comparable with those of the halogen tungsten lamp-AOTF based instruments. In fact, this spectrophotometer can be used to detect water in ethanol at a limit of detection of 10 ppm. More importantly is its high light throughput. The intensity of this EDFA light source was found to be about 20 times higher than that of 250 W halogen tungsten lamp. As a consequence, it can be used for measurements which are not possible with lamp based instruments. Two measurements were performed to demonstrate this advantage. Shown in Figure 4 is the intensity of the light transmitted through 6 sheets of photocopy paper (Cascade X-9000 white paper). As illustrated, because of the high absorption (of the papers) and low intensity (of the halogen tungsten lamp) no light was transmitted when the halogen tungsten lamp based spectrophotometer was used. Because of its high intensity, a substantial amount light was transmitted through the papers. In the second measurement which is shown in Figure 5, it was not possible to use a lamp based spectrometer to measure absorption spectrum of 1.0 M solution of  $\text{Pr}^{3+}$  in  $\text{D}_2\text{O}$  (in a 2-mm cell) placed after 4 sheets of photocopy paper (dashed line). Because of its high intensity, substantial amount of EDFA light was transmitted through the papers and  $\text{Pr}^{3+}$  solution, and as a consequence, absorption spectrum of the latter can be recorded (Fig. 5 insert). This high throughput advantage is of particular importance in NIR measurements because NIR techniques are often used for measurements in which the signal of interested is very small and riding on top of a very large background signal. As such, it is very difficult, inaccurate and sometimes not possible to perform such measurements with low-light-throughput spectrophotometers.



### 3. APPLICATIONS IN CHEMICAL SEPARATIONS

#### 3.1. AOTF based Detector for HPLC

High performance liquid chromatography (HPLC) has increasingly become the technique of choice for chemical separations. As the technique becomes more prevalent the demand for detectors that can provide quantitative as well as qualitative information on the analyte increases.

Variable wavelength absorption detectors are the most widely used detectors for HPLC. However, this type of detector can only be used as a quantitative technique because the qualitative information obtained from this detector is rather limited, namely, it relies on the use of the retention time as the only tool for identification. The development of diode array detectors (DADs) in the early 1980's made it possible to obtain information on peak purity and identity [28]. Specifically, with a DAD based detector, the spectrum obtained for each peak in the chromatogram can be stored, and the subsequent comparison with standard spectra will facilitate the identification of peaks [28]. The optimum wavelength for single wavelength detection can easily be found [28]. Wavelength changes can be programmed to occur at different points in the chromatogram, either to provide maximum sensitivity for peaks, or to edit out unwanted peaks, or both [28]. Unfortunately, in spite of their advantages, DADs still suffer from limitations including their relatively high cost and their low sensitivity (compared to variable and fixed wavelength detectors). It is therefore, of particular importance that a novel detector which has higher sensitivity, low cost and possesses all of the DADs' advantages be developed. The AOTF with its unique features is particularly suited for the development of such a detector. Specifically, with its microsecond scanning speed, the AOTF based detector can rapidly record absorption spectrum of a compound as it elutes from the column. The random access to wavelength(s) makes it possible to change and/or to program the detector to any wavelength(s) to obtain optimal detection. However, different from the DADs, the AOTF-based detector is a single channel detection technique, i.e., it is based on a photomultiplier tube. Its sensitivity is, therefore, higher and its cost is lower than the multichannel detectors (i.e., DADs).

The schematic diagram of the AOTF based detector is shown in Fig 6. A 150-W xenon arc lamp was used as the light source. Its output radiation which contains UV and visible light was focussed onto the AOTF by a combination of a reflector, collimator and lens. Acoustic waves will be generated in the AOTF when the RF signal is applied into the filter by a signal generator. To reduce noise and to facilitate the phase sensitive detection the rf signal was sinusoidally modulated at 50 kHz by the microcomputer through the D/A. Prior to being connected to the AOTF, the AM modulated RF signal was amplified to 5 W power by an RF power amplifier. The intensity of the light diffracted from the AOTF was detected by a photomultiplier tube and demodulated (at 50 kHz) by a lock-in amplifier prior to being recorded by a microcomputer.

The chromatographic system consists of an isocratic pump and a sample injector valve equipped with a 40- $\mu$ L loop. A 250 mm X 4.6 mm I.D. stainless-steel column packed with Nucleosil 5 silica was used. The chromatographic microflow cell used in this study, which has 8-mm path length and 8- $\mu$ L volume, is similar to that used previously [16].

Shown in Fig 7 is the three dimensional graph plotting the chromatogram as a function of time and wavelength of a sample which was a mixture of three phenol derivatives, i.e., 4-chloro-, trichloro- and pentachlorophenol. The chromatogram as a function of time was obtained by setting the AOTF at a single wavelength of 292 nm. Absorption spectrum of each compound was measured as it eluted out of the column by rapidly scanning the AOTF. Each single spectrum was obtained by scanning the AOTF for 100 nm (from 250 nm to 350 nm) and recording 100 points (i.e., 1 point for each nanometer). The setting was selected so that it required 2 ms to record each point. Therefore, the time required to record a single spectrum is 200 ms, and it took 4 s to obtain the spectrum which is the average of 20 spectra for each compound. However, as evident from the figures, only 60 nm (i.e., from 260 nm to 320 nm) is required to record the whole spectrum for all three compounds. Therefore, with the optimal setting of 300  $\mu$ s time constant, 12 dB rolloff, and 2 ms/pt (on the lock-in amplifier), it requires only 900 ms to obtain an average of 5 spectra which has relatively good S/N.

The calibration curve was constructed for each compound over a concentration range of  $1.0 \times 10^{-4}$  M to  $2.0 \times 10^{-3}$  M using the data obtained when the AOTF was fixed at a single wavelength corresponding to the peak of the absorption spectrum of each compound, i.e., 285, 300 and 306 nm for 4-chloro-, trichloro- and pentachlorophenol, respectively. As expected, good linear relationship was obtained for all three compounds (the correlation coefficients for all three compounds were larger than 0.999). The limits of detection (LODs) defined as twice the peak-to-peak noise of the baseline divided by the slope of the calibration graph, are estimated to be  $1.0 \times 10^{-5}$ ,  $1.1 \times 10^{-5}$  and  $1.7 \times 10^{-5}$  M for trichloro-, pentachloro- and 4-chlorophenol, respectively. These LOD values correspond to the mass detectivity of 59, 88 and 65 ng, respectively, and to the absorbance unit of  $4.0 \times 10^{-4}$ . These detection limit are comparable with those found on commercially available (grating or filter based) single wavelength absorption detectors. Particularly, its detectability of  $4.0 \times 10^{-4}$  absorption unit is similar to the value of  $3.9 \times 10^{-4}$  absorbance unit which we have previously determined for 4-chlorophenol using the Shimadzu model SPD-6AV UV-visible absorption detector [16]. The LOD value of  $4.0 \times 10^{-4}$  AU is much smaller than those obtained using commercially available diode array detectors [28]. This is as expected because the present AOTF based detector is a single channel detection technique which is more sensitive than the multichannel detection employed in the diode array detectors. Furthermore, the light source used in this AOTF based detector is modulated at 50 kHz (through modulating the applied RF signal) which facilitates the phase lock detection. The S/N is further enhanced by this phase sensitive detection. Other feature which makes this AOTF-based detector more desirable than diode array detectors is its high spectral resolution. Specifically, the resolution of this AOTF-based detector is less than one angstrom at 253 nm. This spectral resolution is

much smaller than those of the DAD which are generally on the order of several nanometers [12].

### 3. 2. AOTF based Detectors for Flow Injection Analysis

Flow injection analysis (FIA) is among the most widely used methods for automated analysis. Its applications to several fields of chemistry has been demonstrated in recent years. [29,30]. Several operational modes of FIA have been realized by appropriately modifying traditional wet chemical methods (dilution, extraction, titration, fast kinetic reactions) into automated flow devices [13,14]. Different types of detectors, including electrochemical, (UV and visible) spectrophotometric, and luminescent, have been applied to the FIA. [29,30]. However, there has not been a FIA detector which is truly universal.

As described in previous section, spectrochemical applications of the near infrared absorption technique (NIR) has increased significantly in recent years [15]. The popularity stems from advantages of the technique including the wide applicability (all compounds that have C-H, O-H and/or N-H groups have absorption in this spectral region), the possibility of in situ applications (no need for sample pretreatment) and the availability of powerful and effective multivariate statistical methods for data analysis. These features enable the NIR to serve as a universal detector for FIA. However, the detection of FIA by NIR has not been fully exploited. In fact, in there are only two reports describing the utilization of NIR for continuous-flow FIA detection [31,32]. Unfortunately, in these studies, the potentials of the NIR technique have not been fully exploited because they were based on the use of only a single wavelength [31,32]. As a consequence, the multivariate calibration methods cannot be used to analyze data in these studies. This drawback can be overcome by use of an AOTF based NIR detector.

The construction of the AOTF based NIR detector for FIA, shown in Figure 8, is essentially the same as that of the AOTF based UV-visible detector for HPLC which was described above. The only differences were those of the light source (a 100 W, 12 V halogen tungsten lamp), the AOTF for the NIR region, and a the detector (InGaAs photodiodes)

This AOTF based detector covers a near IR region from 1000 to 1600 nm. Because the combination and overtone absorption bands of O-H and C-H groups are in this region, this FIA-AOTF detector can be used for such determinations as water in chloroform, and water and benzene in ethanol. For example, Figure 9 shows the FIA absorption peak profile (i.e., absorption spectrum as a function of time and wavelength), obtained when a solution of 0.10% (v:v) water was injected into chloroform. It is evident that as the concentration of water in the flow cell increases, there is an increase in the absorption in the 1300 - 1500 nm region. This can be attributed to the first overtone transition, and the combination of stretching and bending of the O-H group at 1450 and 1180 nm, respectively [17]. The absorption reaches its maximum 12 seconds after the injection and then starts to decrease. Using the spectra measured 12 seconds after the

injection for different concentrations of water a calibration model based on the partial least square method (PLS) was developed for the determination of water in chloroform. Good correlation was obtained between the concentration of water injected and the concentration of water calculated by the model ( $r = 0.99$ ). The RMSD for this determination was calculated to be 0.002 %. The LOD at 1400 nm was found to be 15 ppm of water.

It is possible to sensitively and simultaneously determine the concentrations of water and benzene in ethanol by NIR spectrometry. Figure 10 shows the absorption measured as a function of time and wavelength after the injection of sample containing 0.6 and 1.5 % of water and benzene respectively. As can be seen from the figure, when the sample is passing through the detector between 8 to 26 seconds there is an increase in the absorption in the 1650-1700 nm and 1390-1500 nm regions (due to absorption of benzene and water, respectively) and a decrease in the 1500-1650 nm region (due to benzene). These spectral profiles are the same to those observed in the previous measurements using the non-flowing 1-cm cuvette (figure not shown). In order to produce a calibration model for the simultaneous determination of benzene and water in ethanol using NIR-FIA technique, 21 samples containing different concentrations of water and benzene were prepared. Each sample was injected four times. Good correlation was obtained between the concentration of water and benzene injected and the concentration of both components calculated by the PLS model (SR = 1450-1496 nm, 1672-1700 nm, 1583-1602 nm; NF = 4 and 3 for water and benzene respectively). The statistical parameters obtained were  $r = 0.997$  and RMSD = 0.015 % and  $r = 0.997$  and RMSD = 0.033 % for water and benzene respectively.

In summary, it has been demonstrated that due to its high scanning velocity and wavelength accuracy the AOTF based detector for FIA can measure whole NIR spectra of flowing samples within the time frame required for flow analysis. This allowed the utilization of multivariate statistical methods of analysis, which in turn, increase the sensitivity, accuracy and applicability of the technique. In fact it was possible to perform not only a simple analysis, such as the determination of dryness of organic solvent (i.e., the concentration of water in chloroform) but also a more complex analysis including the simultaneous determination of two component systems (i.e., the concentration of water and benzene in ethanol). For simple one component systems, the LOD of this AOTF-NIR-FIA technique is comparable to that of the FIA spectrophotometry as well as to that of the single wavelength NIR-FIA technique. In this case the advantages of the AOTF-NIR-FIA instrumentation are its sensitivity, automation and wide applicability.

For relatively more complex systems (e.g., two component systems) the advantages become more prevalent. In fact, there is not a method currently available that can be easily coupled with FIA instrument for the sensitive and simultaneous determination of the concentrations of two or more components without any sample pretreatment. The present automated and real-time determination of water and benzene in ethanol is important because ethanol is increasingly being used as a substitute and/or additive to gasoline (i.e., it is important to know the concentrations of water and benzene impurities

in such systems).

### **Acknowledgment**

The author wishes to thank his present and former coworkers, whose work is cited in the references. Acknowledgment is made to the National Institutes of Health for financial support of this work.

## REFERENCES

1. C. D. Tran, *Anal. Chem.* **64** (1992) 971A-981A
2. C. D. Tran and R. J. Furlan, *Anal. Chem.* **64**(1992) 2775-2782.
3. C. D. Tran and R. J. Furlan, *Anal. Chem.* **65**(1993) 1675-1681.
4. C. D. Tran and V. Simianu, *Anal. Chem.* **64** (1992) 1419-1425.
5. C. D. Tran and J. Lu, *Anal. Chim. Acta*, **314** (1995) 57-66.
6. M. J. Politi, C. D. Tran and G. H. Gao, *J. Phys. Chem.* **99** (1995) 14137-14141.
7. M. S. Baptista, C. D. Tran and G. H. Gao, *Anal. Chem.* **68** (1996) 971-976.
8. C. D. Tran and G. H. Gao, *Anal. Chem.* **68** (1996) 2264-2269
9. C. Pasquini, J. Lu, C. D. Tran and S. Smirnov, *Anal. Chim. Acta* **319** (1996) 315-324.
10. I. M. Warner, G. Patonay and M. P. Thomas, *Anal. Chem.* **57**, 463A (1985).
11. T. T. Ndou and I. M. Warner, *Chem. Rev.* **91**, 493 (1991).
12. C. D. Tran, "Analytical Thermal Lens Spectrometry: Past, Present and Future Prospects" in "Photoacoustic and Photothermal Phenomena III", Diane Bicanic Ed., Springer-Verlag, pp 463-473 (1992).
13. M. Franko and C. D. Tran, *Rev. Sci. Instrum.* **67** (1996) 1-18.
14. C. D. Tran and V. I. Grishko, *Appl. Spectrosc.* **48** (1994) 96-100.
15. C. D. Tran and V. I. Grishko, *Anal. Biochem.* **218** (1994) 197-203.
16. C. D. Tran, G. Huang and V. I. Grishko, *Anal. Chim Acta*, **299** (1994) 361-369.
17. C. D. Tran, V. I. Grishko and M. S. Baptista, *Appl. Spectrosc.* **48**, (1994) 833-842.
18. C. D. Tran, R. J. Furlan and J. Lu, *Appl. Spectrosc.* **48** (1994) 101-106.
19. L. Murray, L. A. Cowe, "Making Ligth Work: Advances in Near Infrared Spectroscopy"; VCH Publishing: New York, 1992.
20. K. L. Hildrum, T. Isaksson, T. Naes and A. Tandberg, "Near Infra-Red Spectroscopy, Bridging the Gap between Data Analysis and NIR Applications"; Ellis Horwood: Chichester, 1992, chapter 23.
21. D. A. Burns and E. W. Ciurczak, "Handbook of Near-Infrared Analysis"; Marcel Dekker: New York, 1992, chapter 3.
22. G. Patonay, "Advances in Near-Infrared Measurements"; JAI Press: Greenwich, Connecticut, 1993
23. L. G. Weyer, *Appl. Spectrosc.Rev.*, **21** (1985) 1-43.
24. G. Patonay and M. D. Antoine, *Anal. Chem.* **63** (1991) 321A-327A.
25. T. Imasaka and N. Ishibashi, *Anal. Chem.* **62** (1990) 363A-371A.
26. A. Bjarklev, "Optical Fiber Amplifiers: Design and System Applications"; Artech House: Boston, 1993.
27. E. Desurvire, "Erbium-Doped Fiber Amplifiers Principles and Applications"; John Wiley: New York, 1994.
28. L. Huber and S. A. George, "Diode Array Detection in HPLC", Marcel Dekker, Inc., New York, 1993.
29. Z. Fang, "Flow Injection Separation and Preconcentration", VCH Press, New York, 1993.
30. J. Ruzicka and E. H. Hansen, "Flow Injection Analysis", 2nd ed., Wiley, New

York, 1988.

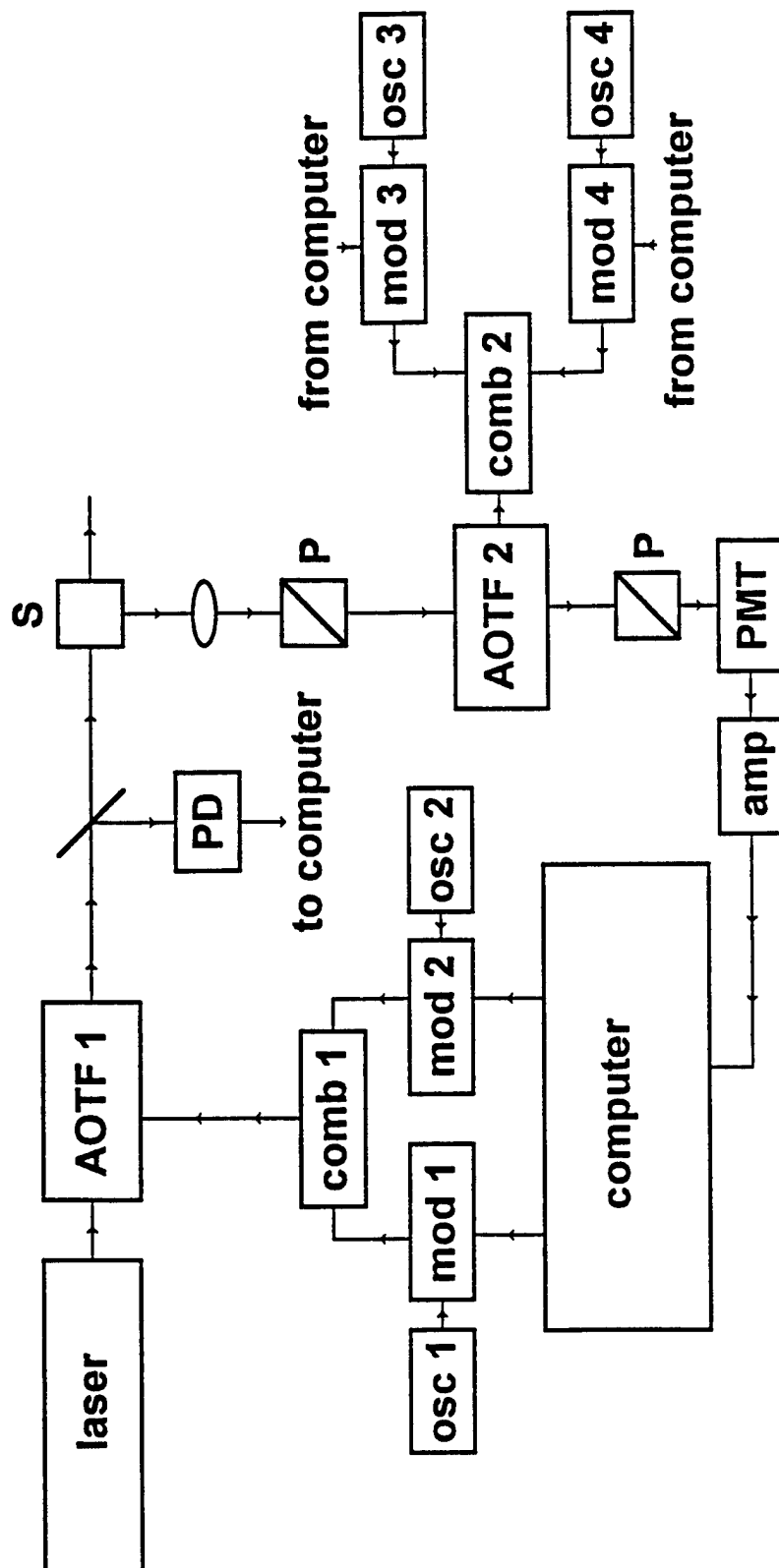
31. E. L. Anreus, S. Garrigues and M. Guardia, *Fresenius J. Anal. Chem.* **351** (1995) 724-728.
32. S. Garrigues, M. Gallignani and M. Guardia, *Anal. Chim. Acta* **351** (1993) 259-264.

## FIGURE LEGENDS

- Figure 1.** Schematic diagram of the AOTF based fluorimeter: PD, photodiode; S, sample; P, polarizer; PMT, photomultiplier tube; amp, amplifier; osc, oscillator; mod, modulator; comb, combiner.
- Figure 2.** Schematic diagram of the multiwavelength thermal lens spectrometer based on an AOTF as a polychromator: amp, rf power amplifier; osc, oscillator; mod, sinusoidal modulator; PIN, photodiode; F, interference filter; Ph, pinhole.
- Figure 3.** Schematic diagram of the near infrared spectrophotometer based on the use of the EDFA as a light source and AOTF as a dispersive element: EDFA, erbium doped fiber amplifier; P, polarizer; AOTF, acousto-optic tunable filter; PH, pinhole; BS, beamsplitter; L, lens; RF amp, RF power amplifier; Rf gen, RF generator; InGaAs, detector. *Insert:* Schematic diagram of the erbium-doped fiber amplifier system: LD, laser diode; WDM, wavelength division multiplexer.
- Figure 4.** Relative intensity of the light transmitted through six sheets of paper, measured with a 250 W halogen tungsten lamp based spectrophotometer (-----), and with the EDFA based spectrophotometer (————).
- Figure 5.** Relative intensity of the light transmitted through four sheets of paper and 1.0 M solution of  $\text{Pr}^{3+}$  in  $\text{D}_2\text{O}$  (in a 2-mm pathlength cell), measured with a 250-W halogen tungsten lamp based spectrophotometer (— — — —), and with the EDFA based spectrophotometer (————). *Insert:* spectra of the same sample plotted as absorption spectra.
- Figure 6.** Schematic diagram of the AOTF based detector for HPLC: PMT, photomultiplier tube; lock-in, lock-in amplifier; rf, rf power amplifier; rf gen, rf signal generator.
- Figure 7.** Three dimensional graph plotting the chromatogram of mixture of pentachloro-, trichloro- and 4-chlorophenol as a function of time and wavelength.
- Figure 8.** Near-infrared-FIA instrument: W, waste; C, carrier; Pump, peristaltic pump; S, sample; I, injector; T, T connector; FC, flow cell; Ph, pinhole; Po, polarizer; L, lens; BS, beamsplitter.
- Figure 9.** Absorption (flow cell using chloroform as blank) as a function of time and wavelength after the injection of 0.10% (v/v) water solution in chloroform.
- Figure 10.** Absorption (flow cell using ethanol as blank) as a function of time and



wavelength measured after the injection of ethanol solution containing 0.6% and 1.5% (v/v) of water and benzene, respectively.



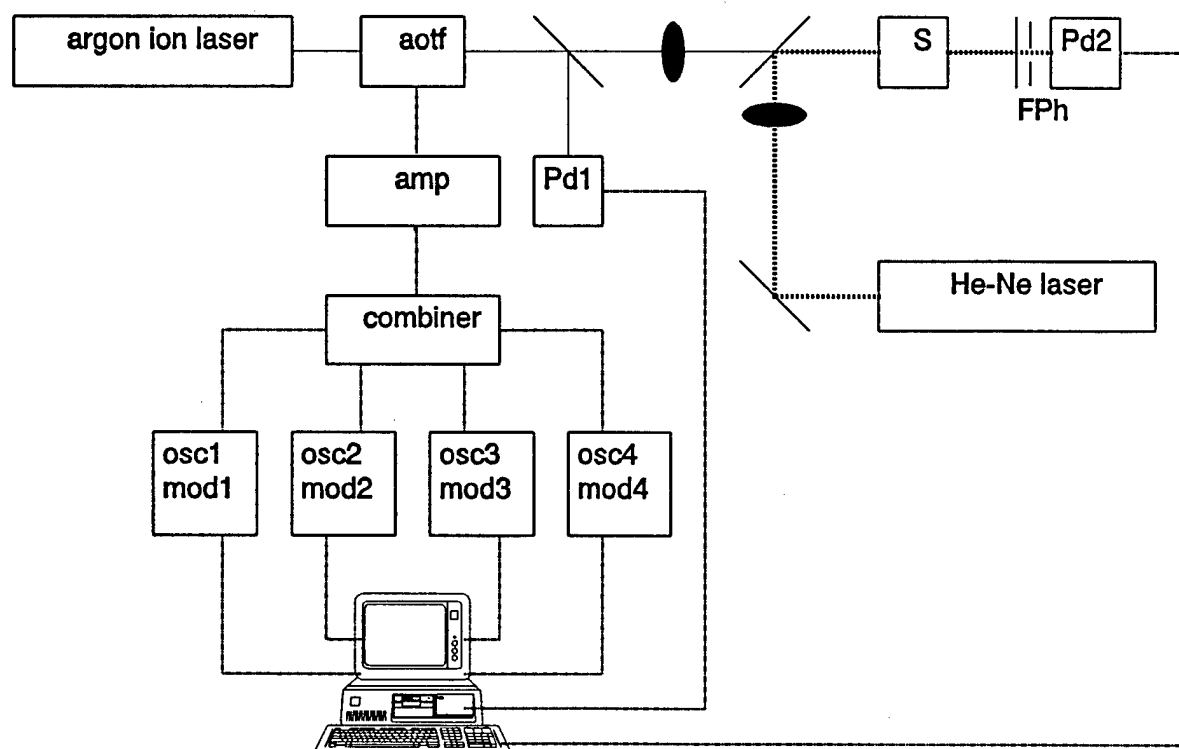


Fig 2

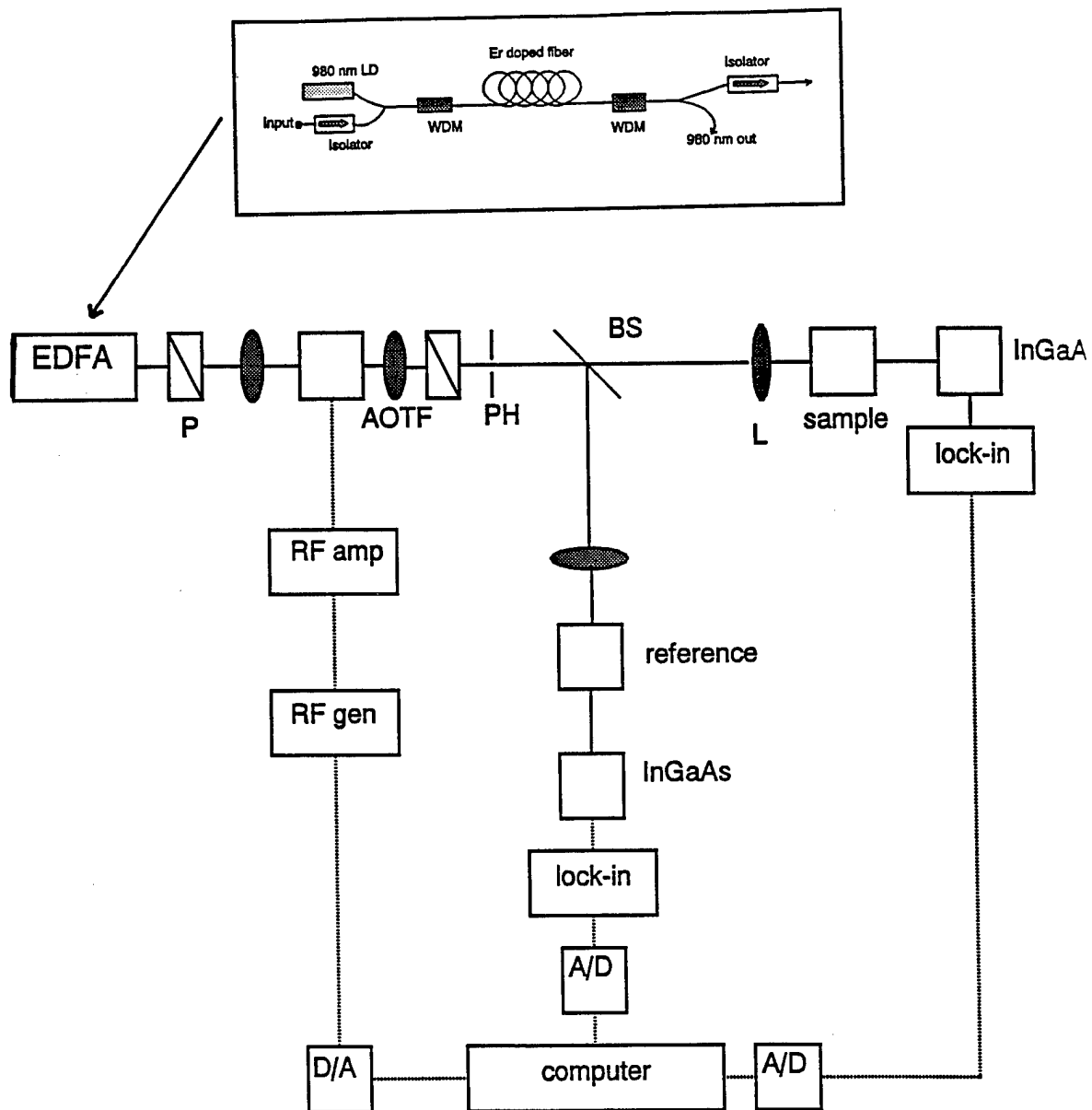


Fig 3

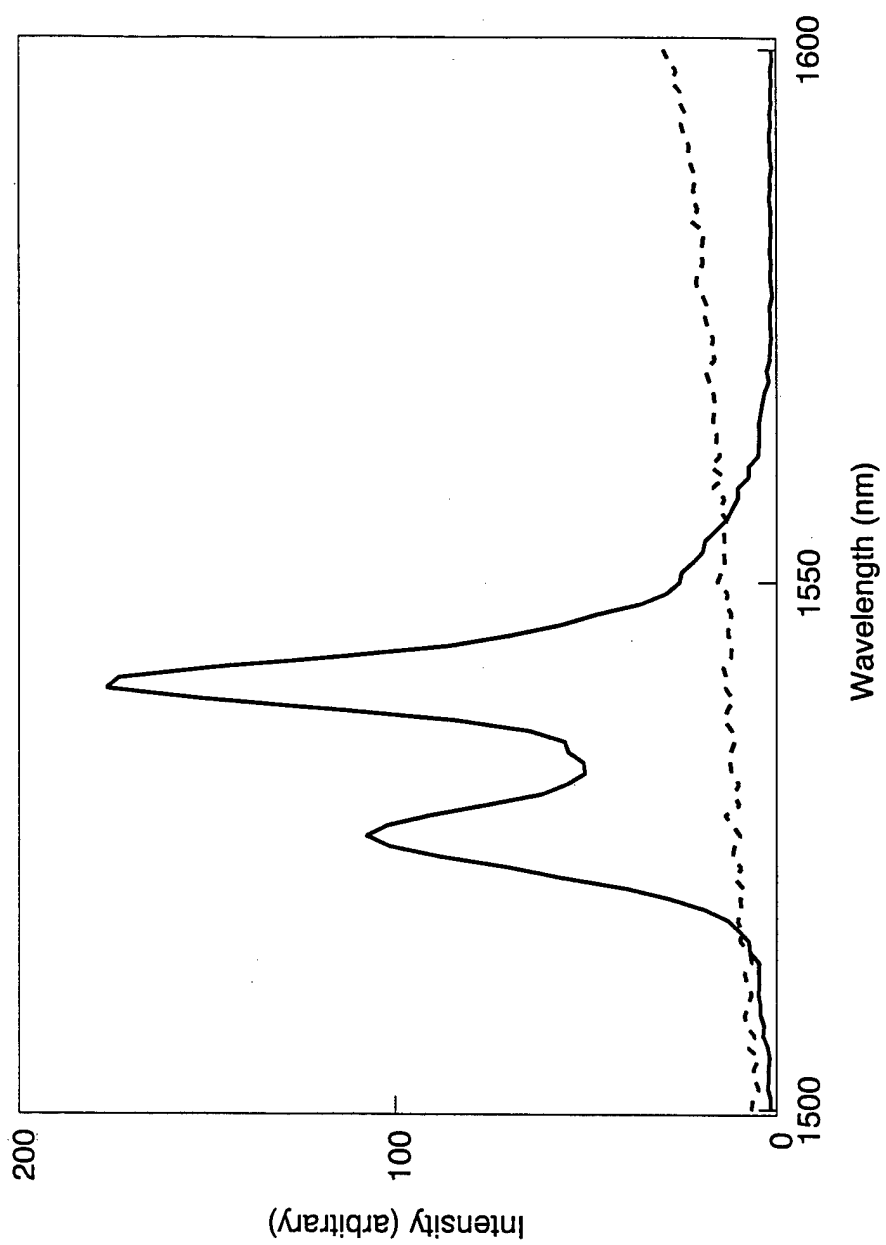


Fig 4

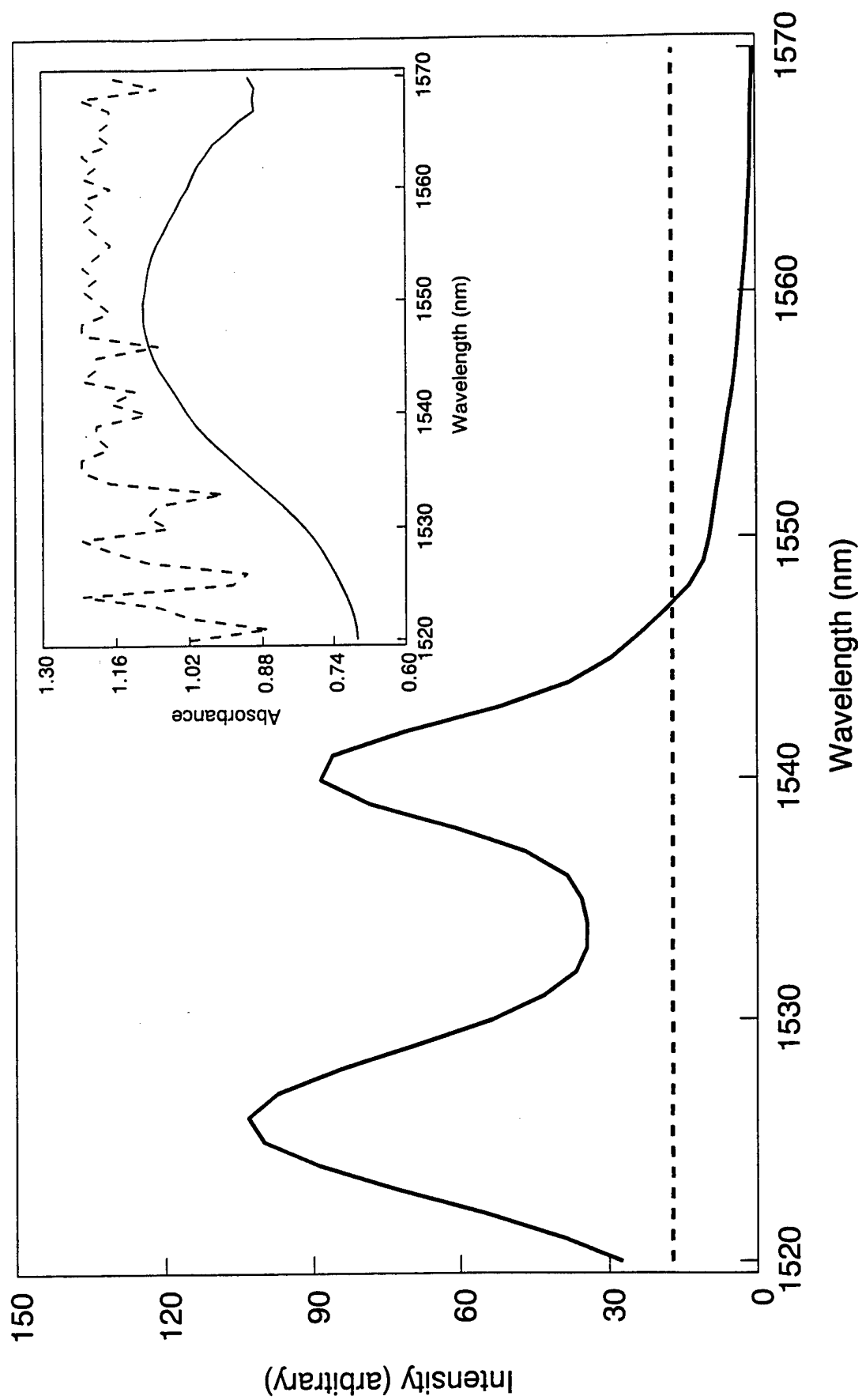


Fig 5

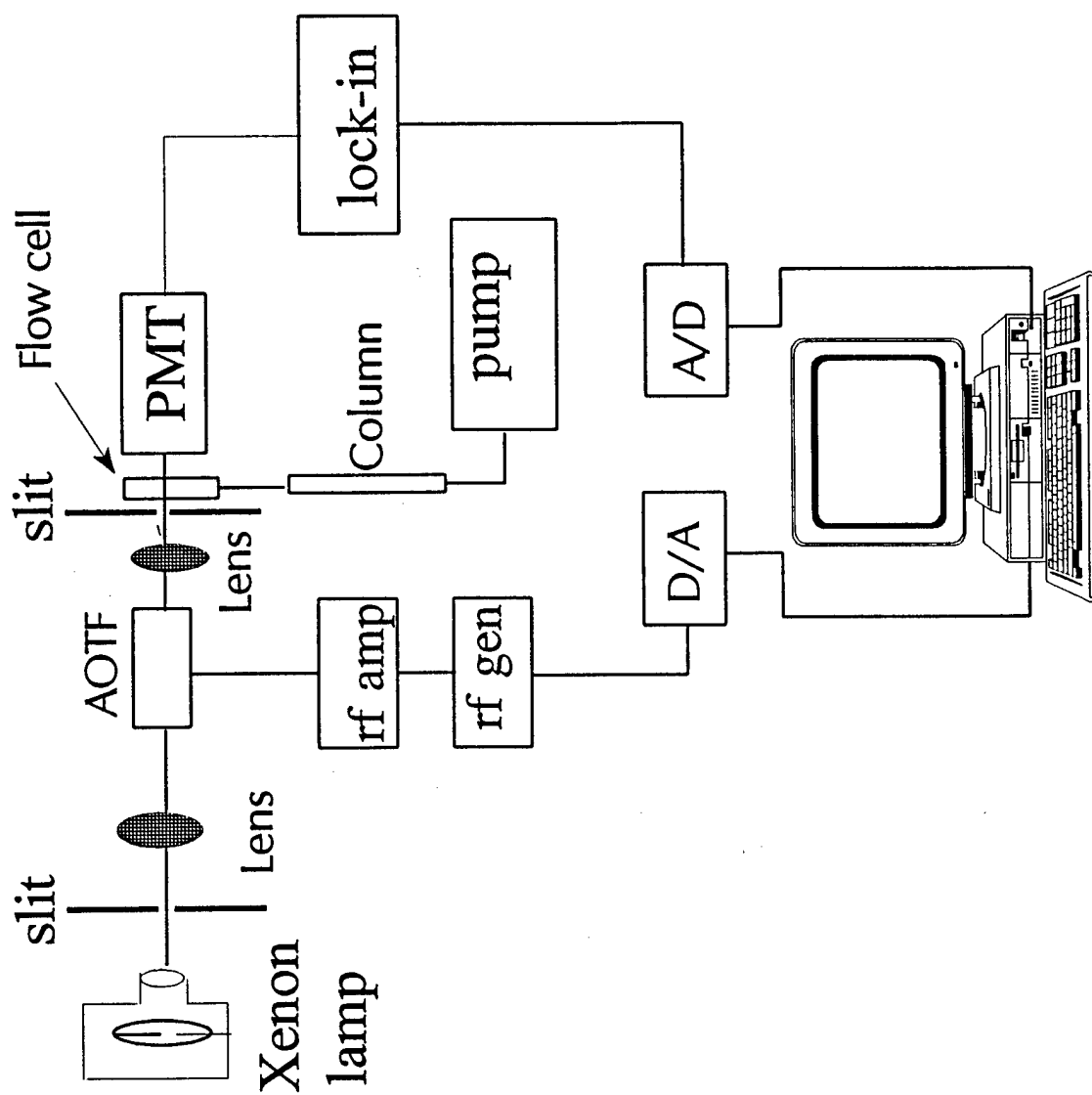


Fig 6

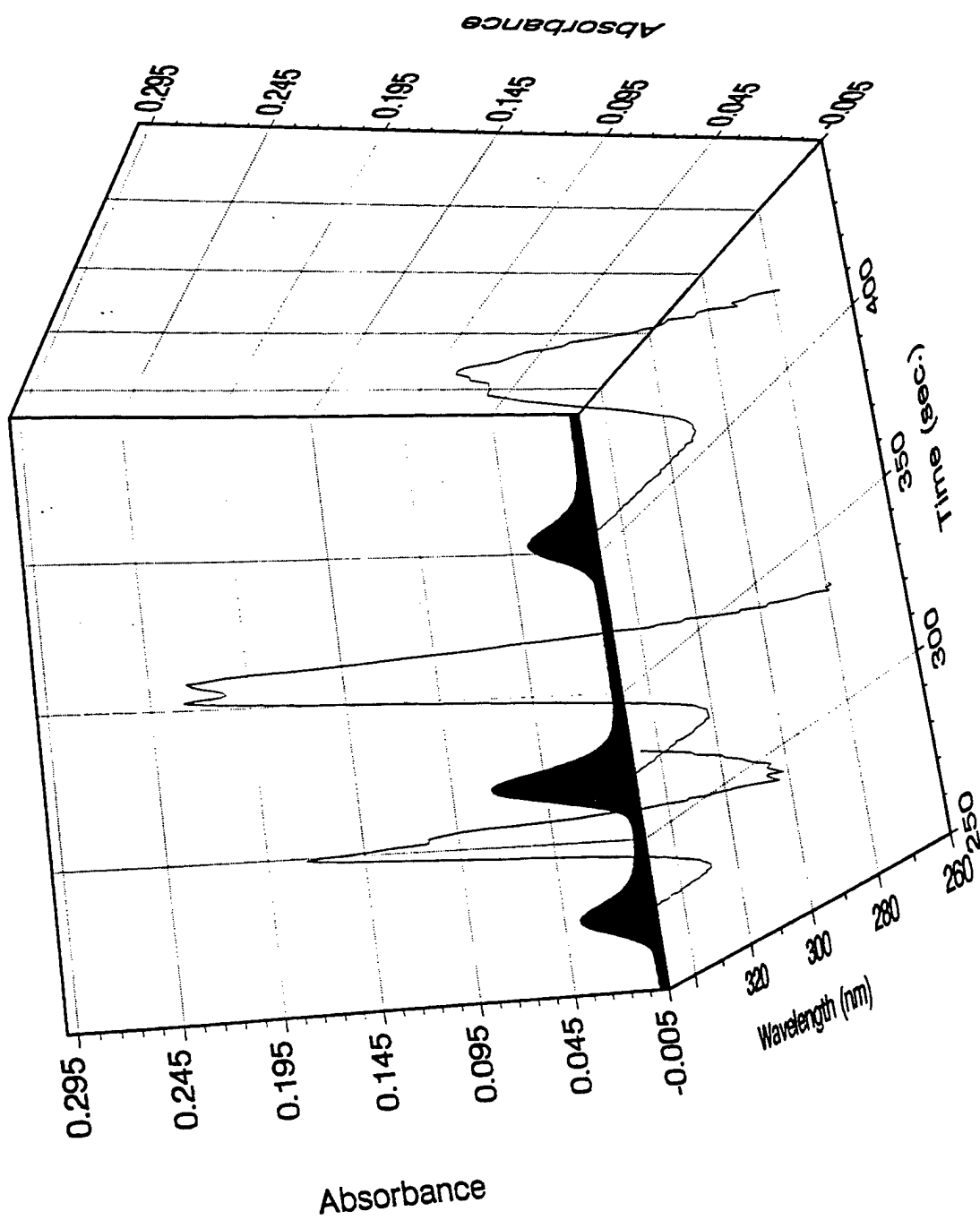


Fig 7



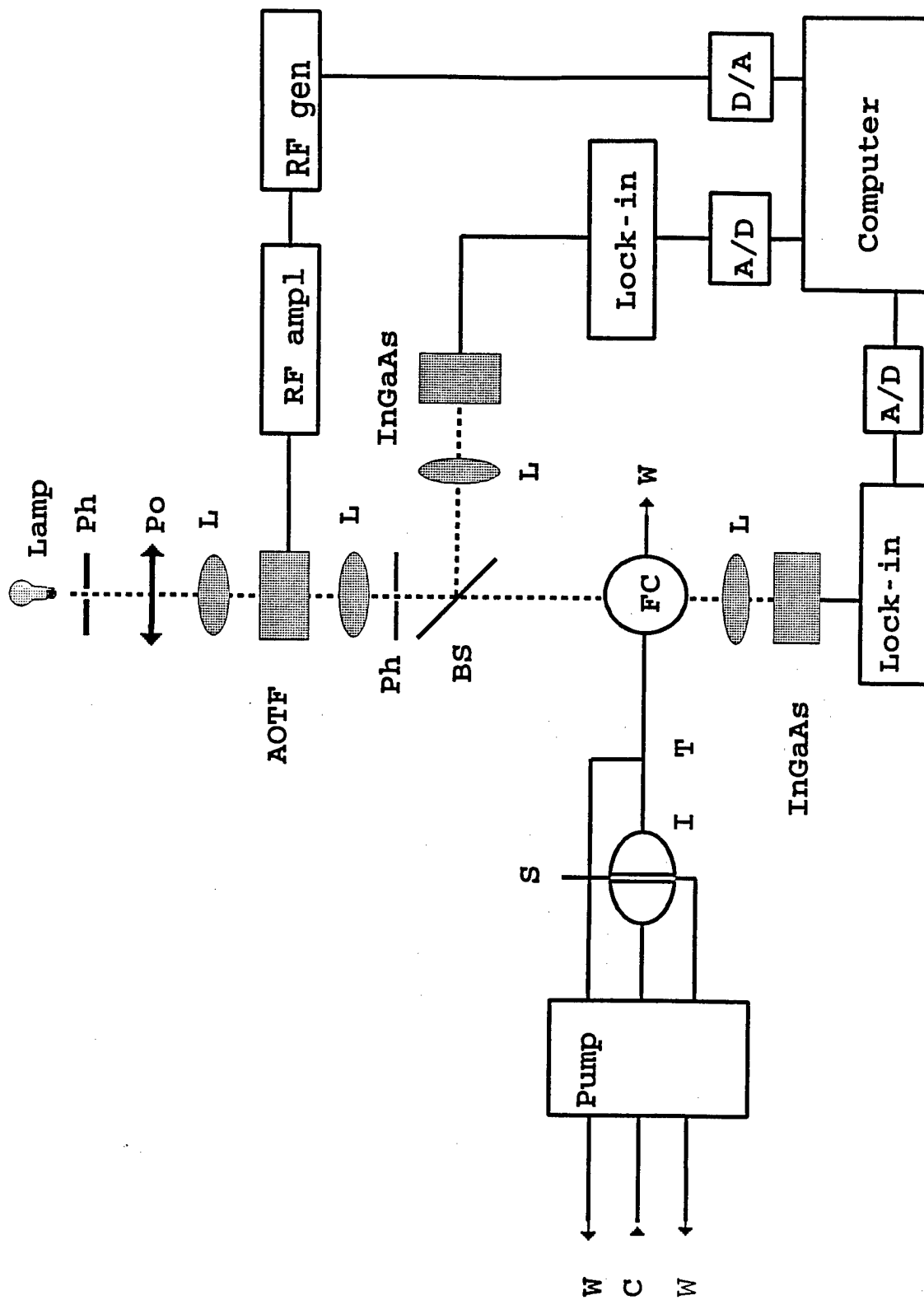


Fig 8

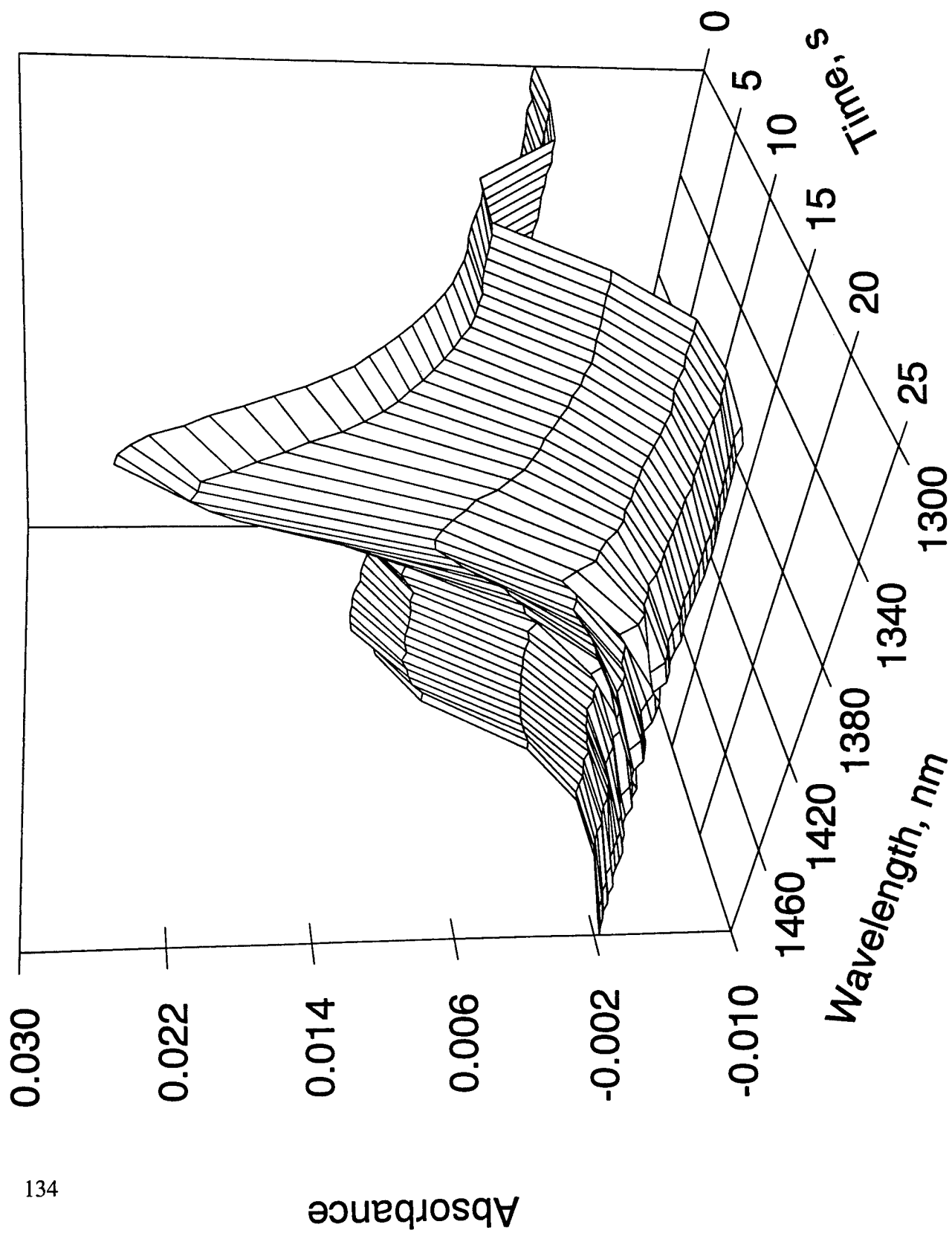


Fig 9

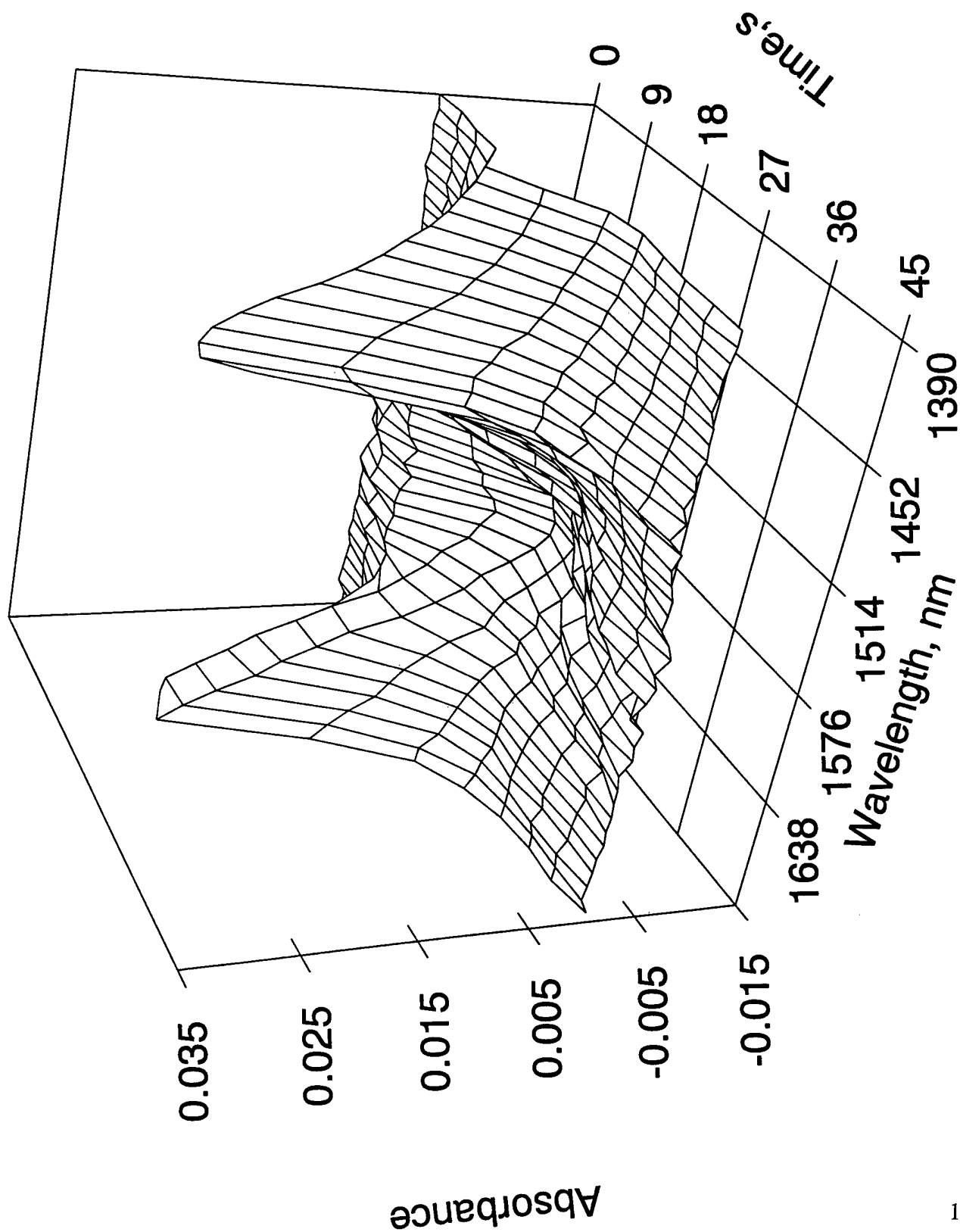


Fig 10

# Application of AOTF Technology for Chem/Bio Detection

Neelam Gupta and N. F. Fell, Jr.

*Sensors and Electron Devices Directorate*

*Army Research Laboratory*

*2800 Powder Mill Road*

*Adelphi, MD 20783-1197*

*Phone: (301) 394-2451*

*email:NGupta@arl.mil*

## Abstract

Remote detection and monitoring of chemical and biological agents in the field are extremely important spectroscopic applications that require the development of highly sensitive, ruggedized, low-cost, lightweight, compact, and portable analytical instruments. Acousto-optic tunable-filter (AOTF) technology is a recent development that offers potential for rapid, frequency-agile tuning over a large optical wavelength range; this is all-solid-state technology that can be easily automated with computer control and made ultrasensitive by the use of advanced signal processing algorithms. We are evaluating a number of collinear AOTF spectrometers and cells in our laboratory for application in remote sensing of chemical and biological agents using absorption, fluorescence, and Raman spectral measurements. The spectral range covered is 255–800 nm, with very high resolution; the instruments operate with no external cooling. We detected 40 parts per trillion (ppt) of fluorescein using laser-induced fluorescence (LIF), obtained good Raman signatures from naphthalene, and measured UV-induced fluorescence (UIF) spectra of a bio agent simulant.

## 1. Introduction

An acousto-optic tunable-filter (AOTF) is an electronically tunable phase grating set up in an anisotropic crystal by the propagation of an ultrasonic wave in the crystal. An AOTF functions by scattering light from one linear polarization into the other by resonant coupling of the optical wave with the acoustic wave in the crystal; this coupling is caused by the elasto-optic effect. AOTFs contain no moving parts and offer high-speed wavelength tuning; tuning can be done sequentially or randomly, depending upon the frequency of the applied radio frequency (rf).

The AO interaction in anisotropic crystals was first discovered in 1967 by Dixon [1]. Two years later, Harris and Wallace [2] used this effect to propose the design of a collinear AOTF in lithium niobate ( $\text{LiNbO}_3$ ), and in 1970, the first collinear AOTF in calcium molybdate,  $\text{CaMoO}_4$  was demonstrated [3]. In such a collinear AOTF, the incident light, the acoustic wave, and the diffracted beam all travel in the same direction. A number of different crystals (e.g., quartz,  $\text{LiNbO}_3$ , etc.) with different crystal orientations allow collinear diffraction of light into the orthogonal polarization by propagation of either longitudinal or shear acoustic waves. Chang [4] generalized the concept of the AOTF design by designing a noncollinear AOTF in  $\text{TeO}_2$ , a birefringent crystal, which cannot be used for collinear interaction based on its crystal symmetry; in such a cell, the incident light, the diffracted light, and the acoustic wave do not travel in the same direction.

Performance of AOTFs is primarily limited by the availability of superior materials. To qualify as a candidate for use as an interaction medium for an AOTF, a material must be optically birefringent and transparent in the operating wavelength range of interest, it must have a low acoustic attenuation in the acoustic frequency range of operation, and it must have a large AO figure of merit. Crystal quartz is used to design AOTFs in the spectral range of 255–800 nm (mostly collinear);  $\text{TeO}_2$  is used for 350–4500 nm (noncollinear);  $\text{CaMoO}_4$  is used for 400–4500 nm (collinear);  $\text{LiNbO}_3$  is used for 400–4500 nm (collinear); and so forth. Several excellent review articles are available on AOTF technology in the literature [4–7]. AOTFs are very powerful tools for all kinds of spectroscopic applications, including absorption, emission, fluorescence, Raman, and laser-induced breakdown spectroscopy (LIBS) [8–11]. A number of tellurium dioxide ( $\text{TeO}_2$ ) AOTFs are now commercially available.

As a result of an ongoing collaboration effort, we presently have a number of collinear quartz AOTF cells and spectrometers operating from the UV to near-IR spectral range (255–800 nm) that were fabricated at the Central Bureau of Unique Instrumentation (CBUI) of the Russian Academy of Sciences in Moscow [5]. These instruments are designed primarily for spectral emission and absorption measurements. We are presently using these instruments for laser-induced fluorescence (LIF), Raman [8], and UV-induced fluorescence (UIF) measurements and have obtained very good results. LIF and Raman spectra are very useful for the identification of chemical agents, and UIF is used for detection of biological agents.

### Collinear AOTF Concepts

This section is a brief overview of the concepts underlying collinear AO diffraction in an anisotropic crystal. The acoustic waves are generated by the application of an rf signal to a piezoelectric oscillator (transducer) bonded to the crystal. The incident light is linearly polarized by a polarizer in front of the birefringent crystal medium. As the polarized light passes through the crystal perpendicular to the optic axis, it is diffracted in the same direction by an acoustic wave traveling collinear to the incident optical beam; this diffraction is a result of resonant coupling of the optical wave with the acoustic wave in the crystal, due to the elasto-optic effect. Since the polarization of the diffracted beam is perpendicular to the incident light beam, it can be separated from the incident beam by an analyzer. We can compute the energy and momentum of the diffracted photons using the principles of conservation of energy and momentum. The frequency of the diffracted light is almost the same as the incident light, because the Doppler shift is insignificant. We can write the equation for conservation of momentum to derive a tuning relationship (eq. (2)) between the light wavelength and the applied acoustic frequency for the filter:

$$\kappa_{\text{diff}} = \kappa_{\text{in}} + \mathbf{q}, \quad (1)$$

$$\lambda = (n_o - n_e)v_s/\Omega, \quad (2)$$

where  $\kappa_{\text{diff}}$  and  $\kappa_{\text{in}}$  are the wavevectors of the diffracted and incident light,  $\mathbf{q}$  is the wavevector corresponding to the propagating acoustic wave,  $\lambda$  is the wavelength of light,  $n_o$  and  $n_e$  are the refractive indices of the crystal corresponding to the propagation of light along the ordinary and extraordinary axes, and  $v_s$  and  $\Omega$  are the speed and frequency of the acoustic wave. The band-

width,  $\Delta\lambda$ , of the AOTF is equal to  $\lambda^2/\Delta nL$ , where  $L$  is the length of the AO interaction (same as the length of the crystal), and  $\Delta n$  is the difference of the two refractive indices [4]. The wavenumber bandwidth,  $\Delta k = 1/L\Delta n$ , depends on the wavelength indirectly, because in general the refractive indices vary as a function of the wavelength.

As an example we can calculate the rf frequency range and the corresponding filter bandwidth for a quartz collinear AOTF operating in the spectral wavelength region 400–800 nm. Using  $\Delta n$  equal to 0.009,  $v_s = 5.75 \times 10^5$  cm/sec, and for a 15-cm-long crystal, we can show that the rf frequency range is 130 to 65 MHz, and  $\Delta\lambda$  is 0.12 nm at 400 nm. Neglecting the spectral dependence of the refractive index values,  $\Delta k$  has a value of  $7.4 \text{ cm}^{-1}$  in the entire spectral region of interest.

### 3. Collinear AOTF Spectrometers

All of the experiments described in this paper were performed with either a UV or a visible to near-IR (VNIR) collinear AOTF spectrometer. We have two types of VNIR instruments available: Quartz4 and the new VNIR (from now on, only the new instrument will be referred to as VNIR). The complete spectrometer system consists of two parts: an optical unit and an electronic controller unit. The optical unit consists of a quartz AOTF cell, a set of crossed polarizers with an extinction ratio of 55 dB, input/output lenses, and a photomultiplier tube (PMT). A photograph of the optical unit of the new instrument is shown in figure 1. The optical layout of the spectrometer is shown in figure 2, and the system architecture of the complete system is shown in figure 3.

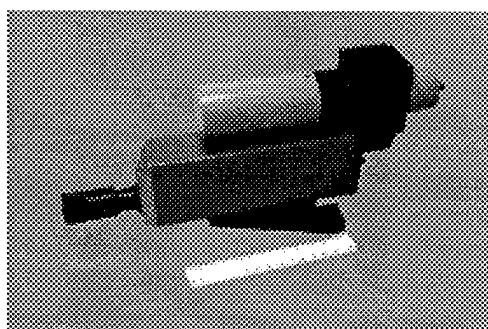


Figure 1. VNIR AOTF spectrometer.

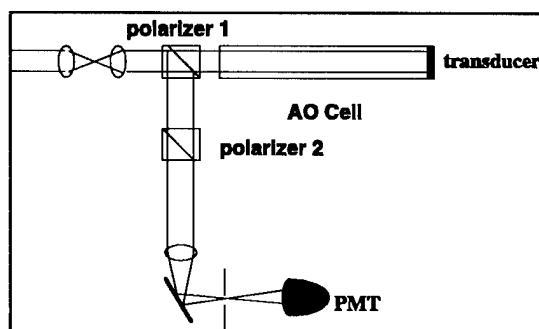
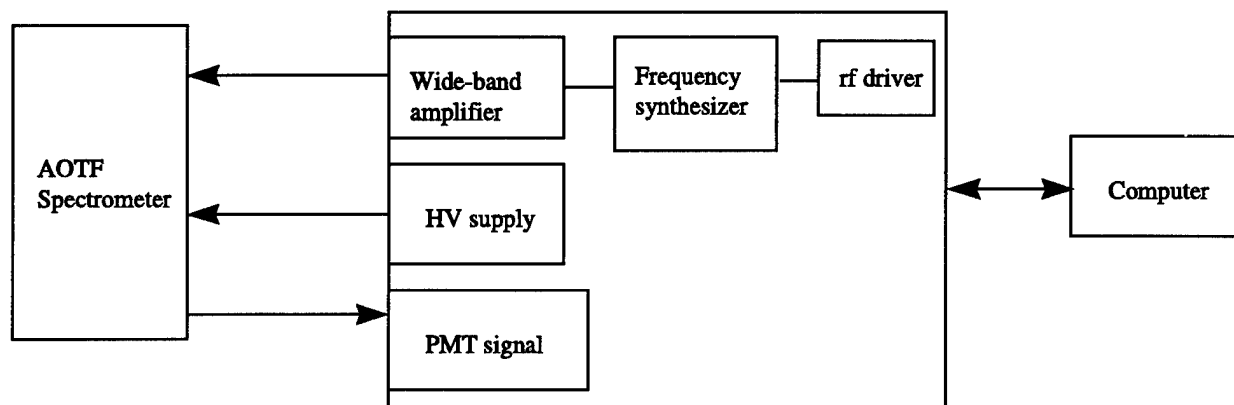


Figure 2. Optical layout of spectrometer.

The Quartz4 spectrometer works from 420–785 nm, it has a separate electronic controller box, and it is controlled from a 386 PC. The electronic controller consists of an rf synthesizer, wide-band rf amplifier, PMT high-voltage power supply, and a signal processing unit for the PMT signals. The computer interface is handled by a PC interface card. This spectrometer has been now completely redesigned and the new spectrometer system has two optical units: the first one works in UV spectral range (255–430 nm) and the second one operates in VNIR range (400–800 nm). Both these units work with the same electronic controller, which resides inside a standard 386 PC tower.



**Figure 3. System architecture of the spectrometer system.**

Some of the important operating specifications for this instrument are listed in table 1. The values for the analog-to-digital converter (ADC), the amplification factor, and the PMT voltage sensitivity are multiplied to define the effective dynamic range for the instrument. The new VNIR instrument is approximately two orders of magnitude more sensitive than the older Quartz4 model. This sensitivity has been achieved by using a novel AOTF cell architecture to minimize undesired acoustic reflections, using the state-of-the-art integrated electronics chips, and using a newly designed PMT. The software is written in C++ and allows the selection of the start and stop wavelengths, the amplification factor, the number of spectra to be accumulated and averaged, the PMT voltage setting, and the number of points to be collected. A spectrum is displayed on the monitor as each data point is taken, and a complete averaged spectrum is displayed at the end of each measurement. Data files can be saved in ASCII format for use with other software.

**Table 1. AOTF spectrometer specifications**

Parameter	Value for Quartz4	Value for VNIR	Value for UV
Spectral range (nm)	420-785	400-800	255-430
Resolution (nm)	0.12-0.5	0.1-0.54	0.05-0.2
Position error (nm)	$\pm 0.5$	$\pm 0.2$	$\pm 0.2$
Maximum # of points	4096	4790	7892
ADC conversion range	10 bits	12 bits	12 bits
Maximum amplification	31	15	15
PMT voltage sensitivity		1:3:9:30	1:3:9:30
Effective dynamic range	45 dB	63 dB	63 dB
Diameter of aperture (mm)	6	10	10
Field-of-view (degrees)	2	2	2

#### 4. Experiment

We first checked the wavelength calibration and resolution of the spectrometers discussed above by measuring the emission spectrum of a mercury pen lamp. Next we carried out LIF, Raman and UIF experiments. The LIF, Raman, and UIF experiments described here used the optical train shown in figure 4. The source of light was either an argon ion laser or a 150-W xenon arc lamp with 260 nm bandpass filter. A pair of mirrors (M) were used to steer the beam to the sample and

a lens (L) was used to focus the excitation beam on the sample. A set of three lenses was used for collecting the scattered photons into the AOTF spectrometer. A holographic Rayleigh rejection filter (HRF) with 60 dB rejection and  $50\text{ cm}^{-1}$  bandwidth was used to reduce the strong Rayleigh-scattered light that entered the AOTF spectrometer in Raman measurements.

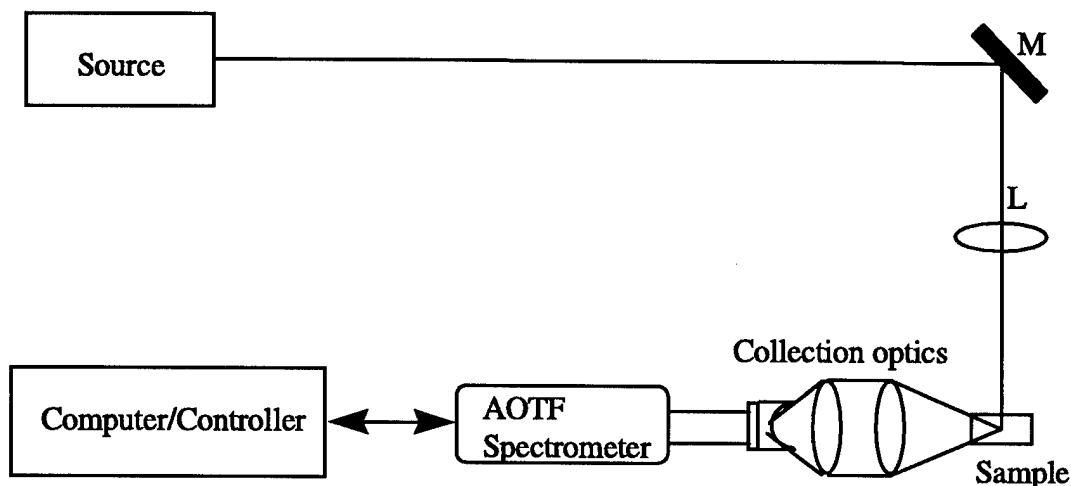


Figure 4. Spectral measurement setup.

Several different samples have been examined in these experiments: fluorescein (Eastman Chemical) solutions in methanol (Sigma Chemical) for measuring the sensitivity of LIF measurements; naphthalene (Matheson, Coleman, & Bell) for Raman measurements; and insecticide containing *Bacillus thuringensis* (BT) (Safer Vegetable Insect Attack Dust, Safer Inc., 0.3% BT content) for UIF.

The wavelength ranges for various experiments were chosen based on the sample involved. In the LIF experiments, the incident wavelength was 488 nm and the measurement range was from 490 to 650 nm with 630 points. In the Raman experiments, the incident wavelength was 514.45 nm and the measurements were taken from 515 to 631.5 nm (or 58 to  $3600\text{ cm}^{-1}$ ) with the 1348 points (maximum available) and scans took approximately 6 minutes for 10 accumulations and 50 minutes for 50 accumulations. The UIF experiments were performed with a scan of the entire UV AOTF range, from 255 to 430 nm, with 1974 points. The VNIR spectrometer was used for LIF and Raman, and the UV spectrometer was used for UIF measurements.

## 5. Results and Discussion

In this section we present the results of our measurements. Figure 5 shows the mercury lamp spectrum from 255 to 800 nm. This spectrum was measured by the UV and VNIR instruments. The spectra taken by the two separate optical heads can be combined in the software and displayed on the same graph. Figure 6 shows the resolution of the two closest spectral lines in the UV range which are 0.65 nm apart.



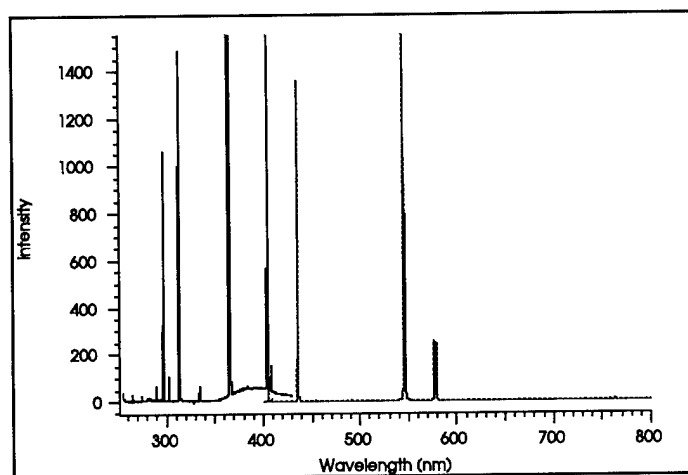


Figure 5. Spectrum of mercury lamp.

In figure 7, the spectrum shown is the sunlight reflected off a white paper, taken by the VNIR spectrometer looking out through an office window. The absorption bands of atmospheric constituents were clearly seen, especially the overtone of the water vibrational absorption at approximately 760 nm.

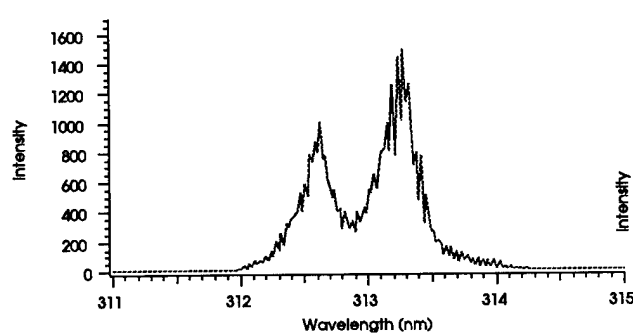


Figure 6. Details of Hg spectrum in the UV.

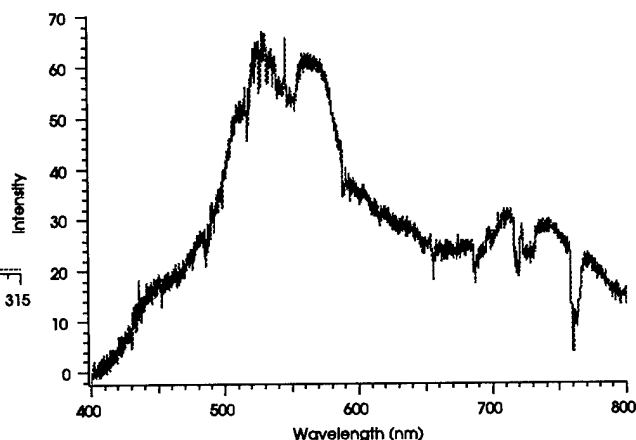


Figure 7. Emission spectrum of the sun through a window.

## 5.1 LIF Measurements

The first LIF measurements were performed with the Quartz4 spectrometer to check the linearity of its amplification factor. Fluorescein solutions in methanol (MeOH) were prepared by serial dilution from a stock solution of  $5.0555 \times 10^{-4}$  M concentration. Dilutions to  $1.0111 \times 10^{-5}$  M,  $1.0111 \times 10^{-6}$  M,  $1.0111 \times 10^{-7}$  M,  $1.0111 \times 10^{-8}$  M,  $1.0111 \times 10^{-9}$  M, and  $1.0111 \times 10^{-10}$  M were prepared in MeOH. A regression analysis of the fluorescein peak height as a function of the amplification factor yielded a correlation coefficient equal to 0.991, indicating an acceptable linearity. The limit of detection (LOD) for fluorescein LIF was  $1.0111 \times 10^{-9}$  M. The LOD was defined as the lowest concentration for which a signal-to-noise (S/N) ratio of at least 3 was obtained. This value could be improved by improving the collection optics used with the system. The concentration was found to be linear from  $10^{-8}$  to  $10^{-5}$  M. The VNIR has two adjustable amplifi-

cation parameters and they were each examined independently. Since the software for the VNIR spectrometer automatically corrects for the amplification factor, spectra collected under the same conditions except for the amplification factor should be identical. The percent relative standard deviation (%RSD) for the peak value for a set of spectra collected from a  $1.0111 \times 10^{-7}$  M fluorescein solution at each of the 15 possible values of the amplification factor was 3.749 %. The correction for the PMT voltage setting is not automatic in the software. Our examination of this sensitivity was performed with a  $1.0111 \times 10^{-7}$  M fluorescein solution, and the experimental results are close to the instrument specification within the margin of experimental error. The concentration dependence of fluorescein fluorescence was also examined from  $5.0555 \times 10^{-4}$  to  $1.0111 \times 10^{-10}$  M. Figure 8 shows the LOD of  $1.0111 \times 10^{-10}$  M fluorescein. The additional peaks at 515 and 526 nm were due to plasma lines from the laser, which were not sufficiently filtered from the incident beam. We have not yet identified the peak at 570 nm. This limit of detection matches that previously reported for uranine, which is another name for fluorescein, using a dual-AOTF system [8]. The spectra here were collected only using the first collimating lens in the optical train shown in figure 4. The spectra obtained from  $1.0111 \times 10^{-5}$  to  $1.0111 \times 10^{-10}$  M are seen in figure 9. The observed fluorescence for the  $5.0555 \times 10^{-10}$  M solution was actually less than that for  $1.0111 \times 10^{-5}$  M, so it was clear that significant self-absorption was occurring. Figure 10 shows a side-by-side comparison of  $1.0111 \times 10^{-7}$  M fluorescein spectra collected under identical conditions in order to compare the two visible AOTFs. It is clear from this comparison and the LODs for the two devices that the VNIR spectrometer is 1 to 2 orders of magnitude more sensitive than the Quartz 4. Table 2 gives a summary of the results discussed.

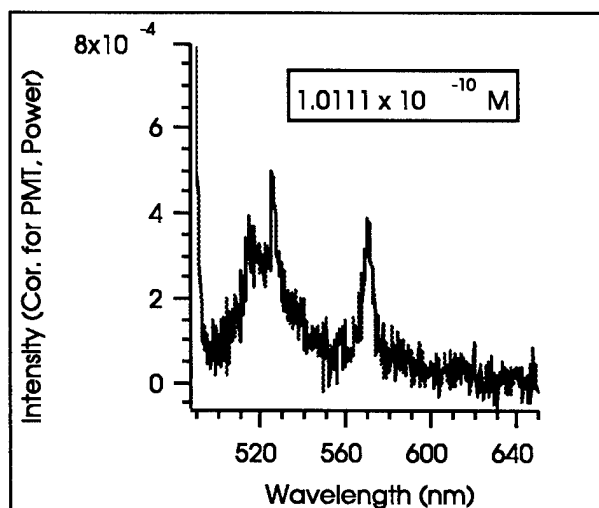


Figure 8. Limit of detection for fluorescein spectrum.

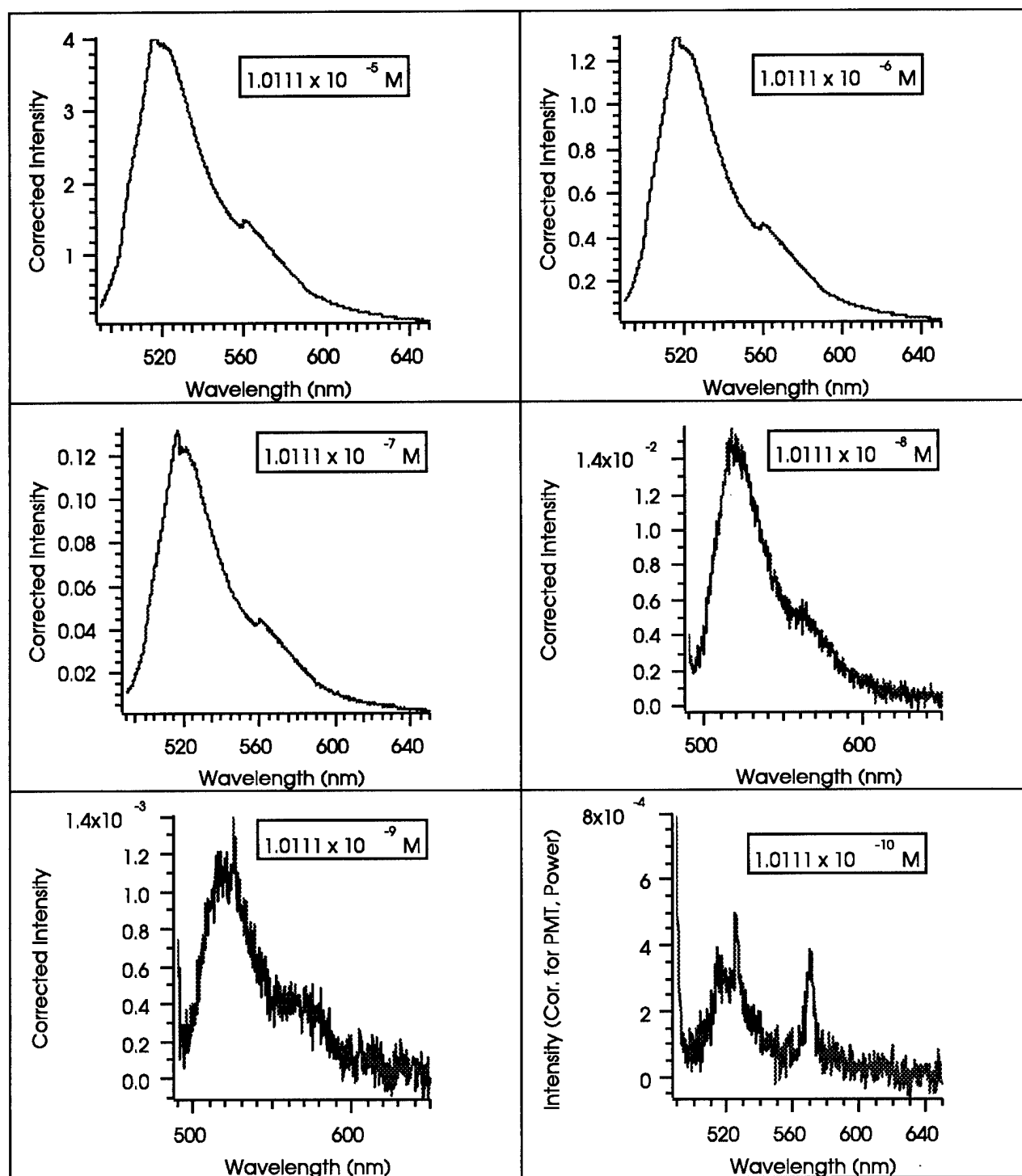


Figure 9. Spectra of fluorescein at different concentrations.

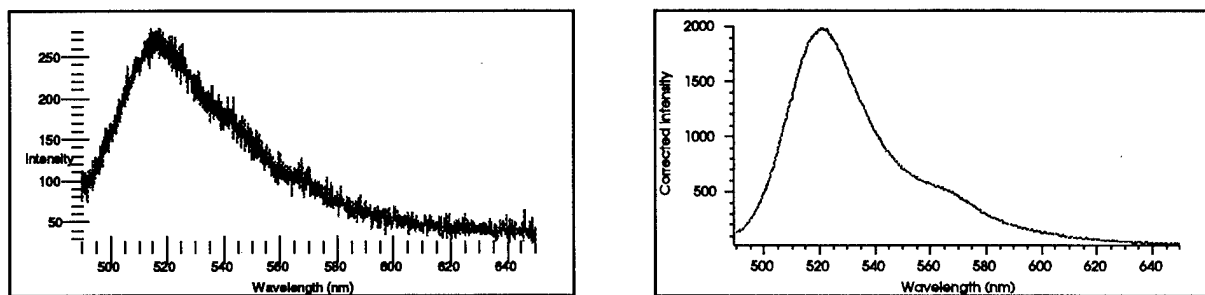


Figure 10. Comparison of spectrum of fluorescein ( $1.0111 \times 10^{-7}$  M) taken by Quartz4 and the new VNIR spectrometers.

Table 2. AOTF Performance Evaluation

Parameter Evaluated		Result for Quartz4	Result for VNIR
Amplification factor linearity		Within experimental error	Within experimental error
PMT setting linearity			Within experimental error
Concentration	Linearity	4.245 to 4245 ppb	0.04245 to 4245 ppb
	Limit of detection	$1 \times 10^{-9}$ M fluorescein	$1 \times 10^{-10}$ M fluorescein

## 5.2 Raman Measurements

The next experiment we conducted was the collection of a Raman spectrum from an organic powder. Naphthalene was chosen for this experiment due to its strong Raman scattering. In figure 11, both the AOTF Raman spectrum and a reference Fourier transform (FT) Raman spectrum are shown for comparison. While the S/N was poorer in the AOTF spectrum, the major peaks were still clearly visible. Data collection time for the AOTF spectrometer was only 6 minutes, compared to 20 minutes for the FTR. Accumulating more spectra would be a simple method to improving S/N ratio, although at the cost of extending the acquisition time. Since the AOTF spectrometer was not designed for Raman measurements, this result is quite impressive.

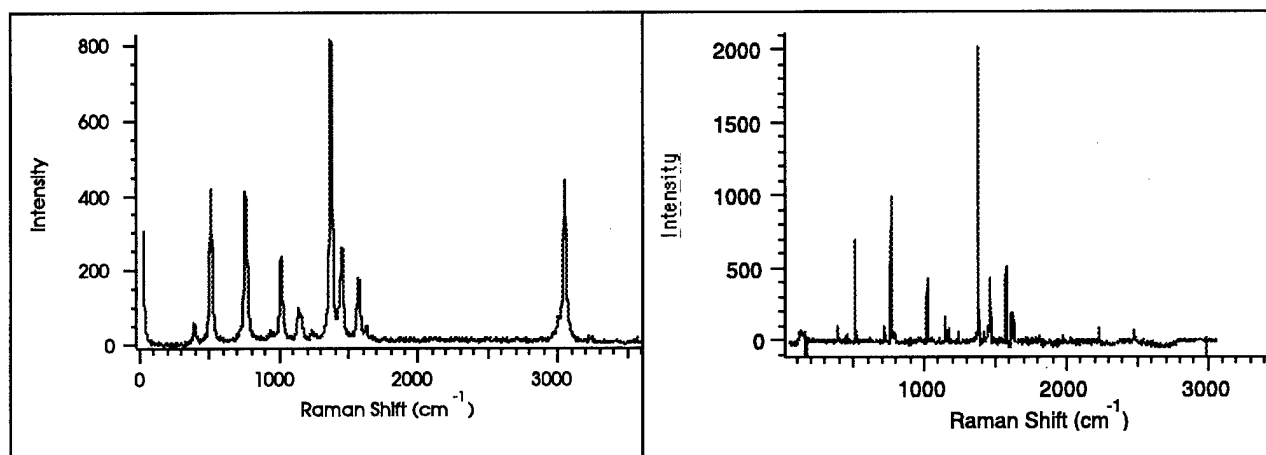


Figure 11. AOTF (left) and FT (right) Raman spectra of naphthalene.

### 5.3 UIF Measurements

Our most recent efforts have been directed at the use of the UV AOTF spectrometer for the detection of biological agents. In these experiments, we have chosen to examine *Bacillus thuringiensis* (BT), a standard biological agent simulant. BT has been used as the active ingredient in some insecticides, and we examined one of these. The fluorescence spectrum of the dry sample is shown in figure 12. The peak at 347 nm was within 15 nm of the reported position of the fluorescence of pure BT; however we are still in the process of determining whether the inert ingredients, which make up 99.7 percent of the insecticide, fluoresce. The fluorescence of bacteria has been shown to be very sensitive to growth conditions and environment, and this may have resulted in the observed shift of the peak position from the expected 330 nm [12].

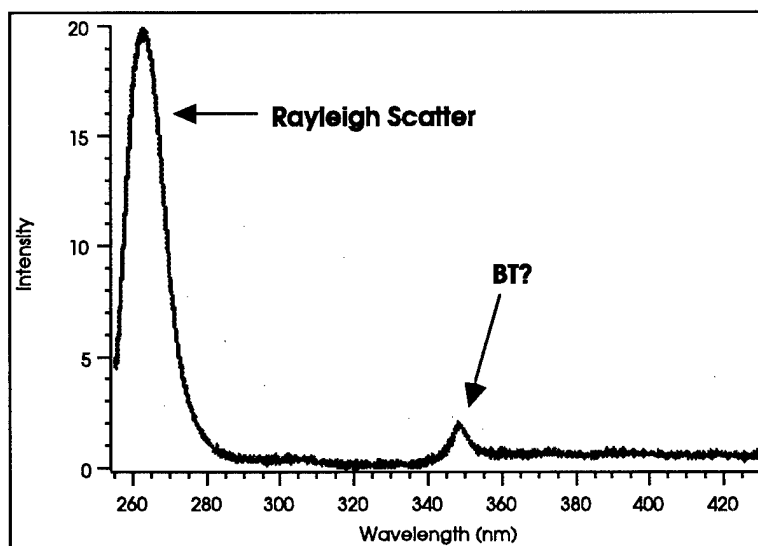


Figure 12. Emission spectrum of BT-containing insecticide.

All the above results clearly illustrate the great advantages in size, time of measurement, cost, and sensitivity offered by these collinear AOTF spectrometers in sensing both the chemical and biological agents in a laboratory setup. The next step would be to use them in some field applications.

### Acknowledgments

The authors would like to thank Prof. V. I. Pustovoit for many useful discussions. This work was performed while one of the authors, N. F. Fell, Jr., held a National Research Council-U.S. Army Research Laboratory research associateship.

### References

1. R. W. Dixon, "Acoustic Diffraction of Light in Anisotropic Media," *IEEE J. Quantum Electron.* **QE-3**, 85-93, 1967.
2. S. E. Harris and R. W. Wallace, "Acousto-Optic Tunable Filter," *J. Opt. Soc. Am.* **59**, 744-747, 1969.
3. S. E. Harris, S. T. K. Nieh, and D. K. Winslow, "CaMoO<sub>4</sub> Electronically Tunable Optical Filter," *Appl. Phys. Lett.* **17**, 223-225, 1970.
4. I. C. Chang, "Acousto-Optic Tunable Filter," *Acousto-Optic Signal Processing Theory and Implementation*, N. J. Berg and J. N. Lee, eds., Marcel Dekker, New York, 139-159, 1983.
5. V. I. Pustovoit and V. E. Pozhar, "Collinear Diffraction of Light by Sound Waves in Crystals: Devices, Applications, New Ideas," *Photonics and Optoelectronics* **2**, 53-69, 1994.
6. M. S. Gottlieb, "Acousto-Optic Tunable Filter," *Design and Fabrication of Acousto-Optic Devices*, A. P. Goutzoulis and D. R. Pepe, eds., Marcel Dekker, New York, 197-283, 1994.
7. C. D. Tran, "Acousto-Optic Devices," *Anal. Chem.* **64**, 971A-981A, 1992.
8. D. H. Hueber, C. L. Stevenson, and T. Vo-Dinh, "Fast Scanning Synchronous Luminescence Spectrometer Based on Acousto-Optic Tunable Filters," *Appl. Spectrosc.* **49**, 1624-1631, 1995.
9. N. Gupta and N. F. Fell, Jr., "A Compact Collinear AOTF Spectrometer for Raman Spectroscopy," submitted for publication in a special issue of *Talanta* on applications of AOTF, 1997.
10. E. N. Lewis, P. J. Treado, and I. W. Levin, "A Miniaturized, No-Moving-Parts Raman Spectrometer," *Appl. Spectrosc.* **47**, 539-543, 1993.
11. P. J. Treado, I. W. Levin, and E. N. Lewis, "High-Fidelity Raman Imaging Spectrometry: A Rapid Method Using an Acousto-Optic Filter," *Appl. Spectrosc.* **46**, 1211-1216, 1992.
12. B. V. Bronk and L. Reinisch, "Variability of Steady-State Bacterial Fluorescence with Respect to Growth Conditions," *Appl. Spectrosc.* **47**, 436-440, 1993..

## Solving Process Problems with AOTF—Based NIR Spectroscopy

Stephen Medlin, Charles Westgate, William Danley, and Ursula Eschenauer, Brimrose Corporation of America, 5020 Campbell Boulevard, Baltimore, MD 21236-4968

### I. Introduction

In today's market, it is essential that plants minimize production costs via maximization of plant efficiency while maintaining product specifications. Without tight control limits, the process plant may have to exceed the target value of the product to ensure that the consumer receives the amount of product listed on the label. By employing tighter specifications, the plant can hit its target more reliably without having to provide this additional, "free," product.

Near-infrared (NIR) spectroscopy is highly suited for the process analysis of chemical species. NIR requires minimal, or no, sample preparation and is a non-destructive technique. The wavelengths used in the NIR region can penetrate significantly through samples. This feature can be exploited to analyze the interiors of samples or to analyze samples through glass bottles or blister packs.

The transitions seen in the NIR region occur from the overtones and combination bands of the fundamental vibrations that occur in the mid-IR region. Since multiple bands occur from the combinations and overtones, peaks with low absorption coefficients can be used to monitor concentrated species while peaks with high coefficients can be used for dilute species. This phenomenon is the basis for NIR advantages such as large dynamic ranges, and the high accuracy and precision resulting from corroborative data. However, the presence of multiple peaks from one vibration transition leads to complex spectra. It was the advent of fast computers and chemometric techniques capable of correlating the rich spectra to the species concentrations that has led to the increase in the application of NIR spectroscopy.

To capitalize on NIR spectroscopy for process-control, several instrumental criteria must be met. The instrument must be able to monitor a rapid process stream (whether it is a flowing stream or vials coming down the assembly line) in real-time. It is also desirable to acquire the complete spectral range to take advantage of the information-rich spectra. This necessitates the use of a rapid wavelength dispersive device that does not sacrifice wavelength accuracy and precision at the expense of rapid scanning. The device must also be compact to fit in the close-fitting quarters of the process line. Finally, the instrument must be insensitive to the vibrations, often intense, that are encountered in an operating plant.

In this paper we describe a NIR spectrometer that uses an acousto-optic tunable filter (AOTF) as the wavelength dispersive device. The basis of the AOTF is that when an RF signal is applied to a birefringent crystal, such as  $\text{TeO}_2$ , incident light can be resolved into its separate wavelengths. Since the AOTF is a solid-state device capable of rapid wavelength selection, the spectrometer is capable of real-time monitoring of analyte concentrations. This rapid monitoring capability provides a control signal to keep the product or process within specification. The wavelength reproducibility and accuracy are extremely high and are not effected by the rapid scanning. This ensures that NIR chemometric models may be used reliably over long periods of time (months to years) without recalibrations. Being a solid state device, the instrument is vibrationally insensitive and can be used in harsh environments such as process plants and streams.

This paper describes the application of a Brimrose Luminar 2010 NIR spectrometer as a process control analyzer. The advantages of an AOTF spectrometer will be described by two different

applications. In the first application, the physical and chemical properties of energetic materials are determined using NIR spectroscopy. In the second, the spectrometer is used for both qualitative analysis of the different constituents in adhesives and for monitoring the kinetics of the reaction to form one of the co-polymers of the adhesive.

## **II. Analysis of M1 Propellants**

### **A. Background**

The U. S. Army produces large quantities of energetic materials that are kept in storage facilities called igloos. While the environmental conditions in the igloos are kept fairly constant, there are sufficient changes during the long storage periods (in terms of years) that may lead to possible changes in the chemical and morphological properties of the propellants. While in the field, these propellants undergo even more dramatic environmental changes. These changes lead to non-uniform performance in the gun systems and effect the projectile ballistics.

The most common propellant for the U. S. Army, comprising ~20% of the inventory, is M1. M1 consists of nitrocellulose (NC), dinitrotoluene (DNT), dibutylphthalate, lead carbonate, and diphenylamine (DPA). Approximately 1% DPA is added to the formulation as a stabilizer to prevent the degradation of NC. Previous studies had indicated that this material was difficult to measure due to the large absorbance coefficient of the propellant grains. Using the AOTF speed advantage, we were able to accumulate a large number of spectra in a short period of time to improve the signal to noise ratio.

### **B. Experimentation:**

M1 samples, artificially aged for varying times (up to 112 days), were analyzed. Chemical analysis indicated that the six sample sets had 1, 0.9, 0.8, 0.7, 0.6, and 0.3 percent DPA. Each propellant grain was approximately 2 cm long by 1 cm diameter with 6 perforations in the center of grain.

A Luminar 2000 NIR Spectrometer was used to collect spectra. A diffuse reflectance probe was connected to the spectrometer via a bifurcated fiber optic bundle. Spectra were collected from 1200 to 2200 nm at 2.0 nm wavelength intervals. The reflectance signal was ratioed to the signal from a matched internal reference detector to correct for any light source fluctuations and a background spectrum of pure NC was used to correct for matrix and optical component absorptions. A representative spectrum, consisting of 500 averages, is shown in Figure 1.

The time require to obtain the spectrum in Figure 1 was about two minutes. This length of averaging was important to compensate for the propellant variations in size and in external color and texture. The bottles were moved on a rotating stage with respect to the probe tip to measure a representative sample of the propellant. Three replicate spectra were measured for each sample except for the 0.3% DPA sample. Since the 0.3% DPA sample consisted of **only** six grains, spectra were obtained by placing two gains on the probe tip at a time.

### **C. Results of the analysis of M1 Propellants**

The absorbance spectral data collected for the various DPA concentrations were imported into Grams/32 (Galactic Industries) and analyzed using the Grams PLSPlus/IQ chemometrics module.



Successful models were generated using two factors to predict the DPA concentration. The first two factor loadings, shown in Figure 2, indicates that there are several peaks in the 1800 to 2200 nm region that are highly correlated to the DPA concentration. Specifically, the peaks from 2130 to 2160 in the first two factor loadings correlate to the two intense peaks of pure DPA [1].

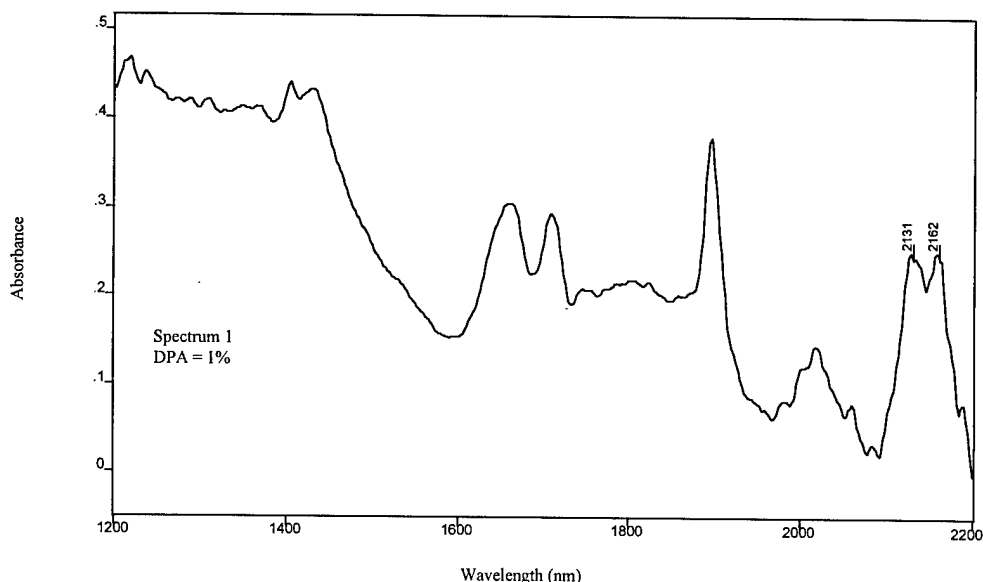


**Figure 1:** Typical spectrum of M1 propellant. Peaks at 2131 and 2162 nm are due primarily to DPA absorption.

Using all of the spectra (including the limited sample of 0.3% DPA) an optimum model was developed with mean centering and variance scaling of the spectra. A standard error of cross-validation (SECV) of 0.0861 and a correlation coefficient ( $R^2$ ) value of 0.8816 were obtained. The calibration line for the best model is shown in Figure 3. As seen in Figure 3, the 0.3% DPA sample was not similar to the other M1 data due to sampling differences of the limited amount of sample.

The model was re-generated with the 0.3% DPA spectra excluded. An SECV of 0.0159 and a  $R^2$  of 0.996 were obtained and the calibration line is shown in Figure 4. This figure shows excellent agreement between the predicted and measured values. The SECV value indicates that we can distinguish differences of  $\pm 0.016\%$  DPA.

#### **D. Propellant Analysis Conclusion**

The results from this study demonstrate that NIR spectroscopy is a powerful technique for characterizing propellants. Because the technique is non-destructive and provides real-time results, propellant analysis is done easily and rapidly. Since the NIR radiation penetrates several millimeters into the grain, the spectra represent the DPA concentration of the total propellant, not just that of the surface, concentration. Since an AOTF wavelength selector is used, the all solid—state nature of the spectrometer ensures solid state reliability and ruggedness. The speed of the AOTF also allowed for many spectra to be averaged in a short time period to obtain high signal to noise data.

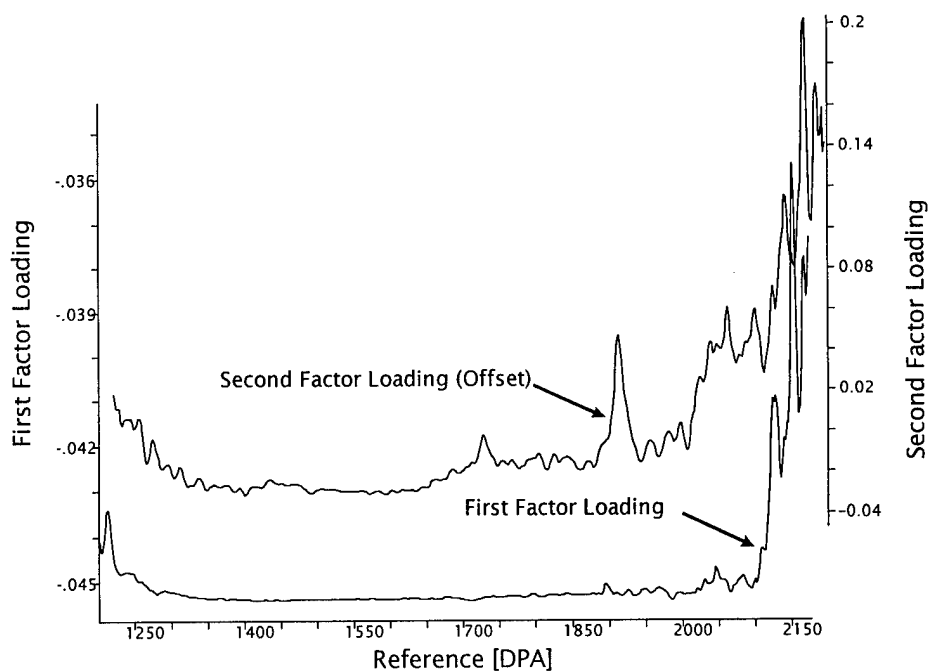


**Figure 2:** First and second factor loadings for the chemometric model to predict DPA concentration. The second factor has been offset for clarity purposes.

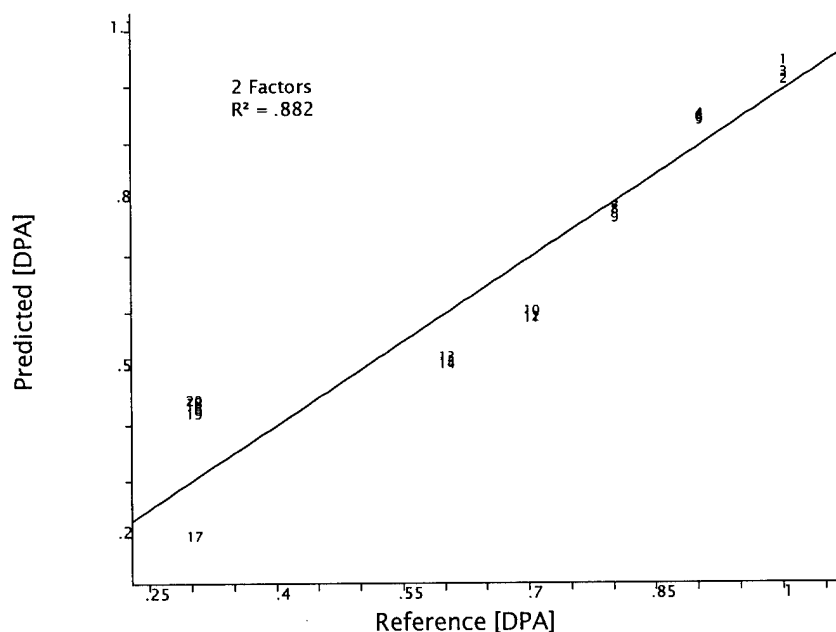


**Figure 3:** Calibration line for DPA using all of the data to develop the model.

### III. Analysis of Adhesives

This application describes a method for the analysis of specialty adhesives. A polyol blend is mixed with toluene-di-isocyanate (TDI) to form a pre-polymer that is used as part of the adhesive. We describe in this report a near-infrared (NIR) spectroscopic technique that provides a means of monitoring the reaction to determine when equilibrium is reached.

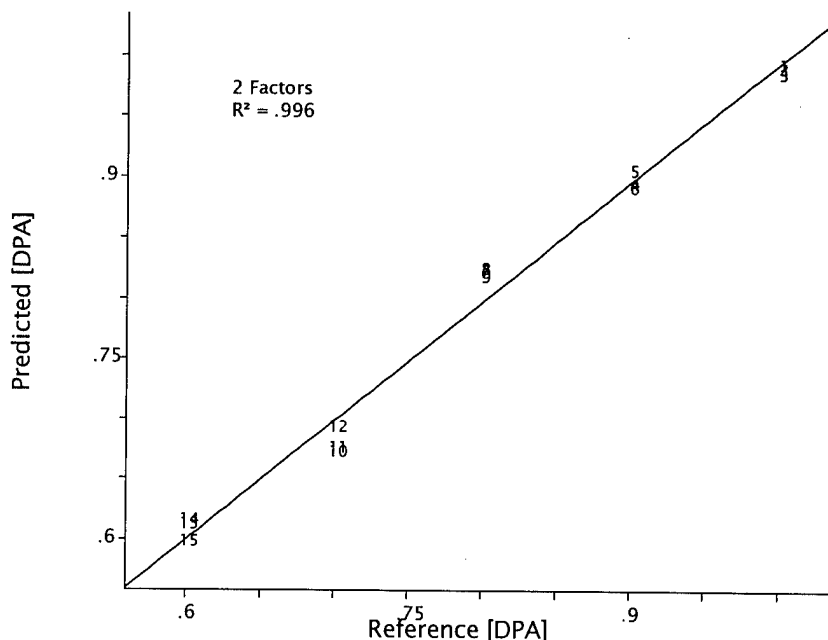


**Figure 4:** Calibration curve for DPA prediction. Model excluded the 0.3% DPA spectra.

Two different experiments are described in the analysis of adhesives. The first involves a discriminant analysis technique to determine which chemical species are present in a sample. The results could be used to select the appropriate quantitative chemometrics model to determine the component concentration. The second experiment uses the NIR spectrometer to follow the kinetics of the reaction between polyols and TDI. The ability of the spectrometer to measure the kinetics of the reaction provides a feedback mechanism to optimize the chemical system in the process plant.

## A. Methodology

A transfectance probe, with a total pathlength of 3.5 mm, was used to analyze the samples. Two multimode fiber optics, 2 m long and with a 600  $\mu\text{m}$  core diameter, connected the probe and the spectrometer. Spectra consisting of 100 co-added scans were measured from 1200 to 2100 nm at 2 nm intervals. The spectrometer gain was maximized, using the air background, to obtain ~62000 digital counts. Specific experimental details for the two experiments are provided below.

### 1. Discriminant Analysis of Individual Components

The ingredient viscosities complicated sampling. To ensure that air was not entrained in the mechanical gap of the probe, the probe was positioned at an angle for gravity assistance in the sample flow. An aliquot of the sample was taken with a large disposable Pasteur pipette. Using a rubber bulb on the pipette, the samples were continuously injected into the gap during spectral acquisition. Between samples, the probe was cleaned with toluene. Figure 5 shows a schematic of the probe and sample.

### 2. Kinetics Monitoring of the Polyols and TDI reaction

To obtain the kinetics data, the transfectance probe was placed into a beaker that contained a stoichiometric quantity of the polyols. During the reaction,  $\text{CO}_2$  gas was evolved. To minimize the entrapment of these bubbles, the probe was angled with respect to the solution. Flow of the sample

through the gap was facilitated by the air stirrer that mixed the polyols and TDI. A schematic of the experimental arrangement can be seen in Figure 6.

The polyol solution was blended for several minutes. Spectra, consisting of the average of 100 scans, were then collected from 1200 to 2100 nm with 2 nm intervals. One hundred scans were acquired in 11 seconds and a delay of 19 seconds was applied after each spectral acquisition. This gave a 30 second period between each spectrum. All spectra were corrected with an air background spectrum.

TDI was added to the beaker after spectrum #3, and the reaction was observed from spectrum #4 onwards. At room temperature, the expected equilibration point should occur at ~30 minutes; therefore, the reaction was monitored for 40 minutes. All spectra were collected in transmission mode. A five point Savitsky-Golay first derivative was applied to the data, and the data were then converted into Grams/32 format for the chemometrics processing.

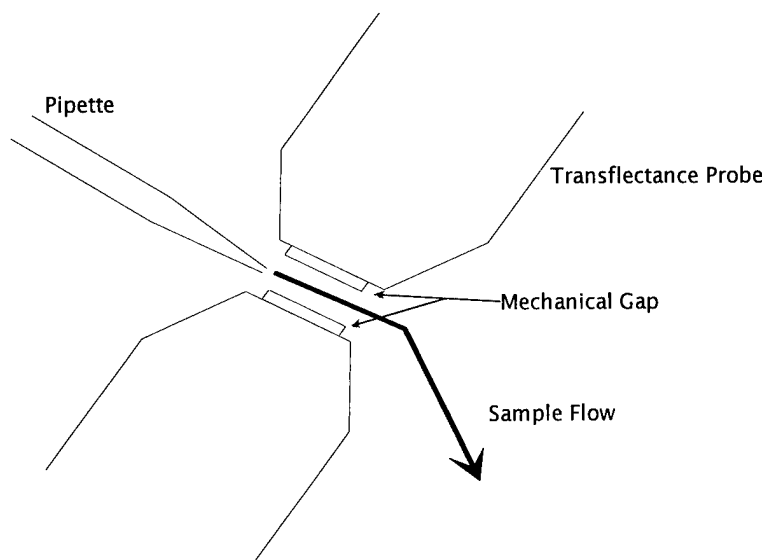


**Figure 5:** Schematic of the transfectance probe showing the sample injection occurring in the mechanical gap.

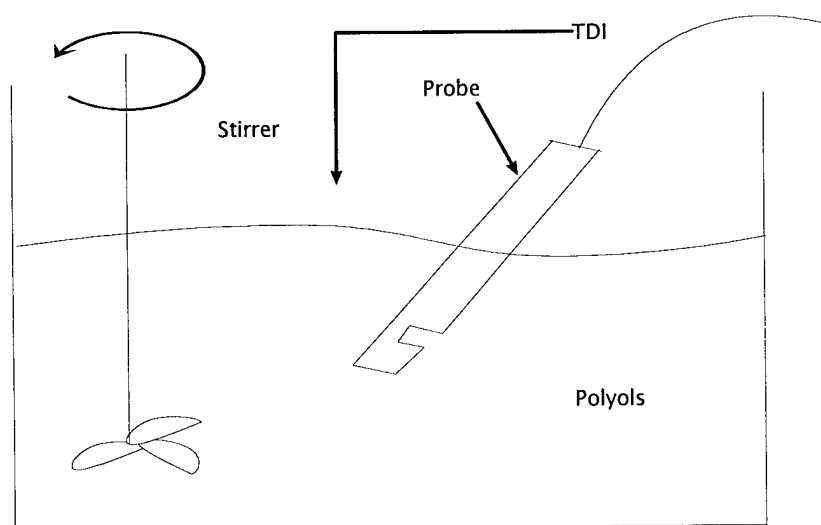


**Figure 6:** Experimental schematic for kinetics monitoring. Figure shows beaker containing the polyols to which the TDI was added.

## B. Data and Models for Discriminant Analysis of Adhesives

### 1. Original Data

The absorption and first derivative spectra for the reagents and the product are shown in Figure 7 and 8. There are several peaks that can serve as identifiers for the different components. The peaks at 1431, 1661, 1864, and 1909 nm can be attributed to TDI. The peaks at 1631, 1711 and 1757 are due to the polyol backbone. The pre-polymer has unique absorptions at 1470, 1630, 1837, and 2007.

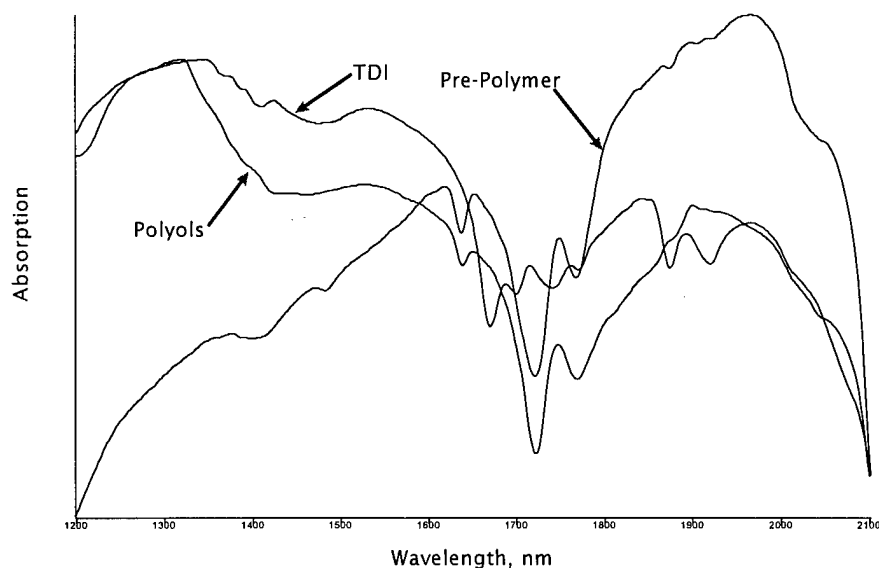


Figure 7: Representative absorption spectra of the polyols, pre-polymer, and TDI.

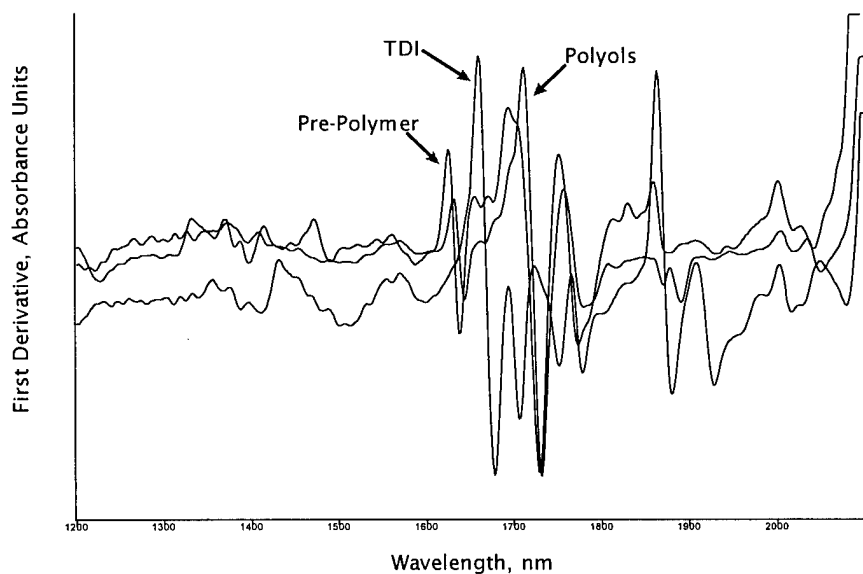


Figure 8: Savitsky-Golay five point smoothed first derivative spectra.

Spectra 1 and 7 were outliers and were excluded from the models. Details of the calibration samples are provided in Table 1. A polyol and a pre-polymer spectrum were randomly selected and removed to form prediction sets. Models were then re-generated from the reduced calibration data set and

used to predict the composition of the prediction data sets. The details for the three prediction sets are provided in Table 2.

**Table 1: Details of the calibration samples.**

Spectrum #	Sample Label	Descriptor	Remarks
01-03	A	Polyols	#1 was an outlier
04-06	B	Polyols	
07-09	C	Polyols	#7 was an outlier
10-11	B	Polyols	Repeated samples
12-13	C	Polyols	Repeated samples
14-16	D	Pre-Polymer	
17-19	E	Pre-Polymer	
20-22	F	Pre-Polymer	
23-24	D	Pre-Polymer	Repeated samples
25-26	E	Pre-Polymer	Repeated samples
27-29	G	Pre-Polymer	TDI-Stripped
30-32	TDI	Pure TDI	

**Table 2: Prediction data set member details**

Prediction Set	Spectra Removed	Sample
#1	3, 16	A, D
#2	4, 21	B, F
#3	11, 23	B, D

## 2. Preliminary Discriminant Analysis Model

The first model that was generated used all of the spectra (excluding the outlier spectra) in the calibration data set. The objective was to determine if NIR spectroscopy would be able to resolve, or separate, the different components into unique clusters. The best model was generated using the spectral range from 1200 to 2100 nm. A 5 point Savitsky-Golay first derivative was applied to the data which were then were mean centered and variance scaled.

A score cluster plot, shown in Figure 9, for the first two factors indicates that there appears to be good discrimination between the polyols, the pre-polymer with residual TDI, and the pure TDI spectra. The stripped pre-polymer seems to lie in the distance between the pre-polymer and the polyols. The shaded areas in the figure are artistic renditions of the clustering area for the different constituents.

It is possible via the analysis of the factor loadings to deduce with which physical properties for which the factors may be associated. Factor loading plots indicate which spectral regions contribute significantly to the model. The first two factor loading plots are shown in Figure 10 and 11. The wavelengths for the positive peaks have been marked and compared to the spectra of the individual constituents. Peaks that can be assigned to a unique constituent are indicated in the plots. Analysis indicates that the first factor separates the pre-polymer and polyols based on several different peaks due to the polyol and polymer. The loading plot for the second factor can be associated to the contributions from the TDI. Consideration of the score cluster plot of Figure 9 indicates that these

conclusions are supported. Thus, the stripped pre-polymer, with little residual TDI, should cluster lower on the 2<sup>nd</sup> factor.

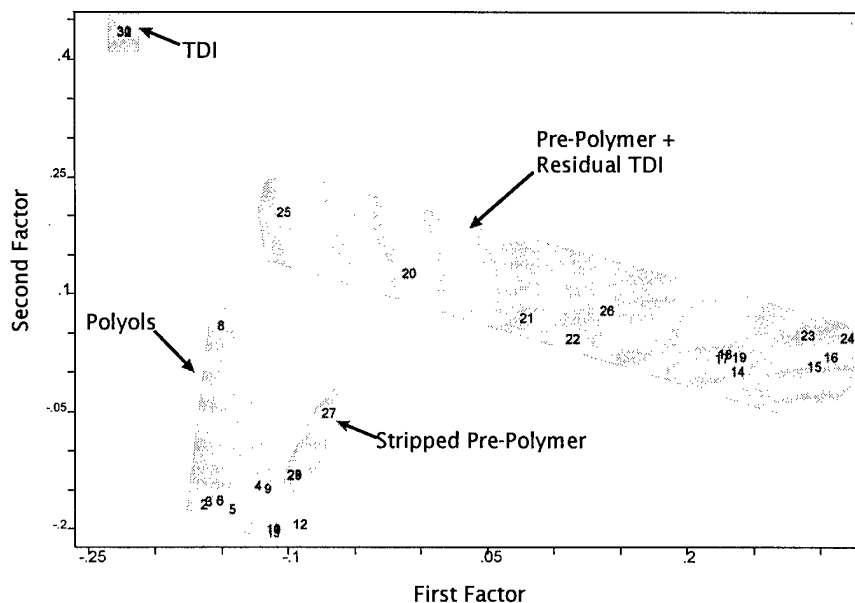


Figure 9: Score cluster plot for the exploration model using all of the spectra. The 2<sup>nd</sup> factor is plotted versus the 1<sup>st</sup> factor.

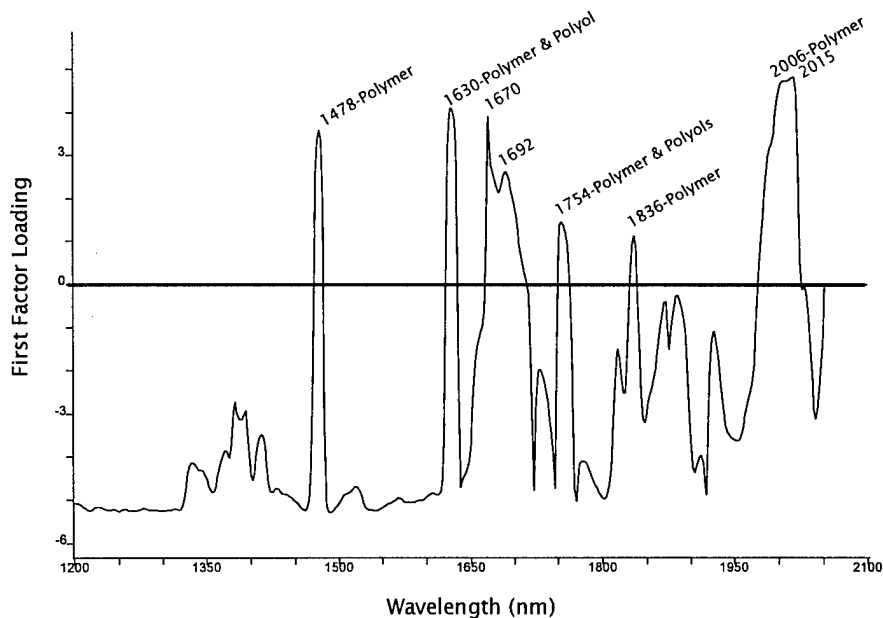
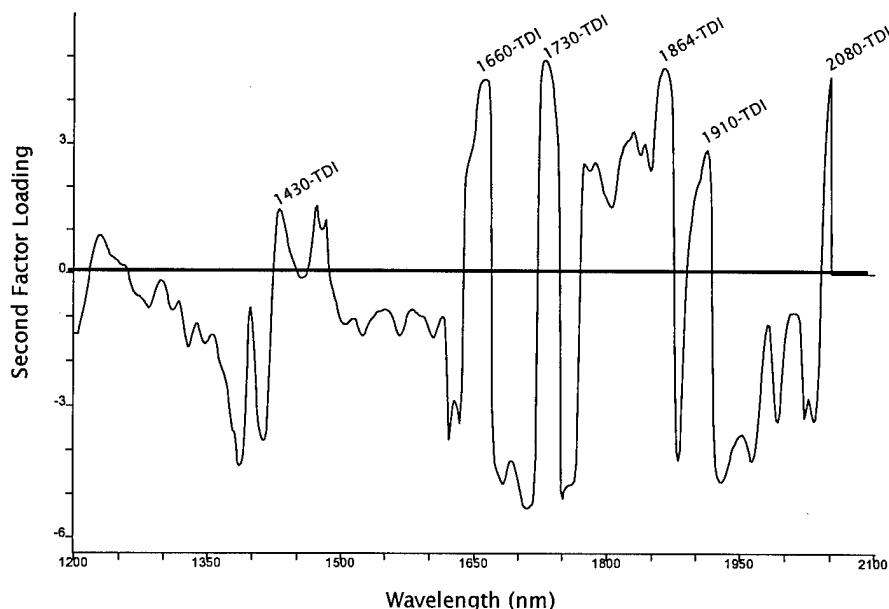


Figure 10: First factor loading for the exploratory discriminant analysis model.

### 3. *Individual Models for the different Constituents*

Since the score cluster plot (Figure 9) indicates that the clusters are well separated, individual models were generated for the polyols and pre-polymers. Using the previous parameters, three different models for each constituent were generated from the three reduced calibration data sets. The appropriate models were then used to predict the composition for the different validation sets. To

determine the effect of residual TDI, the stripped pre-polymer spectra were excluded from the calibration sets. All calibration models used two factors except for the polyol model for the 2<sup>nd</sup> validation set which used 3 factors.



**Figure 11:** Second factor loading for the exploratory discriminant analysis model.

The results for the predictions are listed in Table 3. In this table, the Mahalanobis Distance, MD, (indicative of the similarity between a sample and a specific cluster) is indicated by the number in each cell of the table. If the MD is below the acceptance value, the sample belongs to the cluster (Y). If the MD is between the acceptance and rejection criteria, the sample is given a possible match (P). If the MD is larger than the rejection criterion, the sample does not belong to the cluster (N). For these models, the acceptance and rejection criteria were set to 1 and 3 standard deviations, respectively, of the cluster variation.

**Table 3:** Results for the prediction of the three validation set members. Y = Belongs to the cluster, P = Perhaps belongs to the cluster, and N = Does not belong to the cluster.

Samples	Prediction Set #1		Prediction Set #2		Prediction Set #3	
	Polyol	Pre-Polymer	Polyol	Pre-Polymer	Polyol	Pre-Polymer
3	P 1.24	N 64.48				
16	N 140.13	Y 0.76				
4			Y 0.66	N 60.89		
21			N 42.04	P 1.02		
11					Y 0.72	N 98.12
23					N 149.51	Y 0.66

The results from the discriminant analysis for the prediction sets indicate good predictive ability. One concern is that the residual TDI in the pre-polymers may have inflated the discrimination between the polyols and the pre-polymer. To check this, the above models were used to predict an "unknown" data set which consisted of the pure TDI and the stripped pre-polymer spectra. The models should not recognize TDI if it has not contributed to the discrimination and should still recognize the stripped pre-polymer. The results for this test are listed in Table 4. The TDI spectra were very different from either the polyols and the pre-polymers as evidenced by the large MD for



the TDI spectra. This is corroborated by the large separation of the TDI cluster from the other clusters (Figure 9). The stripped pre-polymer, however, was not recognized as belonging to the pre-polymer cluster and was actually more similar to the polyols. This discrimination can be utilized to determine the amount of residual TDI that is left after the reaction has gone to equilibrium.

**Table 4: Results from the discriminant analysis models (not containing the stripped pre-polymer) in predicting the pure TDI and stripped pre-polymer samples.**

Samples	Models (Set #1)		Models (Set #2)		Models (Set #3)	
	Polyol	Pre-Polymer	Polyol	Pre-Polymer	Polyol	Pre-Polymer
TDI						
#1	N 94.14	N 76.19	N 120.94	N 74.54	N 120.67	N 73.17
#2	N 93.78	N 75.77	N 120.79	N 74.13	N 120.30	N 72.73
#3	N 93.74	N 75.88	N 120.83	N 74.16	N 120.20	N 72.81
Stripped						
#1	N 5.94	N 19.74	N 8.26	N 17.94	N 8.17	N 19.82
#2	N 7.45	N 48.70	N 9.45	N 45.12	N 11.59	N 47.53
#3	N 7.79	N 48.62	N 9.40	N 44.95	N 12.37	N 47.37

#### ***4. Discriminant Analysis Models using the Stripped Pre-Polymer Spectra***

To improve the discrimination, new models were generated that used the stripped pre-polymer as part of the polymer calibration data set. Six additional models were generated for the pre-polymer with certain spectra removed for validation purposes. The resulting six models (denoted by the corresponding validation data set numbers) were then used to predict both the validation data set and also the TDI spectra. The details of the validation sets and the results for these predictions are provided in Table 5. Models 1 and 3 used four factors and the other models used 3 factors for the predictions.

Several observations can be made. First, the addition of the stripped pre-polymer to the polymer calibration data set did not degrade the discrimination against the polyols. This indicates that there are spectral features, besides those due to the isocyanate functional groups on the polymers, that are used in the discrimination models. Second, TDI is still recognized as distinctly different from the polymer as evidenced by a MD greater than 70. Third, the new polymer models were unable to recognize one of the stripped polymers (spectrum #27). Observation of the cluster plot in Figure 9 shows that two of the stripped polymers, spectra #28 and #29, are very similar to each other while #27 was different from these two replicates. It was noted empirically during the experiments that it often took several aliquot injections in the gap of the probe to obtain consistent readings. Therefore, #27 may be rejected as an outlier if there were additional stripped polymer samples that could have been used in the calibration data set. Finally, the stripped polymer spectra did not reduce the ability of the models to recognize the polymer samples.

### **C. Kinetic Reaction Monitoring**

An experiment was performed to monitor the progress of the reaction between the polyols and the TDI. The experimental details have been described previously. After spectral acquisition, the data were converted into absorbance units and a 5 point Savitsky-Golay first derivative algorithm was applied to the data. The spectra were imported into Grams/32 so that different time slices could be taken at different wavelength regions of interest. Cross-sections were taken at 1412, 1709, and 1868

nm. These cross-sections are shown in Figure 12—14. Since each spectrum was taken every 30 seconds, the x-axis can be converted directly into time units. The inset in each figure shows a zoomed view of the spectral region for which the time slice was taken.

**Table 5: Prediction data set details and discriminant analysis results for the pre-polymer models that incorporated the stripped pre-polymer as part of the calibration data set.**

Validation Set #	Spectrum #	Sample Description	Model Number					
			#1	#2	#3	#4	#5	#6
1	3	Polyols Polymer	N 46					
	16		Y 0.66					
2	4	Polyols Polymer		N 17				
	21			Y 0.60				
3	11	Polyols Polymer			N 20			
	23				Y 0.49			
4	3	Polyols Polymer Stripped Polymer				N 39		
	16					Y 0.74		
	27					N 9.02		
5	4	Polyols Polymer Stripped Polymer					N 16	
	21						Y 0.60	
	28						P 1.68	
6	11	Polyols Polymer Stripped Polymer						N 18
	23							Y 0.51
	29							P 1.67
	TDI #1	Pure TDI	N 70	N 79	N 68	N 80	N 77	N 70
	TDI #2	Pure TDI	N 70	N 79	N 68	N 80	N 77	N 70
	TDI #3	Pure TDI	N 70	N 79	N 67	N 80	N 76	N 70

The peak at 1412 nm (Figure 12) can be attributed predominately to the polyol reagent. The reaction with the TDI started after the first 2 minutes. For the next several minutes, there appears to be a slight increase in the peak, followed by a typical kinetics curve. It appears that the reaction has approached equilibrium after 20 to 30 minutes.

The response for the 1709 nm cross-section (Figure 13) may be attributed to an absorption peak at 1711 for the polyols and a peak at ~1708 for the pre-polymer. There appears to be an induction period for the first 4-6 minutes after the addition of the TDI. Another explanation for this initial behavior is that the reaction is slow enough that the consumption of the polyols is less than the detection limit. Around 15 minutes, there is an increase in the intensity at 1709 nm. This can be attributed to the two processes that are occurring. Initially, there is an excess of the polyols. As they are consumed, the intensity decreases. Towards the middle of the reaction, the concentration of the polymer starts to exceed that of the remaining polyols, and we see the increase in the intensity. Again, after approximately 30 minutes, the reaction appears to have reached equilibrium.

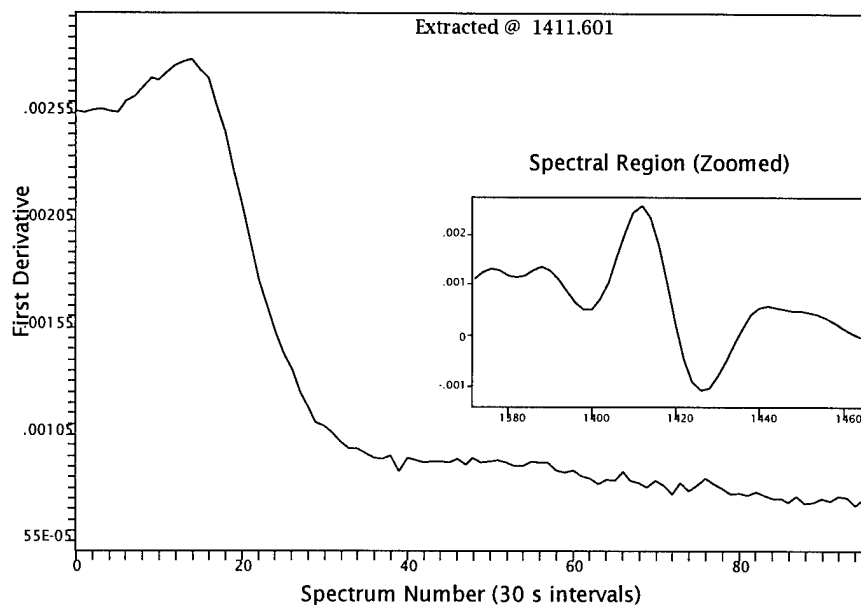


**Figure 12:** Spectral response versus the spectrum number taken at 1411.601 nm. Inset shows the spectral region from which this time slice was taken.

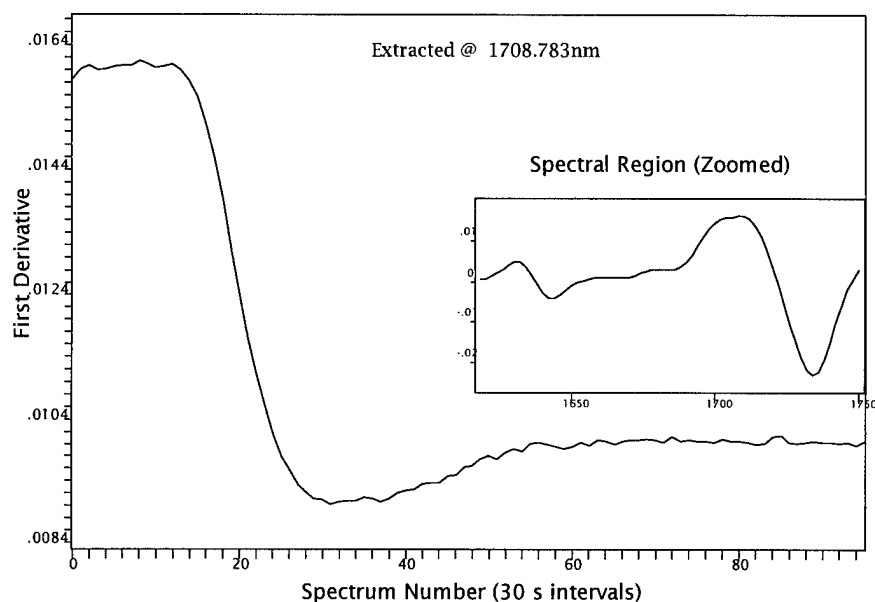


**Figure 13:** Spectral response versus the spectrum number taken at 1708.78 nm. Inset shows the spectral region from which this time slice was taken.

The cross-section at 1866.96 nm (Figure 14) can be attributed mainly to the pre-polymer peak. The apparent induction period in this plot is much smaller. Since the addition of the TDI onto the polymer backbone probably increases the absorption coefficients of the pre-polymer, the longer induction period in the previous figures may indicate that the sensitivity for the polyol is not as strong as is the pre-polymer. (The unusual behavior around 15 minutes may be due to absorption from the TDI or from some other physical property such as entrained gas in the gap of the transfectance probe.) The reaction appears to be completed after 30 minutes.

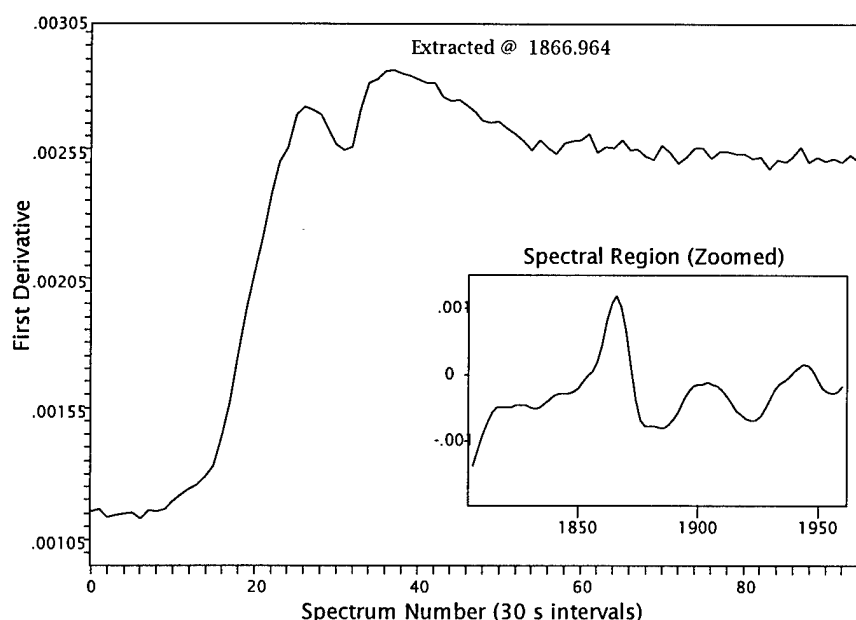


**Figure 14:** Spectral response versus the spectrum number taken at 1866.96 nm.

#### **D. Discussion: Analysis of Adhesives via AOTF—Based NIR Spectroscopy**

The first set of models that did not use the stripped pre-polymer indicates that NIR spectroscopy can be used to determine the differences between the pre-polymer, the polyols, and the TDI. Since the models indicated that the stripped pre-polymer was a separate cluster of data points, these models could also be calibrated to measure the amount of residual TDI in the pre-polymer. Successful discrimination of the different components was achieved with the models. Additional samples of stripped pre-polymer should be incorporated into the calibration data set so that a more rigorous model could be created for the detection of the stripped polymer.

If one takes the cross-section at 1708.78 nm and inverts it, the slopes of the two figures appear to be very similar (seen in Figure 15). This corroborative data can be exploited when monitoring the reaction by the Luminar spectrometer. Since the complete spectral range can be acquired very rapidly, a chemometric model can be generated that will use all of the information contained in the absorptions of the polyols, pre-polymer, and the TDI. Since the wavelength dispersive device of the Luminar 2000 NIR spectrometer is a solid-state acousto-optic tunable filter, spectra can be acquired at high rates without any loss in wavelength accuracy or precision.

## **IV. Conclusion**

In this report, we have shown the ability to perform process control and sample evaluation using NIR spectroscopy. The analysis of M1 propellant grains was complicated due to the physical and morphological properties of the grains. The speed of the AOTF device enabled over 1000 full spectral range scans to be acquired in ~2 minutes. Using only the spectral regions that have strong correlation to DPA prediction, based on chemometric results, a subset of the spectral region could be scanned so that 1000 scans would require even less time. The high throughput, speed, and

wavelength accuracy made the analysis of the propellant possible; whereas, the analysis had not been possible using non-AOTF based NIR spectrometers.

Using the full spectral range, discriminant analysis of the reagents and products in the formation of adhesives is possible. When coupled to the high speed wavelength scanning of the AOTF, kinetics monitoring of the reaction in the process stream is possible. Where other dispersive devices would be deleteriously effected by the vibrations in the process plant, the solid-state AOTF is unaffected by either the vibrations or by the high scan rates that are required to collect complete spectra.

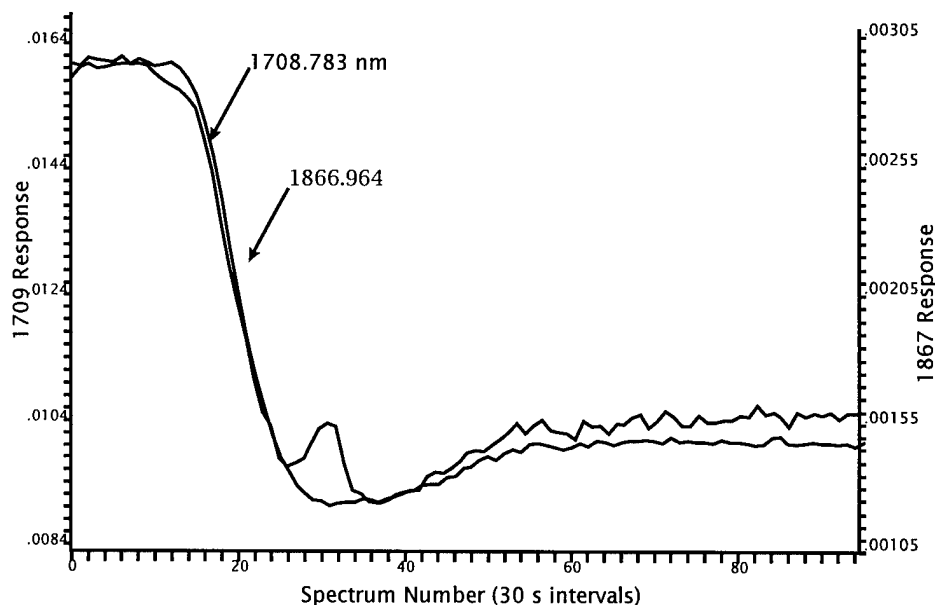


**Figure 15:** Overlaid cross-section responses for the 1709 and 1867 nm regions. The 1867 nm peak has been inverted to assist in the comparison of the slopes.

## V. References

1. *The Atlas of Near Infrared Spectra* (Philadelphia: Sadtler Research Laboratories, 1981), Spectrum #28.

For further information on chemometrics, please refer to:

2. Howard Mark and Jerry Workman, *Statistics in Spectroscopy*, Academic Press: Boston, 1991, Chapters 32-37.
3. *PLSPlus/IQ for Grams/32 and Grams/386*, Galactic Industries, Salem, NH, 1996.
4. Kim Esbensen, Suzanne Schönkopf, and Tonje Midtgaard, *Multivariate Analysis in Practice*, CAMO: Trondheim, Norway, 1994.

# Application of AOTFs to High Fidelity Spectroscopic Imaging

E. Neil Lewis<sup>†</sup>, Linda H. Kidder<sup>†</sup>, Ira W. Levin<sup>†</sup>, and Seth R. Goldstein<sup>‡</sup>

National Institutes of Health  
Bethesda, MD 20892

<sup>†</sup>Lab of Chemical Physics, NIDDK

<sup>‡</sup>Biomedical Engineering and Instrumentation Program, NCRR

## 1. Introduction

Raman spectroscopy is a powerful analytical tool used for basic chemical identification of samples, and also as a extremely sensitive and non-invasive probe of molecular structure. The technique has applications in fields as diverse as biophysics, polymer and materials sciences and geology, largely because it is capable of accurately determining the constituents of multicomponent mixtures.<sup>1-5</sup> Although traditional Raman spectroscopy provides information at the molecular level and can determine the composition of multicomponent mixtures, it does not generate specific information pertaining to the *spatial distribution* of these components. The functionality and properties of complex systems are often predicted by knowledge of the microscopic spatial distribution of components. Therefore, the ability to map these distributions is crucial in activities ranging from the design and fabrication of advanced materials to the elucidation of biomolecular functionality.

Coupling Raman spectroscopy with microscopic imaging represents a powerful approach in attaining these goals. The combination unites the analytical capabilities of spectroscopy with the ability to visualize the spatial distribution of the chemical constituents within a system. For example, the technique can detect microscopic chemical heterogeneities in samples which, using conventional optical microscopies and bulk sample spectral analysis, appear spatially and spectrally homogeneous. As with traditional Raman spectroscopy, these images can be recorded without the use of potentially invasive contrast enhancing

agents, providing a highly specific, non-destructive means to analyze chemical distributions within heterogeneous samples.

Typically Raman scattered radiation is on the order of  $10^{-8}$  of the incident radiation, and must be detected in the presence of shot noise, detector noise, stray light and auto-fluorescence. Therefore, the major challenge in Raman imaging microscopy has been to achieve acceptable signal-to-noise (S/N) levels from samples. Within the past several years, a variety of instrumental developments have increased the practicality of Raman spectroscopy and consequently Raman imaging.

Of primary importance has been the continuing development of silicon charge-coupled devices (CCD) as high sensitivity detectors.<sup>6</sup> CCDs have recently been used in conjunction with single-stage spectrographs to provide high signal-to-noise Raman spectra, exploiting the multichannel advantage of these detectors relative to PMTs and other single point detectors. CCDs also have a high quantum efficiency, low readout noise, and extremely low detector dark current.<sup>7</sup> The high sensitivity of these two-dimensional solid state arrays make them well suited for detection of low light levels, and their low dark current make them capable of long integration times. CCD detectors also have an extended red response, which compensates for the decrease of Raman scattering cross section at longer excitation wavelengths.<sup>8,9</sup> For biological applications this is significant, since longer excitation wavelengths produce significantly less sample fluorescence and laser-induced photothermal degradation.<sup>10</sup> The qualities that make CCDs extremely well suited as simple multichannel detectors for Raman spectroscopy, coupled with their intrinsic array detection capabilities, make them ideal for acquiring Raman spectroscopic images.

Another technological development of major importance is the acousto-optic tunable filter (AOTF). This device contains an optically transparent birefringent crystal, which can be electronically controlled to pass a selectable narrow band of optical wavelengths. The application of AOTFs to Raman spectroscopy<sup>11</sup> and Raman imaging<sup>12,13</sup> have been previously described. A third technological that has provided impetus to the widespread application of Raman spectroscopy is the holographic filter.<sup>14,15,16</sup> Holographic Raman notch filters are spectroscopic devices for efficient Rayleigh line rejection, and are readily available for a variety of laser wavelengths. They provide between 5-6 orders of laser line rejection while uniformly transmitting 75-80% of the Raman scattering beyond  $75\text{ cm}^{-1}$  of the exciting line.

In this study, we describe a technique for performing high-fidelity Raman spectroscopic imaging, integrating a commercial optical microscope with laser epi-illumination, holographic filters, an AOTF and a liquid nitrogen cooled CCD. The images recorded at each wavelength are stored individually, or together in a single data file creating a series of images and spectra. Results are presented that display the image quality, and spatial and spectral resolution of the instrument.

## 2. Mechanical And Optical Layout

Figure 1 is a scale drawing of the Raman imaging microscope's major aspects. It is built around an infinity-corrected metallurgical microscope (Olympus BH-2). The optical components are mounted to a superstructure attached to the microscope vertical port and fastened to the underlying optical bench. The frame provides stable and reproducible mounting for the optical components and was designed to shield from room light the optical components located after the AOTF in the optical path.

In the laser scanning mode, light from a krypton ion laser (Coherent Laser Group, Innova 300) is filtered by a 647.1 nm holographic laser bandpass filter (Kaiser Optical Systems, HLBF-647) and directed to a computer controlled x-y galvanometer scanner (two Cambridge Instruments, 6850 optical scanners). Lenses L1 and L2 ( $f = 300$  mm) constitute an afocal unity magnification relay which images the "center" of the scanner into the objective rear entrance pupil, providing scanning epi-illumination. The scanning beam passes through a half wave plate (Newport Corporation, 10RP12-25), is directed by mirrors M1 and M2 onto a holographic beamsplitter (Kaiser Optical Systems, HB-647-C), and then through the microscope objective onto the sample. The laser beam is approximately 2 mm in diameter at the microscope objective, resulting in a larger than diffraction limited spot size.

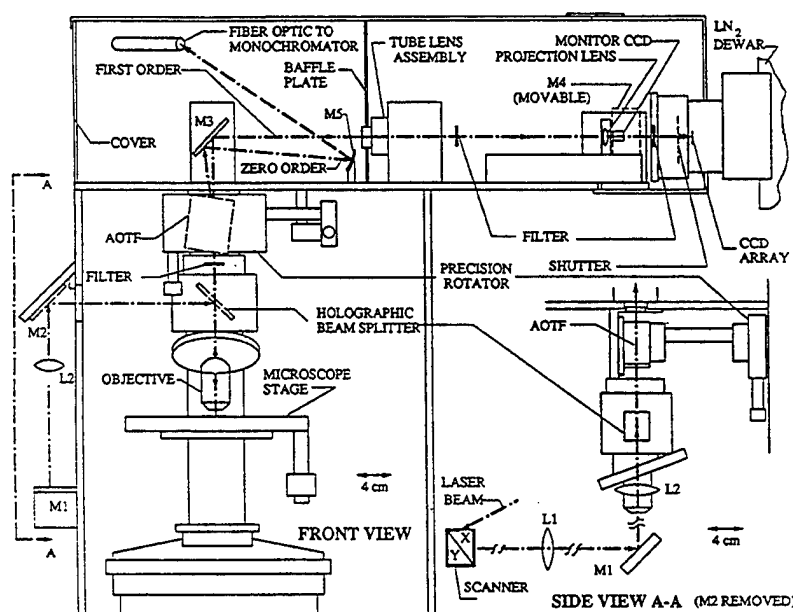


Figure 1 Schematic diagram of the Raman imaging microscope. Laser scanning illumination is provided with a 647.1 nm krypton ion laser. The AOTF is used to continuously tune the wavelength of the Raman emission image, which is collected by the CCD array. Elements include mirrors (M) and Lenses (L).



We also have provided a laser fiber optic wide field illumination system to be used with more fragile specimens that might be damaged by the higher power densities of the scanning configuration. The standard epi-illuminator optics are used with the lamp housing removed, and the optic fiber output placed approximately where the lamp filament is normally located. Krypton laser light is coupled into the fiber, filtered through a laser bandpass filter, directed through the beamsplitter, and passed through the microscope objective to illuminate the sample. A small unbalanced fan applies a vibration to the fiber in order to remove laser speckle.<sup>17</sup> The wide-field fiber illumination is more convenient for sample alignment and system focusing. For transparent specimens, transmission illumination provided by the standard incandescent white light illuminator can be used for this purpose.

The sample return light leaving the infinity corrected microscope objective passes through a holographic Raman notch filter (Kaiser Optical Systems, HNF-647) to reduce the Rayleigh scattered light. It then enters the AOTF (Brimrose Corporation, TEAF-0.6-1.2L) located directly above the epi-illumination beamsplitter slide assembly as close as possible to the objective to avoid significant vignetting. The collimated light exiting the AOTF is directed by mirror M3 through the microscope tube lens ( $f = 180$  mm), forming an intermediate image. The clear aperture of this lens, combined with a baffle plate, separates out the unwanted orders transmitted by the AOTF, and passes only the desired first order. The projection lens, whose focal length depends on the microscope objective in use (see below), follows the tube lens and projects the intermediate image onto the cooled CCD array (Spex, Spectrum One). This array is comprised of  $578 \times 385$  pixels on  $22 \mu\text{m}$  centers. A retractable mirror, M4, between the projection lens and the CCD allows the image to be projected onto a standard video rate CCD camera (Javelin Systems, JE7742), which is parfocal with the cooled CCD array. This is used for sample alignment and focusing using either transmitted white light or scattered Rayleigh light (with the Raman notch filters removed). For precise calibration of the AOTF, an alternate position of M4 directs its monochromatic output into an optic fiber leading to an interferometer (Bomem DA3).

The AOTF is based on the non-collinear design first developed by Chang.<sup>18</sup> It consists of an optically transparent birefringent  $\text{TeO}_2$  crystal bonded to a piezoelectric transducer. Application of an rf signal to the transducer produces acoustic waves in the crystal, which in turn generates a periodic modulation of the index of refraction by the elasto-optic effect.<sup>19</sup> This creates a moving phase grating, diffracting those wavelengths of the incident light beam which satisfy necessary phase-matching conditions. First order diffracted light emerges from the crystal at a small angle from the undiffracted light (zero order), which passes straight through the crystal. Since the transducer is of finite size, the acoustic wave is not perfectly planar, resulting in a finite width of the first order optical passband. The center of this optical passband is selected by changing the rf frequency applied to the transducer, which thereby varies the acoustic wavelength. Therefore, by digitally controlling the frequency of the waveform applied to the AOTF transducer, the center wavelength of the Raman image on the CCD detector is tuned with remarkable speed,

accuracy, and repeatability. The AOTF can either be tuned continuously over a specified wavelength range, or it can be randomly switched between discretely specified wavelengths. In theory, the speed with which wavelength tuning can occur is determined by the AOTF optical aperture and the acoustic velocity within the AOTF. For our device this is on the order of 11  $\mu$ sec. In practice, because of the speed of the computer and the electronics associated with the rf synthesizer, the actual time it takes to change the wavelength is approximately 20  $\mu$ sec. Since polarization is preserved during Raman scattering and the AOTF is polarization sensitive, it is possible to optimize the AOTF output by suitably rotating the half wave plate located in the input laser beam.

To minimize data acquisition time, it is desirable to maintain the overall magnification as small as is consistent with resolving details of interest. However, since the image is sampled by the discrete pixels of the CCD camera, the Nyquist sampling condition must be obeyed to avoid generating sample artifacts. This requires that the overall magnification between the object and the CCD be greater than a lower limit given by  $MR > 2p$  e.g.  $MR = 2.3p$ .<sup>20</sup> Here the CCD pixel size is  $p$ , and it is assumed that the microscope optical resolution is characterized by a resolution element or "resel" of size  $R = 0.61\lambda/NA$ , where  $NA$  is the numerical aperture of the objective, and  $\lambda$  is the wavelength of Raman scattered light. If this condition is not maintained, the excess magnification increases the image acquisition time, or, the insufficient magnification introduces the possibility of sampling artifacts. To adhere to this requirement, it is necessary to couple different projection lenses with different objectives in accordance with their magnification and  $NA$ .

The system has the potential to perform sub-micron resolution Raman microspectroscopy. The laser scanning galvanometer can be stopped at a predetermined position, corresponding to a small region of the sample. A spherical mirror, M5, placed below and in front of the tube lens focuses the zero order light from the AOTF into a fiber optic bundle. This light can be coupled into a single stage monochromator, (Chromex, 500IS), equipped with a holographic filter (Kaiser Optical Systems, HNF-647) and CCD (Spex, Spectrum One). This will allow a more rapid determination of the Raman spectra of the selected micro-region at a higher spectral resolution than that provided by the AOTF.

### 3. Computer Control And System Software

Data collection and device control are integrated in a coherent fashion by custom software written primarily in the C programming language. A 486-based PC contains both the CCD and AOTF controller cards. The software enables the user to specify a variety of scan parameters; namely, the wavelength range and increment size, exposure time and number of exposures taken at each wavelength. The user also can change parameters effecting the size and format of the collected images. At present, due to computer memory limitations, as well as the way these compound data sets are stored, the acquired images must have the same number of pixels in both the x and y dimensions, with the upper limit for the number of pixels contained in any one image plane not exceeding 128 x

128 or 16,384. In versions of the software currently under development, these limitations will be removed. The number of CCD pixels in the image x and y dimensions can be specified. Also, if less than the whole CCD chip is illuminated, the position of the activated pixels can be selected. Finally, it is also possible to specify rectangular binning of neighboring pixels.

Data acquisition proceeds by applying the appropriate rf frequency and power to the AOTF piezoelectric transducer to select the starting bandpass wavelength. The frequency is calculated by evaluation of a polynomial, fitting the relationship between rf frequency and wavelength. The CCD camera is then instructed to take a single image, and the result is stored on the computer hard disk. The experiment continues by tuning the AOTF to subsequent wavelengths and recording CCD frames until the final wavelength is reached. The resulting single data file, SPIFF,<sup>21</sup> contains all the images recorded over the entire wavelength range. Each pixel is stored as a single 32 bit floating point number along with a custom designed file header, which gives the data analysis software the information required to properly visualize and analyze the data.

The primary data acquisition program also interfaces with the galvanometer controllers (Cambridge Instruments, 6585), sending an RS232 control string to a slave PC which generates the appropriate laser scanning waveform. The waveform is generated by a data acquisition card (National Instruments, ATMIO16) containing two 12 bit D/A channels. The user can specify either a fixed voltage pair for laser pointing or a range of voltages (angles) over which the system will scan. The range of voltages is used to provide a continuous sweep of the laser over the rectangular area specified. The nominal accuracy of the galvanometer is typically 20  $\mu$ rad, which for the smallest scan angle condition is still three times smaller than a CCD pixel. Taking into account the speed of the computer and data acquisition hardware as well as the speed of the galvanometer, the laser beam can be positioned at up to 20,000 discrete positions per second.

## 4. Results And Discussion

Our tests were designed to demonstrate the features and limitations of using an AOTF in a Raman microscopic imaging system. The main determinant of the optical quality of an image passed through the AOTF is its finite spectral bandwidth. This was determined by epi-illuminating a mirror target with the 647.1 nm krypton laser line and recording the spectra of various pixels as the AOTF was tuned through this wavelength region. The full width at half max (FWHM) of the laser line spectrum was measured to be 2 nm, giving a system resolution of 50  $\text{cm}^{-1}$ . Dispersion in the  $\text{TeO}_2$  crystal results in a slight smearing of the output image along one axis. This degradation, given by the internal beam spread in the crystal,  $\Delta\theta_{\text{di}}$ , can be estimated from the following approximate relationship<sup>22</sup>

$$\Delta\theta_{\text{di}} / \Delta\lambda = (\Delta n / \lambda_0)(\sin 4\theta_1 + \sin 2\theta_1)^{1/2} \quad (1)$$

where  $\Delta\lambda$  is the passband,  $\lambda_0$  is the center frequency,  $\Delta n$  is the difference between the ordinary and the extraordinary indices of refraction of the  $\text{TeO}_2$  crystal at  $\lambda_0$ , and  $\theta_i$  is the angle between the incident beam and the optical axis of the crystal. The values of these parameters are respectively: 2 nm, 700 nm, 0.138, and  $22.5^\circ$ , leading to a  $\Delta\theta_d$  of 0.29 mrad. This value is to be compared to  $\Delta\theta_a = 2\lambda_0/D_{\text{aotf}}$ , the diffraction beam spread due to the 7 mm square aperture presented by the AOTF entrance pupil,  $D_{\text{aotf}}$ . This beam spread is 0.19 mrad, which is less than the beam dispersion due to the finite spectral bandwidth. Thus, one would expect the image resolution along one axis to be degraded by approximately a factor of two and a half upon passing through the AOTF.

To qualitatively show the degradation introduced into the system by the AOTF, we illuminated a USAF-1951 standard resolution target with white light in transmission mode. A 100X (0.95NA) infinity corrected objective was used to take CCD images, first with the AOTF in place (tuned to 647 nm), figure 2a, and then removed, figure 2b. In group seven of the resolution target, the three bars in element five have a center-to-center spacing of  $4.9\ \mu\text{m}$ , whereas the bars in element six are spaced by  $4.4\ \mu\text{m}$ . The pixel size at the object is about  $0.2\ \mu\text{m}$  ( $M_{\text{proj}}$  is not exactly 1.23), and the "resel" is assumed to be  $0.41\ \mu\text{m}$ . The effect of the AOTF can be quantified by measuring the contrast transfer ratio (CTR) of the system for each of these two images;<sup>23</sup> that is, the maximum minus the minimum brightness divided by their mean. This was determined with the CCD image data by plotting a section of brightness through the image, and is shown in figure 3. It is clear that the AOTF results in little loss of detail when objects of several microns in size are viewed with a 100X objective.

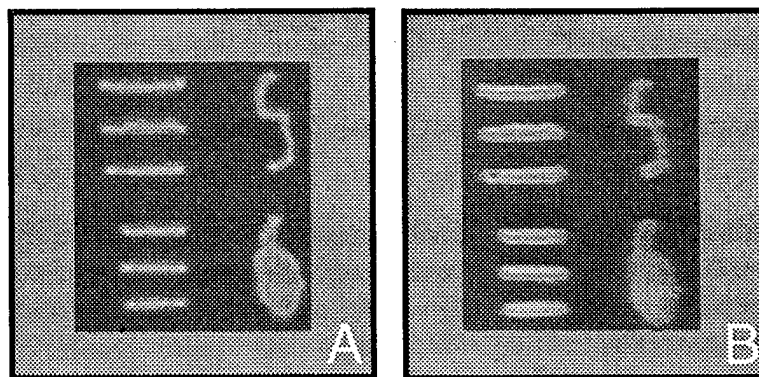


Figure 2 Transmission image of a resolution target illuminated with a 100X (0.95NA) infinity corrected objective. (A) With the AOTF removed from the optical path, (B) AOTF in the optical path. The center-to-center spacing of the elements is  $4.9\ \mu\text{m}$  for element 5 and  $4.4\ \mu\text{m}$  for element 6. The original image contained  $128 \times 128$  pixels, but the figure has been cropped for clarity.

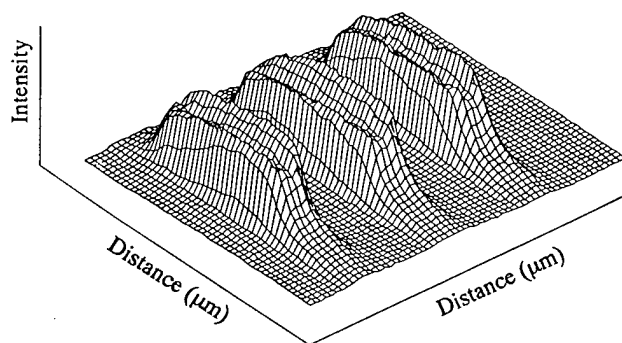


Figure 3 Axonometric plot of the resolution target group 6 bars from figure 2b showing baseline resolution. The center-to-center spacing of the bars is 4.4  $\mu\text{m}$ .

In order to better characterize the AOTF at higher spatial frequencies, we used a 5X (0.13NA) infinity corrected objective, and a projection lens of magnification 2.98, to image the resolution target with and without the AOTF in the optical path. Figure 4 shows the resolution target image with the AOTF in the optical path, demonstrating the optical degradation caused by the AOTF crystal dispersion along the vertical axis. The degradation is quantified by determining the contrast transfer function (CTF), which is the CTR as a function of bar target spatial frequency (line pairs/mm). To compare the CTF in the horizontal and vertical directions, slices parallel to both axes through the CCD images were taken. It was determined that the 50% CTF in the horizontal direction (no AOTF dispersion effect) was reached using the 90.5 line pairs/mm target; whereas in the vertical direction, a CTF of 50% occurs with the 32 line pairs/mm target. Similarly, 33% CTFs were obtained using the 114 and 40.3 line pairs/mm targets. For both of these CTFs, the ratio of horizontal to vertical line pairs/mm is 2.83. This degradation is within 12% of the estimate predicted by the ratio  $(\Delta\theta_d + \Delta\theta_a)/\Delta\theta_a$  with  $\Delta\theta_d$  computed using equation (1).

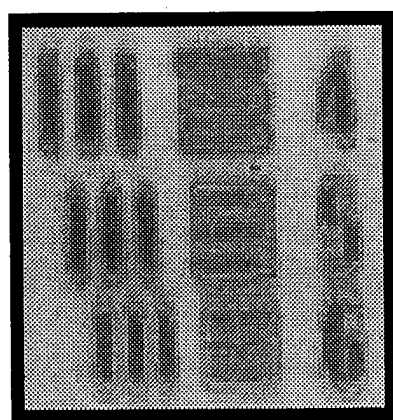


Figure 4 Transmission image of a resolution target illuminated with a 5X (0.13NA) infinity corrected objective. The figure highlights the image degradation in the vertical axis relative to the horizontal axis, caused by the wavelength dispersion in the AOTF 2nm wide bandpass. The center-to-center spacing of the smallest bars (element 6) is 17.4  $\mu\text{m}$ .

The additional aperture effect of inserting the AOTF into the system depends on how the AOTF entrance pupil compares in size with the exit pupil of the objective being used. In

this instance, the 7 mm square entrance pupil will not cause an appreciable effect unless very low power objectives are used; e.g. a 100X objective has an exit pupil much smaller than 7mm. With the 5X objective, when the AOTF is removed from the system, the number of line pairs/mm for 63% CTF increased by 12% over the comparable number in the horizontal (no dispersion) direction with the AOTF in place. This is reasonably consistent with the measured size of the beam exiting the 5X objective if one allows for the square shape of the AOTF aperture.

The amount of image shift as a function of wavelength was determined using the same resolution target/transmission illumination configuration as given above, but by tuning the AOTF from 660 nm to 770 nm, and collecting 20 images over the wavelength range. The x-coordinate of the edge of a single bar shifted linearly with wavelength by 6 pixels, corresponding to an AOTF angular dispersion of 1.26 mrad over this range. A prism designed to compensate for this shift is being fabricated. A simulation using published index of refraction data indicate that the compensation should be accurate to within a small fraction of a pixel.

Figure 5a shows the Raman image of 1  $\mu\text{m}$  diameter polystyrene beads recorded with a 100X (0.95NA) infinity corrected objective. This image corresponds to a Raman shift of approximately  $1000\text{ cm}^{-1}$ , the peak position of the polystyrene aromatic ring symmetric stretching mode. The complete data set was generated by tuning the AOTF in  $7\text{ cm}^{-1}$  steps over the range  $747 - 1363\text{ cm}^{-1}$ . For each wavelength, 20 exposures of 30 seconds duration were averaged, collecting images of  $128 \times 128$  unbinned pixels. The spectrum of a pixel nominally located at the center of one of the polystyrene beads is shown in figure 5b. It is generated by plotting the intensity of a specific x,y coordinate of the CCD as a function of image wavelength. It is one of 16,384 Raman spectra contained within this data set; however, since one resel corresponds to 2.3 pixels, the number of uniquely resolvable spectra is reduced by  $(2.3)^2$ .

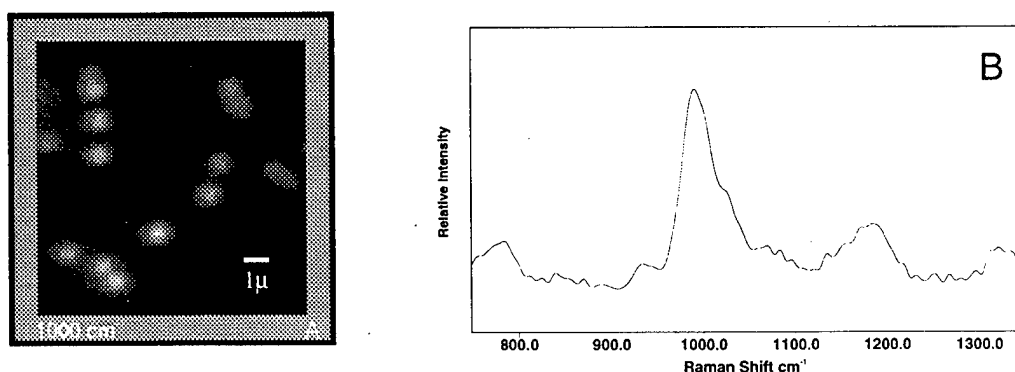


Figure 5 (A) Raman image of  $1\mu\text{m}$  diameter polystyrene spheres recorded with a 100X (0.95NA) infinity corrected microscope objective. The image displayed was recorded with the AOTF tuned to  $1000\text{ cm}^{-1}$ , the peak position of the polystyrene aromatic ring symmetric stretching mode. (B) Raman spectrum corresponding to a single pixel in the center of one of the polystyrene beads. Note the peak maximum at  $1000\text{ cm}^{-1}$ .

## 5. Conclusions And Future Directions

We have described an implementation of a highly efficient AOTF based microscope system for simultaneously obtaining Raman images and spatially resolved Raman spectra of materials. We have outlined the broad applicability of Raman microscopic imaging for materials analysis. Inasmuch as it provides both Raman spectra and images, applications of this new technique will strongly complement fields where traditional Raman spectroscopy is applied. Potential applications include polymer and semi-conductor characterization, the study of diamond film deposition and *in situ* Raman imaging of metal corrosion, as well as chemical and pharmaceutical analyses of complex matrices, emulsions and gels.

The instrument discussed was able to obtain Raman images and spectra from 1  $\mu\text{m}$  diameter polystyrene spheres. Qualitatively, resolution target images of 2.2  $\mu\text{m}$  wide bars taken with a 100X (0.95NA) objective do not substantially differ either with or without the AOTF in the optical path. The effect of introducing an AOTF into the optical path was quantitatively determined by calculating contrast transfer functions for images taken with a 5X (0.13NA) objective. The test results, demonstrating that the system resolution was reduced by a factor of 2.83 from the diffraction limit for our AOTF with a 2 nm passband, agree to within 12% of predictions for AOTF image degradation derived from the literature. This is unlikely to significantly limit the overall performance, since in most Raman imaging situations, in the interest of reasonable data acquisition times, it is desirable to bin adjacent CCD pixels.

In biological applications, the emphasis of traditional Raman spectroscopic approaches has been on extracting spectroscopic information from samples, with little or no information gleaned concerning the structure of biomolecular aggregates. This imaging technique is readily able to discern reorganizations in these systems as a result of changes in temperature or from perturbations originating from exogenous molecules. The integration of Raman spectroscopy with sample imaging should prove to be a potent tool for the study of intact biological and histological samples with the ultimate goal to image spectroscopically intact cells and organelles. We are currently using this technique to visualize foreign inclusions in human tissue.

In the future, we anticipate the Raman imaging microscope will find use in a host of scientific and technological disciplines where it is advantageous to obtain structural and spectral data simultaneously.

## 6. References

1. Levin, I.W., *Vibrational spectroscopy of membrane assemblies*, Advances in Raman and Infrared Spectroscopy, ed. by R.J.H. Clark & R.E. Hester, Vol 11, pp. 1-48. Wiley Heyden, New York, NY, 1984.

2. Parker, F.S., *Applications of Infrared, Raman, and Resonance Raman Spectroscopy in Biochemistry*, Plenum, New York, NY, 1983.
3. Parker, R.W. and Siegal, R.W., *Calibration of the Raman spectrum to the oxygen stoichiometry of nanophase TiO<sub>2</sub>*, Appl. Phys. Lett. **57**, (1990), 943.
4. Hemley, R.J., Mao, H.-K., and Chao, E.C.T., *Raman spectrum of natural and synthetic stishovite*, Phys. Chem. Minerals **13**, (1986), 285.
5. Bulkin, B.J., *Polymer Applications*, Analytical Raman Spectroscopy, ed by J.G. Grasselli and B.J. Bulkin, Vol. 114 in Chemical Analysis: A Series of Monographs on Analytical Chemistry and its Applications, pp. 223-273. John Wiley and Sons, New York, NY, 1991.
6. Murray, C.A. and Dierker, S.B., *Use of an unintensified charge-coupled device detector for low-light-level Raman spectroscopy*, J. Opt. Soc. Am. **3**, (1986), 2151-2159.
7. Denton, M., Lewis, H., and Simms, G., *Charge-injection and charge-coupled devices in practical chemical analysis - operational characteristics and considerations*, Multichannel Image Detectors, ed by Y. Talmi, Vol. 2 of ACS Symposium Series 236, pp. 133-153. American Chemical Society, Washington DC, 1983.
8. Williamson, J.M., Bowling, R.J., and McCreery, R.L., *Near-infrared Raman spectroscopy with a 783 nm diode laser and CCD array detector*, Appl. Spectrosc. **43**, (1989), 372-375.
9. Harris, T.D., Schoes, M.L., and Seibles, L., *High-sensitivity electronic Raman spectroscopy for acceptor determination in gallium arsenide*, Anal. Chem. **61**, (1989), 994.
10. Frank, C.J., McCreery, R.L., Redd, D.C.B., and Gansler, T.S., *Detection of silicone in lymph node biopsy specimens by near-infrared Raman spectroscopy*, Appl. Spectrosc. **47**, (1993), 387-390.
11. Lewis, E.N., Treado, P.J., and Levin, I.W., *A miniaturized, no-moving-parts Raman spectrometer*, Appl. Spectrosc. **47**, (1993), 539-543.
12. Treado, P.J., Levin, I.W., and Lewis, E.N., *High fidelity Raman imaging spectrometry: a rapid method using an acousto-optic tunable filter*, Appl. Spectrosc. **46**, (1992), 1211-1216.
13. Morris, H.R., Hoyt, C.C., and Treado, P.J., *Imaging spectrometers for fluorescence and Raman microscopy: acousto-optic and liquid crystal tunable filters*, Appl. Spectrosc. **48**, (1994), 857-866.
14. Carrabba, M.M., Spencer, K.M., Rich, C., & Rauh, D., *The utilization of a holographic Bragg diffraction filter for Rayleigh line rejection in Raman spectroscopy*, Appl. Spectrosc. **44**, (1990), 1558-1561.
15. Pelletier, M.J. and Reeder, R.C., *Characterization of holographic band rejection filters designed for Raman spectroscopy*, Appl. Spectrosc. **45**, (1991), 765-770.
16. Yang, B., Morris, M.D., and Owen, H., *Holographic notch filter for low-wavenumber Stokes and anti-Stokes Raman spectroscopy*, Appl. Spectrosc. **45**, (1991) 1533-1536.
17. Ellis, G.W., *A fiber-optic phase-randomizer for microscope illumination by laser*, J. Cell Biol. **83**, (1979), 303a.
18. Chang, I.C., *Noncollinear acousto-optic filter with large angular aperture*, Appl. Phys. Lett **25**, (1974) 370-372.



19. Yariv, A. and Yeh, P., *Optical Waves in Crystals*. John Wiley, New York, NY, 1984.
20. Webb, R. and Dorey, K., *Handbook of Confocal Microscopy*, ed. by J. Pawley, chap 4. Plenum Press, New York, NY, 1990.
21. ChemImag Technical Reference Manual, ChemIcon Inc., Pittsburgh PA, 1995.
22. Suhre, D.R., Gottlieb, M., Taylor, L.H., Taylor, L.H., and Melamed, N.T., *Spatial resolution of imaging noncollinear acousto-optic tunable filters*, Opt. Eng. **31**, (1992), 2118-2121.
23. Smith, W., *Modern Optical Engineering*, 2<sup>nd</sup> ed., chap. 8. Mc-Graw Hill, New York, NY, 1990.

## **Applications for Imaging**

# FACTORS AFFECTING AOTF IMAGE QUALITY

L.J. Denes, B. Kaminsky, M. Gottlieb and P. Metes  
Carnegie-Mellon Research Institute  
700 Technology Drive  
Pittsburgh, Pennsylvania 15230

## 1. Introduction

The advantages of the acousto-optic tunable filters (AOTF) in spectral imaging systems are largely the same as for non-imaging systems, and have been well established by recent work. The published literature contains many examples of AOTF's being successfully incorporated in imaging systems to be used for a variety of applications, but also point to several critical issues that must be addressed. These issues are largely driven by the particular requirements for high quality imaging, and often are not relevant for non-imaging applications. It is generally necessary to pay close attention to optimizing the design of the AOTF to assure good imaging quality, and to recognize the limitations that may be imposed by the fundamental physical effects.

A variety of physical factors must be considered in high image quality AOTF spectral imaging systems. The factors are manifested both in the basic design and in the implementation of AOTF-based imaging systems. The spatial resolution, background level and other quality criteria of the AOTF spectral image depend critically on the AOTF design details. We have analyzed the factors as they relate to spectral resolution, spatial resolution and AO interaction dispersion. Fabrication issues affect suppression of background through acoustic scattering, acoustic field homogeneity and optical scattering. In this paper we will review these effects and describe some measurements and analysis that we carried out for both infrared (IR) and visible wavelength AOTFs.

## 2. Image Blur

One of the major advantages of the AOTF is the relatively large angular aperture which enhances the throughput of the device. The large acceptance aperture results from the birefringent character of the diffraction process, so that there will be a dependence of diffracted image angle on wavelength; there will therefore be a blur, or angular spread, in the image due to the finite spectral bandpass of the AOTF. This angular spread can seriously degrade the image quality unless steps are taken in the design to minimize it. In this case it may even be possible to produce practical systems where the image resolution is no worse than that imposed by aperture diffraction.

We recently reported<sup>(1)</sup> on AOTF imaging in the 8 to 12 micrometer range using a TAS device. Calculations were made for  $\Delta\Theta_d$ , the internal angular spread of the diffracted light

as a function of  $\Delta\lambda$ , the bandpass of the AOTF. Plots of these results are shown in figure 1 for values of  $\Theta_i$ , the angle of incidence, from 5 degrees to 55 degrees. The increase in  $\Delta\Theta_d$  with bandpass is expected, since for a fixed value of  $\Theta_i$ , the acoustic beam spread must increase to accommodate increasing values of bandpass. This must be done by decreasing the acoustic interaction length, the only remaining design parameter. The increasing values of  $\Delta\Theta_d$  with increasing  $\Theta_i$  can be understood through some simplifying approximations in the analysis. For small values of  $n_i - n_d$  ( $n_i, n_d$  - refractive indices corresponding to the incident and diffracted beams) and  $\Theta_i - \Theta_d$ , the non-critical phase matching (NPM) condition can be approximated as

$$\lambda_0 / \Lambda = n_d (\Theta_i - \Theta_d), \quad (1)$$

where  $\lambda_0$  is the wavelength of the light wave,  $\Lambda$  is the wavelength of the acoustic wave.

The usual NPM approximation for the acoustic tuning wavelength is

$$\lambda_0 / \Lambda = \Delta n (\sin^4 \Theta_i + \sin^2 2\Theta_i)^{1/2}, \quad (2)$$

so that an approximation to the beamspread is

$$\Delta\Theta_d / \Delta\lambda = (\Delta n / n_d \lambda_0) (\sin^4 \Theta_i + \sin^2 2\Theta_i)^{1/2} \quad (3)$$

This approximation agrees well with the exact calculations plotted in figure 1, showing that maximum beamspread occurs at the  $\Theta_i = 55^\circ$  design, as expected.

While this simplified formulation shows the explicit dependence of the blur on the AOTF bandpass, it is straightforward to recast the dependence on the transducer length by substituting for  $\Delta\lambda$  its dependence on transducer length  $L$ ,

$$\Delta\lambda = 1.8\pi\lambda_0^2 / (\Delta n L \sin^2 \Theta_i) \quad (4)$$

to obtain

$$\Delta\Theta_d = 1.8\pi\lambda_0 (\sin^4 \Theta_i + \sin^2 2\Theta_i)^{1/2} / (n_d L \sin^2 \Theta_i) \quad (5)$$

It is clear that near diffraction limited performance for practical designs will only be achieved for fairly long interaction lengths yielding high spectral resolution, since we must satisfy the condition that  $\Delta\Theta_d < \lambda/D$ , where  $D$  is the aperture size. For a 1 cm aperture and a wavelength of 10 micrometers, this will be a beamspread of about 1 milliradian; from figure 1, this suggests that values of  $\Theta_i$  must, in general, be kept small for good spatial resolution.

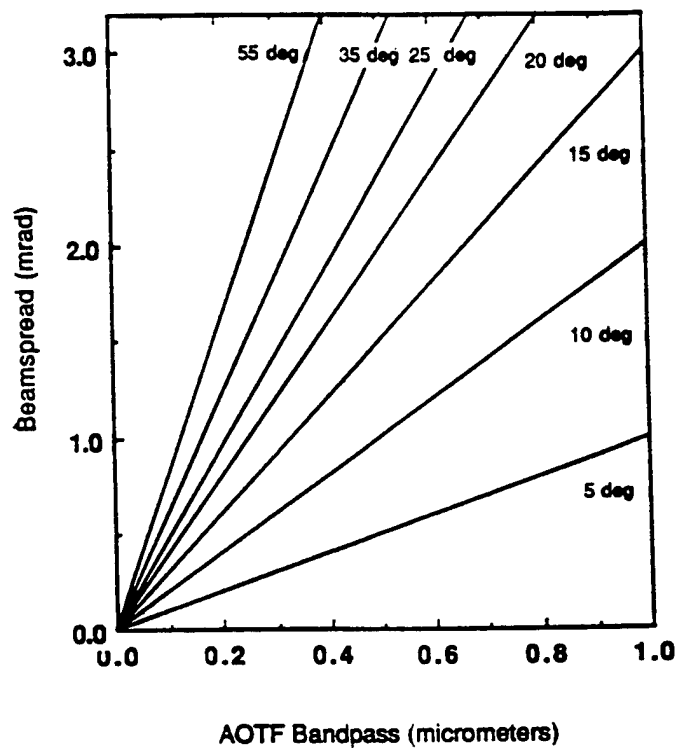


Figure 1. Calculated internal beam spread due to filter bandpass for various  $\theta_1$ .

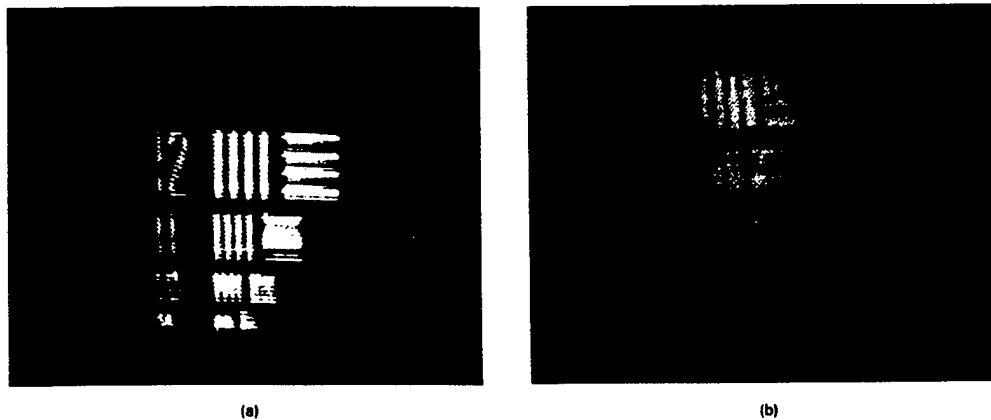


Figure 2. Infrared target image (a) without AOTF and (b) with AOTF.

Experimental measurements were carried out in the wavelength range from 7 to 11 micrometers with a TAS AOTF with  $\Theta_i = 35^\circ$ , 1 cm aperture and a bandpass of 0.13 micrometers. A standard IR resolution cutout target, illuminated with a  $300^\circ$  source was placed at a distance of 1.85 meters from the AOTF. The zero order and the diffracted images are shown in figure 2. The just resolved pattern is the no. 10, for which the bar periodicity is 0.2 inches, corresponding to 2.74 milliradians angular spacing. The calculated external beam spread for this AOTF due to its 0.13 micrometer bandpass, is 2.65 milliradians, so that the expected combined beams spread is 4.65 milliradians. Examination of the diffracted image patterns in figure 2 is in good agreement with this.

Effects of image blur are more prominent in the visible and near IR using  $\text{TeO}_2$  crystals, and great care is needed in designing imaging AOTF's to minimize blur effects. The two critical effects are due to bandpass, as described above, and image shift due to dispersion. Analysis and measurements were carried out at CMU<sup>(2)</sup> on a  $\text{TeO}_2$  AOTF custom built for this purpose by NEOS. Transducer length could be varied by external interconnections. The basic AOTF design parameters are listed in table 1.

Table 1  
AOTF-1 Parameters

$\Theta_i = 12$ degrees
$\Delta\theta_i = 6.5$ degrees (ext)
$\Theta_a = 5.9$ degrees
$L_1 = 0.33$ cm
$L_2 = 0.66$ cm
$L_3 = 1.32$ cm
$L_4 = 2.32$ cm
$\Delta\lambda/\lambda = .01$ (for $L = 2.32$ cm)

The transducer structure consisted of four elements, each wired to a connector on the mount so that it could be driven independently. Analysis and measurements on image blur were carried out, and the results are summarized in figure 3 for the four values of transducer length. The analysis indicates that a transducer length of about 3.5 cm is required to reduce the image blur to no greater than that due to aperture diffraction from a 1 cm aperture at 0.7 micrometers wavelength. This calculation is in good agreement with the experimental results in figure 3, which shows spectrally filtered photographs of a resolution chart taken with the four transducer lengths. The horizontal bars, unaffected by AO diffraction, are near diffraction limited resolution. For  $L = 2.32$  cm the analysis predicts the AO blur to be about 1.5x the diffraction limit, while it is about 6x for  $L = 0.33$  cm. This AOTF design is a reasonably good match between the spectral and spatial resolution characteristics.

### 3. Background Illumination

Another major source of AOTF image degradation is the loss of contrast due to high background levels. This background is largely out-of-band wavelengths, and is principally due to three causes: high sideband levels, light diffracted by acoustic energy reflected at various crystal surfaces, and light scattered by the crystal from its bulk, surfaces, and coatings. Measurements of this spectrally broadband background were made on the AOTF described in section 2, and the results are summarized in figure 4.

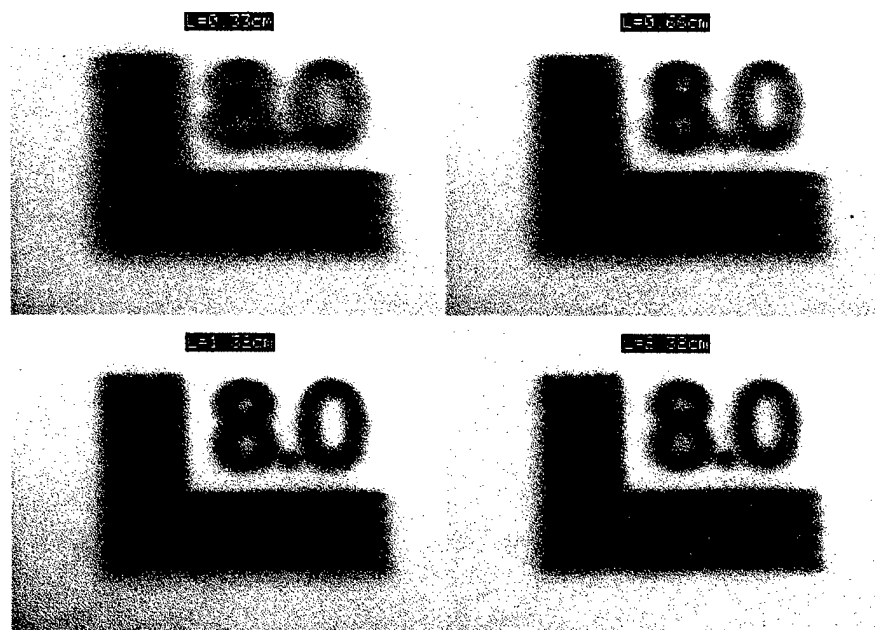


Figure 3. Target images taken with various transducer lengths.

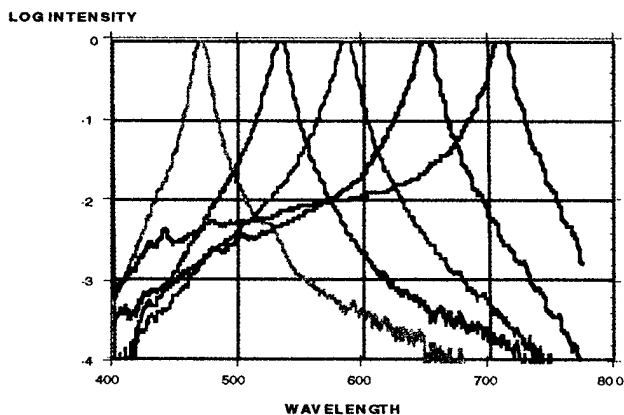


Figure 4. Spectral intensity distribution for several AOTF tuned wavelengths.

The AOTF was tuned for peak transmission at 5 wavelengths across its range: 470 nm, 486 nm, 535 nm, 650 nm and 710 nm. A spectrometer was used to measure the intensity from 400 to 770 nm for each of these tuning conditions. Close to the main peak, high sidelobes are the principal cause of the background, while further from the main peak phase matching to reflected acoustic energy may be dominant. The latter contribution was measured by using pulsed RF power and gating the detector so as to discriminate against the diffracted light due to the first transit acoustic wave. The background due to this cause is greater than -20 dB from about 450 to 650 nm. For imaging application for which a dynamic range of more than 30 dB is needed, it is clear that steps must be taken to greatly reduce the background from these effects through proper AOTF design .

We addressed the background issues with a TeO<sub>2</sub> AOTF imaging system based on a design described in table 2. We have found that a major cause of image degradation relates to the transducer structure and method of interconnecting elements. In order to achieve good impedance matching for a large area transducer, it is necessary to either interconnect several small elements in series, or drive each independently from a power splitter.

Table 2  
AOTF-2 Parameters

$$\begin{aligned}\Theta_i &= 10.7 \text{ degrees} \\ \Delta\theta_i &= 6.5 \text{ degrees (ext)} \\ \Theta_a &= 4.0 \text{ degrees} \\ \theta_{\text{face wedge}} &= 3 \text{ degrees} \\ \theta_{\text{blur}} &= 0.5 \text{ mrad (ext); } 3\times \text{ diffraction limit} \\ L &= 1.43 \text{ cm (3 elements, parallel or series)} \\ \Delta\lambda/\lambda &= .01\end{aligned}$$

In the latter case, the elements may have either a common ground plane or isolated grounds. For series connection a single matching circuit is used, and for parallel connection each element has its own matching circuit. The imaging results we obtained using multiple elements generally shows that there are distinct, multiple images, and a blur for each image corresponding not to the entire transducer length, but only to that corresponding to a single element length. This behavior suggests that the acoustic wave components generated at each element are not coherent, possibly not co-directional. We have found with one AOTF with parallel connected transducer elements multiple images resulted from cross-talk between the matching circuit due to inadequate isolation. In each case, we found, as expected, a strong correlation between image quality and how closely the passband of the AOTF adhere to the sinc<sup>2</sup> function. Two such passband characteristics are illustrated in figures 5 and 6; the former showing good agreement with theory, and the latter showing significant departure. We did not anticipate departure from theory for the series-connected configuration shown in figure 6.



It is important to realize that even in the case of perfect passband behavior, the image will be corrupted by the sidelobes, the first of which is only 13 dB below the main signal. This level is inadequate for many imaging applications. Attempts to address this problem by apodization of the acoustic field have not been successful because of the transducer fabrication difficulties in achieving a good enough approximation to the required field profile. We have demonstrated an alternative approach to sidelobe reduction which is based on the use of two AOTF's in series, for which the passband characteristic is  $\text{sinc}^4$ . The expected transmission for two identical filters in series is a reduction of the first sidelobes to -26 dB, and a reduction in the FWHM of the main lobe to about 75% of the single filter. A measurement of the passband was made for two AOTF's in series, and the results are shown in figure 7. The first sidelobe is about 25 dB below the main peak, in good agreement with theory.

Transmittance, a.u.

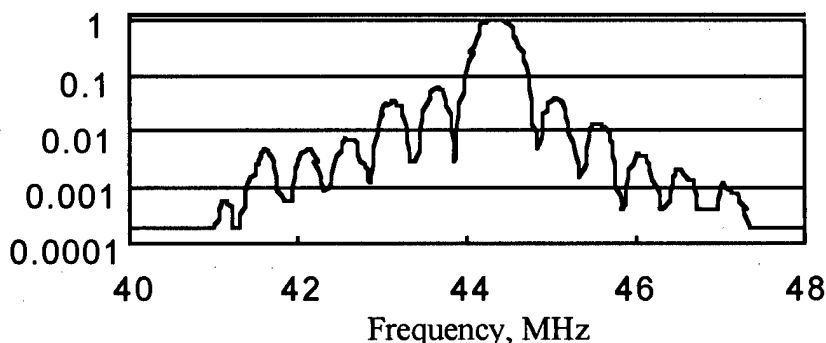


**Figure 5. Spectral resolution of NEOS 4-3-P-1 AOTF.**

Transmittance, a.u.

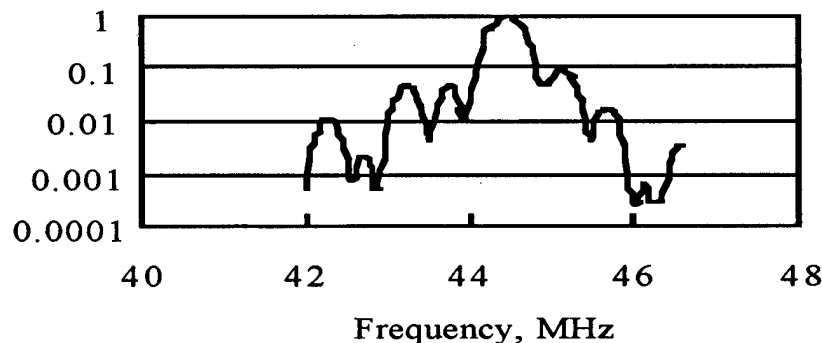


**Figure 6. Spectral resolution of NEOS 4-3-S-1 AOTF.**

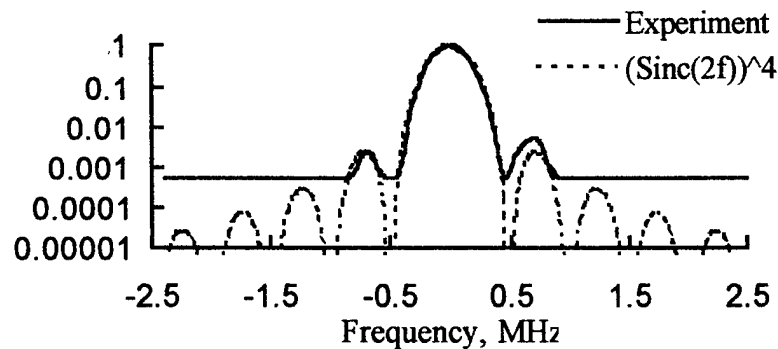


**Figure 7. Spectral resolution of NEOS 4-3-P-1 and 4-3-S-1 in series.**

Measurements were made of the white light spectral imaging characteristics of the same two AOTF's, individually and with both in series in the optical train. The target consisted of a cross cut into sheet metal, and illuminated from behind. The width of the cutout slit was 3 mm, and the target was placed a distance of 2.5 meters from the camera; therefore the slit subtended an angle of 1.2 milliradians at the input optics. Figure 8 shows the image of the target, and the intensity traces of the slit perpendicular to the AO diffraction plane, and parallel to the diffraction plane. The image of the vertical slit is corrupted by the blur and sidelobe effects, and this is reflected in the trace. In figure 9 we show the image taken with the two AOTF's in series, in which the sidelobe images are no longer visible. We also show the intensity trace for the vertical slit, superposed on the trace for the single AOTF to show the same effect.

#### **4. Scattering**

A contribution to broad spectral background illumination limiting dynamic range will be caused by scattering of the incident white light image from the AOTF crystal volume, and its surfaces. This is not normally a problem, except for very high dynamic range systems, or very high resolution filters. A rough estimate of this limit can be made from existing scattering data, which suggests that for the best optical quality oxide crystals such as  $\text{TeO}_2$ , forward scattering values are about -50 dB; the scattering will be greater for most infrared AO crystals, such as TAS or very high resolution filters. A rough estimate of this limit can be made from existing scattering data, which suggests that for the best optical quality oxide crystals such as  $\text{TeO}_2$ , forward scattering values are about -50 dB; the scattering will be greater for most infrared AO crystals, such as TAS or  $\text{Hg}_2\text{Cl}_2$ . Assuming a  $\cos^2$  intensity dependence with respect to the forward direction, scattering into the diffracted image acceptance aperture is nearly the same value for typical AOTF designs. The ratio of scattered light intensity to diffracted image signal is approximately

$$I_{\text{scat}} / I_{\text{image}} = S (\Delta\lambda\delta\lambda) \cos^2 \phi / (p \eta), \quad (6)$$

where:

$S$  = scattering coefficient,

$\phi$  = scattering angle,

$\delta\lambda$  = AOTF resolution,

$\Delta\lambda$  = spectral range of light source and detector,

$p$  = polarization loss, at least 50%,

$\eta$  = AOTF efficiency.

For the AOTF design of table 2,  $S \sim 10^{-5}$ ,  $(\Delta\lambda\delta\lambda) = 100$ ,  $p = 0.5$ , and  $\eta = 0.5$ , so that the estimated scattered light intensity is about 24 dB below the image signal.

Measurements were made of the scattering level from the experimental AOTF's using a He-Ne laser as source, and scanning the detector in the image plane. These results are in reasonably good agreement with this estimate.

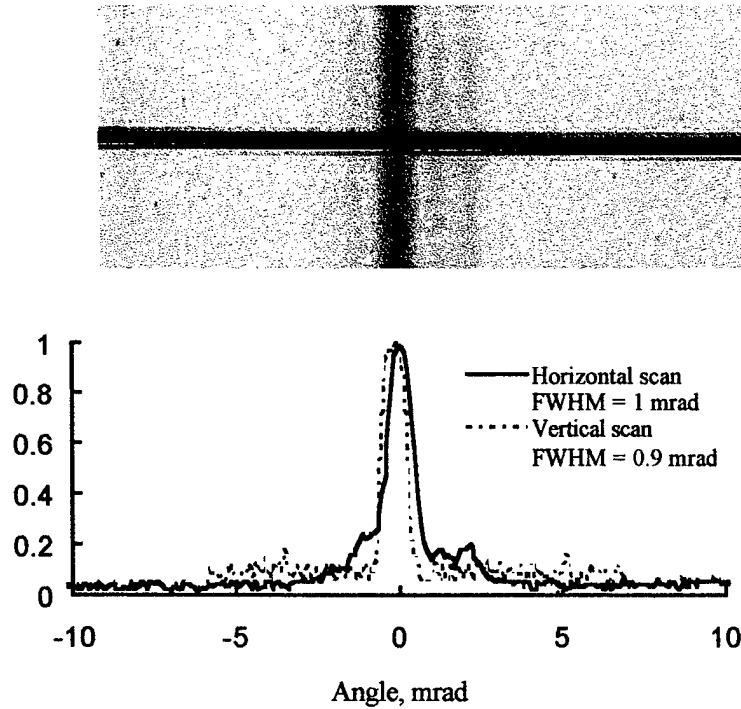


**Figure 8. Negative image recorded with NEOS 4-3-S-1 AOTF, and intensity scans parallel (i.e., horizontal) and perpendicular (i.e., vertical) to diffraction direction.**

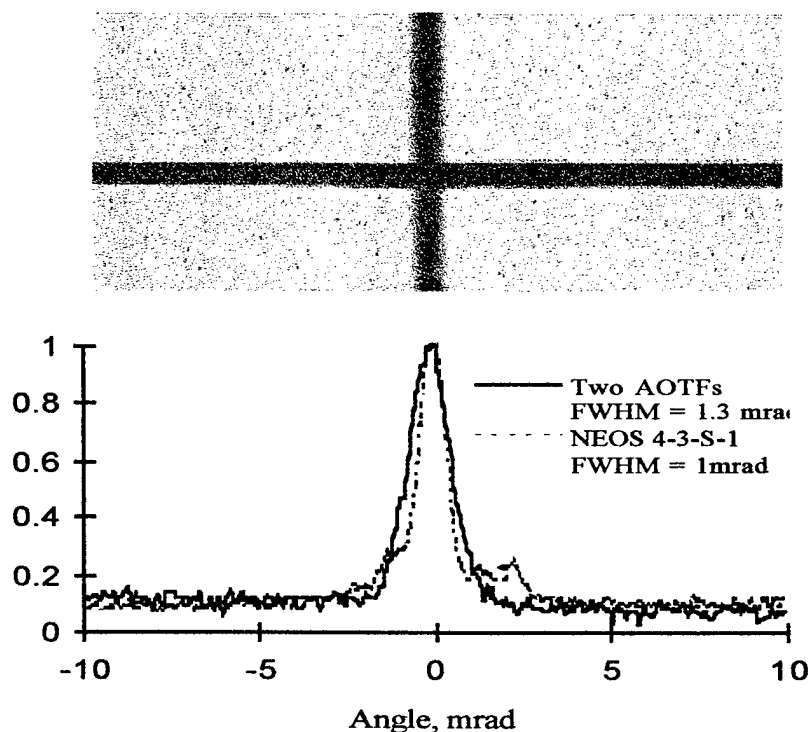


**Figure 9. Negative image using tandem AOTFs, and intensity scans comparing the tandem configuration with a single AOTF configuration parallel to diffraction.**

## 5. Conclusions

We have characterized several current-art AOTFs for spectral imaging application. Key measures of performance include: image blur, relative contribution from side lobes, contribution from background illumination and broadband scattering. The physics of operation is reasonably understood. Strides are being made towards implementation of the AOTF concept into useful spectral imaging hardware. AOTF design is application driven; no one design will optimally fill a variety of applications. Blur and ghost images are two areas not easily resolved using a single optimized AOTF design. We show that blur and ghost images can be obviated using a two AOTF design with little additional complexity.

## 6. References

1. D. R. Suhre, M. Gottlieb, L. H. Taylor, and N. T. Melamed, "Spatial resolution of imaging noncollinear acousto-optic tunable filters", *Optical Engineering* **31**, 2118-21 (1992).
2. E. S. Wachman, Carnegie Mellon University Center for Light Microscope Imaging and Biotechnology, private communication.

This work was supported under U.S. Army SBIR subcontract, No. DAAB07-93-C-0005, and U.S. Navy contract N00014-95-1-0591.

# **An AOTF Camera for Multispectral Imaging\***

**S. Simizu, R. T. Obermyer, C. J. Thong, M. J. Uschak, and S. G. Sankar**

**Advanced Materials Corporation  
700 Technology Drive, Pittsburgh, PA 15230**

**and**

**L. J. Denes, D. A. Purta, and M. Gottlieb**

**Carnegie Mellon Research Institute  
Pittsburgh, PA 15230**

## **Abstract**

In this paper, we describe the construction and performance of an AOTF camera in obtaining images in the range of 450 ~ 1000 nm using a TeO<sub>2</sub> crystal. The camera is equipped with a zoom lens with a focal length of 80 ~ 8 mm to obtain a variable field of view of 1.6 ~ 16°. A combination of a 10-bit digital video camera and a high speed frame grabber board allows continuous display of high-resolution, filtered images on a computer monitor at 30 frames per second. Ability for target recognition can be significantly enhanced by processing filtered images. In a basic operation that requires two frame grabs at two different filter settings and image processing, a typical operating speed is currently limited to 6 fps. The pre-processing of the target image by the AOTF simplifies subsequent image processing and the processed image may be obtained in real time.

## **1. Introduction**

A non-collinear acousto-optic tunable filter (AOTF) offers a unique opportunity to combine spectroscopy and imaging.<sup>1</sup> A highly reliable system may be built for the range of 400 ~ 4,500 nm using a TeO<sub>2</sub> crystal whose acousto-optic characteristics are now well understood. With high resolution spectral data, a much higher level of image discrimination is possible than can be achieved by broadband color imaging. Because the

---

\* Supported by the US Army under Contract No. DAAB07-95-C-M042

switching time of the AOTF is in the range of microseconds, acquisition of spectral data can be performed in real time. In this paper, we discuss the construction and performance of such a system and will give an example of how it may be applied to enhance the imaging capability. A block diagram of the system is given in Fig. 1. Some details of each component are given in Section 2. The performance of the current system is discussed in Section 3. An example of target identification is discussed in Section 4.

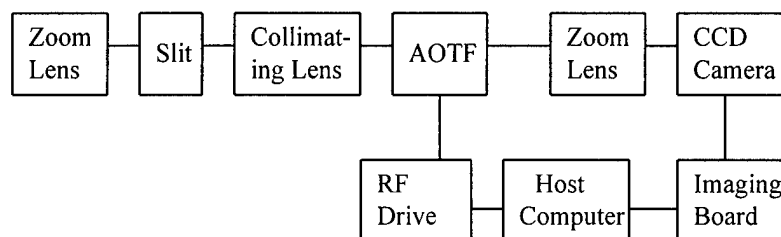


**Fig. 1. A block diagram of the AOTF camera system.**

## 2. System Overview

### 2.1 AOTF Design and Accompanied Optics

To apply the AOTF for imaging, the diffracted, filtered image must be separated from the unfiltered image. With the non-collinear AOTF that involves polarization of light, this may be accomplished by using crossed polarizers. To maximize transmission efficiency, however, we prefer spatial separation of the filtered and unfiltered images. The angle of separation depends on the AOTF design, but is typically a few degrees. With our design\* based on  $\text{TeO}_2$ , this angle is  $2.3^\circ$  (40 mrad). The output face is wedged so that no appreciable image shift occurs in the designed operating range of 450 ~ 900 nm. The corresponding acoustic frequency range is 60 MHz to 30 MHz. The expected filter bandwidth is about 1 % of the wavelength.

The field-of-view of the camera may be adjusted by using a zoom lens and a matching camera lens that serves as a collimating lens for the AOTF. By changing the ratio of the focal lengths of the zoom lens and the collimating lens, the effective field-of-view can be varied easily. Using a 8 - 80 mm zoom lens and a 50 mm collimating lens, we were able to obtain a field-of-view of  $1.6 \sim 16^\circ$  in the horizontal direction whereas the filtered image is diffracted vertically. The lens for the camera is selected to match the maximum

---

\* The AOTF for this work was fabricated by NEOS, Inc. of Melbourne, Florida.

acceptance angle of the AOTF with the size of the image array. For example, to match with a CCD image array of 4.8 mm, the focal length of the camera lens should be  $(4.8 \text{ mm} / 2) / \tan(2.3^\circ / 2) \sim 120 \text{ mm}$ . We selected a zoom lens so that the system may be used for a variety of cameras.

## 2.2 Camera/Imaging Board

Because the filtered image contains only a small fraction of the incoming light, its acquisition requires a high sensitivity, low noise camera. We have selected a camera that features a signal-to-noise ratio of 63 dB at 0.5 lux, a 30 frames per second speed, and a digital output of 10-bit pixel depth (DVC-10D, DVC Co.) However, because of an initial installation problem, most of the data presented in this paper were acquired by a 'security' grade CCD camera (46 dB S/N ratio). The camera is interfaced with a PCI-based frame grabber board (Matrox Pulsar) for real time image processing.

## 2.3 RF Drive

We drive the AOTF from an arbitrary waveform generator (Tektronix/SONY AWG2040) for maximum flexibility. AWG2040 features a sampling speed of one giga samples per second and a one megabyte memory for the waveform storage with 8 bit data length. The unit communicates with the host computer via IEEE488 bus. The output of the generator drives a one Watt wide band amplifier, the output of which is split into three and fed into three transducers via an impedance matching network. The arbitrary waveform generator affords us a high degree of flexibility to drive the AOTF. For example, waveforms that achieve multiple passbands and a spread spectrum can be easily programmed. However, in many applications, desired effects may be obtained simply by switching between sinusoidal waves of selected frequencies. Such control functions may be implemented using a voltage controlled oscillator and a computer controlled D/A converter.

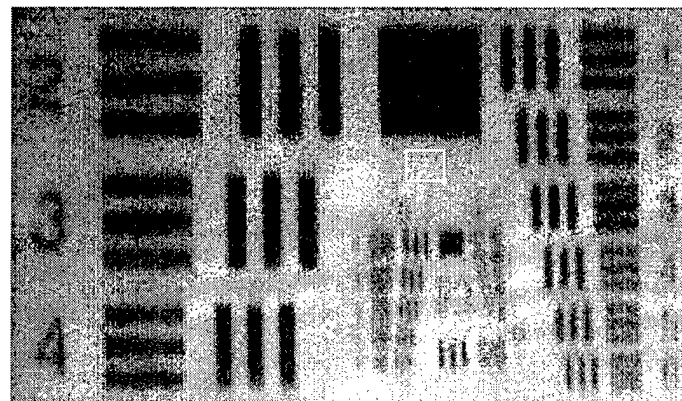
# 3. System Performance

## 3.1 Image Quality

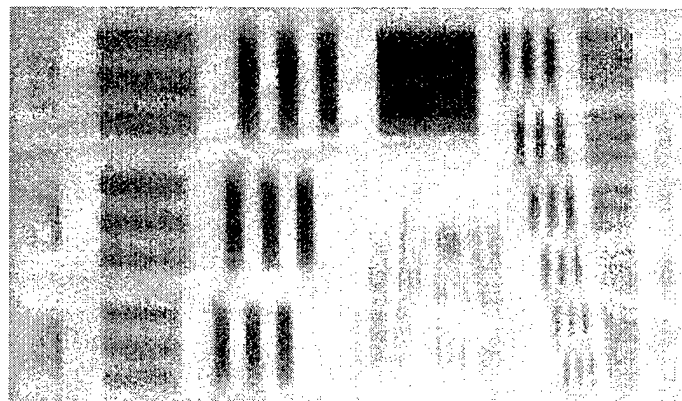
A detailed analysis of the factors that affect the image quality of the AOTF camera was conducted by L. Denes et al.<sup>2</sup> The quality of the image obtained with this camera may be judged by inspecting Fig. 2a, taken at 535 nm. Because the AOTF is mounted so that the direction of the diffraction is vertical, blur and smear are much more noticeable in the vertical direction. As a result, the vertical resolution is limited to 0.28 mrad while the horizontal resolution is 0.14 mrad. Because a single pixel corresponds to a 0.04 mrad in this case, the horizontal image resolution is limited primarily by the optics. The vertical blur of 0.28 mrad is comparable with the expected blur of  $\lambda/(zLn\theta) \sim 0.17 \text{ mrad}$ , where  $\lambda$

is the passband wavelength,  $z$  is the zoom factor of image,  $L$  is the length of the transducer,  $n$  is the index of refraction of the AOTF crystal, and  $\theta$  is the angle of the diffracted ray with the transducer plane ( $\lambda = 535$  nm,  $z = 2$ ,  $L = 0.01$  m,  $\theta = 0.07$  rad,  $n = 2.3$ ).

The image shown in Fig. 2a was obtained with  $\sim 0.19$  Watts of RF power to the transducer. The light throughput improves as the RF power is increased as shown in Fig. 3. However, the image quality begins to degrade as the throughput shows signs of saturation. The image taken with an RF power of 0.65 Watts (Fig. 2b) is considerably blurrier.



(a)



(b)

**Fig. 2. Images of a resolution chart taken by the AOTF camera at 535 nm and with an RF power of a) 0.19 Watts and b) 0.65 Watts. Although the higher RF power increases the light throughput, it tends to degrade the image.**



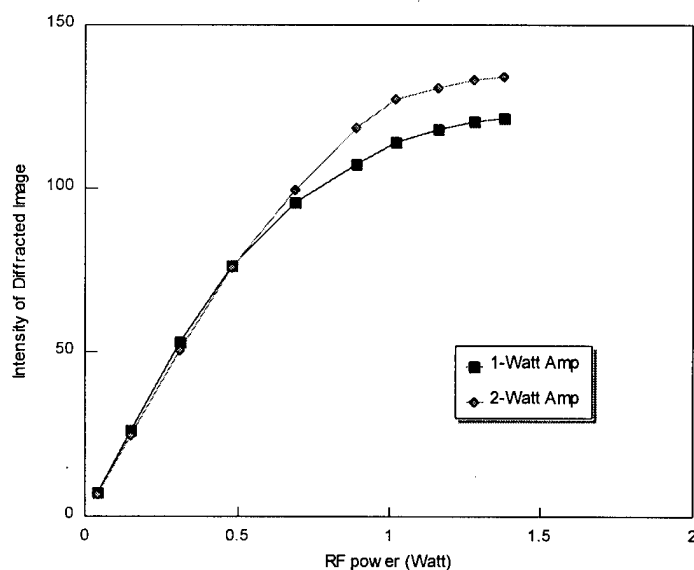


**Fig. 3. The light intensity and the RF power input. The light throughput increases proportionally to the RF power input but begins to show saturation above 0.5 Watts. Use of a power amplifier of a higher rating improves the linearity slightly in the high wattage range. However, noticeable image degradation begins at a wattage as low as 0.5 Watts. (See Fig. 2.)**

### 3.2 Filter Characteristics

With this camera system, spectral data can be easily obtained for a selected portion of the image by scanning the RF frequency. The camera is pointed so that the specified window in the view is locked on the target. An average pixel value is calculated for the window that typically consists of 8 x 8 pixels. Such spectral data were first obtained for the light source with a known spectrum (projector lamp). Figure 4 shows the spectrum of the reflected light off a white piece of paper along with the spectrum of the light source. Results are specific to the camera and show considerable differences between the two tested cameras. The results indicate that the useful range of this AOTF camera is 450 ~ 950 nm as expected from the AOTF design and the characteristics of the CCD camera. The spectral data for other targets were then normalized against the spectrum of the reflected light off white paper. Several targets made of color filters backed with white paper were examined. Examples of such spectral scan are given in Figure 5. They show good agreement with the spectral data provided by the supplier.

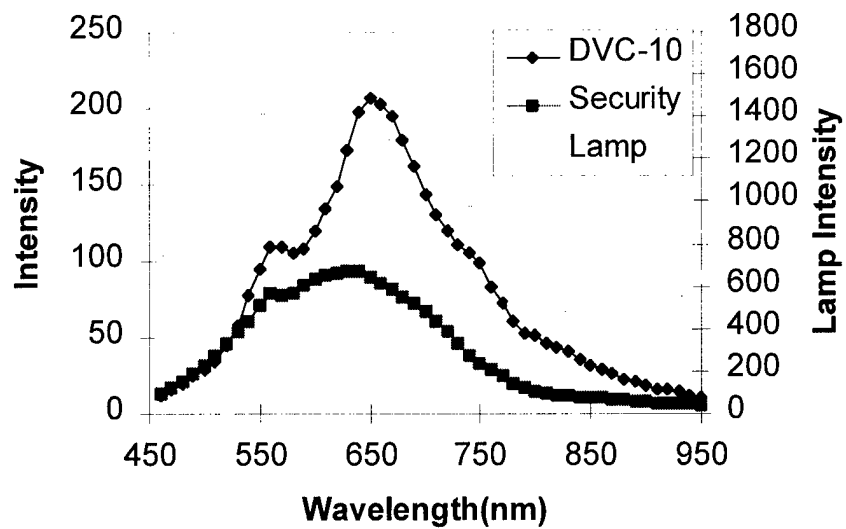


Fig. 4. The spectrum of the light source and the response of the AOTF camera system. In addition to the throughput of the AOTF, the spectral response of the camera system is strongly dependent on the CCD characteristics of the camera.

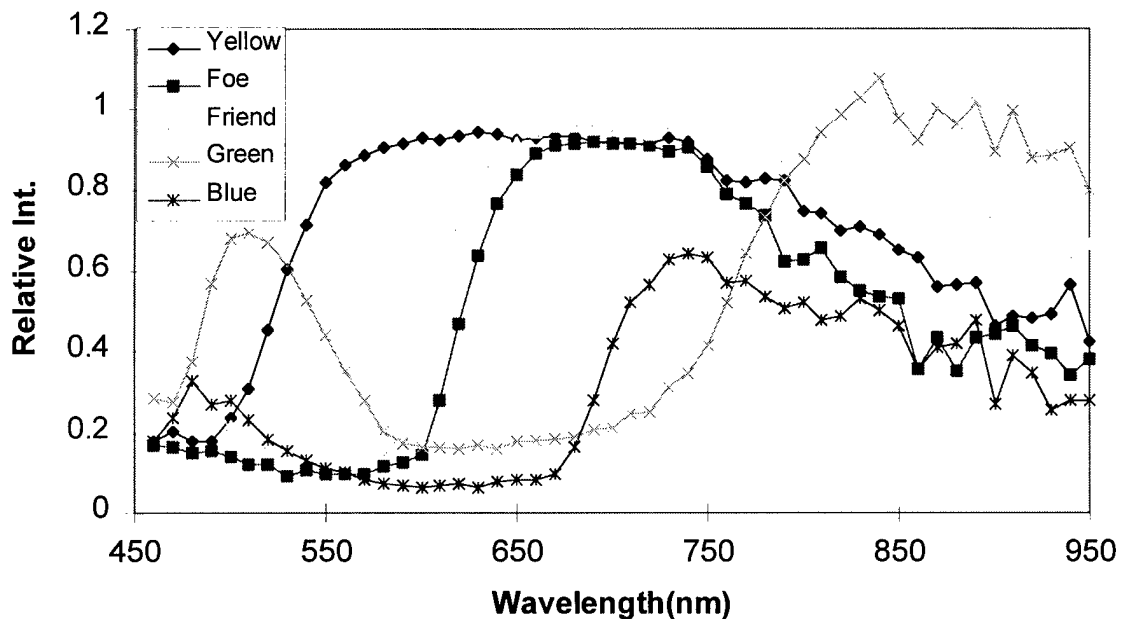
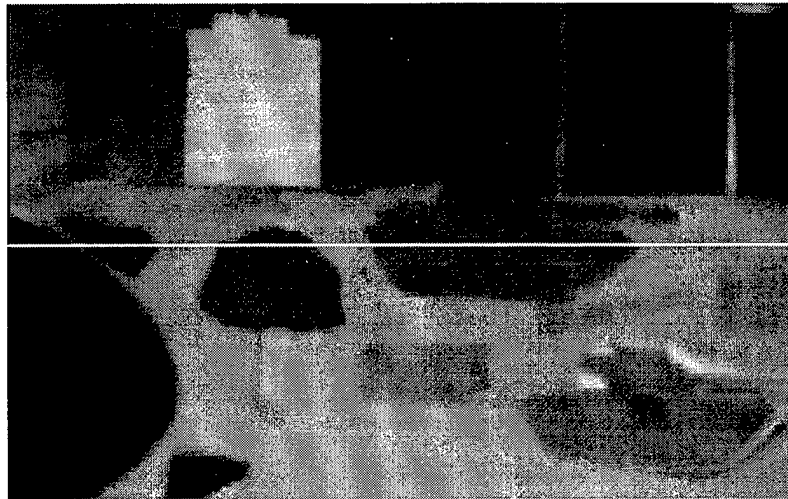


Fig. 5. Spectra of several color filters obtained by the AOTF camera. Filters denoted as 'Foe' and 'Friend' are red filters with slightly different spectra. These two filters were used for target identification tests described in Section 4.

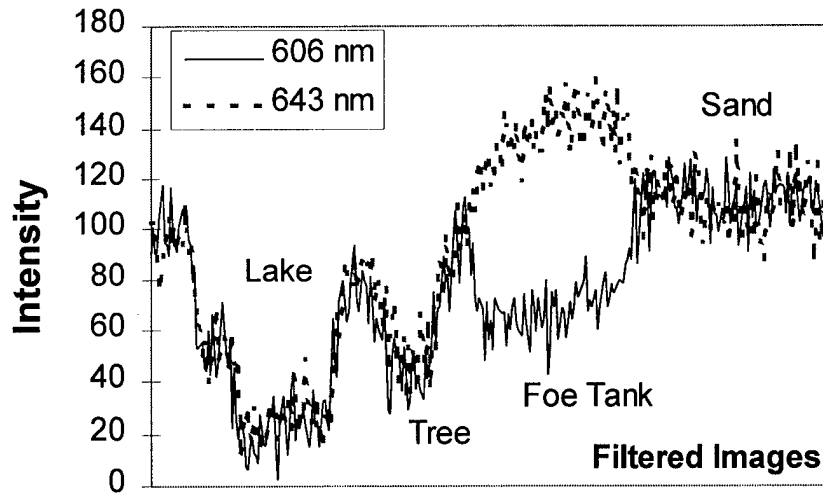
## 4. Target Recognition by Multi-spectral Imaging

To demonstrate the target recognition capability of the AOTF camera beyond the level of broadband color camera, we created a 'war' scene that contains two red colors with slightly different shades. Their spectra obtained with this camera are shown in Fig. 5. The color of the 'foe' tank (at the top of Fig. 6) cuts off at a slightly longer wavelength than the color of the 'friend' tank (at the bottom of Fig. 6) and it appears slightly less intense than the 'friend' tank in this unfiltered image. However, the differences are subtle and it is difficult to discriminate the two tanks with ordinary monochrome or color camera images. We selected two passbands at 643 nm and 606 nm and acquired images with the AOTF camera at these passbands. (The 'security' camera was used for this run.) Figure 7a shows the intensity of each pixel in a horizontal scan that runs across the 'foe' tank in the image. Similar data for the 'friend' tank is shown in Fig. 7b. Despite the considerable amount of noise in these pixel-by-pixel data, both 'foe' and 'friend' tanks stand out by this modulation. Thus both targets can be identified unambiguously with a simple pixel-by-pixel operation. Because the change in the intensity is much larger for the 'foe' tank than for the 'friend' tank, both tanks can be easily discriminated against each other and all other objects in the image.

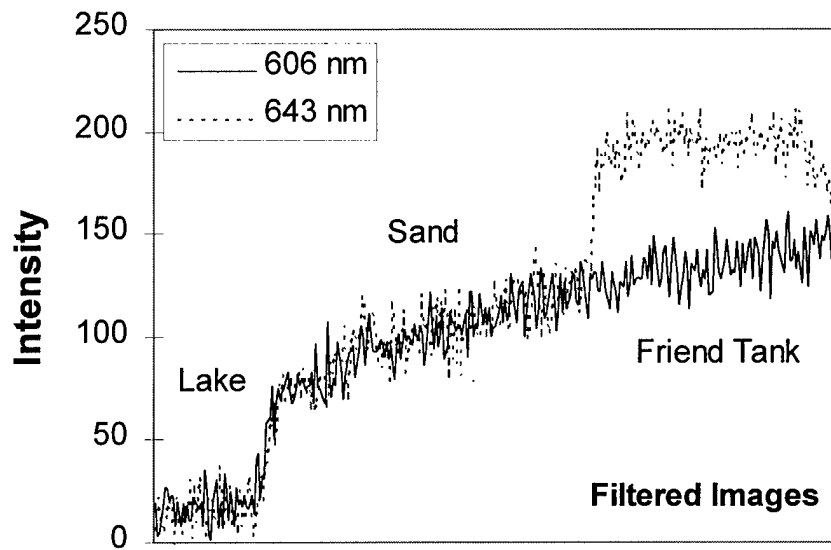
The host computer was programmed to give continuous display of two filtered images and a processed image. Figure 8 shows a snap shot of this process. Compared with the unfiltered image in Fig. 6, filtered images appear to be somewhat blurred. This is due



**Fig. 6. A 'war' scene created by several color filters. Two 'tanks' are made of red color filters with slightly different shades (see Fig. 5). This image was taken without the AOTF. A white line in the middle indicates where the intensity data shown in Fig. 7a were scanned through. (Data in Fig. 7 were obtained for filtered images, however.)**

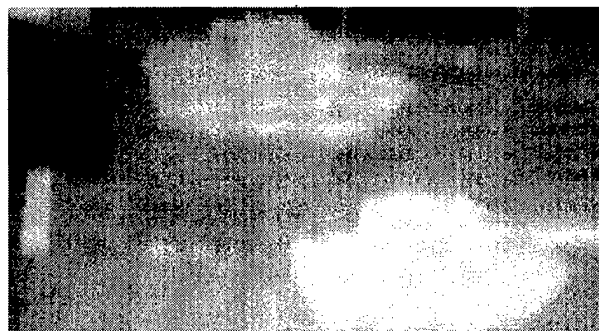


(a)

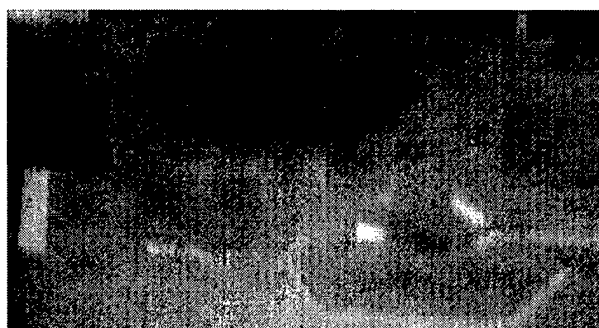


(b)

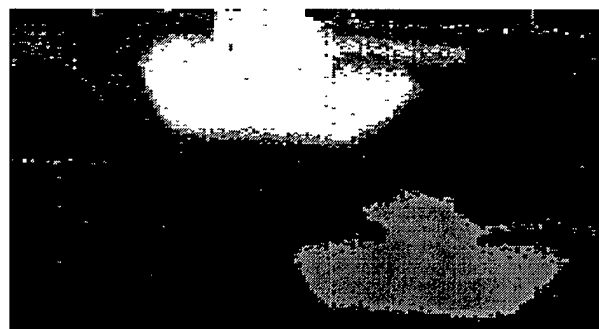
**Fig. 7. Horizontal scan of the intensity of each pixel in filtered images. The light intensity seen by each pixel is plotted for two horizontal lines: a) scans through the 'foe' tank and b) scans through the 'friend' tank. Tanks made of red colors filters stand out above the background noise and baseline bias when the passband wavelength is switched between 643 and 603 nm. Because the amount of the change is much larger for the 'foe' tank, it can be easily discriminated against the 'friend' tank.**



**(a) Filtered at 643 nm**



**(b) Filtered at 603 nm**



**(c) Processed Image**

**Fig. 8. A snap shot of target identification operation. The target identification operation based on two filtered images are run continuously at a rate of 6 frames per second. The processed image shows the pixels that belong to the 'foe' tank in white, the 'friend' tank in gray, and all other pixels in black. Almost all the pixels were identified correctly.**

mainly to lower light intensity which results in poor signal-to-noise ratio. Nevertheless, two tanks were clearly identified with only a small number of mis-identified pixels. (For ease of reproduction, the pixels identified as 'foe' were assigned the highest gray scale value of 255 (white) and those for 'friend' were given a value of 128. All other pixels were set to 0 (black). In real time display, these pixels are shown by more conspicuous colors [red and green] using pseudo-coloring.)

Because the image processing itself is straightforward and not very time-consuming, this target identification scheme can be processed in real time or near-real time. Presently, operating on an image of 320 x 200 pixels, the frame rate for the processed image is about 6 frames per second. As shown in Table I, the speed is actually limited by the RF switching speed of the arbitrary waveform generator. For this simple method, however, the time for switching may be eliminated by running from a voltage controlled oscillator, for example. By processing in parallel, real time operation of up to 30 frames per seconds should be achievable without requiring specialized imaging equipment and computer hardware.

**Table I. Typical processing speed for target identification. A single image process requires acquisition of two frames at two different RF drive settings. Electrim 1000L is an ISA board-based digital camera. Digitized image frame is directly saved on the host computer's main memory. Matrox Pulsar is a PCI-based frame grabber/display board. Most of the data presented here were acquired with this configuration. Note that the total processing time is less than the sum of each step because some of the processing steps are done in parallel.**

	Electrim 1000L	RS170/Matrox Pulsar
RF Switching (x 2)	100 msec	100 msec
Exposure Time (x 2)	200 msec	33 msec
Frame Grabbing (x 2)	700 msec	50 msec
Memory Copying (x 3)		15 msec
Image Processing/Display	400 msec	50 msec
Total	1300 msec	175 msec

## References

1. "Design and Fabrications of Acousto-Optic Devices", Eds., A. P. Goutzoulis and D. R. Pope, Marcel Dekker, New York, 1994.
2. L. J. Denes, B. Kaminsky, M. Gottlieb, and P. Metes, "Factors Affecting AOTF Image Quality", First ARL Workshop on Acousto-optic Tunable Filter Technology, University of Maryland, September 24 and 25, 1996.

# Simultaneous Multispectral Imaging with 12 Parallel Channel Tunable Camera

J. A. Carter III, D. R. Pape, Photonic Systems Inc., Melbourne, Florida

URL <http://photon-sys.com/>

M. L. Shah, MVM Electronics, Inc., Melbourne Florida

## Abstract

The Simultaneous Multispectral Imaging System (SMIS) utilizes 2 polychromatic acousto-optic tunable filters (PAOTF) and 6 CCD arrays with polarization optics and dichroic filters in each of two parallel optical paths to provide simultaneous polarimetric imaging in six tunable wavelength bands in the 420 to 700 nm range. Optical aberrations introduced by the acousto-optic interaction in the PAOTF are controlled by a unique transducer apodization scheme and compensated with a novel optical system design yielding good spectral resolution and image quality.

## Introduction

This paper describes the Simultaneous Multispectral Imaging System design and development. Fundamentally, the Acousto-Optical Tunable Filter (AOTF) provides an efficient and easily tuned filter for spectral imaging. However, the AOTF suffers from aberrations and dispersive effects that are difficult to model in image analysis and optimization software. These effects significantly degrade the performance of even a moderate resolution imaging system. Photonic Systems Inc. (PSI) and MVM Electronics (MVM) have developed the capability to control and compensate these aberrations using proprietary software and AOTF fabrication techniques. PSI and MVM plan to release a tunable camera based on a low cost RS170 video sensor to the research and color process communities in the fourth quarter of 1996.

## Background and Chronology

In 1991, PSI and MVM began collaborating on tunable filter imaging approaches. On July, 20, 1992, PSI and MVM jointly proposed "*A Simultaneous electronically variable Multi-spectral Imaging System*" to NASA JPL as a Phase I SBIR effort. This proposal was funded as Contract NAS7-1222. In August of 1993, the Phase II proposal was submitted to JPL and it describes the development of the *Simultaneous Multispectral Imaging System* (SMIS). The Phase II SBIR effort was funded and the contract NAS7-1311 was let in April of 1994. PSI and MVM are now completing that system. A prototype AOTF and compensation optics set were presented at the SPIE AeroSense Technical Exhibit to provide a preliminary demonstration of these technologies.

# Simultaneous Multispectral Imaging System

We have completed the design of a high resolution tunable camera system. The design is based on 12 separate image sensors that give 6 separate wavelengths in two polarization states or 12 separate wavelengths for randomly polarized scenes. The system is based on the visible spectrum with 512 by 512 image sensors for each channel and is designed for ground based astronomy. Table 1 lists the salient performance specifications for the Simultaneous Multispectral Imaging System (SMIS).

Wavelength Range	420 nm to 700 nm	6 or 12 selections, continuous range
Spectral Resolution	3 nm, 9 nm, or 15 nm	Programmable, user defined *
Spatial Resolution	500 resolvable elements	Rayleigh criteria *
Throughput Efficiency	greater than 80%	peak at center wavelength for each of two polarized fields

\* *spectrally dependent*

Table 1: SMIS Performance Specifications

## System Description

The SMIS operates on an input image field and can be made to accommodate a number of application specific fore-optic systems. The input field is separated into two fields with orthogonal polarization states. Each of these channels is filtered by two separate AOTF stages. Each AOTF is specially designed to operate with multiple tones and diffract three separate spectral images. A schematic of the SMIS is shown in Figure 1.

Separating the polarizations at the input increases the number of AOTFs from two to four; however, this allows us to independently select the wavelength set in each polarization. Therefore, the SMIS operates with up to 12 different wavelengths simultaneously when the polarimetric information is not important.

The three spectral bands diffracted from each PAOTF pass through a dispersion correcting system and are imaged by a well corrected lens. Two dichroic beam splitters in the path of diffracted light

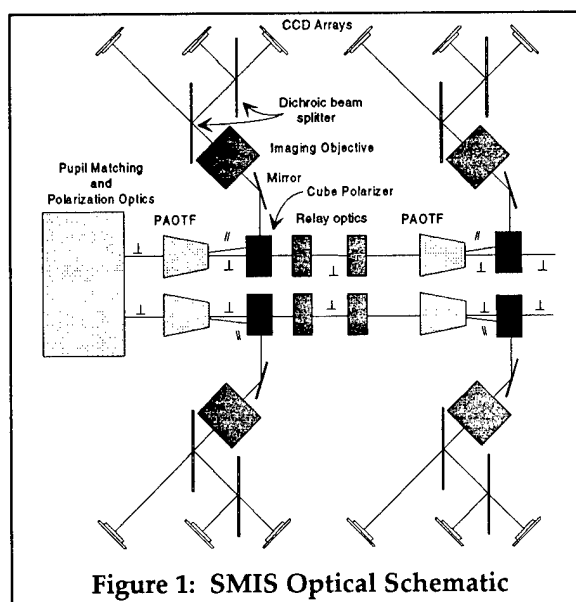
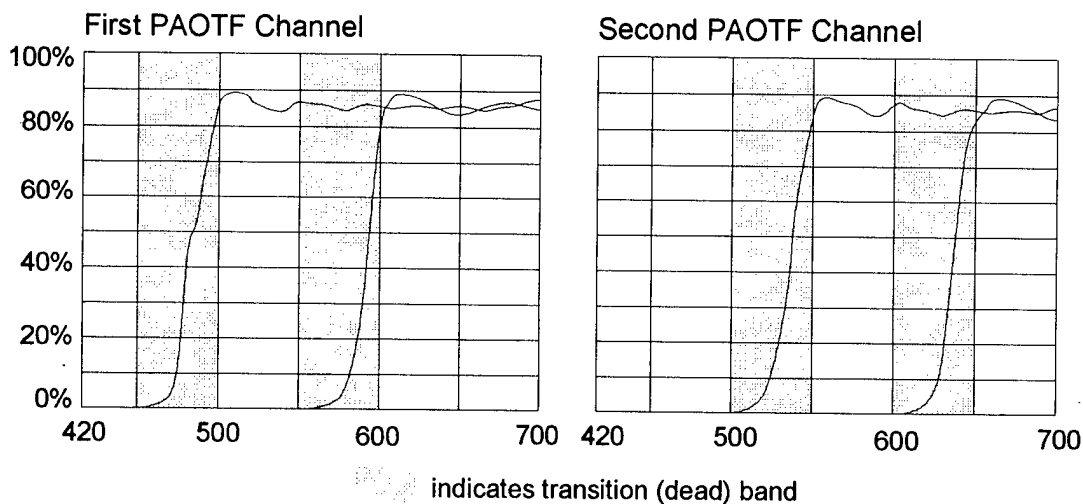


Figure 1: SMIS Optical Schematic



distribute, about evenly, the whole visible spectrum to three CCD arrays, which are placed at the image position. Thus, each of the three narrow spectral bands images on to separate CCD arrays. Two PAOTFs in tandem separate six narrow spectral bands. Unfortunately, a finite amount of band (approximately 10% of the cut-off frequency) is required to transition between the stop and pass bands. This transition region is not suitable for discriminating spectral energy. Therefore, two separate PAOTF channels are required to cover the entire spectral band so that the dead bands of one channel are covered by the other. Figure 2 shows the final selection of the dichroic filters such that the transition regions do not overlap and ensure that no dead band occurs.



**Figure 2: Spectral Passband Map of the SMIS**

The prototype SMIS targets ground based visible astronomy applications for NASA JPL. Astronomical imaging usually involves very low light scenes. The SMIS is designed to use high precision, cooled CCD arrays that can integrate for up to 5 minutes. Note that all preliminary image scenes and data are taken with a commercially available RS170 video sensor with 1/30th of a second integration time and using less than 20 milliwatts of RF drive power.

## Design Methodology

The development of this system lead to creating several key capabilities. The first and second relate to modeling and designing the compensation optics, respectively. A custom FORTRAN routine provides the capability to model the AOTF within an imaging system using CodeV from Optical Research Associates in Pasadena. This module interfaces to the User Defined Surface option in CodeV. The complete parametric description of the AOTF allows this module to model any AOTF device including the entrance and exit angels, acoustic transducer angle and crystal axes with their nonisometric acoustic and optical tensors. Unfortunately, the User Defined Surface traces rays too slowly to be an effective approach for optimization in CodeV which must trace many hundreds of rays in each optimization cycle. The second capability involves the development and test of stand alone software that traces rays through the AOTF and compensation optics. This program uses Damped Least Squares to optimize the compensation

optics. The compensation design is then placed in CodeV with the AOTF and imaging optics for design verification. Figure 3 shows the image plane analysis of the prototype AOTF and compensation optics with the color corrected objective that was designed and fabricated specifically for the SMIS.

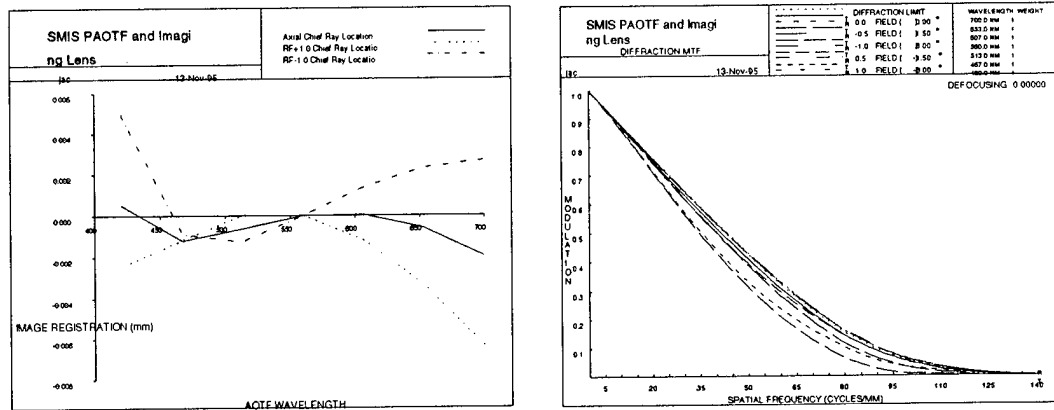


**Figure 3: SMIS Optical Performance: Chief Ray Deviation, and Polychromatic MTF**

The pixel subtends 19 by 19 microns for the SMIS system. The registration for the center of the image is well within 4 microns while the edges of the image register within at least 9. While the SMIS design requires the use on parallel faced (non-wedged) crystals, the compensation method can be applied to wedged devices. However, wedged devices will almost certainly require more expense than parallel. The use of external compensation gives the added bonus of adjusting the compensation to provide for variance in the fabrication of AOTF devices. This gives better device yield for compensated imagers due to increased acceptance criteria.

The third and perhaps most important development regards the AOTF device and its acoustic transducer design. The design of the transducer represents a very important aspect of the system performance. The transducer must be shaped to provide the minimum level of acoustic beam side-lobes in the propagation of the sonic field. The side lobes of acoustic energy create ghost images in the sensor field that cannot be compensated with passive optics. Figure 4 shows the image data recorded from an early prototype and the final prototype that is presented for demonstration.

Also, the impedance matching of the very large area of the transducer that has the effective impedance of only a few ohms is of equal importance. MVM has developed a unique and novel approach to the AOTF transducer that is currently submitted for patent protection.

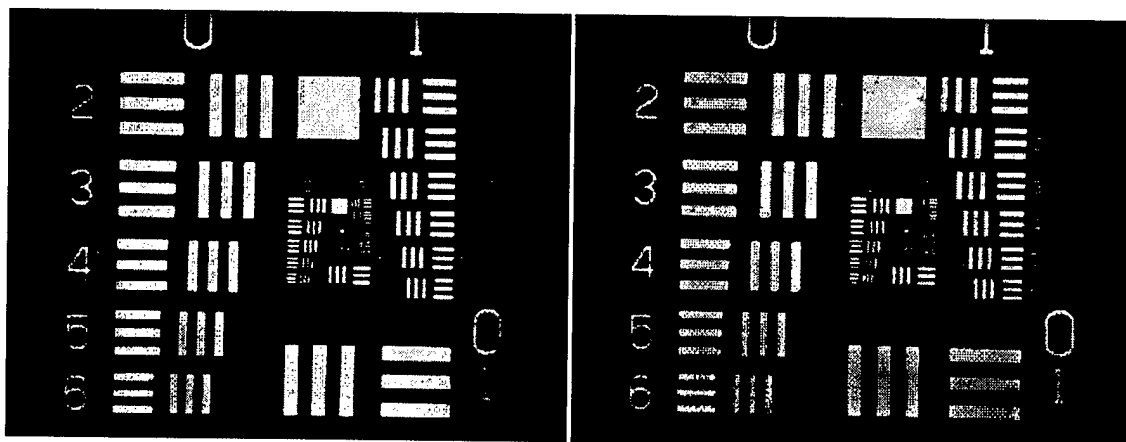


Figure 4a: Early AOTF Prototype

Figure 4b: Final AOTF Design

Figure 4 Air Force Resolution Chart

## Prototype Performance

The Simultaneous Multispectral Imaging System is currently in the fabrication and integration process. Preliminary results are limited to the lab bench breadboard optical system.

## Conclusion

PSI and MVM Electronics have developed a completely compensated tunable camera system that provides for simultaneous multispectral imaging. The compensation for this system provides fraction of a pixel image registration for all points in the image over the entire spectral band. Since the compensation optics are designed externally to the AOTF design and fabrication, they represent a reduced cost when compared to high precision wedges in the AOTF crystal fabrication. Further, external compensation provides adjustment for AOTF fabrication variance at the time of system integration and thus improves the yield of acceptable AOTF devices. These developments and methods provide the basis of spectral sensors from the UV to the mid-IR. PSI and MVM welcome the opportunity to provide state-of-the-art tunable cameras to our customers. The visible camera outlined above in single or multispectral versions will be available in the fourth quarter of 1996. We also welcome the opportunity to provide quotations for special application sensors and designs for additional wavelength bands.

## Credits

PSI and MVM would like to thank Dr. Robert Nelson of the NASA Jet Propulsion Laboratories for his encouragement, guidance, and support. Without the funding from the NASA Small Business Innovative Research grant sponsored by Dr. Nelson, this important technology would not be available to the research and commercial communities.

# Polarimetric Hyperspectral Imaging Systems and Applications

Li-Jen Cheng, Colin Mahoney, George Reyes, and Clayton La Baw  
Center for Space Microelectronics Technology  
Jet Propulsion Laboratory  
California Institute of Technology  
Pasadena, CA 91109

and

G.P. Li  
Department of Electrical and Computer Engineering  
University of California  
Irvine, CA 92717

This paper reports activities in the development of AOTF Polarimetric Hyperspectral Imaging (PHI) systems at JPL along with field observation results for illustrating the technology capabilities and advantages in remote sensing. In addition, the technology was also used to measure thickness distribution and structural imperfections of silicon-on-silicon wafers using white light interference phenomenon for demonstrating the potential in scientific and industrial applications.

## 1. Introduction

The noncollinear acousto-optic tunable filter (AOTF) was invented by I. C. Chang<sup>1</sup>. Functionally, the AOTF is a real-time programmable high-resolution spectral bandpass filter with polarization beamsplitting capability. With proper optics and focal plane arrays, one can build a polarimetric hyperspectral imaging (PHI) system capable of measuring spatial, spectral, and polarization characteristics of a target with a single instrument.

We developed an AOTF-PHI prototype system operating in a wavelength range of 0.48-0.75 microns<sup>2</sup> and did a number of outdoor field experiments which demonstrated unique advantages of using AOTF-PHI in remote sensing applications. In addition, we investigated the potential applications of the AOTF technology in the non-remote sensing areas, specifically, in the area of semiconductor materials characterization.

Currently, we are in the process to develop an AOTF-PHI prototype system operating in the short-wave infrared range of 1.2-2.4 micron with the objective to demonstrate the technology capability from an airborne platform for USASSDC.

## 2 Ground Prototype System

The PHI system contains an optical subsystem, two integrating CCD cameras, a RF generator and a power amplifier, a PC computer for control and data acquisition, and monitors. The unique part of the system is the optical configuration as illustrated in Figure 1.

The system contains a 3 inch aperture, zoom telelens set with variable focal length of 80-200 mm as the objective lens; an aperture located at the objective lens image plane for allowing only photons from the desired scene to pass through; a collimating lens to create an intermediate pupil plane whose cross section is comparable with that of the AOTF locating at the pupil plane; a field lens to create adequate beam diversion for imaging at the cameras; and two cameras for recording two polarized images simultaneously.

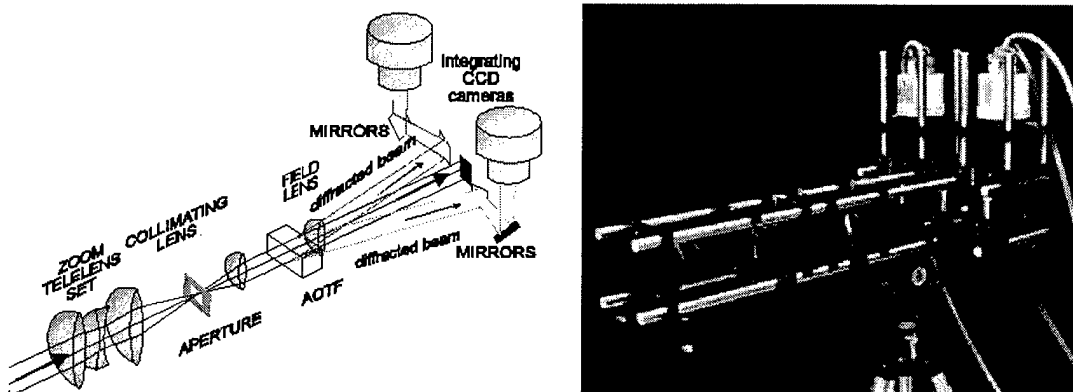


Figure 1. Left: Schematic diagram of the system optical configuration  
Right: Photo of the optical system without the cover.

## 3. Remote Sensing Results

### 3.1 Field Observations at Ft. Huachuca, AZ

Figure 2 gives a grayscale image of the scene taken by an ordinary 35 mm camera. The scene contained a variety of typical southern Arizona plants and a small number of Army facilities. The observation condition and data processing techniques were given in a previous paper<sup>3</sup>. In this report, the important observations are given. There was a reflection reference plate of BaSO<sub>4</sub> observable as a small bright rectangular object in the upper left part of the picture,

that was used for intensity normalization. The distance between the plate and the instrument was about 3.6 km. The observation was carried at the noon time of a sunny day. The atmosphere was clear with observable haze only when one looked at distant objects. The instrument directed at the north with 12 degrees off to the east.

### 3.1.1 Results

#### 3.1.1.1 Vegetation Signatures

Figure 3 gives a spectral image of the scene at  $0.67 \mu\text{m}$  at which the chlorophyll absorption is at maximum. Consequently, oak trees appeared to be dark, whereas mesquites were in gray. In general, all dark and gray areas were related to vegetation. The bright areas contained mainly dry grass and bare soil. Figure 4 gives reflected intensity spectra of oak and mesquite located in the lower left part of the scene, illustrating that the reflectance of oak is considerably lower than that of mesquite in the  $0.62\text{-}0.69 \mu\text{m}$  wavelength range, consistent with the observed image.

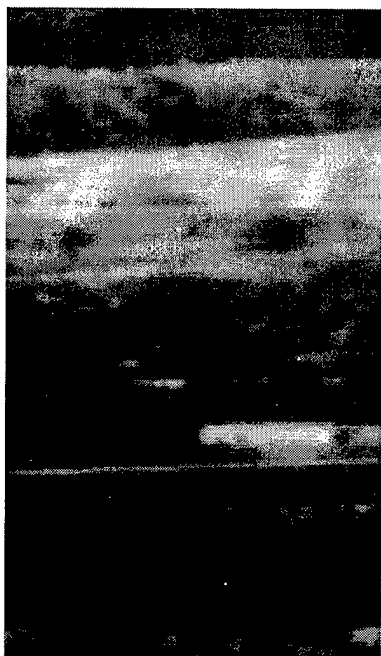


Figure 3. Spectral image at  $0.67 \mu\text{m}$ .

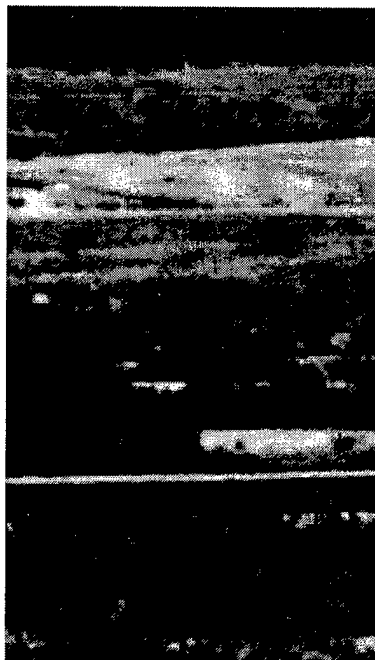


Figure 2. Grayscale image of the scene

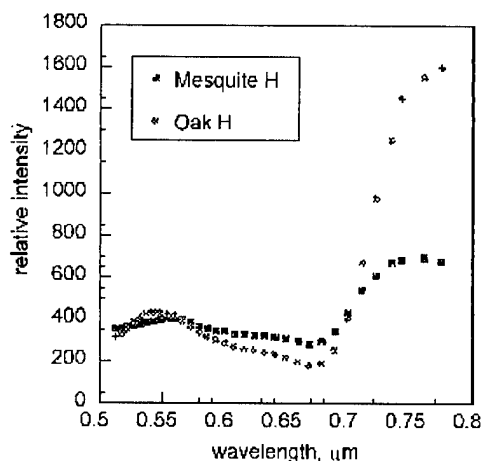


Figure 4. Reflectance spectra of oak and mesquite with horizontal polarization.

The observed spectra also show a sharp rise in the reflectance between  $0.69$  and  $0.73 \mu\text{m}$ , due to chlorophyll, illustrating an effective way to map vegetation using

spectral derivatives. Figure 5 gives a spectral derivative image of the scene at  $0.71\ \mu\text{m}$ . Bare ground and dry grass are often bright objects in the intensity image. Because of lack of chlorophyll, they become dark in this wavelength range. The brightness in the spectral derivative image mainly relates to leaf chlorophyll concentration. Therefore, the spectral derivative image is an effective approach for monitoring health state and stress response in vegetation.

### 2.1.1.2 Polarization Signatures

Polarization is an important parameter for analyzing signatures of objects obtained from a remote sensing instrument. The AOTF system provides two spectral image set with linear polarization directions orthogonal to each other. The data reported here were taken with polarization parallel and perpendicular to the ground. So we defined the measured polarization to be  $(I_v - I_h)/(I_v + I_h)$  where  $I_v$  and  $I_h$  are intensities at a same pixel of vertical and horizontal polarization images, respectively.

Figure 6 gives measured polarization spectra of oak, mesquite, and a unknown tree for illustrating some interesting spectral polarization features of tree leaves.

It is well known that vegetation has polarization signatures. The data in Figure 7 have revealed that leaves of these trees have a similar polarization spectral signature, namely a sharp descending step at  $0.69\ \mu\text{m}$  beyond which the signal is low. This descending step coincides with the increase of the red absorption edge. The observation suggests that the sharp decreasing feature could be related to the chlorophyll.

Figure 7 gives the polarization image at  $0.56\ \mu\text{m}$ . The polarization image quality was more shaper than that of spectral images. The loss of the spatial resolution in the spectral images can be attributed to be spectral mixing due to light scattering among neighboring objects.<sup>4</sup>



Figure 5. Spectral derivative image of the scene at  $0.71\ \mu\text{m}$  with horizontal polarization.

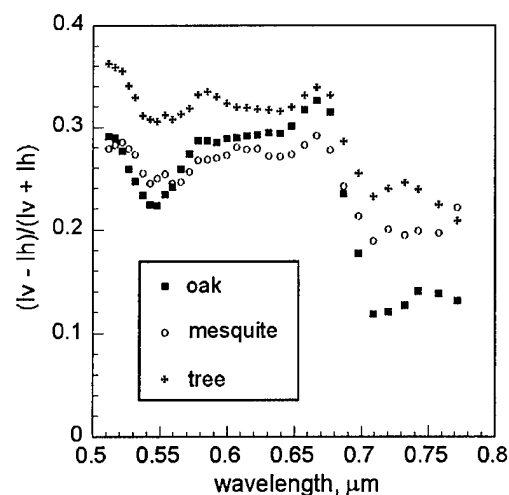


Figure 6. Polarization spectra of oak, mesquite, and unknown tree.

### 2.1.1.3 Target Detection

This polarization image has an inverse triangular dark pattern at the location left from the center of the scene. The pattern was composed several different objects. Each object has its own spectral dependence. Around 0.56  $\mu\text{m}$ , they appeared together as the observed pattern.

In the color picture taken by a 35 mm camera, the top corresponding part of the observed pattern is a small diamond-shape open area surround by brush. However, in the enlarged polarization image of Figure 8, only the brush at the left had normal vegetation polarization signal. There were two short dark line segments along the 'brush' edges at the upper, right, and lower sides of the open area. The darkness of the line segments indicated strongly that their origin must be some materials different from those of the vegetation. The neighboring area at the upper, right, and lower parts of the segments was also darker in comparison with the brush signal. These observations suggest that the line segments and some of their surrounding were man-made objects.

In the color image, the rest of the target appeared to be bright green trees with two separated green spherical objects. In the polarization picture, the spherical objects were very dark dots with a dark line between them forming a dumbbell pattern. The dumbbell pattern is likely to be a man-made object. In addition, in the polarization picture, the image of the 'green tree' area was composed with several broad horizontal gray line segments arranged in the shape of an inverted acute triangle.

These contradicting observations between the color and spectral polarization images, we concluded that we detected a camouflaged target area. A detailed observation at the enlarged picture provided a verification that the 'green tree' was green camouflage nets covering unknown objects and neighboring tree tops. The detection was mainly due to the spectral polarization imaging capability of the AOTF-PHI system. It ought to note that the lower part of the pattern was also



Figure 7. Spectral polarization image at 0.56  $\mu\text{m}$ .

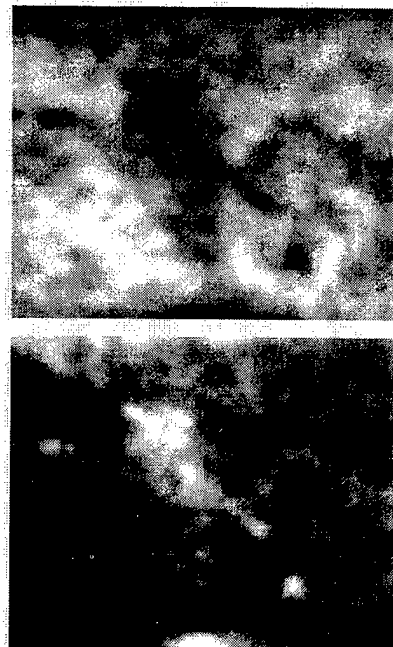


Figure 8. Enlarged positive (upper) and negative (lower) images of the pattern.



observable in spectral images of green wavelengths. However, the spectral polarization data provided the evidence for the determination of the target being camouflaged.

#### **3.1.1.4 Aerosol Scattering Effects**

The existence of atmospheric boundary-layer aerosols affects the magnitude, shape, and polarization of the spectra. The effects become substantial in the observation of distant objects. The measured differences in intensity, spectrum, and polarization due to the distance can provide important information about the aerosol. Using spectral and polarization data of two oak trees located at different distances from the instrument, we obtained the wavelength dependence of the scattering in the air at the observation site, from which one can obtain a smooth inverted wavelength power function, normally used to characterize light scattering in the atmosphere. More information on this subject was given previously.<sup>3</sup>

### **3.2 Mine Detection in An Iceplant Field <sup>4</sup>**

Figure 9 gives a grayscale image of an iceplant field scene with a group of targets of interest whose locations were indicated in a sketch at the right. The targets included seven inactive mines: one green square plastic (D), two green round metallic (A and C), two dark green round metallic (G and H), and dark brown round metallic (I and J). Some mines were placed on the top of the iceplant and some were pushed into the iceplant field so that only a portion of the target was visible. In addition, there were two partially observable cement blocks (B and E), and one buried white plastic pipe with one foot length being observable (F). The iceplant field was a mixture of healthy and dead iceplants with uneven distribution. In addition, portions of healthy iceplants were in blossom with orange flowers. This arrangement did provide an interesting challenge for testing the system capability.

The right upper corner of the scene were a pile of metallic sheets and parts whose images were removed during the data analysis so that we can obtain a better dynamic range in the area of interest. Two Halon plates (K and L) of the Lambertian surface reflectance over the instrument wavelength range were also placed in the scene for intensity normalization among different wavelengths. The PHI system was on the top of a small hill and looked at the area with a downward angle of about 30 degrees and directed at 210 degrees south. The observation was carried out at the noon. The iceplant field was located about 40 meter away from the system and on a small plateau of the hill. The weather was sunny with typical Los Angeles basin smog in June.

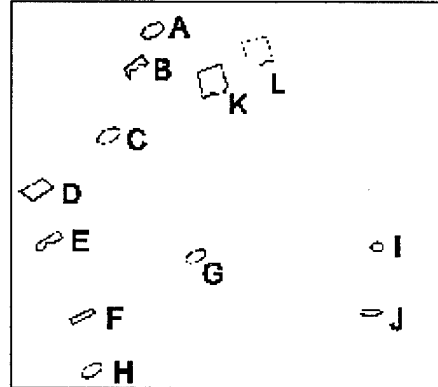


Figure 9. Left: Image of the iceplant field taken with an ordinary camera.  
Right: Sketch of locations of objects of interest in the iceplant field.

After image processing, we found that all the mines in the polarization difference images at the green wavelength range appeared as bright spots, whereas other objects were more difficult to be seen, as illustrated in Figure 10.

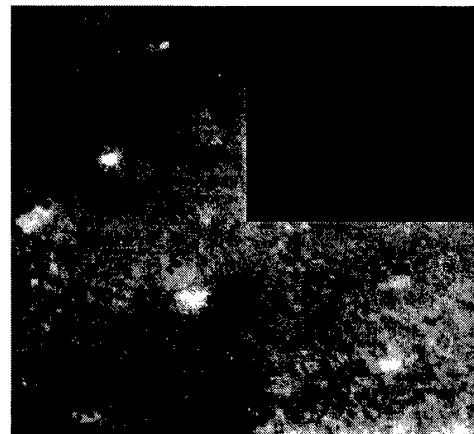


Figure 10. Polarization difference image at 0.55 micron illustrating that mines appear to be bright spots.

## 4. Non-remote Sensing Applications

### 4.1 Characterization of Silicon-On-Insulator (SOI) Wafers<sup>6</sup>

We successfully demonstrated the use of PHI to measure white light interference at the sample as a non-invasive characterization tool for SOI wafers. The samples were silicon-on-silicon wafers manufactured by subsidiaries of Hughes and IBM. The results have illustrated the PHI capability of providing high-resolution thickness maps of both Si and oxide layers with high accuracy and observing optically active imperfections and distributions in the SOI structure.

Each point on the wafer has its own interference spectrum plus a DC background. The DC component was removed for obtaining the interference amplitude spectrum (Figure 11). By comparison of the spectrum with the result from an

interference model, the layer thickness of silicon and oxide each location was obtained. In addition, a correlation function between the measured spectrum and that predicted from the model was also computed. This process provides a correlation map from which the structure imperfections can be detected and located. Figure 12 gives measured thickness maps for silicon and oxide layers at one sampled area as well as the correlation factor between the experimental spectrum and that predicted by the model. The means and standard deviations of silicon and oxide thickness and the correlation factor are shown at the lower part of the figure. The black spot in the correlation image was a serious structure imperfection.

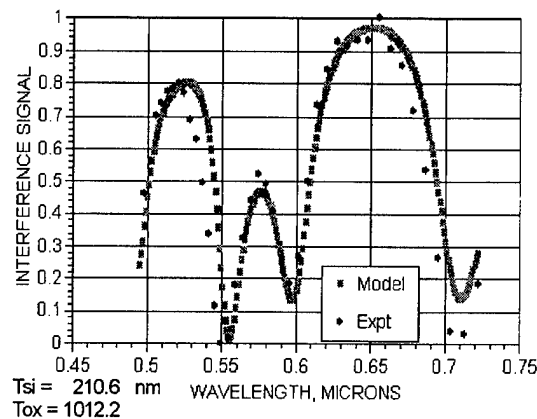


Figure 11. Comparison of theoretical and experimental interference spectra for obtaining the thickness of Si and oxide layers.

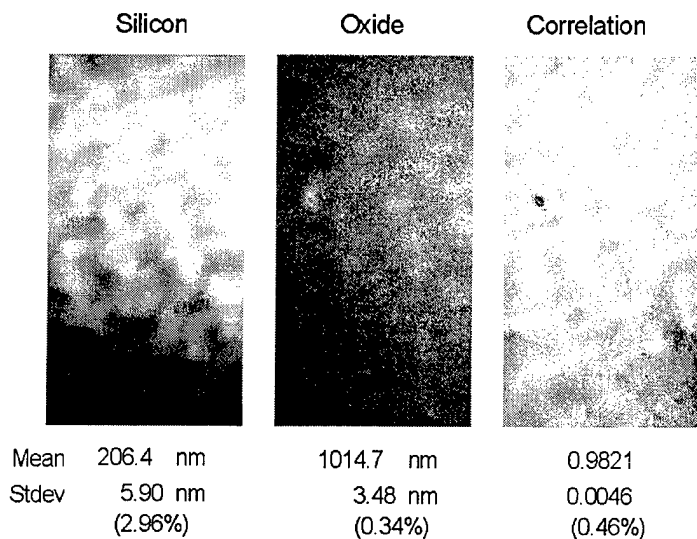


Figure 12. Silicon and oxide thickness distributions obtained from white light interference images as well as the correlation factor distribution of model prediction and measured data. The black spot in the correlation image reveals a serious structure imperfection at the location.

## 4.2 Microscopic PHI

An optical connection between the PHI system and a microscope was successfully made. This allowed us to obtain PHI images of small objects commonly observed only under a microscope. Figure 15 gives a pair of images on an individual FET test device in a VLSI wafer at two orthogonal polarization conditions.

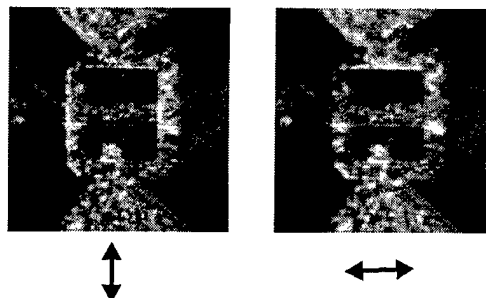


Figure 13. PHI images of an individual FET test device on a VLSI wafer at 0.685 micron with two orthogonal polarization directions. The dimension of the line width was about 5 microns.

## 5 **Brief Description of 1.2-2.4 Micron Infrared Airborne Prototype System**

We are developing a 1.2-2.4  $\mu\text{m}$ , short-wave infrared PHI prototype system for USASSDC. After successful ground tests, the prototype system will be flown on the ASETS C-130 plane based at the Eglin Air Force Base. The instrument will be mounted in the turret assembly and will observe selected targets on the ground.

The instrument will have one cooled focal plane array of HgCdTe, manufactured by Rockwell. A specially designed optical configuration currently during manufacturing will be used in the system. The configuration allows the system to record simultaneously two polarization images side by side on the focal plane array. This approach is an economic way, due to high cost of the focal plane array.

The system was designed to be a real-time instrument that will be able to collect an image cube data in seconds.

The system will use a  $\text{TeO}_2$  AOTF designed and manufactured by Aurora Associates.

### 5.1 **Important spectral features in this wavelength range**

#### 5.1.1 *Two major absorption bands due to $\text{H}_2\text{O}$ and $\text{CO}_2$ in the Atmosphere*

There are two major absorption bands centered at 1.4 and 1.9 micron due to water and carbon dioxide molecules in the atmosphere. No useful solar radiation are available within the wavelength ranges of these two bands.

#### 5.1.2 *Characteristic spectral signatures of man-made materials*

Nowadays, textures and paints are often made of synthetic materials, originally from petroleum products. These products often have characteristic spectral absorption features located at 1.7 and 2.3 microns. These two absorption bands occur in the atmosphere windows and are observable remotely. According to known spectra of organic materials, the spectral bands are likely vibration spectral overtones of hydrocarbon polymers. Therefore, they could occur in many synthetic materials, such as paints, clothes, and plastic wares, as well as camouflaged clothes and painted surfaces. The similarity shows that observation of these spectral bands only implies detection of a man-made object, and not necessarily detection of a military target. However, this is a necessary classification process for distinguishing man-made objects from natural substances. Target shape and polarization properties could provide further evidence for detection and identification.

## 6 Acknowledgments

The work described in this paper was performed by the Center for Space Microelectronics Technology, Jet Propulsion Laboratory, California Institute of Technology, and was jointly sponsored by the Army Space Technology and Research Office, the Marine Corps System Command, Code AW, the Army Space and Strategic Defense Command, and the National Aeronautics and Space Administration.

## References

1. I.C. Chang, "Noncollinear Acousto-Optic Filter with Large Angle Aperture", *Appl. Phys. Lett.*, Vol. 25, p.370 (1974).
2. Li-Jen Cheng, Tien-Hsin Chao, Mack Dowdy, Clayton LaBar, Colin Mahoney, George Reyes, and Ken Bergman, " Multispectral Imaging Systems Using Acousto-Optic Tunable Filter" , in "Infrared and Millimeter Wave Engineering" , SPIE Proceedings Vol. 1874, p. 224 (1993).
3. L.J. Cheng, M.K. Hamilton, J.C. Mahoney, G.F. Reyes  
"Analysis of AOTF Hyperspectral Imagery", in *"Algorithms for Multispectral and Hyperspectral Imagery"*, SPIE Proceedings, Vol. 2231, p158-166 (1994).
4. L. J. Cheng, J.C. Mahoney, G.F. Reyes, and H.R. Suiter, "Target Detection Using an AOTF Hyperspectral Imager", in "Optical Pattern Recognition V", SPIE Proceedings, Vol. 2237, p.251-259 (1994).
5. Li-Jen Cheng and George Reyes, "Polarimetric Hyperspectral Imaging for Mine Detection", in "Detection Technologies for Mines and Minelike Targets", SPIE Proceedings, No. 2496, p.305 (1995)
6. Li-Jen Cheng, Guann-Pyng Li, and De Yu Zang "SOI Characterization Using AOTF Polarimetric Hyperspectral Imaging" *Proceedings of 1994 IEEE International SOI Conference*, October 3-6, 1994, Nantucket Island, MA.

# Multispectral Imaging Using Acousto-Optic Tunable Filter (AOTF)

T. Vo-Dinh, D. Hueber and F. Moreau  
Advanced Monitoring Development Group,  
Health Sciences Research Division,  
Oak Ridge National Laboratory, Oak Ridge TN, 37831-6101

## ABSTRACT

This paper discusses the development of a multispectral imaging (MSI) device using acousto-optic tunable filters (AOTF). A two-dimensional charge-coupled device (CCD) was used as a detector. The AOTF was used as a wavelength selector. Unlike a tunable grating or prism based monochromator, the tunable filter has no moving parts, and it can be rapidly tuned to any wavelength in its operating range. The large aperture of the AOTF and its high spatial resolution allowed the optical image from an IFP to be recorded by the CCD. These characteristics, combined with their small size, make AOTFs important new alternatives to conventional monochromators, especially for spectral imaging in biomedical applications.

## 1. INTRODUCTION

Unlike a grating monochromator, an AOTF offers the advantage of having no moving parts and can be scanned at very high rates (millisecond time scale) without the possibility of error due to gear backlash or other mechanical problems. Since AOTFs with high spatial resolution (typically 100 lines per mm) and large optical apertures are available, they can be applied for spectral imaging applications.<sup>1,2,3</sup>

Our laboratory has particular interest in the development of molecular spectroscopic methods, portable instrumentation and/or remote sensors for field applications using fiberoptic probes<sup>4-9</sup>. Instrumentation utilizing conventional light sources<sup>10</sup> or small lasers<sup>11</sup> has been recently developed for this purpose. The use of AOTFs for UV-visible, near infrared and fluorescence spectroscopy has recently appeared in the literature<sup>12,13,14</sup> and several reviews have been published.<sup>15,16</sup> Levin<sup>17</sup> and coworkers have described a portable AOTF-based Raman spectrometer, a device which is also capable of fluorescence measurement. Since the invention of coherent fiber optic bundles in the middle of the century<sup>18</sup>, fiberscopes (or fiberoptic endoscopes) have been used in many fields<sup>19</sup>. Imaging fiberoptic bundles

have been used extensively in medicine research.

This work involves a multispectral imaging (MSI) system combining a two-dimensional CCD detector, an acousto-optic tunable filter (AOTF) device and optical imaging fiberoptic probe (IFP) technology. [Figure 1](#) illustrates the multispectral imaging concept, which combines spectroscopy and imaging techniques.

## 2. AOTF OPERATING PRINCIPLE

AOTFs use several types of materials. Since tellurium-oxide ( $\text{TeO}_2$ ) has a high acousto-optic figure of merit, it is the preferred AOTF material to be used from the visible to the infrared region. Due to its transmission cutoff at 360 nm, we have restricted this study to the visible range (450-670 nm). Collinear-quartz AOTFs and non-collinear  $\text{MgF}_2$  AOTFs are usable down to 200 nm. However,  $\text{TeO}_2$  AOTFs are preferred in the visible spectral range, since they generally have greater diffraction efficiency, require less cooling, are smaller and lighter, and generally less expensive. In addition,  $\text{TeO}_2$  AOTFs can have a larger optical aperture than the typical collinear-quartz type, which facilitates their use in imaging applications. AOTFs based on other crystals also function in the UV or visible ranges, however these types generally operate over smaller wavelength ranges.

In AOTFs a piezoelectric transducer is bonded to a birefringent crystal. The transducer is excited by a radio frequency (rf) (50-200 MHz) and generates acoustic waves in a birefringent crystal. Those waves establish a periodic modulation of the index of refraction via the elasto-optic effect.<sup>20,21</sup> Under proper conditions, the AOTF will diffract part of the incident light within a narrow frequency range. This is the basis of an electronically tuned optical filter using the Bragg diffraction of light by periodic modulations in the index of refraction in the crystal established by the acoustic waves. Only light that enters the crystal such that its angle to the normal of the face of the crystal is within a certain range can be diffracted by the Bragg grating. This range is called the acceptance angle of the AOTF. The percentage of light diffracted is the diffraction efficiency of the device. This parameter greatly depends on the incidence angle, the wavelength selected and the power of the rf signal.

In general, the diffracted beam is separated from the undiffracted beam by a diffraction angle in a non-collinear AOTF. The undiffracted beam exits the crystal at an angle equal to the incident light beam, while the diffracted beam exits the AOTF at a small angle with respect to the original beam. A detector can be placed at a distance so that the diffracted light can be monitored, while the undiffracted light does not irradiate the detector. In addition, when the incident beam is linearly polarized and aligned with the crystal axis, the polarization of the diffracted beam is rotated  $90^\circ$  with respect to the

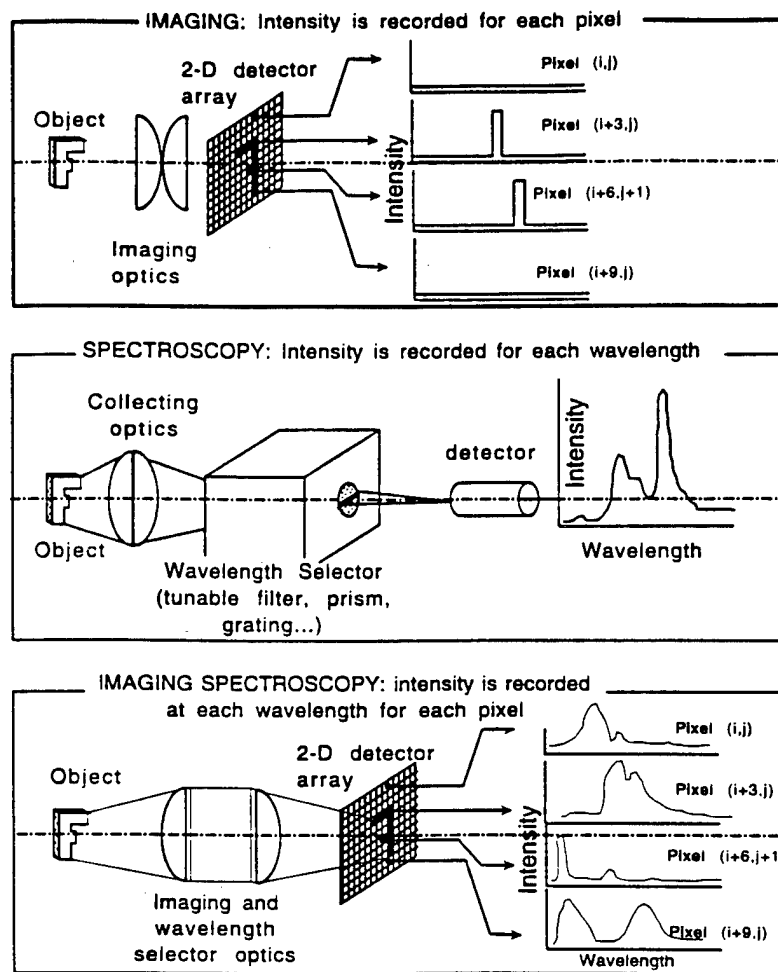


Figure 1: Principle of Multispectral Imaging

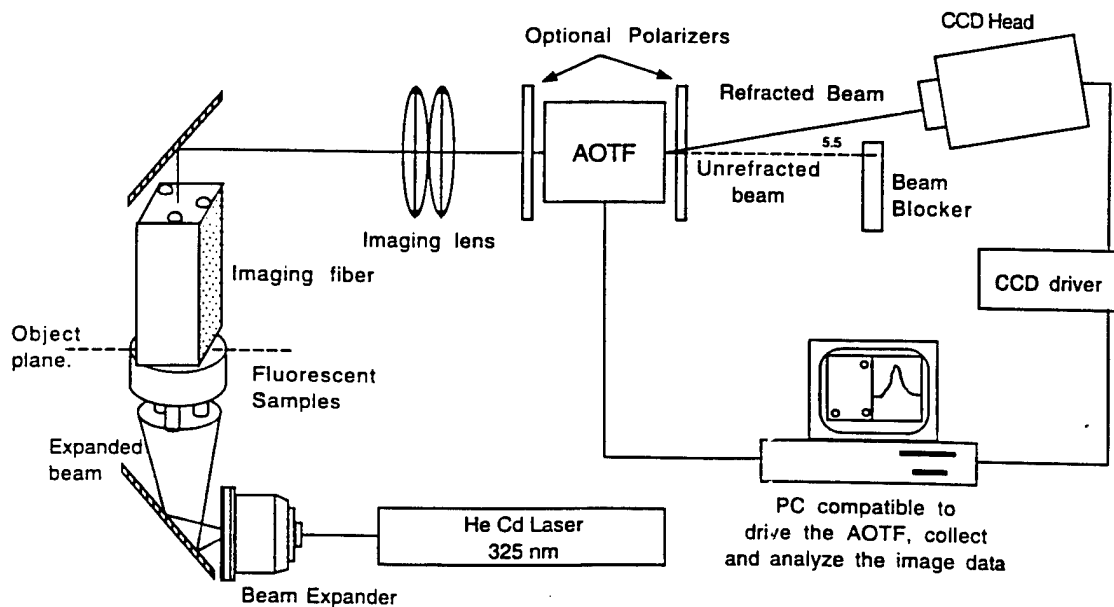


Figure 2: Diagram of the System Developed for Multispectral Imaging



undiffracted beam. This can provide a second means to separate the diffracted and undiffracted beams. One polarizer is placed before the AOTF, and is aligned with the crystal. At the exit of the AOTF, a second polarizer is rotated 90° with respect to the first. The undiffracted light is blocked by the crossed polarizers, while most of the diffracted beam escapes. The reader interested in the theory of AOTF operation is directed to several articles.<sup>22-26</sup>

Imaging systems often use charge-coupled device (CCD) image detectors, which have provided a remarkable tool for light measurement.<sup>27-36</sup> Scientific-grade CCDs offer very low dark current, high quantum efficiency, low readout noise, wide dynamic range, and internal signal integration. The CCD is well suited for imaging under low light conditions. The recent availability of inexpensive cooled CCDs makes them an even more attractive detector for a multi-channel spectrometer.

### 3. AOTF MULTISPECTRAL IMAGING DEVICE

This work involves the design and development of a prototype instrument for spectral imaging. The light emitted from the output end of the IFP was collected by an imaging lens, filtered by the AOTF, and then imaged onto a CCD. By changing the wavelength of the AOTF, a spectrum could be acquired as a series of images (one for each wavelength).

The TeO<sub>2</sub> AOTF used in this work was purchased from Brimrose, Baltimore, MD (model TEAF 10-45-70-S). According to the manufacturer, the AOTF had an effective wavelength range of 450 nm to 700 nm (corresponding drive frequency 178-100 MHz). The spectral resolution given by the manufacturer was 20 nm at 633 nm. The diffraction efficiency was 70% at 633 nm. The optical aperture was 10 by 10 mm and the acceptance angle was greater than 30°. The drive power was 1.0 to 1.5 W. The radio-frequency (rf) generator used (Brimrose-model AT) could apply 0 to 25 W of rf power and was controlled by a DOS-based computer using a 16-bit computer controller board supplied by Brimrose. A custom software was developed at Oak Ridge National laboratory to control the AOTF, supporting various scanning modes and fixed-frequency operation.

The CCD was a model ST-6 purchased from Santa Barbara Instrument Group, Santa Barbara, CA, based on a Texas Instruments TC241 CCD detector. The operating spectral range was 330 to 1100 nm. The detector was 8.63 x 6.53 mm and had a resolution of 750 x 242 pixels, with a two pixels horizontal binning giving an effective resolution of 375 x 242 pixels. Standard pixel size was 23 x 27 µm. Dark current could be kept as low as 13 electron/pixel/second at -20°C. The detector was installed on a regulated thermo-electric Peltier effect based cooler. Anti-blooming protection was also included. The analog-to-digital resolution was 16 bits. A mechanical shutter was included in the optical head to facilitate taking dark frames. The CCD controller is based on the IBM 8088

microprocessor and ran at 8 kHz. The interface to the PC compatible computer was accomplished through a regular RS232 cable and baud rate was 115.2 k baud.

The laser excitation source was a HeCd laser from Omnicrome, Chino, CA (Omnicrome-model 3074-6) with a  $\approx 8$  mW output at 325 nm. The IFP device was purchased from Schott Fiber Optics Inc., Southbridge, MA. It was a rigid image conduit for image transmission made of more than 400,000 individual 12  $\mu\text{m}$  diameter fibers fused together. (resolution is twice as much as the CCD resolution). Flat polished ends were 9.5 x 7.0 mm rectangles. Numerical Aperture was 0.56 (acceptance half-angle  $> 30^\circ$ ). Individual fibers were made of glass translucent from 400 nm up to the IR region and transmittance was higher than 0,990/25mm for the range 480-700 nm. An opaque encapsulation of the IFP provided physical protection as well as light shielding.

The spectral imaging instrument is illustrated in [Figure 2](#). The CCD was oriented  $5.5^\circ$  from the axis of the setup (due to the diffraction angle of the AOTF at a central wavelength: 550 nm). The AOTF was placed  $\approx 10$  cm in front of the CCD. An iris diaphragm was mounted at the entrance of the AOTF to prevent reflection inside the crystal. Two glass lenses (5 cm diameter) were used to collect the light and form an image on the CCD. The output end of the IFP was placed in the object plane of the lenses. The output end of the IFP was  $\approx 10$  cm in front of the lenses. Lenses were chosen to give a total magnification slightly less than unity, since the output end of the IFP is 9.5 x 7.0 mm and the CCD detector is 8,63 x 6,53 mm.

Optical lenses with a focal length greater than 100 mm were used to separate the two images (the diffracted and undiffracted), because the diffracted image and the undiffracted image must not overlap on the CCD detector, . Because the two beams diverged from one another with an angle of  $\approx 5.5^\circ$  after exiting the AOTF, a distance of 100 mm was required to allow a complete separation of the two images ( $100 \text{ mm} > 9.6 \text{ mm} / \sin(5.5^\circ)$ ). A physical black plastic shield was held in front of the CCD to prevent the undiffracted image from hitting the CCD. In addition, cross polarizers were set on both sides of the AOTF to increase the rejection ratio of the filter.

The IFP output end was placed exactly in the object plane by moving it in a micro positioning stage. The focus mode of the software driving the CCD was used to adjust the position of the IFP. The AOTF's wavelength was calibrated using a HeNe laser line and a mercury vapor lamp.

#### 4. CONCLUSION

This research illustrates the potential of a MSI that combines recent advances in several technologies, including a two-dimensional CCD detector, imaging

fiberoptic, and AOTFs. The integration of these technologies leads to a versatile and powerful imaging system that can remotely detect and analyze fluorescent objects. This imaging system could find useful applications in environmental and biological areas where the detection of multiple components in complex media is required. This study demonstrates the potential of the AOTF technology to be used for remote imaging spectroscopy and simultaneous spectrum acquisition of different fluorophor systems.

## 5. ACKNOWLEDGMENTS

This work was sponsored by the Office of Health and Environmental Research, Department of Energy, under Contract DE-AC05-84OR21400 with Lockheed Martin Energy System, Inc. This research was also supported in part by the appointment of D.M.H. to the U.S. Department of Energy Laboratory Cooperative Postgraduate Research Training Program administered by Oak Ridge Institute of Science and Education.

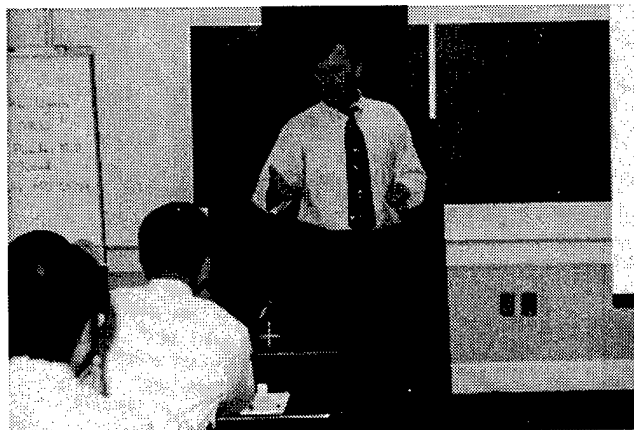
## 6. REFERENCES

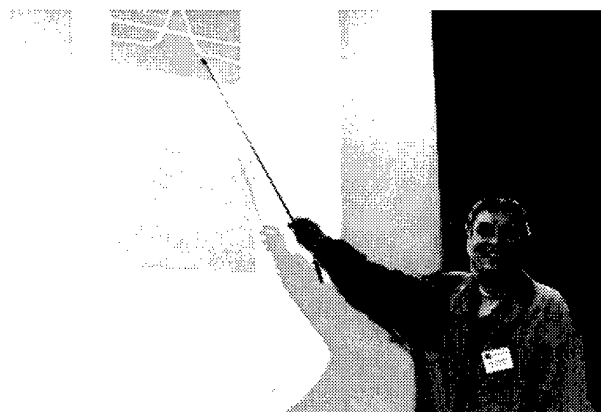
1. W.M. Hayden, W.V. Schempp, and C.P. Conner, *Pub. Astrono. Soc. Pacific*, 99, 1337-1343, (1987).
2. L.J. Cheng, T.H. Chao, M. Dowdy and K. Bergman, "Multispectral imaging systems using acousto-optic tunable filter," *Proceeding of SPIE*, 1874, 224-231 (1993).
3. T.H. Chao, J. Yu, L.J. Cheng, and J. Lambert, *SPIE*, 1347, 655-663, (1990).
4. James D. Ingle, Jr. and Stanley R. Crouch, *Spectrochemical Analysis*, Prentice Hall, Englewood Cliffs, NJ. 1988.
5. Philip J. Elving, *Treatise on Analytical Chemistry*, Part 1 volume 7 second edition. John Wiley & Sons NY. 1978.
6. R.D. Piccard and T. Vo-Dinh, *Rev. Sci. Instr.*, 62, 584-594, (1991).
7. T. Vo-Dinh, B.J. Tromberg, G.D. Griffin, K.R. Ambrose, M.J. Sepaniak, and E.M. Gardenhire, *Appl. Spectrosc.*, 41(5), 735-738 (1987).
8. T. Vo-Dinh, T. Nolan, Y.F. Cheng, M.J. Sepaniak, and J.P. Alarie, *Appl. Spectrosc.*, 44, 128-132, (1990).
9. J.M. Bello, V.A. Narayanan, D.L. Stockes, and T. Vo-Dinh, *Anal. Chem.*, 62, 2437-2441 (1990).
10. J.P. Alarie, T. Vo-Dinh, G. Miller, M.N. Ericson, S.R. Maddox, and W.E. Watts, *Rev.Sci. Instrum.*, 64(9), 2541-2546 (1993).
11. C.L. Stevenson, R. Johnson, and T. Vo-Dinh, *Biothechiques*, 16(6), 1104-1110, (1990).
12. W.S. Shipp, J. Biggins, and C.W. Wade, *Rev.Sci. Instrum.*, 47(5), 565-569, (1976).
13. D.M. Hueber, C.L. Stevenson, and T. Vo-dinh, *Appl. Spectrosc.*, 49(11), 1624-2631, (1995).
14. I. Kurtz, R. Dwell, and P. Katzka, *Rev.Sci. Instrum.*, 58(11), 1996-2003, (1987).

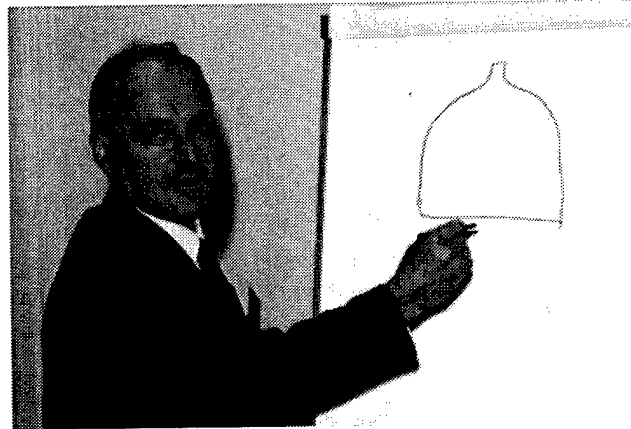
15. D.C. Tran, *Anal. Chem.*, 64(20), 971A-981A, (1992).
16. X.Wang, *Laser Focus World*. May 1992.
17. E.N. Lewis, P.J. Treado, and I.W. Levin, *Appl. Spectrosc.*, 47, 539-543, (1993).
18. H.H. Hopkins, and N.S. Kapany, *Nature*, 2, 41-43, (1954).
19. H.H. Hopkins, In *Endoscopy*, Appleton-Century-Crafts. New York, 27-63, (1976).
20. S.E. Harris, and R.W. Wallace, *J. Opt. Soc. Am.*, 59, 774-781, (1969).
21. I.C. Chang, *Appl. Phys. Lett.*, 25, 370-372, (1974).
22. J. Yu, T.H. Chao, and L.J. Cheng, *Proc. SPIE-Int. Soc. Opt. Eng.*, 1347, 644, (1990).
23. P.J. Treado, I.W. Levin, and E.N. Lewis, *Appl. Spectrosc.*, 46(8), 1211-1216, (1992).
24. I.C. Chang, *Opt. Eng.*, 20, 824-829, (1981).
25. J.M. Lerner, *SPIE Periodic Structures, Gratings, Moiré Patterns and Diffraction Phenomena*, 240, 82, (1980).
26. C.D. Tran and R.J. Furlan, *Appl. Spectrosc.*, 46, 1092-1097, (1990).
27. J. Widom and H.P. Feng, *Rev. Sci. Instr.*, 60, 3231-3238, (1989).
28. R.B. Bilhorn, P.M. Epperson, J.V. Sweedler, and M. Bonner Denton. *Appl. Spectrosc.*, 41(7), 1125-1136, (1987).
29. Y.F. Cheng, R.D. Piccard, and T. Vo-Dinh. *Appl. Spectrosc.*, 44(5), 755-765, (1990).
30. R.B. Bilhorn, P.M. Epperson, J.V. Sweedler, G.R. Sims and M. Bonner Denton. *Anal.Chem.*, 60(5), 327A-335A, (1988).
31. R.B. Bilhorn, P.M. Epperson, J.V. Sweedler, G.R. Sims and M. Bonner Denton. *Anal.Chem.*, 60(4), 282A-291A, (1988).
32. R.B. Bilhorn, P.M. Epperson, J.V. Sweedler, and M. Bonner Denton, *Appl. Spectrosc.*, 41(7), 1114-1125, (1987).
33. J.E. Pemberton, R.L. Sobocinski, and G.R. Sims, *Appl. Spectrosc.*, 44(2), 328-330, (1990).
34. G. Béal, G. Boucharlat, J. Chabbal, J.P. Dupin, B. Fort, and Y. Mellier, *Opt. Eng.*, 26(9), 902-910, (1987).
35. M.E. Dunham. *Rev. Sci. Instrum.*, 60 (9), 2915-2919, (1989).
36. J.P. Alarie, D.L. Stokes, W.S. Sutherland, and T. Vo-Dinh, *Appl. Spectrosc.*, 46, 1608-1614, (1992)



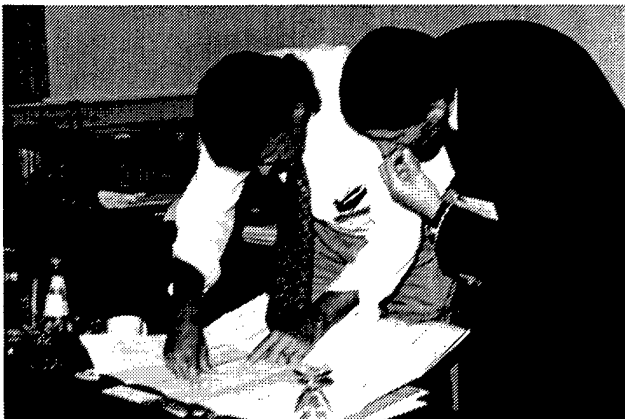
- |                            |                           |                            |
|----------------------------|---------------------------|----------------------------|
| 1. Dr. Andrzej W. Miziolek | 15. J. A. Carter III      | 29. C. J. Thong            |
| 2. Prof. V. B. Voloshinov  | 16. Dr. C. L. Chen        | 30. John Goodell           |
| 3. Prof. V. I. Pustovoi    | 17. Dr. Tuan Vo-Dinh      | 31. Jeffrey S. Himmel      |
| 4. W. Danley               | 18. Dr. J. Turner         | 32. Dr. Victor V. Molotok  |
| 5. Eddie Young             | 19. Satoru Simizu         | 33. Dr. Piotr Becla        |
| 6. Dr. Neelam Gupta        | 20. Lawrence J. Mizerka   | 34. Dan McCarthy           |
| 7. Prof. Chen S. Tsai      | 21. Dr. James O. Jensen   | 35. Dr. Kevin L. McNesby   |
| 8. Dr. Milton Gottlieb     | 22. Capt. Alan C. Samuels | 36. Dr. Edwin D. Lancaster |
| 9. Dr. Yuri B. Pisarevsky  | 23. Dr. L. J. Denes       | 37. Dennis R. Pape         |
| 10. Dr. V. Pelekhaty       | 24. Clyde DeLuca          | 38. Dr. Dan Heglund        |
| 11. Prof. V. V. Kludzin    | 25. Dr. N. F. Fell Jr.    |                            |
| 12. Dr. L.-J. Cheng        | 26. Dr. J. B. Gillespie   |                            |
| 13. Boris Kaminsky         | 27. Dr. E. N. Lewis       |                            |
| 14. Prof. Chieu D. Tran    | 28. Michael J. Uschak     |                            |











## Distribution

Admnstr  
Defns Techl Info Ctr  
Attn DTIC-OCF  
8725 John J Kingman Rd Ste 0944  
FT Belvoir VA 22060-6218

ERDEC  
Attn SCBRD-RTE-E3549 J O Jensen  
Attn CAPT A C Samuels  
APGEA Edgewood MD 21010-5423

Hdqtrs Dept of the Army  
Attn DAMO-FDQ MAJ M McGonagle  
Attn DAMO-FDQ D Schmidt  
400 Army Pentagon  
Washington DC 20310-0460

Night Vsn Dirctr  
Attn L J Mizerka  
10221 Burbeck Rd Ste 430  
FT Belvoir VA 22060-5806

US Military Academy  
Dept of Mathematical Sci  
Attn MAJ D Engen  
West Point NY 10996

Nav Rsrch Lab  
Attn Code 5603 I Aggarwall  
Attn Code 5603 D Daganias  
Washington DC 20375

Oak Ridge Natl Lab  
Attn T Vo-Dinh  
PO Box 2008 MS 6101  
Oak Ridge TN 37831-6101

Case Western Reserve Univ  
Dept of Electrl Engrg  
Attn D A Smith  
Cleveland OH 44106

Institute of Crystallography  
Attn Y Pisarevsky  
Moscow  
Russia

Marquette Univ Dept of Chemistry  
Attn C Tran  
PO Box 1881  
Milwaukee WI 53201

Moscow State Univ Dept of Physics  
Attn V Voloshinov  
Moscow 119899  
Russia

ST Petersburg State Academy of  
Aerospace Instrmntn  
Attn V V Kludzin  
Attn V V Molotok  
67 B Morskaya Str  
ST Petersburg 100000

Univ of California  
Dept of Elect & Computer Engrg  
Attn C S Tsai  
Engineering Gateway Bldg  
Irvine CA 92697

Univ of Pittsburgh  
Chevron Science Center  
Attn J Turner  
Room 314  
Pittsburgh PA 15260

J Goodell  
1201 Southview Rd  
Baltimore MD 21218

Advncd Materials Corp  
Attn C J Thong  
Attn M Uschak  
Attn S G Sankar  
Attn S Simizu  
700 Technology Dr Ste 3311  
Pittsburgh PA 15230-2950

Aurora Assoc  
Attn I C Chang  
3350 Scott Blvd B-20  
Santa Clara CA 95054

## Distribution

Brimrose Corp of America  
Attn S Trivedi  
Attn V Pelekhaty  
Attn W J Danley  
5020 Campbell Blvd  
Baltimore MD 21236

Brookhaven Natl Lab  
Attn C L Chen  
Bldg 197C DAT/SSN  
Upton NY 11973

Brookhaven Natl Lab  
Attn D Heglund  
Box 5000 Bldg 701  
Upton NY 11973

Carnegie Mellon Rsrch Instit  
Attn M Gottlieb  
Attn B Kaminsky  
Attn L J Denes  
700 Technology Dr PO Box 2950  
Pittsburgh PA 15230-2950

Central Design Bureau for Unique  
Instrmnt  
Attn V I Pustovoit  
Moscow 117342  
Russia

Jet Propulsion Lab  
Attn M/S 300-329 L-J Cheng  
4800 Oak Grove Dr  
Pasaolena CA 91109

Massachusetts Instit of Techlgy  
Attn Piotr Becla  
Room 13-4111  
Cambridge MA 02139

Natl Instit of Health  
Attn E N Lewis  
Bldg 5 Room B1-38  
Bethesda MD 20892

Neos Technologies Inc  
Attn E Young  
4300C Fortune Pl  
Melbourne FL 32904

Photonic Sys Inc  
Attn J A Carter III  
Attn D R Pape  
1800 Penn Stret Ste 6  
Melbourne FL 984-8181

Army Rsrch Lab  
Attn AMSRL-PS-ED J S Himmel  
FT Monmouth NJ 07703-5601

US Army Rsrch Lab  
Attn AMSRL-WM-PC A W Miziolek  
Attn AMSRL-WT-PC E D Lancaster  
Attn AMSRL-WT-PC K L McNesby  
Aberdeen Proving Ground MD 21005-  
5066

US Army Rsrch Lab  
Attn AMSRL-CI-LL Tech Lib (3 copies)  
Attn AMSRL-CS-AL-TA Mail & Records  
Mgmt  
Attn AMSRL-CS-AL-TP Techl Pub  
(3 copies)  
Attn AMSRL-IS-EE J B Gillespie  
Attn AMSRL-SE-SS C DeLuca  
Attn AMSRL-SE-EO N Fell  
Attn AMSRL-SE-E J Pellegrino  
Attn AMSRL-SE-EO A Filipov  
Attn AMSRL-SE-EO N Gupta (50 copies)  
Attn AMSRL-SE-ES D McCarthy  
Adelphi MD 20783-1197

<b>REPORT DOCUMENTATION PAGE</b>			Form Approved OMB No. 0704-0188	
Public reporting burden for this collection of information is estimated to average 1 hour per response, including the time for reviewing instructions, searching existing data sources, gathering and maintaining the data needed, and completing and reviewing the collection of information. Send comments regarding this burden estimate or any other aspect of this collection of information, including suggestions for reducing this burden, to Washington Headquarters Services, Directorate for Information Operations and Reports, 1215 Jefferson Davis Highway, Suite 1204, Arlington, VA 22202-4302, and to the Office of Management and Budget, Paperwork Reduction Project (0704-0188), Washington, DC 20503.				
1. AGENCY USE ONLY (Leave blank)		2. REPORT DATE February 1997		3. REPORT TYPE AND DATES COVERED Final, from Jan 1996 to Jan 1997
4. TITLE AND SUBTITLE Proceeding of 1st ARL AOTF Workshop			5. FUNDING NUMBERS PE: 65709A	
6. AUTHOR(S) Neelam Gupta, Editor				
7. PERFORMING ORGANIZATION NAME(S) AND ADDRESS(ES) U.S. Army Research Laboratory Attn: AMSRL-SE-EO 2800 Powder Mill Road Adelphi, MD 20783-1197			8. PERFORMING ORGANIZATION REPORT NUMBER ARL-SR-54	
9. SPONSORING/MONITORING AGENCY NAME(S) AND ADDRESS(ES) U.S. Army Research Laboratory 2800 Powder Mill Road Adelphi, MD 20783-1197			10. SPONSORING/MONITORING AGENCY REPORT NUMBER	
11. SUPPLEMENTARY NOTES AMS Code: P665709.650 ARL Proj: AN7NEGAA				
12a. DISTRIBUTION/AVAILABILITY STATEMENT Approved for public release; distribution unlimited.			12b. DISTRIBUTION CODE	
13. ABSTRACT (Maximum 200 words)  Acousto-optic tunable-filter (AOTF) technology is a recent development that offers potential for rapid, frequency-agile tuning over a large optical wavelength range. An AOTF is an electronically tunable phase grating set up in an anisotropic crystal by the propagation of an ultrasonic wave in the crystal. Such filters have many attractive features, such as small size, lightweight, computer controlled operation, large optical wavelength range of operation, and no moving parts; and their operation can be made ultrasensitive by the use of advanced signal processing algorithms. These filters are being used in many applications such as the design of new spectroscopic instruments, remote detection and monitoring of chemicals, optical communication networks, tuning of laser cavities, etc.				
14. SUBJECT TERMS AOTF, spectrometer, chemical sensing, biological sensing, imaging			15. NUMBER OF PAGES 224	
			16. PRICE CODE	
17. SECURITY CLASSIFICATION OF REPORT Unclassified	18. SECURITY CLASSIFICATION OF THIS PAGE Unclassified	19. SECURITY CLASSIFICATION OF ABSTRACT Unclassified	20. LIMITATION OF ABSTRACT UL	